

# THÈSE

Université de Lille  
réalisée au sein de l'UCCS et de l'IFPEN

## Ecole Doctorale

Sciences de la Matière, du Rayonnement et de l'Environnement

présentée par

**Alexis Sangnier**

en vue de l'obtention du titre de

DOCTEUR EN CHIMIE

Spécialité Molécules et Matière Condensée

Sujet de thèse

---

## **A multiscale approach applied to oxidative heterogeneous catalysis on highly dispersed Pt/Al<sub>2</sub>O<sub>3</sub>**

*Une approche multi-échelle appliquée à la catalyse hétérogène en milieu oxydant sur Pt/Al<sub>2</sub>O<sub>3</sub> hautement dispersé*

---

Soutenue le 19 novembre 2018

## JURY

**Dominique COSTA**, Directrice de recherche CNRS, UPMC

**Rapportrice**

**Laurent CATOIRE**, Professeur des Universités, ENSTA-ParisTech

**Rapporteur**

**Catherine LOUIS**, Directrice de recherche CNRS, Sorbonne Université

**Examinatrice**

**Patrick DA COSTA**, Professeur des Universités, Sorbonne Université

**Examineur et président du jury**

**Christophe DUJARDIN**, Professeur des Universités, ENSCL

**Directeur de thèse**

**Céline CHIZALLET**, Ingénieure H.D.R., IFP Energies nouvelles

**Encadrante de thèse**

**Mickaël MATRAT**, Ingénieur docteur, IFP Energies nouvelles

**Co-encadrant de thèse**



# Résumé

L'objectif de ces travaux réside dans une meilleure compréhension de la catalyse d'oxydation sur un catalyseur Pt/ $\gamma$ -Al<sub>2</sub>O<sub>3</sub> hautement dispersé. La thématique est porteuse dans les domaines de la catalyse de dépollution, de l'oxydation sélective des hydrocarbures ainsi que du développement des piles à combustible. Des phénomènes d'adsorption et d'oxydation ont été étudiés suivant une approche multi-échelle. L'évaluation de phénomènes isolés a été réalisée expérimentalement par désorption et réaction en température programmée, couplée à des analyses de spectrométrie de masse, de FTIR *operando* ainsi que microGC. La modélisation moléculaire *ab initio* a été utilisée afin de comprendre le comportement microscopique de l'interaction adsorbat/catalyseur/support lors de ces réactions. Les données thermodynamiques extraites ont été intégrées à des modèles micro-cinétiques détaillés, et ont permis de comparer les expériences simulées et réelles. Trois systèmes ont été explorés en détail : (i) l'adsorption dissociative de O<sub>2</sub> en oxygène atomique, (ii) l'adsorption de monoxyde de carbone et (iii) son oxydation en CO<sub>2</sub>. L'impact de la structuration du catalyseur a été discuté par rapport aux surfaces idéales telles que Pt(111). L'oxydation d'hydrocarbures légers tels que le méthanol et le propène ont fait l'objet d'une étude préliminaire. Un générateur de réactions de surface a été spécialement développé pour automatiser la génération exhaustive de réactions de surface concernant l'oxydation des hydrocarbures.

---

Mots-clefs : Catalyse d'oxydation, Pt/ $\gamma$ -Al<sub>2</sub>O<sub>3</sub> hautement dispersé, modélisation moléculaire, simulation micro-cinétique, TPR et TPD, état de surface en milieu oxydant, oxydation de CO, hydrocarbures légers

---



# Abstract

This work tackles at a better understanding of oxidation catalysis on highly dispersed Pt/Al<sub>2</sub>O<sub>3</sub> surface. This thematic is of great interest for depollution catalysis, for hydrocarbon selective oxidation or even for fuel cell development. Adsorption and oxidation phenomena were studied with a multi-scale approach. Experimental evaluations of isolated phenomena were performed using temperature programmed adsorption/reaction coupled with mass spectrometry, *operando* FTIR and microGC. *Ab initio* molecular modelling investigations were undertaken to handle the microscopic behaviour of adsorbate/catalyst/support interactions. Thermodynamic data were integrated into exhaustive micro-kinetic models that allow to compare experiments and modelled data. Three systems were fully explored: (i) the dissociative adsorption of O<sub>2</sub> into atomic oxygen, (ii) adsorption of carbon monoxide and (iii) oxidation of CO towards CO<sub>2</sub>. The impact of the catalyst structuration has been discussed with ideal surfaces such as Pt(111). Light hydrocarbons oxidations such as methanol and propene were also investigated in a preliminary way. Surface reaction mechanism generator was specially developed to handle exhaustive hydrocarbon oxidation surface reactions.

---

Keywords : Catalytic oxidation, highly dispersed Pt/ $\gamma$ -Al<sub>2</sub>O<sub>3</sub>, molecular modelling, micro-kinetic simulation, TPR and TPD, oxidation surface state, CO oxidation, light hydrocarbons

---



# Remerciements

En premier lieu, je tiens à remercier IFP Energies nouvelles et Messieurs Antonio Pires Da Cruz et Stéphane Henriot de m'avoir accueilli au sein de la direction Systèmes Moteurs et Véhicules pendant ces trois années et d'avoir permis la réalisation de ce projet de recherche dans d'excellentes conditions.

Je tiens à remercier mon directeur de thèse, Christophe Dujardin, professeur à l'école de chimie de Lille pour avoir suivi l'ensemble de mes travaux avec intérêt.

Je remercie chaleureusement Céline Chizallet de la Direction Catalyse et Séparation d'IFP Energies Nouvelles à Solaize pour ses encouragements et sa patience envers mon apprentissage de la DFT. Ses conseils avisés m'ont été précieux pour réaliser au mieux ces recherches. Nos échanges m'ont beaucoup apporté.

Je remercie Mickaël Matrat et André Nicolle de m'avoir soutenu pendant ma thèse. A André, avec qui nos échanges ont été tant riches que divers. A Mickaël, pour ses conseils techniques et son pragmatisme fort utile.

Je remercie Madame Dominique Costa et Monsieur Laurent Catoire pour avoir accepté de rapporter cette thèse. Je remercie également Madame Catherine Louis et Monsieur Patrick Da Costa d'avoir accepté de faire partie du jury de thèse.

Merci à tous les collègues de l'UCCS qui ont contribué de près ou de loin à ce projet de recherche. Je pense notamment à Eric Genty ainsi qu'Olivier Gardoll pour leurs collaborations aux travaux expérimentaux de cette thèse. Les collègues d'IFP Energies Nouvelles ne sont pas en reste. Merci à Carine Guegan et Fabrice Diehl de m'avoir ouvert les portes de leur laboratoire pour la synthèse des catalyseurs.

Un grand merci à Benoît, Julien, Mamady et Elias pour l'atmosphère de travail agréable et conviviale. A Antoine, Matthieu et Fabien pour nos moments de détente.

Enfin, je remercie mes amis et ma famille pour avoir été à mes côtés non seulement pendant ces trois années, mais aussi tout au long de ma vie.

Un merci tout particulier à mon frère Maxime, pour son rôle d'éclaireur dans les études supérieures, et pour notre discussion sur la théorie des graphes.



# Table of contents

Table of contents.....	9
Introduction .....	15
1  Context .....	17
1.1  Emissions from compression ignition engines .....	17
1.1.1  Combustion and exhaust gas .....	17
1.1.2  Hydrocarbon speciation.....	19
1.2  Diesel oxidation catalyst .....	23
1.2.1  Diesel aftertreatment line .....	23
1.2.2  Catalytic material in DOC.....	24
1.2.3  Catalytic sites and relation with particle size.....	28
1.3  Aim of the thesis .....	29
2  Methods.....	33
2.1  Multi-scale approach .....	33
2.2  Experimental catalysis .....	34
2.2.1  Catalyst preparation and characteristics .....	35
2.2.2  Reactors and analysers.....	37
2.2.3  Temperature programmed experiments .....	39
2.2.4  Determination of heats of adsorption of CO.....	41
2.3  <i>Ab initio</i> quantum molecular modelling .....	42
2.3.1  <i>Ab initio</i> calculations .....	42
2.3.2  Calculations undertaken in this work .....	47
2.4  Micro-kinetic simulations .....	56
2.4.1  Micro-kinetics and catalysis .....	56
2.4.2  Chemkin software .....	60
2.4.3  Micro-kinetics and molecular modelling.....	62

2.4.4	Estimated micro-kinetics.....	64
3	Dissociative adsorption of O <sub>2</sub> on Pt/ $\gamma$ -Al <sub>2</sub> O <sub>3</sub> .....	72
3.1	Introduction .....	72
3.2	Experimental results .....	74
3.2.1	Experimental protocol.....	74
3.2.2	O <sub>2</sub> -TPD experiments .....	74
3.3	<i>Ab initio</i> simulation of oxygen adsorption reactions.....	75
3.3.1	Adsorption of atomic oxygen .....	76
3.3.2	Evolution of adsorption properties with O coverage and cluster structuration.....	78
3.3.3	Activation energy for the dissociation of O <sub>2</sub> .....	83
3.4	Kinetic modelling of O <sub>2</sub> -TPD .....	85
3.4.1	Impact of the dispersion on O <sub>2</sub> -TPD .....	86
3.4.2	Reaction paths analyses.....	88
3.5	Conclusion.....	89
4	Carbon monoxide adsorption on Pt/ $\gamma$ - Al <sub>2</sub> O <sub>3</sub> .....	91
4.1	Introduction .....	91
4.2	<i>Ab initio</i> simulation of carbon monoxide adsorption.....	93
4.2.1	Adsorption of a single carbon monoxide molecule .....	93
4.2.2	Adsorption of CO at higher coverages .....	95
4.3	Determination of experimental CO vibration frequencies and heats of adsorption .....	99
4.3.1	Influence of Pt oxidation state on the IR spectra of adsorbed CO species .....	100
4.3.2	Heat of adsorption of the linear and bridged CO species on the two catalysts.....	103
4.4	Comparison of experimental and DFT data.....	104
4.4.1	At thermodynamic equilibrium.....	104
4.4.2	CO-TPD and micro-kinetic modelling .....	107
4.5	Conclusion.....	111
5	Carbon monoxide oxidation on Pt/ $\gamma$ -Al <sub>2</sub> O <sub>3</sub> .....	113
5.1	Introduction .....	113

5.2	Experimental oxidation of CO .....	114
5.2.1	Light-off measurement .....	115
5.2.2	Global kinetic parameters .....	116
5.3	Molecular modelling of CO oxidation .....	118
5.3.1	Co-adsorption of O and CO on Pt <sub>13</sub> /γ-Al <sub>2</sub> O <sub>3</sub> .....	119
5.3.2	Carbon monoxide oxidation on Pt <sub>13</sub> /γ-Al <sub>2</sub> O <sub>3</sub> .....	125
5.3.3	Impact of adsorbed water .....	128
5.4	Micro-kinetic modelling of CO oxidation.....	132
5.4.1	MOL and DES models: sole oxidation micro-kinetics.....	133
5.4.2	VAR and CPX models: CO <sub>2</sub> desorption dependence.....	135
5.5	Conclusion.....	139
6	Light hydrocarbons oxidation .....	143
6.1	Introduction .....	143
6.2	Oxidation experiments .....	145
6.2.1	Oxidation of methanol .....	145
6.2.2	Oxidation of propene .....	151
6.3	Molecular modelling of C <sub>0</sub> -C <sub>3</sub> on Pt(111) .....	155
6.3.1	Atomic and molecular adsorption .....	156
6.3.2	Adsorption of radicals .....	158
6.4	Preliminary micro-kinetic simulations of methanol oxidation .....	162
6.5	Conclusion.....	166
7	Conclusions and perspectives .....	169
	Appendices .....	173
	Appendices A: Dissociative adsorption of oxygen on Pt/γ-Al <sub>2</sub> O <sub>3</sub> .....	173
	A.1. Determination of dimensionless quantities of experimental reactor .....	173
	A.2. Illustration of a typical velocity-scaled MD run with cluster reconstruction .....	174
	A.3. Optimisation of the TPD protocol.....	175
	A.4. Deconvolution of the TPD profiles .....	176
	A.5. Dissociative adsorption of O <sub>2</sub> on Pt(111) investigated by <i>ab initio</i> calculations .....	177

A.6. Most stable structures found for the supported $\text{Pt}_{13}\text{O}_n$ system from <i>ab initio</i> calculations .....	180
A.7. Transition structures for the dissociation of $\text{O}_2$ .....	182
A.8. Kinetic parameters for the $\text{Pt}_{13}\text{O}_n$ model and Pt(111) model .....	184
Appendices B: Carbon monoxide adsorption on Pt/ $\gamma$ - $\text{Al}_2\text{O}_3$ .....	186
B.1. Non supported $\text{Pt}_{13}$ cluster and Pt(111) extended surface .....	186
B.2. Illustration of a typical velocity-scaled MD run with $\text{Pt}_{13}(\text{CO})_9$ cluster reconstruction .....	187
B.3. Impact of <i>ab initio</i> frequencies treatment on adsorption thermodynamic data.....	187
B.4. Desorption enthalpy and entropy interpolation on $\text{Pt}_{13}(\text{CO})_m$ structures	190
B.5. Most stable structures found for the supported $\text{Pt}_{13}(\text{CO})_m$ from <i>ab initio</i> calculations .....	191
B.6. Bader charges for the supported $\text{Pt}_{13}(\text{CO})_m$ structures .....	194
B.7. Experimental mass spectrometry recording during AEIR .....	195
B.8. Extended study of CO sticking coefficient parameter $s$ on the micro-kinetic scheme .....	196
B.9. Kinetic desorption parameters of $\text{Pt}_{13}(\text{CO})_m$ systems.....	197
Appendices C: Carbon monoxide oxidation on Pt/ $\gamma$ - $\text{Al}_2\text{O}_3$ .....	198
C.1. $\text{Pt}_{13}\text{O}_n(\text{CO})_m$ <i>ab initio</i> structures.....	198
C.2. Thermodynamic diagram snapshots.....	198
C.3. $\text{Pt}_{13}\text{O}_n(\text{CO})_m(\text{CO}_2)$ <i>ab initio</i> structures .....	200
C.4. Bader charge analyses of $\text{Pt}_{13}\text{O}_n(\text{CO})_m$ structures.....	202
C.5. $\text{Pt}_{13}\text{O}_n(\text{CO})_m(\text{CO}_2)\text{H}_2\text{O}$ <i>ab initio</i> structures .....	203
C.6. Simulation of $\text{O}_2$ and CO-TPD with CO oxidation scheme .....	205
C.7. Chemkin calculation conditions for CO oxidation .....	205
C.8. Kinetic parameters of MOL models.....	208
C.9. DES- $\text{Pt}_{13}\text{O}_4(\text{CO})$ : reaction fluxes and surface species.....	210
C.10. DES- $\text{Pt}_{13}\text{O}_{16}(\text{CO})_7$ : reaction fluxes and surface species .....	212
C.11. VAR models: $\text{CO}_2$ desorption parameters.....	214
C.12. VAR- $\text{Pt}_{13}\text{O}_4(\text{CO})$ : reaction fluxes and surface species .....	215
C.13. VAR- $\text{Pt}_{13}\text{O}_{16}(\text{CO})_7$ : reaction fluxes and surface species .....	217
C.14. CPX <sub>spi</sub> - $\text{Pt}_{13}\text{O}_4(\text{CO})$ -eq: reaction fluxes and surface species .....	219
Appendices D: Light hydrocarbons oxidation .....	221
D.1. Infrared differential spectra during methanol and propene oxidation .....	221

D.2. C <sub>0</sub> adsorbed species.....	223
D.3. C <sub>1</sub> adsorbed species.....	225
D.4. C <sub>2</sub> adsorbed species.....	228
D.5. C <sub>3</sub> adsorbed species.....	238
List of figures .....	240
List of tables.....	251
References.....	253



# Introduction

Oxidation catalysis holds a prominent place in surface science and catalytic chemistry. A wide application range has been developed during decades. Catalytic oxidation is nowadays a major tool for both oil industry and sustainable development. These scopes of applications are presently very active.

Historically, petro-chemistry uses oxidation catalysis to convert hydrocarbons into oxygenated intermediate chemicals for other industries: pharmaceutical, polymers, adhesives and paintings, cosmetics or chemicals production<sup>1,2</sup>. These methods are now used in the context of biomass valorisation<sup>3</sup>. Electro-catalysis is also a major domain for fuel cell improvement, as well as water gas shift reaction for dihydrogen production from water and carbon dioxide<sup>4</sup>. Finally one may quote aftertreatment of combustion engines that aim at lowering exhaust gas harmfulness<sup>5,6</sup>.

For all these applications, the catalyst synthesis parameter space has been explored many times, leading to efficient catalysts. The link between catalyst efficiency and its structure (often linked to the particle size) has been explored for some time now in the case of metal catalysts, some reactions being known to be structure sensitive, others not<sup>7</sup>. Yet the deep understanding of molecular phenomenon onto the surface is a wide ongoing topic. Surface molecular modelling is a key tool for this issue. From now, it has been performed on simple models (extended metal surfaces, without consideration of the effect of surface coverage) to answer molecular level issues, with few parameters to benchmark<sup>8</sup>. The consideration of these simple models appeared to be strongly insufficient when dealing with dispersed metallic catalysts for example<sup>9</sup>.

Oxidation catalysis applied to Diesel engine aftertreatment is at the present time a major concern for transport industry, supported by ambitious legislations. In the present study, we opted especially for hydrocarbon (HC) and carbon monoxide (CO) oxidation, that is handled by the Diesel Oxidation Catalyst (DOC). Among the elemental diversity of catalytic materials currently used for Diesel vehicles aftertreatment, platinum supported on gamma alumina is a versatile catalyst model.

What is the oxidation state of highly dispersed Pt/ $\gamma$ -Al<sub>2</sub>O<sub>3</sub> ? How does CO and hydrocarbons reacts on this kind of surface ? What is the behaviour of the adspecie/catalyst/support system? Is all the reactivities different from ideal surfaces ? Are these phenomenon easy to forecast ?

To answer these questions, this thesis used a multi-scale approach developed with the following tools. Experiments (TPD, TPR – temperature programmed desorption/reaction, *in situ* Infra-Red spectroscopy, and light-off measurements) were performed on highly dispersed Pt/ $\gamma$ -Al<sub>2</sub>O<sub>3</sub> to quantify the reactivity of temperature programmed desorptions (O<sub>2</sub>, CO) and oxidation (CO, light hydrocarbons) reactions. This allows to gather macroscopic data on the system, complemented by the characterization at the microscopic scale of reaction intermediates by *in situ* Infra-Red spectroscopy. Molecular modelling studies of a Pt/ $\gamma$ -Al<sub>2</sub>O<sub>3</sub> model representative of the real catalyst were performed to understand the given phenomenon at the atomic scale. The Vienna *ab initio* Simulation Package (VASP) was used. Thermokinetic data were calculated from the investigated configurations to determine micro-kinetic parameters needed to build a kinetic model. The software ChemkinPro allows to simulate the relative experiments, so that both microscopic and macroscopic phenomenon were compared. In addition, the successive studies allow to generate a complex micro-kinetic model representative of oxidation catalysis on highly dispersed Pt/ $\gamma$ -Al<sub>2</sub>O<sub>3</sub>.

The present work intends to apply this multi-scale approach on a peculiar system: carbon monoxide and hydrocarbons oxidation from Diesel exhaust gas. It must however be considered as a fruitful developed method, suitable to a much larger scope. Moreover achieved results are relevant for all the applications stated above.

The first chapter of this manuscript deals with the global context of oxidation catalysis and particularly the Diesel depollution catalysis, that has been used as a case study. The multiscale approach developed for this work is explained in chapter 2, as well as the tools specially developed for this work. The oxidation state of highly dispersed platinum was studied in chapter 3, corresponding to the dissociative adsorption of O<sub>2</sub>. In a similar way, adsorption of CO is handled in chapter 4. The investigation of carbon monoxide oxidation, on the basis of the findings of the two prior chapters, is reported in chapter 5. Chapter 6 deals with light hydrocarbon oxidation, combining experimental TPR and preliminary *ab initio* calculations and kinetic modelling. Finally, the last chapter is devoted to the conclusions and perspectives of this work.

# 1 | Context

## 1.1 | Emissions from compression ignition engines

### 1.1.1 | Combustion and exhaust gas

Combustion is a complex physico-chemical phenomenon used in many applications for energy production. From a chemical point of view, combustion consists of a multitude of reactions being related to the hydrocarbon oxidation. This type of phenomenon is complete when products are limited to water and carbon dioxide. This is an ideal case. Combustion is often incomplete especially when considering the transport applications due to non-stoichiometric conditions and spatial heterogeneities within the combustion chamber. It leads to intermediate products, such as partially oxidized hydrocarbons, carbon monoxide and soot<sup>10,11</sup>.

Being an interesting case study as well as a key technology enabling many developments for oxidation catalysis, Diesel engines have been facing many technical issues related to the combustion emissions. In this kind of engines, combustion is initiated by fuel self-ignition. In a first step, air is injected into the combustion chamber. Then gas compression reaches 25 to 30 bars and 600°C<sup>11</sup>. At the end of compression, fuel injection occurs at high pressure. These conditions allow the fuel to ignite spontaneously. Combustion is rarely reproducible and large heterogeneities exists. There is therefore fluctuations in the exhaust hydrocarbon speciation during steady state engine use. Transient starts and accelerations, among others, add more fluctuations. Also criteria such as fuel composition or driver behaviour play a role<sup>11</sup>.

In order to be approved by the different legislations around the world regarding exhaust gas limitations, an aftertreatment system is located in the exhaust line. It must be considered that the exhaust composition is a complex mixture. The exhaust is a tri-phasic mixture<sup>5</sup>, mainly composed of gas but also solids and liquids. The different classes of compounds of which are listed below (Figure 1):

- Inert gases and final combustion products account for approximately 98% by volume of the exhaust gas composition. Indeed gases such as N<sub>2</sub>, O<sub>2</sub>, CO<sub>2</sub>, H<sub>2</sub>O and noble gases are emitted. It should be noted that the oxygen partial pressure rises at about 10<sup>-1</sup> bar for a stabilized regime. This is one of the main differences

compared to the output of a spark ignition engine. The medium is therefore oxidative. This is one of the main differences compared to the output of a spark ignition engine.  $N_2$  is an inert gas in ambient conditions. However temperature is so high in the combustion chamber that it reacts to produce nitrogen oxides ( $NO_x$ ) as well as nitrogenous hydrocarbons<sup>5,11</sup>. Also ammonia and  $N_2O$  are generated by the post-treatment system<sup>12</sup>. As for  $CO_2$  and  $H_2O$ , they are present at the intake but also produced in large quantities during combustion.

- Carbon monoxide is produced by the incomplete combustion of hydrocarbons. It is highly toxic for every mammals, including human, due to oxygen transport stemming in blood<sup>13</sup>. From an environmental point of view, it contributes to ozone depletion<sup>14</sup>.
- Nitrogen oxides  $NO_x$  ( $NO$  and  $NO_2$ ) are formed during combustion. In the case of nitrogen free hydrocarbons, the main source of  $NO$  comes from oxidation of  $N_2$  by  $O^\bullet$  and  $OH^\bullet$  radicals. The elevated temperature favors nitrogen bond breaking and a  $NO_x$  formation takes place according to the Zeldovich mechanism<sup>15</sup>.
- Sulphur oxides  $SO_x$  ( $SO_2$  and  $SO_3$ ) are produced during the combustion of sulfur-containing hydrocarbons (thiophenes and mercaptans) initially present in the fuel. Despite fuel standards on the sulfur content (less than 10 ppmS), sulphur oxides can poison a Lean  $NO_x$  Trap (abbreviated LNT) catalyst, as they adsorb onto it and instead of  $NO_x$ , stemming further conversion<sup>16</sup>.
- Hydrocarbons present in the exhaust are a multitude of chemical compounds<sup>17-19</sup>. The main two sub-categories are PAHs (Polycyclic Aromatic Hydrocarbons) and VOCs (Volatile Organic Compounds). PAHs are massive hydrocarbons that can lead to soot formation, while VOCs cover organic molecules in the atmosphere<sup>10,11</sup>. PAHs and VOCs are present in gaseous form, such as formaldehyde or liquid (in droplets suspended in the gas or adsorbed on the soot surface), such as naphthalene when exhaust line is cold. There are also oxygenated VOCs, which have a higher reactivity in the atmosphere than non-oxygenated VOCs<sup>20</sup>. The combustion being incomplete, fuel itself can be found as well as intermediate stable products due to a partial fuel oxidation or pyrolysis within the combustion chamber.
- Soots are solid particles ranging from 10 nm to 1  $\mu m$  and mainly composed of carbon. They are formed by dimerization and aggregation of PAH.

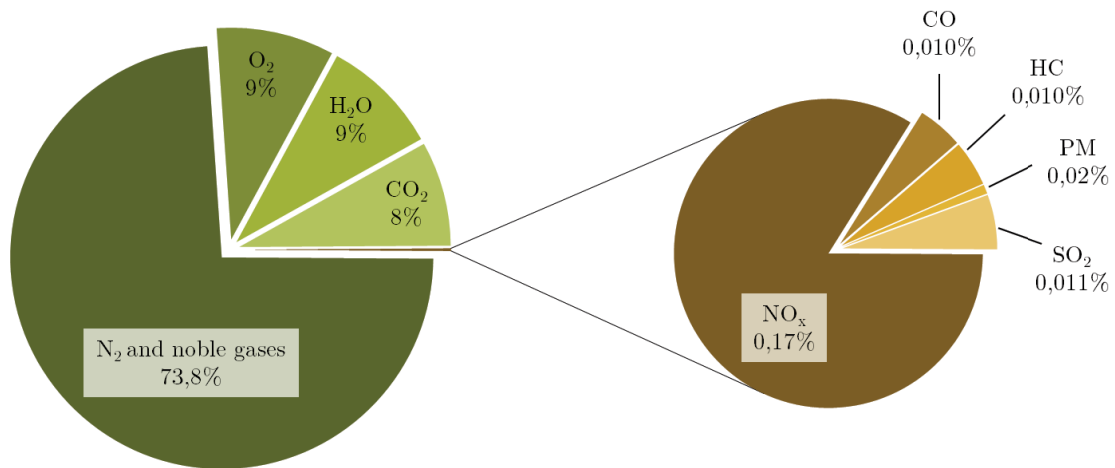


Figure 1: Composition example of an untreated exhaust at the Diesel engine outlet, in volume<sup>21</sup>.

As Diesel contains heavy hydrocarbons (C<sub>14</sub> to C<sub>20</sub>), the production of unburned hydrocarbons and soot is significant. This leads to the search for a compromise and to develop aftertreatment devices that can degrade these two pollutants<sup>11,22</sup>. These differences imply a distinct global approach to automotive pollution control, depending on the type of fuel used, including the generation of soot in Diesel engines and absence of oxygen in the gasoline exhaust.

### 1.1.2| Hydrocarbon speciation

Since hydrocarbons can go through the combustion chamber without being totally consumed, the resulting composition is complex. Many studies have been performed to understand hydrocarbon diversity at the engine exhaust. The choice of assembly, type of analysis and fuel makes difficult any comparison between these studies. In addition and to illustrate the complexity of this analysis, a multitude of quantities are used, for instance ppm, mg.kW<sup>-1</sup>.h<sup>-1</sup>, g.km<sup>-1</sup> traveled, g.kg<sup>-1</sup> of fuel or ppmC.

Concentrations<sup>i</sup> from the study of Dec and Davisson<sup>17</sup> illustrates this diversity and some key compounds detected by other studies (Figure 2). This study is based on an isooctane fueled Diesel engine. As isooctane is the fuel, one can find it in the exhaust in large quantity. It actually provides an overview of the amount of unburned

---

<sup>i</sup> The averages, quartiles, minima and maxima were calculated from the experiments with various richnesses: 0.081, 0.122, 0.162, 0.202, 0.243 and 0.283

hydrocarbons that one can find in real Diesel exhaust. This is confirmed by other studies using real fuels, for which iso-octane is not predominant<sup>23</sup>.

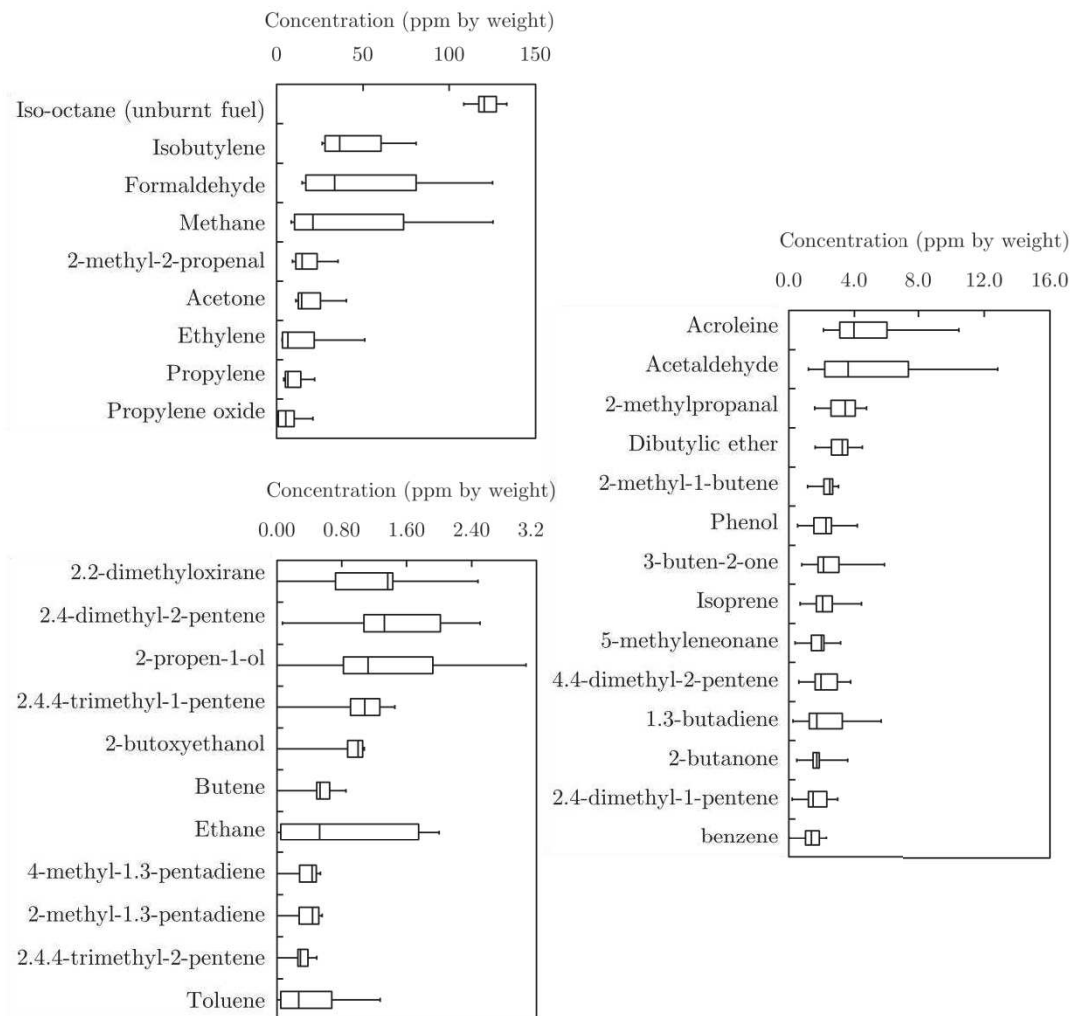


Figure 2: Hydrocarbon concentrations after Diesel engine (iso-octane fuel) with richness ratios from 0.081 to 0.283, adapted from Dec and Davisson<sup>17</sup>.

Alkanes are easily detectable. Small chain alkanes from methane to butane are present<sup>19,23-27</sup>. Linear and branched alkanes from  $C_5$  to  $C_{16}$  are also found<sup>19,23,25-30</sup>. Some studies show long linear molecules such as pristane ( $C_{19}H_{40}$ ), phytane ( $C_{20}H_{42}$ ) or heneicosane ( $C_{21}H_{44}$ )<sup>23</sup>. Cycloalkanes are also recorded with 5 carbons<sup>19,23,25,26</sup> but mainly  $C_6$ <sup>19,23,25</sup> type are found with alkyl substituents of  $-CH_3$  to  $-C_9H_{19}$ . Alkenes are also clearly identified. Ethylene, propene<sup>17,19,23-27,30-32</sup> but also linear and branched alkenes from  $C_4$  to  $C_{11}$ <sup>17,28</sup> are found. Dienes are mainly represented by butadiene<sup>23,25-27,29</sup> but also pentadienes and hexadienes. Alkynes are poorly detected, except in rich environments, probably because of their high reactivity, especially acetylene<sup>19,24-26</sup> and propyne<sup>23,25</sup>. Experimental studies however noticed long-chain alkynes formation during combustion<sup>33</sup>.

Few simple alcohols such as methanol, propanol and isomers of butanol<sup>17,19,23,29,34,35</sup> were detected. Few aldehydes containing 12 carbon atoms are detected<sup>23</sup>, but studies are only unanimous between C<sub>1</sub> and C<sub>4</sub><sup>11,17,19,23,29,34</sup>. Some ketones are present, generally C<sub>3</sub> and C<sub>4</sub><sup>23,29,19,34,17</sup>. Formaldehyde and acetone are predominant hydrocarbons in the exhaust gas. In addition, unsaturated oxidated molecules such as epoxyethylene, acrolein, crotonaldehyde and glyoxal are observed<sup>11,23,30,34</sup>. Concerning carboxylic acids and their derivatives, sparse data exist and testify of long carbon chains up to 20 atoms<sup>23</sup>.

Into the internal combustion engine, key mechanisms are identified within certain temperature ranges<sup>36,37</sup> (Figure 3). The low temperature mechanism is characterized by a mild oxidation of hydrocarbons creating alcohols and peroxide groups. They can induce a dehydrogenation of hydrocarbons, followed by pyrolysis (*i.e.* C-C bond splitting). At high temperature a first pyrolysis step giving light hydrocarbons is noticed. Afterwards they strongly oxidize until the complete oxidation to CO and CO<sub>2</sub> is observed. At intermediate temperatures, the formation of peroxy radicals by dehydrogenation prevails over that of high temperature alkyls. The formation of multiple bonds (alkenes and alkynes) happens, as well as the formation of cyclic ethers.

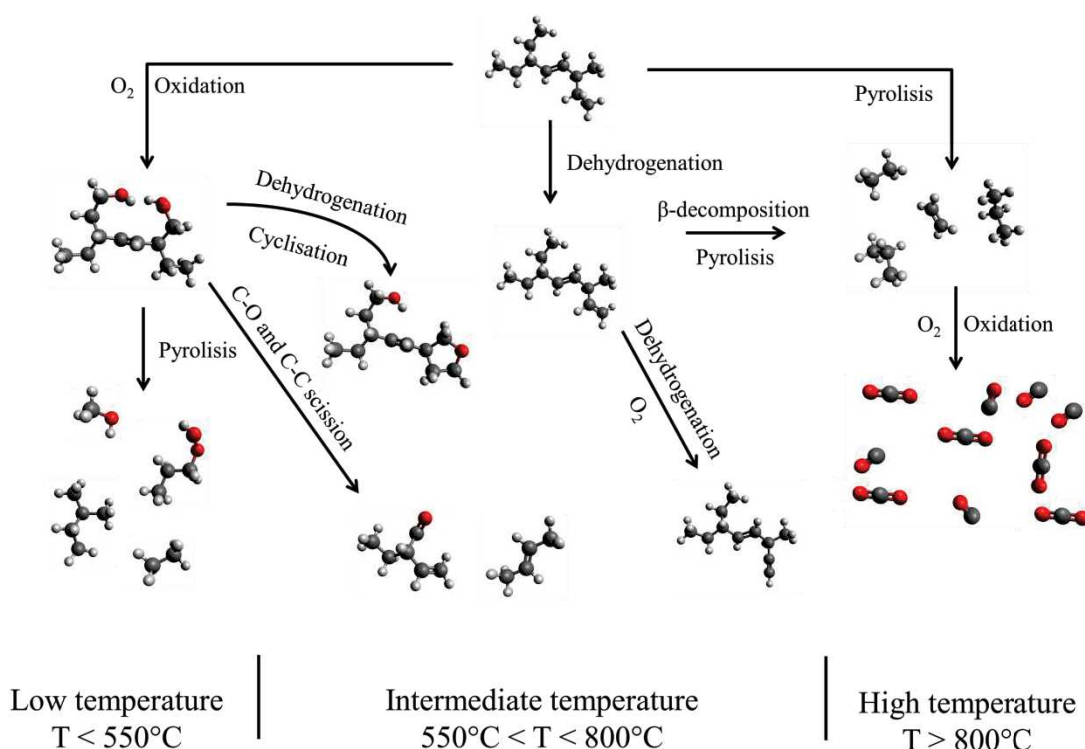
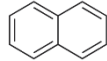
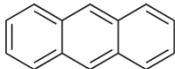
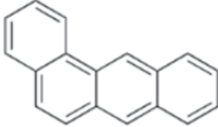
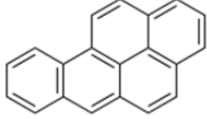
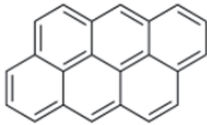


Figure 3: Mechanism of combustion of hydrocarbons in the engine<sup>36,37</sup>.

Benzene derivatives, *i.e.* containing only one aromatic ring, are numerous with alkyl substituents<sup>19,25,27,28,30</sup>, including toluene, cumene<sup>19,25,28</sup>, xylene<sup>19,26,27</sup> or styrene<sup>25,29,26</sup>. Oxidized derivatives have not been well studied. Yet benzaldehyde and its

derivatives<sup>19,23,29,34</sup>, acetophenone, indanone and tolualdehyde<sup>19,23</sup> were found. A recent study has identified indanone, naphthoquinone, naphthaldehyde, 9-fluorenone and 1,2-acenaphthylenequinone among others<sup>18</sup>. Polycyclic aromatic hydrocarbons are easily detected and start with two aromatic rings such as naphthalene<sup>19,23,29,34</sup> and indane<sup>11,25,28</sup> up to seven nuclei with coronene<sup>11,30</sup>. Experimental studies have so far not found larger hydrocarbons than the latter. Table 1 lists mostly found polyaromatic compounds. Some studies have identified oxidized PAHs such as hydrofuran<sup>17</sup>, indanone and xanthene<sup>23</sup>. Other heteroatoms are present such as chlorine or nitrogen, including<sup>11,31</sup> nitropyrene, chlorobenzopyrene, chloropyrene and chloro-fluoranthene<sup>11</sup>.

Table 1: Some PAHs detected in the Diesel exhaust by several studies<sup>11,19,23,27-29,32,34,38,39</sup>. The structural formula corresponds to the name in bold.

Ring number	Detected PAH	Structural formula
2	Naphtalene, indane	
3	Anthracene, phenantrene, acenaphthene, fluorene	
4	Benzo[a]anthracene, chrysene, fluoranthene	
5	Benzo[a]pyrene, benzo[1]fluoranthene, benzo[k]fluoranthene	
6	Anthanthrene, benzo[ghi]perylene, indeno[1,2,3,cd]pyrene	
7	Coronene	

To conclude, the majority of the engine out exhaust gas is composed of inert compounds. Dioxygen concentration is in excess for combustion consideration, around 10% in volume. Regarding pollutants NO<sub>x</sub>, SO<sub>x</sub> and carbon monoxide are the main clearly identified species. Unburnt hydrocarbons constitute however a wide pollutant class. Their emissions are changing in both composition and concentrations due to a

large set of parameters: (i) the fuel composition and (ii) the combustion process are the key drivers.

## 1.2| Diesel oxidation catalystr

### 1.2.1| Diesel aftertreatment line

History of automotive engines after-treatment is marked by key dates. For instance, this is the case of the emergence of oxidation catalysis in 1975 on gasoline vehicles, a technology that will begin in 1995 for Diesel vehicles. This discrepancy is the consequence of two different regulations and pollutant classes. Implementation and improvement of the aftertreatment line greatly affected the reduction of polluting emissions of vehicles. Today Diesel vehicle aftertreatment line consists of several devices (Figure 4).

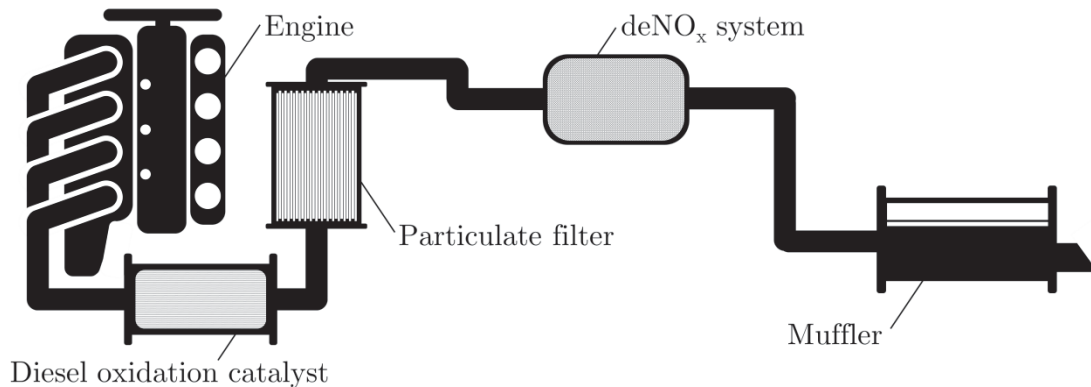


Figure 4: Scheme of Diesel aftertreatment line, adapted from Sassi *et al.* technical notes<sup>40,41</sup>. The Diesel oxidation catalyst is generally placed after the engine. Particulate filter and deNO<sub>x</sub> systems. Exhaust Gas recirculation (abbreviated EGR) system is sometimes installed on the line to lower NO<sub>x</sub> emissions. The muffler is present to reduce noise emitted by the engine.

The particulate filter is set up for the first time in the 2000s on Peugeot 607 to avoid the rejection of exhaust particles down to 10 nanometers, whose average size is of the order of one micrometer<sup>42-44</sup>.

Several techniques for the reduction of NO<sub>x</sub> have been tested. Exhaust Gas Recirculation (EGR) technology that recirculates exhaust gases through the combustion chamber, and Selective Catalyst Reduction (SCR)<sup>45,46</sup> and LNT (Lean NO<sub>x</sub> Trap) technologies, using catalytic reduction, developed in the 1990s<sup>47</sup> are the outstanding systems of NO<sub>x</sub> treatment.

Diesel oxidation catalystr (Figure 5) is generally the closest device to the engine<sup>6</sup>. Indeed, hydrocarbon oxidation depends on exhaust gases temperature. Researches

conducted on DOC position (with one or two devices) demonstrated that it requires more loading of active material if placed further on line<sup>48,49</sup>. The phenomenon is explained by the need to be at a temperature high enough to pass the hydrocarbon oxidation activation barrier. If the temperature is too low, reactions are slower and must be overcome by more active materials.

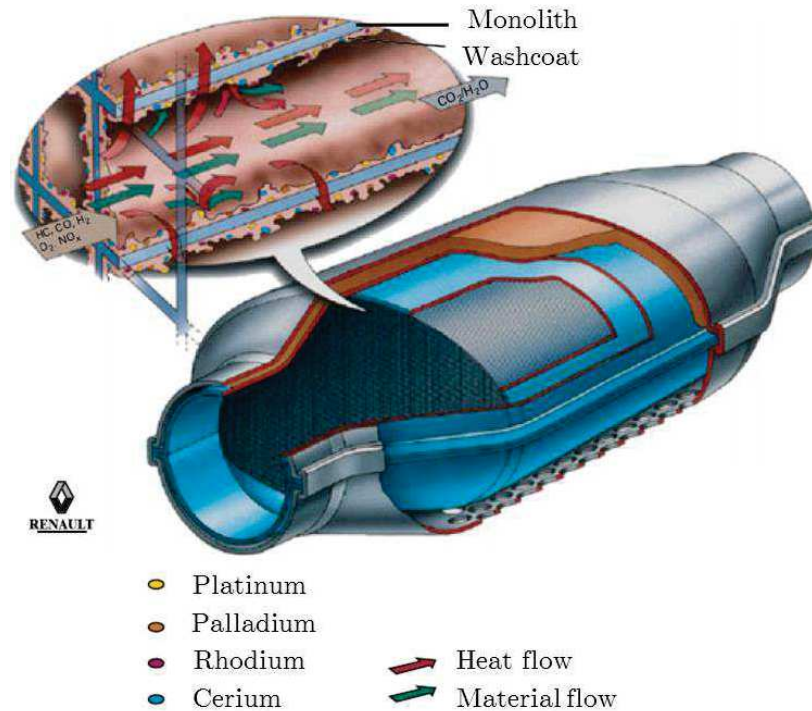


Figure 5: Detailed view of a Diesel oxidation catalyst<sup>41</sup>.

DOC tackles hydrocarbons conversion with oxygen. Ideal products are carbon dioxide and water. The DOC is the first element of exhaust aftertreatment. It is therefore crossed by a flow of three-phase mixture, mainly gaseous. The operating temperature of the DOC is between room temperature and 550°C most of the time, up to 700°C for the close-to-engine ones (close-coupled DOC)<sup>6,41,40</sup>. DOC also plays a role in reducing NO<sub>x</sub> emissions through the oxidation of NO and NO<sub>2</sub>. Thus NO<sub>2</sub>/NO<sub>x</sub> ratio is adjusted for better performance of the LNT and Selective catalytic reduction systems (abbreviated SCR).

### 1.2.2| Catalytic material in DOC

Architecture of the Diesel oxidation catalyst is composed of a monolithic reactor on which a mineral powder, containing the supported catalyst, is coated. The reactor is called monolithic because made of a single block. It comprises a network of fine parallel channels, organized in honeycomb sections. Channel diameter is about one hundred micrometers (Figure 6) in which the exhaust gases flow. This arrangement provides a

large exchange surface to promote catalyst/gas contacts. These elements are made from ceramic or metal alloys<sup>6,40,41</sup>.

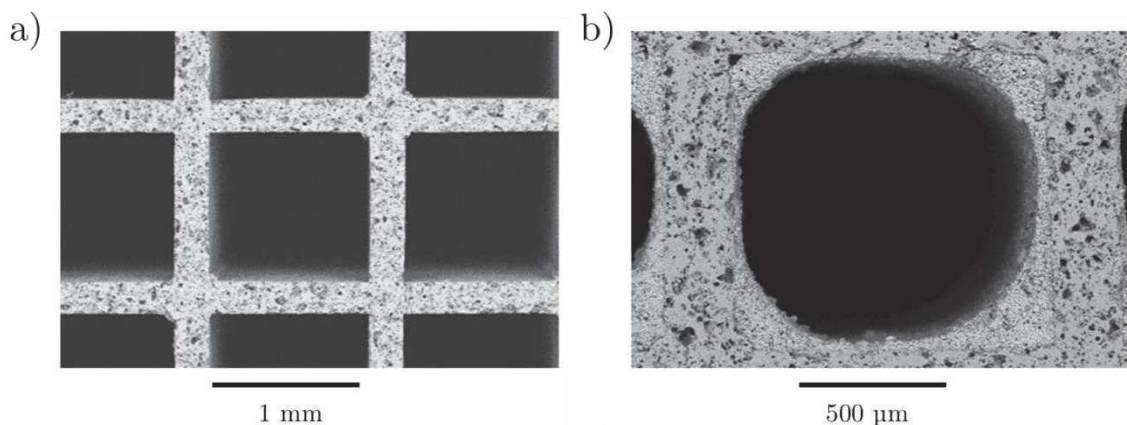


Figure 6: Electron microscopy of channels of a monolith a) without and b) with washcoat<sup>50</sup>.

The structure must meet several technical rules such as the good coating of the catalytic material, a high resistance to thermal and mechanical shocks and a high thermal stability, among others. Finally, the reactor must provide the minimal pressure drop on the exhaust line to not impact the engine performance. This criterion is opposed to the exchange surface, for which optima are preferred<sup>40,41</sup>.

The inner walls of the cells are coated with the catalytic material, called washcoat. With a dimension close to ten micrometers thick, this porous material will allow the diffusion of gases to the catalyst it contains. This washcoat is a mixture often complex, specific to each manufacturer and can be deposited in one or more layers. This mixture contains the catalyst necessary for the oxidation reactions, its support, which influences the catalyst in order to make it more efficient, as well as mineral additives.

Catalyst supports are present in all catalysed post-treatment units such as LNT, SCR or catalysed particulate filters. The use of a support increases the dispersion of the catalyst and thus reduces the necessary amount<sup>6</sup>. Support materials are mainly massive metal oxides such as  $\text{Al}_2\text{O}_3$ ,  $\text{CeO}_2$ ,  $\text{SiO}_2$ ,  $\text{TiO}_2$  and  $\text{ZrO}_2$  as single oxide or as a mixture of oxides. The addition of zeolites allows to store the hydrocarbons before their oxidation on catalyst at higher temperature, to improve the conversion during cold starts<sup>5,50</sup>.

Alumina is the main washcoat compound from 50 to 80% by weight. These oxides are a technical innovation in the aftertreatment line, because they reduce the necessary amount of catalyst, by stabilizing the latter at high temperature and reducing the sintering effect, and finally by improving the adsorption properties of the catalyst. This is particularly the case for  $\text{Al}_2\text{O}_3$  and  $\text{ZrO}_2$ <sup>40,41</sup>. These supports confer a greater

resistance to the formation of catalyst oxides, undesired because they reduce the oxidation performance of hydrocarbons<sup>51</sup>.

The catalysts employed in the various post-treatment units are noble metals. In the case of DOC it is often a catalyst mixture containing platinum, palladium and rhodium which allow to slow down the sintering<sup>52,53</sup> with respect to pure metals. Studies on the impact of the platinum-palladium ratio show optima in the oxidation of CO and dispersion-varying hydrocarbons<sup>54,55</sup>. Proportions of the different elements in the DOC formulation are rarely communicated by manufacturers. Platinum is known to have a very good activity on CO conversion<sup>6</sup>, but a lower activity on hydrocarbons. Palladium has opposite properties with respect to platinum. Rhodium is rather efficient for the conversion of NO<sub>x</sub><sup>6</sup>.

Studies have been conducted concerning the uniformity of DOC<sup>6</sup> catalyst distribution. The interest lies in a variable distribution according to the length of the post-treatment organ. Tronci, Oh and Cavendish<sup>56,57</sup> show that a platinum gradient can lower the light-off temperatures of hydrocarbons and decrease the thermal stresses of materials, a consequence of thermal variations in the DOC. This gradient is beneficial in the case where the catalyst concentration is important at the entrance of the organ and decreases according to the channel length and therefore HC conversion. Attempts to alternate between rich and poor catalyst layers, however, produce adverse effects<sup>58</sup>.

The major interest nowadays deals with more abundant metal catalysts use such as iron. It would lower DOC manufacturing costs and reduce dependency on Group 10 metals (including platinum). Some materials demonstrate satisfactory conversion to carbon monoxide and hydrocarbons, including lanthanum-poor iron perovskites, and strontium-based for NO<sub>x</sub> conversion<sup>59-62</sup>.

Beyond the initial characteristics of the manufacturer, the Diesel oxidation catalyst undergoes changes during its use. Several aging phenomena can alter its properties (Figure 7)<sup>41</sup>. It is observed when the exhaust gas is too rich in hydrocarbons or CO and SO<sub>x</sub> (Figure 7), which are extremely reactive and cover the surface, without the possibility of being oxidized<sup>41</sup>. A hydrothermal deactivation of the support appears when the exhaust contains water vapor in large quantities, resulting in structural change of the support oxides<sup>63</sup>.

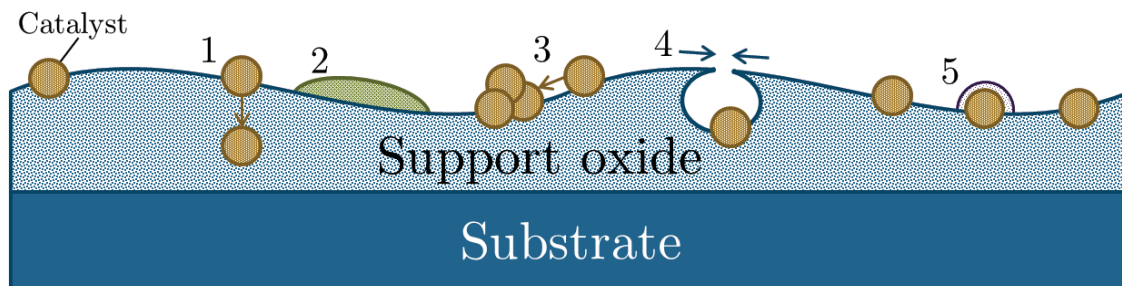


Figure 7: Phenomena of deactivation of the catalyst and its support, adapted from Sassi et. al<sup>41</sup>. 1) metallic diffusion, 2) oxide poisoning, 3) sintering, 4) encapsulation and 5) catalyst poisoning. Some are due to high temperature or catalyst/oxide instabilities (1,3,4) but also too hydrocarbon/CO rich gas (2,5).

Catalyst sintering is very common at high temperature, above 600°C for platinum<sup>6,64</sup>, or when there is a poor affinity between the support and the catalyst<sup>41</sup>. It is then observed that the particles of the latter aggregate and merge to form larger particles<sup>64,65</sup>. The active quantity is then less important and the conversion of the hydrocarbons decreases. These conditions are also adequate to promote particles diffusion in the support, which are then no longer in contact with the gas mixture.

Two mechanisms are generally invoked. The first one is migration. It occurs by the detachment, migration, collision and coalescence of metal crystallites<sup>64,65</sup>. This phenomenon is promoted by the adsorption of certain species, especially water. The second is the Ostwald ripening, that is a thermodynamically controlled process. Platinum aggregates are more stable than small particles. Sufficient temperature then promotes coalescence between nearby aggregates, without the need for migration<sup>66,67</sup>.

Several studies demonstrate a platinum dispersion decrease for catalyst supported on alumina, via the decrease of the hydrogen adsorption capacity<sup>68</sup>. This sintering appears under treatments by hydrogen and oxygen, with different mechanisms. Migration of platinum crystallites is involved in platinum sintering<sup>64</sup>. Periodically alternating oxidation and reduction, high temperatures and soot combustion on the catalyst increase platinum sintering. The phase change of the alumina is moreover a factor in the aggregation<sup>64</sup> of the catalyst particles. Chu *et al.*<sup>64</sup> do not obtain sintering when the catalyst is subjected to pure oxygen or water in an inert atmosphere of N<sub>2</sub>. Conversely, catalyst redispersion of small aggregates is observed for temperatures below 600°C under a flow O<sub>2</sub>/N<sub>2</sub><sup>65</sup>. Addition of other elements such as barium, cerium and calcium oxides also allows greater support stability and constitutes an hindrance to catalyst sintering<sup>6</sup>.

### 1.2.3| Catalytic sites and relation with particle size

Regarding the catalytic phenomenon at molecular level, the Sabatier principle<sup>69</sup> assumes the creation of unstable intermediates and thus the creation of a weak bond between one or more groups and atoms on the catalyst surface. This implies the notion of active site hosting, so-called adsorption reaction. These active sites are described for the first time by Langmuir as independent and identical. Subsequent studies show that these may have different reactivities<sup>70</sup>.

Surface state of the catalyst therefore plays an important role in catalysis. In the case of hydrocarbon oxidation reactions, materials used are mainly platinum, palladium and rhodium. The surfaces of these bulky metals are not perfectly flat and periodic (Figure 8). Analytical techniques highlight surface irregularities. Flat areas host terraces-type sites (facets, 2 dimensions), while steps (1D), corners and adatoms (0D) are singular sites. The vision of an ideal crystalline surface, *i.e.* without defects is however used to simplify the determination of the kinetic constants by taking only into account a single mean adsorption site.

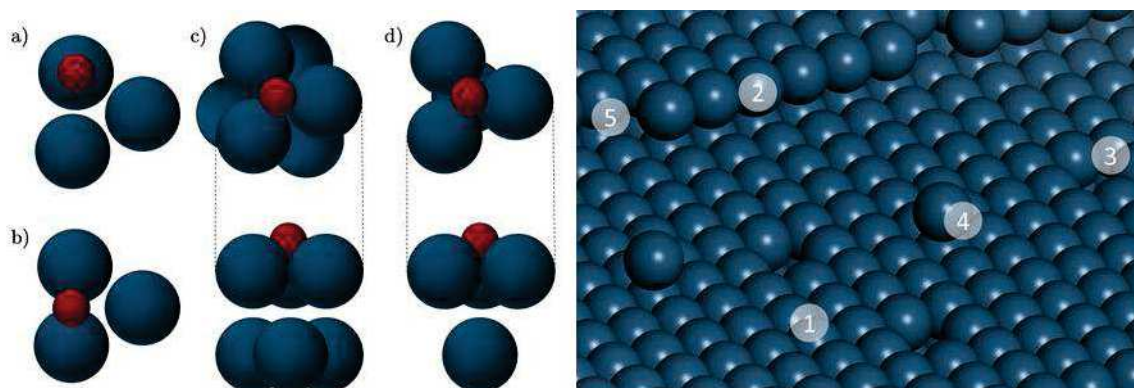


Figure 8: The three common adsorption modes are (a) top, (b) bridge and (c,d) hollow fcc and hcp. Moreover real Pt(111) surface can hold defects such as terraces (1), steps (2), holes (3), adatoms (4) and corners (5) whose reactivities are probably different. The surface of the material is obviously more complex, involving other crystallographic facets (such as Pt(100)) and crystalline defects in the volume (interstitial atoms, dislocations, grain boundaries).

Putna and coworkers<sup>71</sup> report that platinum particles larger than 10nm behave as a Pt(111) type surface with respect to the oxidation of hydrocarbons. Below this size, the particles adsorb more oxygen per platinum atom than reference crystalline surfaces. Higher desorption temperatures also indicate a strong interaction of these particles (with respect to crystalline surfaces such as Pt(111)) with oxygen.

As far as hydrocarbons are concerned, a lot of experimental works have already been done. Light-off temperatures<sup>ii</sup>, hydrocarbon conversions and selectivities<sup>72</sup> on platinum/alumina catalysts were determined for many hydrocarbons. In the case of mixtures, however, it is noted that this relationship is not necessarily verified, in particular by the example of the n-decane/1-methylnaphthalene mixture<sup>73</sup>, a maximum of catalytic activity is obtained for a dispersion of 0.4. In addition, the study of the dissociation of light alkenes on platinum particles with 13 atoms seems less effective than on surfaces with weaker dispersion where the steps are privileged sites for this dissociation<sup>74</sup>.

At the nanometer scale, the reactivity is different than bulk material<sup>75</sup>. It depends on the shape and size of the catalyst. It appears that a sharp contrast between catalyst activity lies between particle size below 40Å and bigger particles for which bulk properties are expected<sup>7</sup>. These differences are assumed to be due to lower coordination number and quantum specific effects as state densities are strongly size-dependent<sup>76</sup>.

Diesel oxidation catalyst is a complex system that engages several materials with distinct application: (i) noble metals used as catalyst to convert CO and hydrocarbon, (ii) metal oxide as catalyst support that stem ageing phenomenon and dope catalyst activity and (iii) the washcoat that allows to fix the material to structure walls and is designed following fluid dynamics and oxidation conversion considerations. Operating conditions are wide, especially temperature and hydrocarbon speciation. In addition to adsorption and reaction phenomena onto the surface, multiple ageing ones can occur and therefore alter catalytic activity. Catalyst sintering and poisoning, respectively due to high temperature and soot/heavy hydrocarbon presence have a major effect on DOC performance.

### 1.3| Aim of the thesis

Despite a commercial use and good pollutant conversion performances, some DOC issues still exist. Indeed a conversion of pollutant higher than 90% is reached in stationary conditions<sup>77,78</sup>, *i.e.* when fuel flow is at steady state, and exhaust line equilibrium temperature is reached<sup>6</sup>. However the conversion drops for transition periods such as acceleration and cold start. The catalytic material needs a sufficient temperature above which conversion can significantly occur. This temperature depends on multiple physico-chemical parameters. In addition, the several adsorbed species onto the surface may have an impact on catalytic activity. Yet the hydrocarbon diversity

---

<sup>ii</sup> Temperature at which CO or HC conversion reaches 50%

does not allow to easily detect the impact of specific species on the whole oxidation process.

Most of all, the dispersion of the catalyst is known to have an influence on both adsorption and oxidation conversion<sup>7</sup>. Yet the impact of this dispersion has hardly been addressed for small molecules. Experimental discrepancies are recorded between small catalyst particles and bigger ones, the latter tend to behave like bulk materials<sup>7</sup>. The deep understanding at a molecular level of this impact is not explained for most of the reactions. The role of oxygen is also of major concern for oxidation reactions. A prior study managed to handle oxygen adsorption/desorption phenomenon on crystalline surfaces, by a multi-scale modelling approach coupled to TPD experiments<sup>79</sup>. Oxygen reactivity might be different with higher catalyst dispersion.

In order to globally handle oxidation catalysis, kinetic modelling is an utmost tool. Concerning small molecules oxidation (methane<sup>80</sup> or CO<sup>81</sup>), few kinetic mechanisms were built. They are mostly developed with experimental fittings for the purpose of forecasting the system reactivity in operating conditions close to the experimental ones. The understanding of complex systems such as Diesel aftertreatment oxidation need kinetic schemes to be robust enough to handle various temperature and gas concentration conditions. Sufficiently exhaustive schemes with compelling kinetic parameters are therefore required.

The objective of the thesis is to address a deep understanding for specific systems in order to handle oxidation catalysis at the molecular level. For this purpose a multiscale approach<sup>82,83</sup> detailed in chapter 2 will be employed. Briefly, this method combines (i) isolated reaction experiments that provide global reactivity indicators, (ii) representative *ab initio* molecular modelling to obtain quantitative molecular data on the given system and (iii) micro-kinetic simulations with *ab initio* based parameters which congruency can directly be evaluated through experimental condition simulations.

This approach implies the choice of a reduced system representative of the DOC to restrain the space parameter. The most prominent and well-documented catalysts on this topic are palladium, rhodium and platinum. From an industrial point of view, they are often combined together but few informations are displayed by manufacturers. A reasonably simple model requires to be limited to a single metal. Since platinum is already highly studied from the point of view of both experimental research and molecular modelling, it is a good starting point for investigating relationships between structures and reactivities in the DOC. The presence of a support is crucial for catalytic material representativity. We chose to work with the most abundant ones present in DOC, *i.e.* alumina. Regarding platinum catalyst dispersion<sup>79,84-86</sup>, crystalline surfaces were already studied for both experimental and modelling point of view, as isotropy and surface symmetry is ensured. Much scarcer are the *ab initio* investigations dealing

with supported subnanometric clusters, that we chose to investigate herein. Exhaust gas speciation also implies to focus on few simple and abundant molecules. The proposed studies tackles only at CO and hydrocarbon oxidation, especially  $C_xH_yO_z$  compounds. Oxidation reactions tend to break molecules into smaller elements until  $CO_2$  formation for carbon-containing species. Therefore the thesis strategy intends to study simplest molecules at first, with increasing species number and size.

To conclude, highly dispersed platinum supported on alumina is the selected catalytic system. This material has the particularity to be representative of Diesel oxidation catalyst and tackles impact of dispersion (thanks to the comparison with reference studies on cristalline surfaces). Oxidation catalysis implies first and foremost to investigate surface oxidation state, and dissociative adsorption of oxygen. This study is detailed in chapter 3. As the simple molecule to oxidize, carbon monoxide is a clear continuation. CO adsorption is investigated in chapter 4 and its oxidation in chapter 5. Finally the oxidation of light hydrocarbon is discussed in chapter 6, especially methanol and propene. The multiscale approach previously mentionned is also developped throughout the thesis and adapted to each studies. Its validation is also part of the thesis objectives.



# 2 | Methods

The work presented here has been undertaken according to a multi-scale approach that already gave fruitful results<sup>82,83,87-95</sup>. This approach is organized around three items: experimental investigations of a selected system, molecular modelling of a representative model system and micro-kinetic simulations of its reactivity. This chapter is devoted to the interests and objectives of the multi-scale approach, as well as methods and tools used and developed within the frame of the thesis studies.

## 2.1 | Multi-scale approach

The understanding of a physical phenomenon systematically relies on two points:

- Experimental studies of simple and controlled cases, that allows to observe real phenomenon,
- Simulation using mathematical tools defined in circumstance, in order to reproduce the phenomenon.

A detailed model needs multiple operating conditions. Therefore complex experiments are segmented into simple laws so that simulation is able to forecast other experiments in close conditions.

The study of reactive systems in heterogeneous catalysis is no exception. Numerous experimental studies that started in the 1970-1980<sup>85,86,96</sup> isolated adsorption and oxidation phenomenon at a molecular level. Latter molecular simulation validated patterns and species adsorption modes, as well as reaction paths on simple periodic surfaces<sup>97,98</sup>. Yet this bottom-up approach has been used on simple cases such as the adsorption of only one or two compounds and their interaction with surface.

The top-down approach focuses on the ability of simulation to predict the transient and final states of a system. In this case, experiments involve multiple compounds under largely heterogeneous conditions<sup>99-101</sup>. Models are simple and do not tend to apprehend the molecular aspect of reactivity. Kinetic data are then adjusted according to empirical laws derived from the said experiments. The advantage of these non-physical

models lies in their simplicity and lightness compared to the studied scale, and can thus be integrated into CFD<sup>iii</sup> simulations for instance.

The bridge between these methods is rarely done. This is the goal of the approach developed in this work. It consists in experimental studies on complex anisotropic materials (top-down method) and simulations using data from molecular modelling at most (bottom-up method). If isolated reactions can be studied using this hybrid method, complex systems can be handled. The different scales interact in a complementary way:

- Experimental studies constitute the larger scale of the method. All the complexity of real phenomenon is represented (poly-dispersity, long time, aerodynamic regime, heterogeneous conditions),
- Molecular modelling is involved in structure and energy determination from models at the molecular scale under homogeneous temperature and pressure conditions. Calculations are performed on very short times (ps) or even in static conditions. At this scale, the aim is to understand energetics of simple phenomenon in depth,
- Micro-kinetic simulations allow to link the two other scales. It is mainly built using thermodynamic data extracted from molecular modelling. By simulating experimental conditions, the comparison of micro- and macroscopic scales is possible. This is also the purpose of the work, namely a model that includes physical parameters relevant for complex systems.

As a reminder of the previous chapter, this approach is applied to the surface state and the oxidation of light hydrocarbons on a platinum material supported on highly dispersed gamma-alumina. Methods and tools are developed in the following sections of this chapter.

## 2.2| Experimental catalysis

Experimental catalysis on highly dispersed catalyst has been performed to study model reactions. Catalyst preparation, experimental set-ups and determinations are gathered in this section.

---

<sup>iii</sup> For Computational Fluid Dynamics.

## 2.2.1| Catalyst preparation and characteristics

The preparation of the catalysts and their characterization were performed by the teams of the Catalysis and Separation, and Physics and analysis Divisions at IFP Energies nouvelles, Solaize.

Ultra-dispersed platinum catalysts were obtained by impregnation of an  $\text{H}_2\text{PtCl}_6$  solution (STREM Chemical, 99.9 % wt. purity). The concentration was adjusted to reach 0.3% wt. and 1% wt. Pt on  $\gamma\text{-Al}_2\text{O}_3$ . Alumina was obtained from the calcination of a SB3 boehmite gel from SASOL (same protocol as in reference <sup>102</sup>) followed by drying at 120°C overnight, and calcination at 520°C under dry air (1 L.hg<sup>-1</sup>.gh<sup>-1</sup>) for 2 h, dechlorination by a wet air flow (8000 ppm.h<sup>-1</sup> water) at 520°C. BET surface of alumina was evaluated at 200 m<sup>2</sup>.g<sup>-1</sup>. The dechlorinated samples were finally reduced under H<sup>2</sup> flow (1 L.g<sup>-1</sup>.h<sup>-1</sup>, 2 h) at 500°C.

The catalysts were characterized by X-ray fluorescence (Thermo scientific ARL Perform'X) to determine the final platinum and chlorine content. The results are presented in Table 2 and show that the expected composition is reached (close to 0.3% wt. and 1% wt. for platinum, low chlorine loadings).

Table 2: Elemental composition of the used Pt/ $\gamma\text{-Al}_2\text{O}_3$  catalysts determined *via* X-ray fluorescence.

Catalysts	Pt (wt. %)	Cl (wt. %)
0.3 wt. % Pt/ $\gamma\text{-Al}_2\text{O}_3$	0.30	0.08
1.0 wt. % 2.0 Pt/ $\gamma\text{-Al}_2\text{O}_3$	1.03	0.08

Platinum dispersion on alumina was determined by hydrogen titration of chemisorbed oxygen ( $\text{H}_2\text{-O}_2$  titration) in a Gira Xsorb apparatus with a thermal conductivity detector. The samples were first calcined under air at 530°C for two hours at 10°C min<sup>-1</sup>. The sample then was cooled down to room temperature and purged with He. The first reduction with H<sub>2</sub> was done at 450°C for two hours with a flow of 87 NmL.min<sup>-1</sup> and a ramp of 5°C.min<sup>-1</sup>. After cooling down to room temperature and purging with He, pulses with pressures from 0.5 to 60 kPa of oxygen were added until saturation occurred at 35°C. This process was repeated once. H<sub>2</sub>/O<sub>2</sub> titration performed gives a 0.98 and 0.90 platinum dispersion respectively for 0.3 wt. % and 1 wt. % catalysts respectively.

HAADF-STEM (High angle annular dark field – scanning transmission electron microscopy) experiments were performed on a STEM/TEM JEOL 2100F microscope operating at 200 kV with a spot size of 0.5 nm. The reduced catalyst sample was

grinded, suspended in ethanol and sonicated. A drop of the resulting suspension was deposited on a copper grid coated with a holey-carbon film, and the alcohol was evaporated. STEM images are gathered in Figure 9 for the 0.3% wt. platinum catalyst. The particle size distribution (Figure 10) allows to determine an average particle size of  $0.85 \pm 0.18$  nm. Also dechlorination has almost no impact on catalyst size distribution. The particles are actually nanoscale. This average corresponds to about ten ionic radii of one platinum atom. Regarding the 1% wt. platinum catalyst, the mean particle size is higher than 0.3% wt., at  $1.07 \pm 0.17$  nm although narrow. The material density was determined at  $0.607 \text{ g.mL}^{-1}$ .

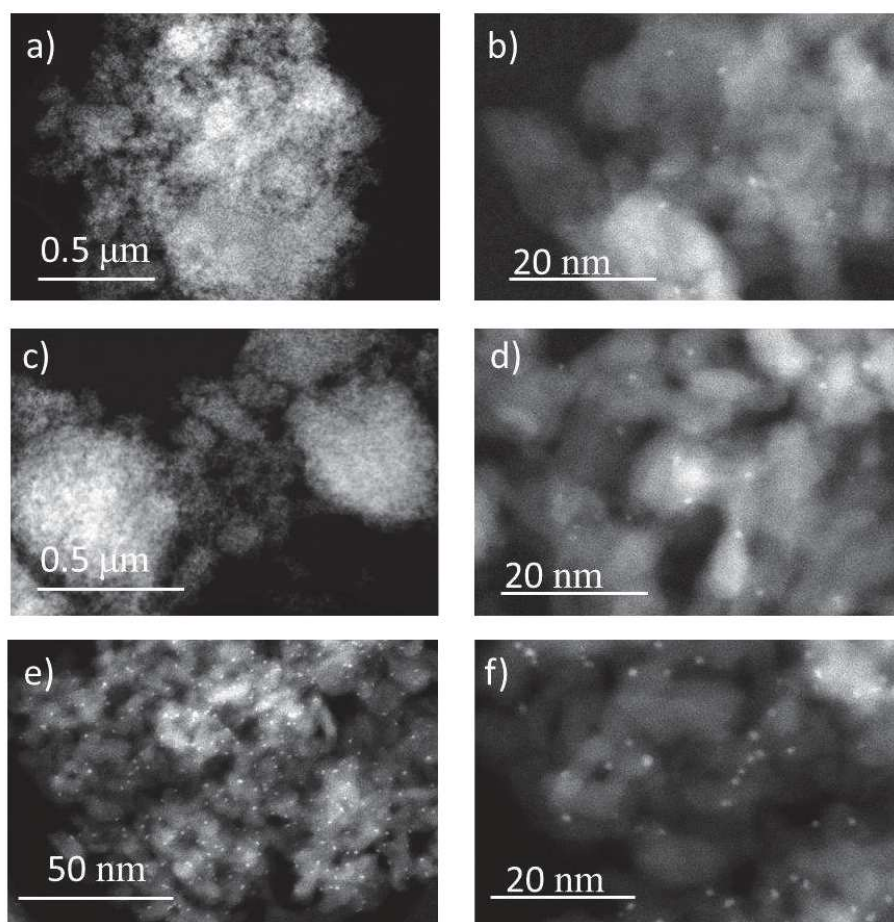


Figure 9: STEM images of fresh catalyst 0.3% wt. platinum (a,b) before and (c,d) after dechlorination. STEM images of fresh catalyst 1% wt. platinum (e,f).

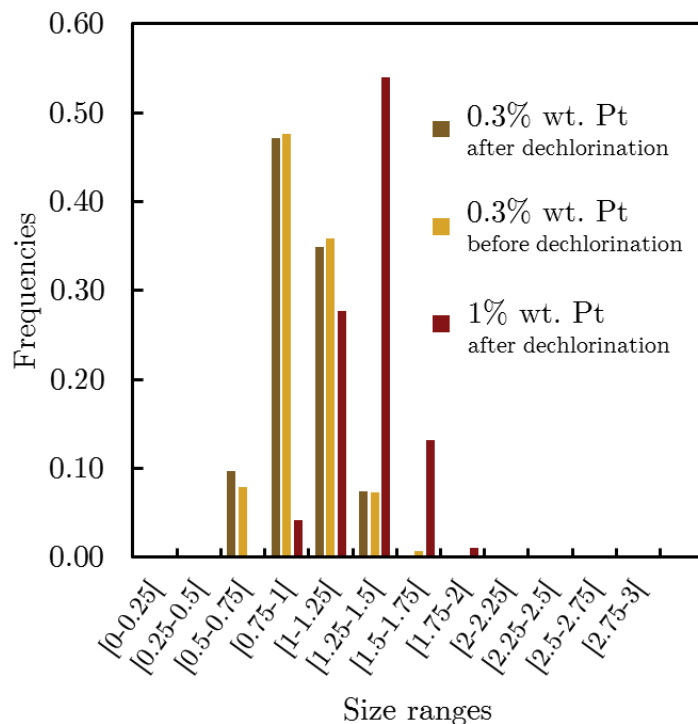


Figure 10: Particle size distribution of the 0.3% wt. platinum loaded catalyst before and after dechlorination (respectively 79 and 143 probed particles). Particle size distribution of the 1% wt. platinum loaded catalyst (289 probed particles).

## 2.2.2| Reactors and analysers

### 2.2.2.1| Infrared *operando* micro-reactor

Reactivity experiments were mostly performed in a micro-reactor (Figure 11a-b). This one allowed to carry out several analyzes. Through a set of valves, several gases was mixed in the required proportions, before being sent to a parallelepipedic reactor of 283 $\mu$ L (11.5 mm side). The gas flowed through six capillary channels (internal diameter of 200 $\mu$ m) at both inlet and outlet.

According to previous studies performed on the reactor itself, laminar regime was reached ( $Re=0.1$ ) for 10mL.min<sup>-1</sup> at 25°C. The residence time of the gas in the reactor was about 2 to 2.5 seconds at a flow rate of 10 mL.min<sup>-1</sup> at 25°C. The reactor behaved similarly to a plug-flow reactor (abbreviated PFR). Yet it has been shown that micro-reactor can be modelled by 19 continuously stirred reactors (abbreviated CSTR)<sup>103</sup>.

The catalytic material was pelletized at 2 tons per 200 mm<sup>2</sup> and shaped into a square pellet of 11.5 mm side (about 12 mg) before being placed in the sample holder. This pellet was changed each time the gas mixture was modified (CO alone, propene alone, methanol/CO, etc.). For each fresh catalyst, a dehydration step was performed by a helium flow for 5 hours at 300°C. In the case of reduced catalysts, the dehydration step

was replaced by a pure He flow (400°C, 3 hours, 10mL.min<sup>-1</sup>) followed by reduction step under an 5% vol. H<sub>2</sub>/He flow (400°C, 5 hours, 10mL.min<sup>-1</sup>), and cooling at room temperature under He flow.

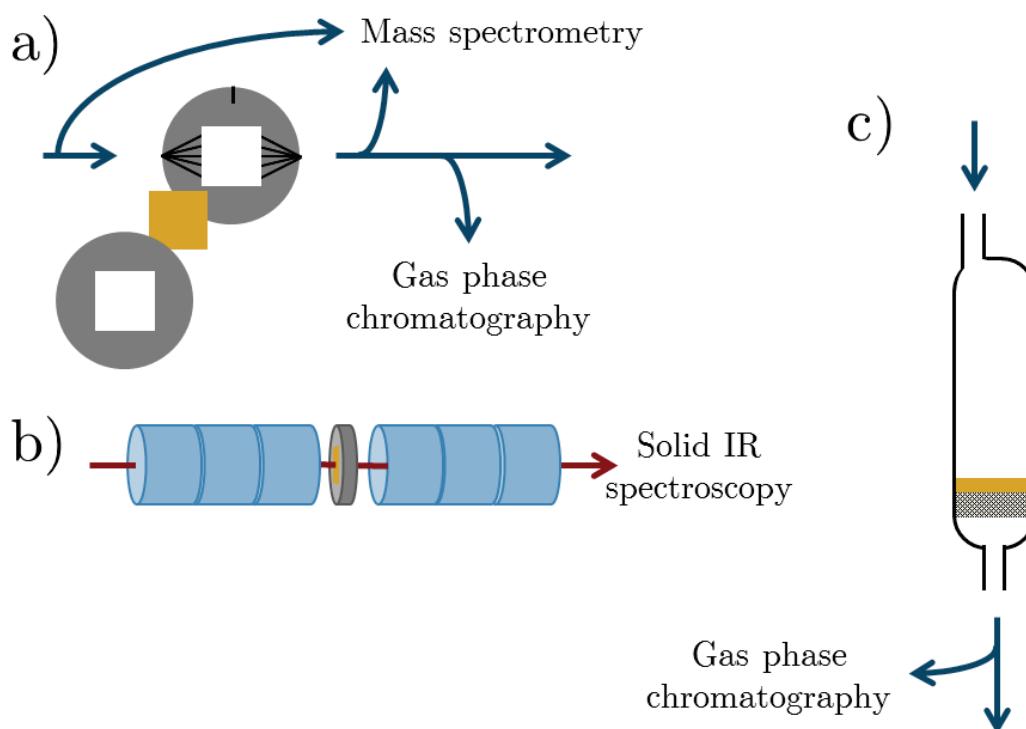


Figure 11: a) Micro-reactor scheme with the pelletized catalyst in yellow. Mass spectrometer can be placed either at the inlet or at the outlet of the reactor. b) represents the monocrystalline windows needed to reactor sealing and IR beam transmission through the cell, and c) fixed bed reactor scheme. The catalyst in yellow was placed in powder form on sintered-glass filter.

An electric resistance heating system was displayed around the pellet, as well as a cooling system at its edges to contain the heat into the reactor. It allowed to scan a temperature range of about 0°C to 380°C. The thermal regulation allowed to carry out temperature ramps.

#### 2.2.2.2| Analysers characteristics

*Operando* solid infrared spectroscopy was performed by Thermo Scientific Nicolet 380 IR spectrometer (128 scans per spectra) equipped with a MCT detector and placed in the perpendicular axis to the wafer. It allowed to observe adsorbed species on the material (*i.e.* the catalyst and the support) with a temporal resolution of 2 minutes. Adsorption bands was thus be observed between 4000 cm<sup>-1</sup> and about 1000 cm<sup>-1</sup>. The infrared beam crossed the pellet perpendicularly. To ensure the tightness on the sides of

the pellet while allowing the infrared flux to pass, monocrystalline KBr or  $\text{CaF}_2^{\text{iv}}$  windows were used. Therefore the IR beam passed through six windows, two gas layers and the catalyst. The resolution of the spectra was  $4\text{ cm}^{-1}$ , but the latter was sometimes noisy by reflection phenomena between windows. Spectra were treated to remove impact of windows and gas flows, thanks to blank spectrum took in non reactive conditions.

By a set of valves, the mass spectrometer Pfeiffer QMS 200 was set either at the inlet or at the outlet of the reactor. The device pumped a part of the gas for analysis. This flow rate has varied between the different experiments. Therefore the total gas flow has been tuned accordingly. Mass spectrometer had a resolution of few seconds, depending on the number of recorded signals. The pressure in the mass spectrometer was systematically set at  $2.6 \times 10^{-6}$  mbar, except for CO oxidation at  $2.3 \times 10^{-6}$  mbar.

Micro-gas chromatography (Varian 490, equipped with a TCD) allowed to quantitatively detect the outlet gases of the reactor. By taking a sample of  $0.2\text{ mL}\cdot\text{min}^{-1}$ , usually during 40 seconds, previously calibrated gas concentrations were determined using two separation columns of 20 meters each. Sample analysis requires five minutes to separate species in the columns. This method is therefore not well time-resolved.

#### 2.2.2.3| Fixed bed reactor

A fixed bed reactor set-up was used specially for  $\text{O}_2$ -TPD (Micromeritics Autochem II 2920, Figure 11c). The catalytic material was used in powder (around 200 mg) and placed onto sintered glass, which allows only gases and liquids to pass through. Gas blend was mixed upstream of the reactor using a set valves. Gas was injected from the top of the reactor so that the catalyst is held on the glass. Total gas flow was set at  $50\text{ mL}\cdot\text{min}^{-1}$ . A cylindrical furnace placed around the reactor allowed to control increasing temperature ramps. Since the set-up was not equipped with a cooling system, the descending temperature ramps were yet not controlled. All data reported here were therefore performed with rising temperature ramps. The oxygen release was quantified with a mass spectrometer (Pfeiffer QMS 200). Catalyst pre-treatment conditions prior  $\text{O}_2$ -TPD will be discussed in chapter 3.

### 2.2.3| Temperature programmed experiments

#### 2.2.3.1| Temperature programmed desorption

---

<sup>iv</sup> These crystal were used because of their wide range infrared transmission.  $\text{CaF}_2$  windows were placed in contact with the reactor for water production reactions, due to its low water solubility. This is not the case of KBr crystal, that is easily soluble. Dissolution of crystal windows leads to IR transmission losses and noise.

TPR experiments were undertaken for O<sub>2</sub> and CO and consisted into three steps : (i) a pre-treatment step at high temperature during five hours with helium enables to remove adsorbed water as well as to clean the surface from adspecies present on the catalyst and on the metal oxide; (ii) a contact step with the studied molecule during one hour at low temperature; (iii) finally, the release the specie was recorded using mass spectrometer (Pfeiffer QMS 200) during the increase of temperature with a ramp of 5 °C.min<sup>-1</sup> using helium as carrier gas. The characteristics of O<sub>2</sub> and CO TPD experiments are gathered in Table 3.

Table 3: Temperature Programmed characteristics concerning O<sub>2</sub> and CO desorption on Pt-γ-Al<sub>2</sub>O<sub>3</sub>.

Experiments	Pretreatment temperature	Contact step characteristics	Probed catalysts	Total gas flow
O <sub>2</sub> -TPD <i>In fixed bed reactor</i>	600°C	5% vol O <sub>2</sub> /He at 100°C	0.3 and 1% wt Pt/γ-Al <sub>2</sub> O <sub>3</sub>	50 mL.min <sup>-1</sup>
CO-TPD <i>In IR operando reactor</i>	400°C	0.3% vol. CO/He at 50°C	1% wt Pt/γ-Al <sub>2</sub> O <sub>3</sub>	12 mL.min <sup>-1</sup>

#### 2.2.3.2| Temperature programmed reaction

Temperature programmed reactions were performed for pure species: CO, methanol and propene, as well as mixtures: methanol/CO and propene/CO. All these experiments were carried out with the IR *operando* reactor.

Considering methanol, propene and CO containing mixtures, the micro-gas chromatography was used to determined the gas concentration at the outlet of the experiment. These data allowed the calculation of the conversion rate for these species according to equation (1). The reactor inlet content was assumed to be constant through the whole experiment and therefore equal to the earliest reactor outlet content (T=T<sub>0</sub>).

$$\tau_{specie} = \frac{Rate_{specie}^{T=T_0} - Rate_{specie}^T}{Rate_{specie}^{T=T_0}} \quad (1)$$

Regarding pure carbon monoxide oxidation detailed in Chapter 4, the mass spectrometrer was used to determine the CO conversion. Conversion rate was calculated according to the relative signal intensity related to the molecule (m/z=28 for CO, m/z=44 for CO<sub>2</sub>). The calculation of the relative intensity I of a m/z signal by the recorded absolute signals is detailed in equation (2).

$$I_{relative} \frac{m}{z}=x = \frac{I_{absolue} \frac{m}{z}=x}{\sum I_{absolue}} \quad (2)$$

Equation (3) details the determination of the conversion rate  $\tau$  of specie at a relative intensity  $I$  during a permanent regime.

$$\tau_{specie} = \frac{I_{relative}^{inlet} - I_{relative}^{outlet}}{I_{relative}^{inlet}} \quad (3)$$

Finally, the calculation of the gas hourly space velocity (abbreviated GHSV) is expressed by equation (4), with  $Q_{total}$  the total gases flow.

$$GHSV = \frac{Q_{total}}{V_{catalyst}} \quad (4)$$

## 2.2.4| Determination of heats of adsorption of CO

### 2.2.4.1| AEIR method

To determine the heat of adsorption of the adsorbed CO species, the AEIR method (Adsorption Equilibrium Infrared spectroscopy method) was used<sup>104-109</sup>. This methodology is set with isobaric condition and is founded on two hypothesis. The model assumes that the adsorbed species are clearly localized and that heat of adsorption decreases (in absolute value) linearly with increasing coverage. This methodology is decomposed in two steps. The first one corresponds to the determination of CO coverage ( $\theta$ ) for each specie and at several temperatures. For the coverage determination, it is assumed that the intensity of the IR band is proportional to the concentration of this species and that temperature has no impact on the intensity. Thereby, the ratio between the intensity of the IR band at the temperature  $T_a$  divided by the intensity at the site saturation corresponds to the given coverage (equation (5)).

$$\theta_x(T_a) = \frac{IR \text{ band intensity at } T_a}{IR \text{ band intensity at the saturation of the sites}} \quad (5)$$

The experimental coverages are reported in Figure 42 for the two catalysts. The second step is the determination of the heat of adsorption for each species. According to the AEIR methodology, the comparison between the experimental data and the theoretical curve is performed with the generalised Temkin adsorption model (equation (6)).

$$\theta = \frac{RT_a}{E_0 - E_1} \ln \left( \frac{1 + K_{(0)}P_a}{1 + K_{(1)}P_a} \right) \quad (6)$$

Where  $K_{(0)}$  and  $K_{(1)}$  corresponds to the adsorption equilibrium constant for the localized species at zero and maximum coverage respectively.  $E_0$  and  $E_1$  are the heats of adsorption at for their respective CO coverage (a negative heat of adsorption states for favourable adsorption).

The adsorption equilibrium constant  $K$  can be estimated thanks to statistical thermodynamics, and relates to the ratio of the rate constant of adsorption, and desorption of the species studied (equation (7)).

$$K = \frac{h^3}{k(2\pi mk)^{3/2}} \frac{1}{T_a^{5/2}} \exp\left(\frac{-E_d}{RT_a}\right) \quad (7)$$

Where  $h$  is the Planck's constant,  $k$  the Boltzmann's constant,  $m$  the molecular mass,  $T_a$  the adsorption temperature,  $E_d$  corresponds to the desorption activation energy. To determine heat of adsorption at  $\theta_{max}$  and  $\theta_{max}$ , a visual fit is performed between merged equations (6) and (7) and experimental data, with  $E_0$  and  $E_1$  the fitting parameters.

#### 2.2.4.2| Operating conditions

*In-situ* treatments of the solid in the temperature range of 20-400 °C were performed with a controlled gas flow rate at atmospheric pressure. Before each analysis, the solid was pre-treated *in-situ* at 350°C under He flow (10mL.min<sup>-1</sup>, 3 hours) to obtain the Pt/Al<sub>2</sub>O<sub>3</sub>-o sample (-o means oxidised sample). For reduced samples Pt/Al<sub>2</sub>O<sub>3</sub>-r was obtained by the following pretreatment sequence: He (400°C, 3 hours, 10mL.min<sup>-1</sup>) → 5% vol. H<sub>2</sub>/He (400°C, 5 hours, 10mL.min<sup>-1</sup>) and cooling at room temperature under He flow.

The experimental procedure of the AEIR method consisted first in introducing at  $T_a = 25^\circ\text{C}$  a 0.3% vol. CO/He mixture (total pressure = 1 atm, flow rate = 12 mL.min<sup>-1</sup>) on the catalyst. Then  $T_a$  was slowly increased (3 °C.min<sup>-1</sup>) to 400 °C while the IR spectra of the adsorbed species were periodically recorded (256 scans/spectrum). The AEIR procedure imposed that the evolutions of a specific IR band with the increase in  $T_a$  were only due to the adsorption equilibrium and not to the overlaps of different processes such as adsorption equilibrium and disappearance of the Pt sites by sintering or poisoning. The recording of the adsorption have also been performed during the cooling of the sample and no difference have been observed with respect to the signals at ambient temperature, showing that maximum coverage rate  $\theta_{max}$  was reached.

## 2.3| *Ab initio* quantum molecular modelling

DFT calculations have been performed using the VASP software<sup>110,111</sup>. These latter were performed on both Pt<sub>13</sub>/γ-Al<sub>2</sub>O<sub>3</sub> and Pt(111) surfaces. In this section, the basis of quantum chemistry are given, as well as the parameters used in the VASP calculations, and finally surface structures and thermodynamic parameters determination.

### 2.3.1| *Ab initio* calculations

#### 2.3.1.1| Resolving Schrödinger equation

The Schrödinger equation was introduced in 1925 by the physicist Erwin Schrödinger. This equation describes the evolution over time of a massive and non-relativistic elementary particle (having a negligible speed in comparison with light), particularly the electron in the case of quantum chemistry. For a given electron-core system characterized by a wave function  $\psi$ , the time independent Schrödinger equation is the following.

$$E\psi = \widehat{H}\psi \quad (8)$$

With  $H$  the Hamiltonian operator, describing the kinetics of the system with the operator  $T$  and the potential energy with  $V$ . In fact the first one is composed of kinetic operators related to the nuclei and the electrons  $\widehat{T}_N$  and  $\widehat{T}_e$ , the second being composed of the kernel-nucleus repulsive operator  $\widehat{V}_{NN}$ , the kernel-electron attractor potential  $\widehat{V}_{Ne}$  and the electron-electron repulsive potential  $\widehat{V}_{ee}$ . For a poly-atomic system with  $N$  electrons and  $M$  nuclei, the Hamiltonian is defined by equations (9) and (10) in atomic units.

$$\widehat{H} = \widehat{T} + \widehat{V} = \widehat{T}_e + \widehat{T}_N + \widehat{V}_{NN} + \widehat{V}_{Ne} + \widehat{V}_{ee} \quad (9)$$

$$\widehat{H} = -\sum_{i=1}^N \frac{1}{2} \nabla_i^2 - \sum_{A=1}^M \frac{1}{2M_A} \nabla_A^2 - \sum_{i=1}^N \sum_{A=1}^M \frac{Z_A}{r_{iA}} + \sum_{i=1}^N \sum_{j>i}^N \frac{1}{r_{ij}} + \sum_{A=1}^M \sum_{B>A}^M \frac{Z_A Z_B}{r_{AB}} \quad (10)$$

With  $Z_A$  the ratio of nuclei over electrons charges ratio,  $M_A$  the ratio of nuclei over electrons masses ratio and  $\nabla^2$  the Laplacian operator with respect to cartesian electron and nuclei coordinates,  $r_{ij}$  the vector position between two  $i$  and  $j$  particles.

Yet this equation is analytically solvable only for one electron cases, *i.e.* hydrogen and few ions. The resolution for a polyelectronic system requires approximations, and so estimated wave function.

The first approximation is the Born-Oppenheimer one. It assumes that nuclei are massive compared to the electrons so that they move slowly. Therefore nuclei movements are negligible and electrons evolve in a fixed field imposed by the nuclei. This leads to a simple Hamiltonian operator of equation (11).

$$\widehat{H}' = \widehat{T}_e + \widehat{V}_{NN} + \widehat{V}_{Ne} + \widehat{V}_{ee} \quad (11)$$

Moreover the wave function can be separated into an electronic and a nuclear wave function, respectively equations (12) and (13).

$$\widehat{H}_{el} = \widehat{T}_e + \widehat{V}_{Ne} + \widehat{V}_{ee} \quad (12)$$

$$\widehat{H}|\Psi\rangle = \widehat{E}_{el}|\Psi\rangle + \widehat{V}_{NN}|\Psi\rangle \quad (13)$$

Other approximations are made that depend on the studied system. Therefore the assumptions made in the case of gas phase will be different from those applied to condensed matter. This is due to electron density probability shape (*i.e.* bonds nature), desired precision and computational limits.

### 2.3.1.2| Density Functional Theory

Density Functional Theory (DFT) is an *ab initio* method (*i.e.* without empirical parameters) that is widely used in the case of condensed matter. This method evaluates the charge density  $\rho(\mathbf{r})$  instead of electron position probability. For N electron as a system, charge density is described by 4N variables, including 3N space variables and N spin coordinates (Equation (14)).

$$\rho(\mathbf{r}) = N \int \dots \int |\Psi(r, s_1, r_2, s_2, \dots, r_N, s_N)|^2 ds_1 ds_2 \dots ds_N, dr_2, \dots dr_N \quad (14)$$

The method is based on Hohenberg-Kohn theorems<sup>112</sup>. The first theorem indicates that the system, in its fundamental (non-excited) state, is completely defined using electron density, and that the nuclei-electron interactions  $\widehat{V}_{Ne}$  are determined by the electron density by an additive constant. The total electronic energy is then determined by equation (15).

$$E_{el}[\rho(\mathbf{r})] = \widehat{T}[\rho(\mathbf{r})] + \widehat{V}_{ee}[\rho(\mathbf{r})] + \widehat{V}_{Ne}[\rho(\mathbf{r})] = F_{HK}[\rho(\mathbf{r})] + \int \rho(\mathbf{r})v(\mathbf{r})d\mathbf{r} \quad (15)$$

With  $F_{HK}[\rho(\mathbf{r})]$  the universal functional of the electronic density which does not depend on the external potential,  $v(\mathbf{r})$ .

The second Hohenberg and Kohn theorem demonstrates that electronic state is minimal only when the electronic system density is in its fundamental state. Thus the non-excited state can be obtained by using a variational method, solving the function  $\rho(\mathbf{r})$  in three dimensions, meaning to minimize functional  $E_{el}[\rho(\mathbf{r})]$ .

In 1965 Kohn and Sham limited the problem to a system without electron-electron interaction. The universal functional of Hohenberg-Kohn gives the equation (16).

$$F_{HK}[\rho(\mathbf{r})] = \widehat{T}_s[\rho(\mathbf{r})] + \frac{1}{2} \int \frac{\rho(\mathbf{r}_1)\rho(\mathbf{r}_2)}{r_{12}} d\mathbf{r}_1 d\mathbf{r}_2 + E_{xc}[\rho(\mathbf{r})] \quad (16)$$

With  $\widehat{T}_s[\rho(\mathbf{r})]$  the electronic kinetic operator without electron-electron interactions. The second term is the Coulombic interaction, and  $E_{xc}[\rho(\mathbf{r})]$  the exchange-correlation term, which gathers electronic interactions and a part of the kinetic energy.  $E_{xc}[\rho(\mathbf{r})]$  is described with equations (17), (18) and (19).

$$E_{xc}[\rho(r)] = \int \rho(r)v_{eff}(r)dr + \widehat{T}_s[\rho(r)] \quad (17)$$

With

$$v_{eff}(r) = v(r) + \int \frac{\rho(r')}{|r-r'|}dr' + v_{xc}(r) \quad (18)$$

and

$$v_{xc}(r) = \frac{\delta E_{xc}[\rho]}{\delta \rho(r)} \quad (19)$$

This functional describes a system without electron-electron interactions with electrons moving in an external potential. Therefore the wave function is solvable as mono-electronic orbital tensor and the Hamiltonian operator is altered as equation (20).

$$\widehat{H}_{el} = \sum_i^N \left[ -\frac{1}{2}\nabla_i^2 + v_{eff}(r_i) \right] \quad (20)$$

System resolution gives the Kohn-Sham equation <sup>113</sup> as a sum of mono-electronic orbitals: the Kohn-Sham orbitals  $\chi_i(r_i)$  as presented by equations (21) and (22).

$$\left[ -\frac{1}{2}\nabla_i^2 + v_{eff}(r_i) \right] \chi_a(r_i) = \epsilon_a \chi_a(r_i) \quad (21)$$

With

$$\rho(r) = \sum_{a=1}^N |\chi_a(r_i)|^2 \quad (22)$$

Equations system is self-consistent, so that the solution can be refined by iteration to the desired convergence. Electronic energy of all mono-electronic contributions is given by equation (23).

$$E_{el}[\rho(r)] = \sum_{a=1}^N \epsilon_a + E_{xc}[\rho(r)] - \int \rho(r)v_{xc}(r)dr - \frac{1}{2} \int \frac{\rho(r')\rho(r)}{|r-r'|}drdr' \quad (23)$$

The only approximation made so far is Born-Oppenheimer, and equations are still analytical. Yet exchange-correlation energy  $E_{xc}[\rho(r)]$  is not described, approximations are thus necessary.

### 2.3.1.3| Exchange-correlation functional

The first exchange-correlation functional was proposed by Kohn and Sham in 1965, named Local Density Approximation (abbreviated LDA). It takes into account local density  $\rho(r)$  according to equation (24).

$$E_{xc}[\rho(r)] = \int \epsilon_{xc}[\rho(r)]\rho(r)dr \quad (24)$$

With  $\epsilon_{xc}[\rho(r)]$  the volumetric exchange-correlation energy, which is composed of two parts: exchange energy and correlation energy. The first one was proposed by Bloch as follows.

$$\epsilon_x(\rho) = \frac{3}{4} \left( \frac{3}{\pi} \right)^{\frac{1}{3}} \int \rho(r)^{\frac{4}{3}} dr \quad (25)$$

While correlation energy is estimated accurately, especially by prior Monte-Carlo calculations<sup>114</sup>. The main weakness of this functional lies in the cohesive energy overestimation and is not appropriate for condensed anisotropic system.

For this purpose Generalized Gradient Approximation (abbreviated GGA) functionals has been developed. Exchange-correlation functional then takes into account the local density as well as its gradient (expressed in equation (26)). Several functionals have been proposed within GGA. Table 4 gathers the most common functionals and their characteristics.

$$E_{xc}[\rho(r)] = \int \epsilon_{xc}[\rho(r), \nabla\rho(r)]\rho(r)dr \quad (26)$$

Table 4: Commonly used GGA functionals in *ab initio* molecular modelling with their main advantages and drawbacks.

Functional	Advantages	Drawbacks
PW91 <sup>115</sup>	Does not contain non-local correlation terms but compensates a part of the missing dispersion force <sup>116</sup>	Overestimates adsorption energies for strong covalent bounds <sup>116</sup> Bad for Van der Waals contributions <sup>116</sup>
PBE <sup>117</sup>	Does not contain non-local correlation terms and compensates a part of the missing dispersion force <sup>116</sup>	Overestimates chemisorption energies for strong covalent bounds <sup>116</sup> Bad for Van der Waals contributions <sup>116</sup> Over-estimates CO bond on Pt(111) <sup>118</sup>
RPBE <sup>119</sup>	Very good estimation for strongly adsorbed systems <sup>116</sup>	Fail for species with large Van der Waals contributions <sup>116</sup> Time-consuming calculations
optPBE-	Good description of unsaturated	Poor description of O and CO

VdW	hydrocarbons adsorbed <sup>118</sup>	adsorption on Pt(111) <sup>118</sup>
BEEF-VdW <sup>120</sup>	Same level of theory than RPBE for strongly adsorbed system <sup>116</sup> Correct for covalently bonded adspecies <sup>118</sup> Good prediction of Van der Waals forces <sup>116</sup> Good description of CO adsorption <sup>118</sup>	Underestimates adsorption energies for unsaturated hydrocarbons <sup>118</sup>

Very distinct adspecies have been studied in the present work. Therefore a versatile functional was needed. Also the comparison with previous data considering the peculiar highly dispersed surface model was a key to evaluate discrepancies with extended surface. Considering the studied adspecies, the Van der Waals contribution was not needed to be accurately estimated. The functional PBE was thus chosen as a suitable functional.

## 2.3.2| Calculations undertaken in this work

### 2.3.2.1| Platinum surface models

Molecular simulations were mainly performed on two modelled surfaces. The first consists of a massive five layers of face-centered cubic platinum with exposition of the (111) surface (Figure 12). This surface is known to be the most stable and most compact as all atoms are in contact. Also it does not contain any typical defects encountered on real surfaces (steps, adatoms, corner, etc.). Periodicity box dimensions are 8.47x8.47x29.2 Angstrom<sup>3</sup>.

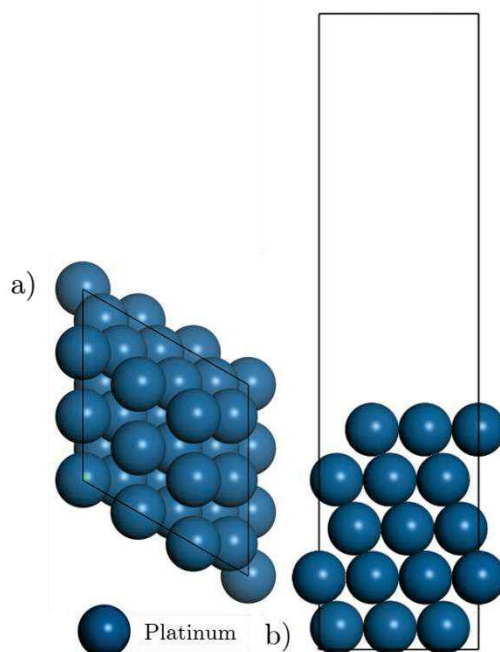
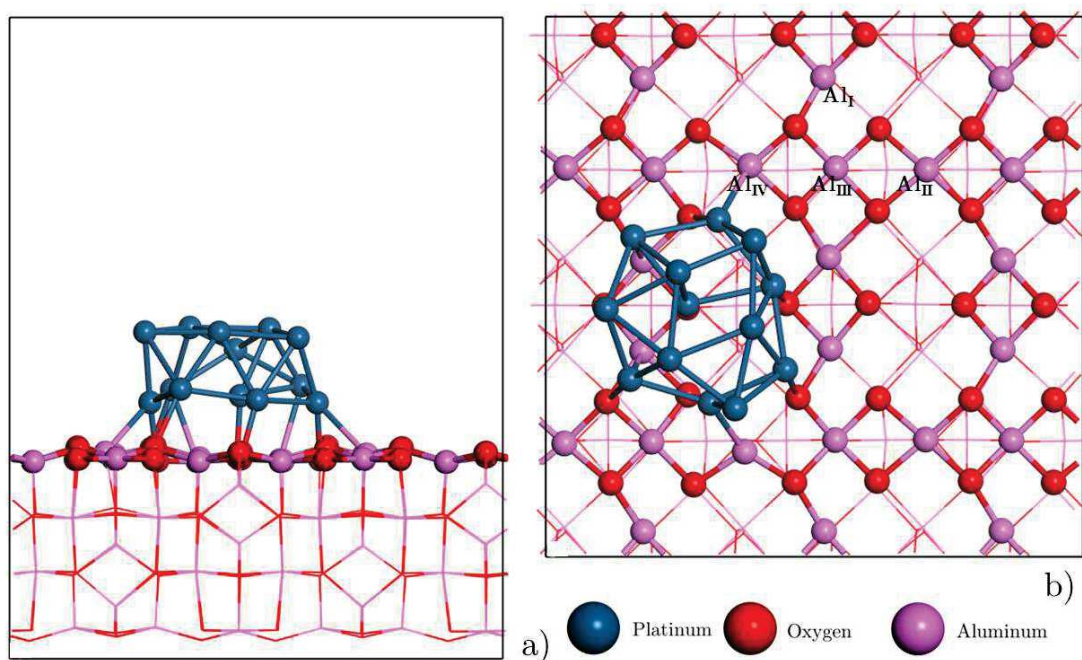


Figure 12: a) Top view and b) side view of the Pt(111) surface model. Black lines correspond to the perodic box limits.

The second structure is a four-layer gamma alumina with (100) surface on which 13 platinum atoms aggregate is anchored (Figure 13). We chose the dehydrated  $\gamma\text{-Al}_2\text{O}_3$  (100) surface model of Digne *et al.* as the support model<sup>121,122</sup>. Indeed, from previous studies about monometallic or bimetallic catalysts, models involving  $\gamma\text{-Al}_2\text{O}_3$ (100) dehydrated surface as a first approach, already provided fruitful detailed information<sup>123-127</sup>. A two platinum-layers  $\text{Pt}_{13}$  structure was found the most stable on this alumina facet<sup>125</sup>.

Unlike the first one, the platinum surface here is irregular and exhibits no symmetry. Platinum surface is not extended by the box of periodicity and we can consider the surface as an island that does not interact with neighboring ones. The shape of the 13-platinum aggregate used here is the result of a study of several similar structures. This is the most stable obtained. The dimensions of the periodicity box are 16.7x16.8x21.8 Angstrom<sup>3</sup>. As for the previous structure, the last two alumina layers of are frozen to keep bulk properties<sup>v</sup>. Molecular dynamics has been extensively used for calculations involving this structure.



<sup>v</sup> An exception exists for molecular dynamics calculations. In this case, to lower the calculation time and thus scan a larger number of geometries, entire alumina was frozen.

Figure 13: a) Side view of Pt<sub>13</sub>/γ-Al<sub>2</sub>O<sub>3</sub> and b) top view of Pt<sub>13</sub>/γ-Al<sub>2</sub>O<sub>3</sub> with aluminum nomenclature. Black lines correspond to the perodic box limits.

### 2.3.2.2| Electronic convergence

Molecular-scale system modelling was performed from the Vienna *Ab initio* Simulation Package<sup>110,111</sup> (abbreviated VASP). Calculations are performed on periodic systems in three dimensions. The GGA-Perdew-Burke-Erzenhof exchange correlation functional<sup>117</sup> was used for the whole study. The threshold energy (cut-off) applied to the calculations is 400eV for all systems. Calculations were performed at the  $\Gamma$  point. Gaussian smearing with  $\sigma = 0.02$  eV was used for the supported clusters. Dipolar correction was added in the direction perpendicular to the slab. The electronic optimizations were done up to a convergence of  $10^{-6}$  eV for the self-consistent loop, and geometries were optimized until all forces on atoms were lower than 0.02 eV/Å. Kpoint was set to 5x5x1 and 1x1x1 respectively for Pt(111) and Pt<sub>13</sub>/γ-Al<sub>2</sub>O<sub>3</sub> surfaces<sup>vi</sup>.

### 2.3.2.3| Geometry optimizations

Geometry optimization tackles at finding the lowest energy configuration from a guess geometry. Calculations were performed without thermal energy, *i.e.* at 0K. Given a system with M cores and N electrons, the total energy of the system is as:

$$E_{tot}(R_A) = E_{elec}(R_A) + \sum_{A=1}^M \sum_{B=A}^M \frac{Z_A Z_B}{R_{AB}} \quad (27)$$

Using self-consistency, VASP determines the total energy of the system as well as the forces applied on each particle. Then the software proposes a new geometry that minimizes all forces and a new iteration begins. Figure 14 illustrates O<sub>2</sub> geometry optimization by VASP as an example. Crosses show the O-O bond (*i.e.* that is the only geometric parameter) and related system energies.

---

<sup>vi</sup> In VASP, the KPOINT file sets the mesh of the Brillouin zone. Brillouin zone is the primary in the reciprocal lattice. The reciprocal lattice is used for the description of electron wavefunctions.

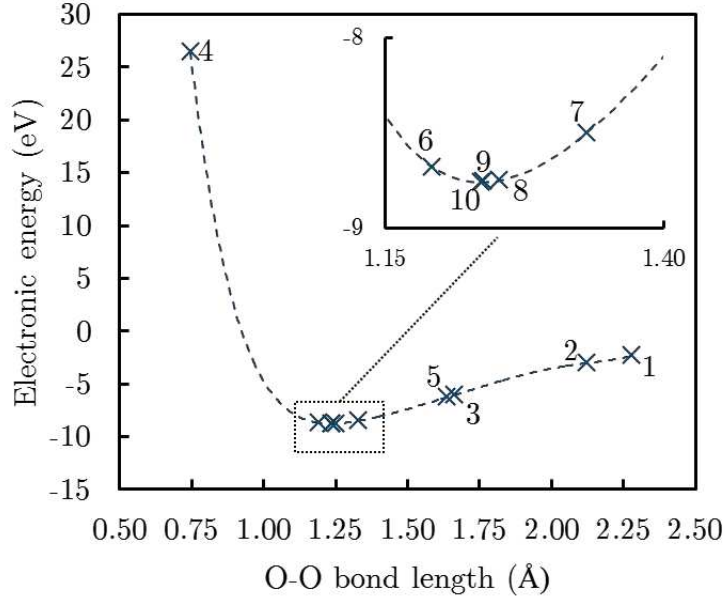


Figure 14: Electronic energy of the  $\text{O}_2(\text{g})$  system with O-O bond length guesses made by VASP (crosses), during geometry optimisation. The dotted line is the interpolated electronic energy.

This calculation type is fundamental to determine initial geometries and energies. Yet geometry optimizations can lead to a high energy local minimum. Therefore other potential geometries might be more stable. This is particularly the case for anisotropic supported cluster that geometry can greatly vary.

#### 2.3.2.4| Bader charge calculation

During optimization geometry, density charge is determined inside a chosen volume around each nuclei so that atoms are assigned an electronic charge ( $q_{\text{VASP},\text{valence}}$ ). Therefore Bader ( $q_{\text{Bader}}$ ) charges<sup>128,129</sup> were determined according to the following equation, with  $q_{\text{valence}}$  the elemental valence charge.

$$q_{\text{Bader}} = q_{\text{VASP},\text{valence}} - q_{\text{valence}} \quad (28)$$

#### 2.3.2.5| *Ab initio* molecular dynamics

Molecular dynamics allows to overcome the limitations of geometry optimization and to obtain complex systems at lower energies. Thermal energy is given in VASP as a temperature. At first, the software assigns to each atom a thermal velocity, following a Maxwell-Boltzmann distribution. Subsequently, forces and potentials between the particles provide acceleration, velocity and position. Molecular dynamics algorithm is based on laws of classical dynamics, discretized according to time. VASP uses the Verlet algorithm developed in 1967 by Loup Verlet<sup>130</sup>. It uses two Taylor developments to describe position of the particles at  $t - \Delta t$  and  $t + \Delta t$  (equations (29) and (30)).

$$\vec{x}(t - \Delta t) = \vec{x} - \vec{v}(t)\Delta t + \frac{\vec{a}(t)\Delta t^2}{2} - \frac{\vec{b}(t)\Delta t^3}{6} + O(\Delta t^4) \quad (29)$$

$$\vec{x}(t + \Delta t) = \vec{x} + \vec{v}(t)\Delta t + \frac{\vec{a}(t)\Delta t^2}{2} + \frac{\vec{b}(t)\Delta t^3}{6} + O(\Delta t^4) \quad (30)$$

With  $\vec{a}$  acceleration,  $\vec{b}$  the third derivative of the position with respect to time, which corresponds to the jolt felt by the particle. This gives the equation (31) determining the next position at  $t + \Delta t$ .

$$\vec{x}(t + \Delta t) = 2\vec{x} - \vec{x}(t - \Delta t) + \vec{a}(t)\Delta t^2 + O(\Delta t^4) \quad (31)$$

Atoms move and explore the potential energy hypersurface rather than staying in a local minimum. Temperature needs to be chosen so that adspecies do not desorb and atoms can overpass local maximums (Table 5). In the present work, we performed velocity-scaled MD, for which the temperature was adjusted at each step by scaling the velocities to reach the desired kinetic energy (thus temperature), without using a thermostat. This approach was chosen as it proved to be successful for the investigation of platinum-based clusters<sup>126,123,127</sup>.

Table 5: Molecular dynamics characteristics for Pt<sub>13</sub>/γ-Al<sub>2</sub>O<sub>3</sub> models

Modelled structures	Temperature (°C)	Step-time (fs)	Minimum number of steps
Pt <sub>13</sub> O <sub>n</sub> /γ-Al <sub>2</sub> O <sub>3</sub>	327	5	1500
Pt <sub>13</sub> (CO) <sub>m</sub> /γ-Al <sub>2</sub> O <sub>3</sub>	127	1	2000

Step time is necessary to assign a displacement to atoms that move due to thermal energy, that defines the next probed geometry. One can take into account bonds vibrations. Step time must not be too high compared to vibration periods otherwise atoms can move too much leading to atomisation.

For complex system that needed molecular dynamics, the following process was applied:

- Geometry optimization of a set of four initial guesses,
- Molecular dynamics on the previous most stable system,
- Geometry optimization of the three most stable systems from molecular dynamics
- Identification of the previous most stable system after geometry optimization

Other calculations were made on the latter structure, such as the determination of vibration frequencies, Bader charge analyses and metal/support interaction energy.

#### 2.3.2.6| Vibration frequencies calculations

The harmonic vibration frequencies were determined as follows. Given a system with  $N$  atoms and their  $3N$  known coordinates, forces caused by local displacements  $F_j(\mathbf{q}_i + d\mathbf{q}_i)$  are determined by slightly moving the atoms of their equilibrium position. The force  $F$  relative to atom coordinate  $j$  is expressed as linear approximation (equation (32)).

$$F_j(q_1, \dots, q_i + dq_i, \dots, q_{3N}) = F_j(q_1, \dots, q_i, \dots, q_{3N}) + dq_i \frac{\partial F_j}{\partial q_i}(q_1, \dots, q_i, \dots, q_{3N}) \quad (32)$$

These forces are also the total energy derived from the force relative to atom coordinates.

$$F_j(q_1, \dots, q_i, \dots, q_{3N}) = -\frac{\partial E}{\partial q_j} \quad (33)$$

Also these forces around the equilibrium point are in theory equal to zero. The force  $F_j(\mathbf{q}_i + d\mathbf{q}_i)$  can therefore be expressed as a second derivative of the energy with respect to atom coordinates.

$$\frac{\partial^2 E}{\partial q_i \partial q_j} = \frac{F_j(q_1, \dots, q_i + dq_i, \dots, q_{3N})}{-dq_i} \quad (34)$$

These equations form the Hessian matrix that gives by diagonalization eigenvalues. These values correspond to the harmonic vibration frequencies of the system. For the sake of accuracy we chose to use two displacements to avoid residual forces that may come from initial geometry that is not exactly at electronic equilibrium. A displacement is carried out on one side  $+d\mathbf{q}_i$  and on the other  $-d\mathbf{q}_i$ , of equilibrium according to each coordinates. This corresponds to  $6N$  displacement for  $3N$  atoms. In addition, displacements must not be too large, otherwise harmonic approximation made on the force no longer makes sense. It must also not be too weak at the risk of obtaining a numerical uncertainty and therefore erroneous frequency values. A displacement of  $\pm 0.01$  Angstrom has been applied. To compare modelled and real adsorption frequencies, one can work in shifted wavelength ( $\nu_{shift}$ ) so that anharmonic contributions are not taken into account (assuming that they do not differ between the gas state and the adsorbed state). Thus simulated wavelength of adsorbed vibration ( $\nu_{adsorbed}$ ) is subtracted to simulated wavelength of free specie vibrations ( $\nu_{gas}$ ). Same is done for experimental frequencies.

$$\nu_{shift} = \nu_{adsorbed} - \nu_{gas} \quad (35)$$

### 2.3.2.7| Transition state search

In order to determine transition states, Nudged Elastic Band method<sup>129</sup> (abbreviated NEB) were performed. It consists to get close of a minimum energy path (abbreviated MEP, Figure 15) between two local minima of potential energy (*i.e.* initial and final reaction states). Images that constitute the MEP have a minimum energy except for reaction engaged atoms. The MEP necessarily passes through at least one saddle point that corresponds to a local maximum energy of the system. This saddle point is close to transition state geometry.

The initial guess for eight intermediate images was determined by Opt'n Path<sup>131</sup> via a cartesian translation of the atoms from the initial to the final state. After completion of the NEB optimization, a quasi-newtonian<sup>132</sup> calculation was performed on the image that was the closest to the transition state. A vibrational calculation was finally done to validate the transition structure, with a single imaginary vibrational mode corresponding to the reaction studied.

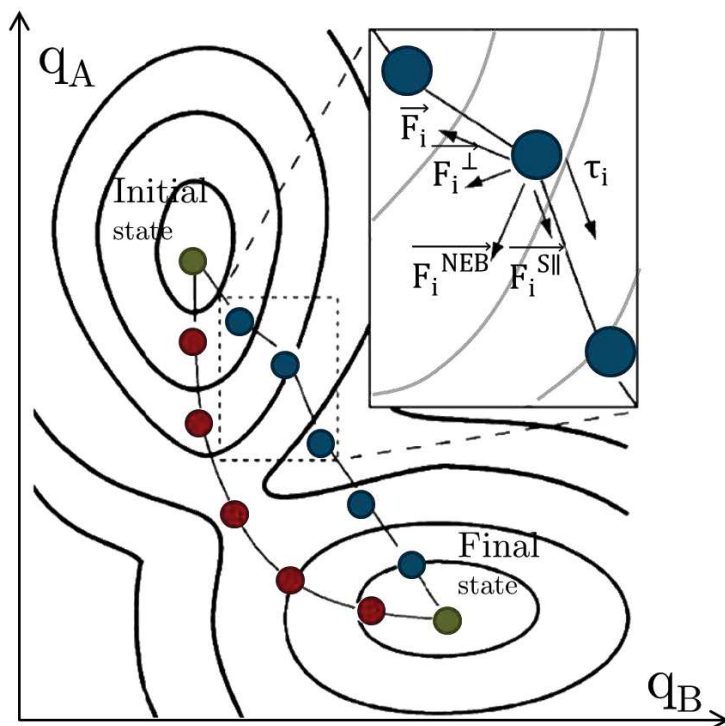


Figure 15: Schematic diagrams of the NEB method for a systems with two coordinate ( $q_A, q_B$ ). The potential isosurfaces (black), the MEP (red) and the NEB path (blue) are represented. Representation of the forces exerted on a geometry.

NEB method consists in searching for a MEP. Starting with a set of system, VASP jointly optimizes geometries. In order to look for a local maximum energy for the system, elastic forces are introduced between the successive geometries. For geometry optimization, atoms are relaxed by lowering the force  $\vec{F}_1$ , due solely to the potential energy gradient.

$$\vec{F}_i = -\vec{\nabla}E_i = -\sum \frac{\partial E_i}{\partial q_{i,j}} \vec{e}_j \quad (36)$$

In the case of NEB calculation the force  $\overrightarrow{F}_i^{\text{NEB}}$  is applied.

$$\overrightarrow{F}_i^{\text{NEB}} = \overrightarrow{F}_i^{\text{S}\parallel} + \overrightarrow{F}_i^{\perp} \quad (37)$$

We consider a system of N atoms, therefore 3N coordinates, and we denote  $\overrightarrow{R}_i = (q_{i,1}, \dots, q_{i,3N})$  the multiplet describing the image i, of energy  $E_i$ . We further define the unit vector  $\tau_i$  which characterises the tangent to the path NEB for the image i, and given by the equation (38).

$$\tau_i = \frac{\overrightarrow{R}_{i+1} - \overrightarrow{R}_{i-1}}{|\overrightarrow{R}_{i+1} - \overrightarrow{R}_{i-1}|} \quad (38)$$

The force  $\overrightarrow{F}_i^{\text{NEB}}$  is the resultant of two components: one parallel to the NEB path  $\overrightarrow{F}_i^{\text{S}\parallel}$  due to the elastic restoring forces between images.

$$\overrightarrow{F}_i^{\perp} = \overrightarrow{F}_i - (\overrightarrow{F}_i * \tau_i)\tau_i \quad (39)$$

On the other hand,  $\overrightarrow{F}_i^{\perp}$  is the force orthogonal to the NEB path  $\overrightarrow{F}_i^{\perp}$  which results from force projection  $\overrightarrow{F}_i$  on the hypersurface orthogonal to  $\tau_i$ , with k the stiffness constant.

$$\overrightarrow{F}_i^{\text{S}\parallel} = k(|\overrightarrow{R}_{i+1} - \overrightarrow{R}_i| - |\overrightarrow{R}_i - \overrightarrow{R}_{i-1}|)\tau_i \quad (40)$$

In this work, the convergence criterion for the relaxation loop was set to 0.02 eV/Å. The initial guess for eight intermediate images was determined by Opt'n Path<sup>131</sup> *via* a cartesian translation of the atoms from the initial to the final state. After completion of the NEB optimization, a quasi-newtonian<sup>132</sup> calculation was performed on the image that was the closest to the transition state. A vibrational calculation was finally done to validate the transition structure, with a single imaginary vibrational mode.

### 2.3.2.8| Thermodynamic parameters determination

Several data have been calculated from molecular simulations. One of the most used in this work is the adsorption energy of a specie  $E_{\text{adsorption}}$ , which defines the energy

needed to desorb a species on a surface<sup>vii</sup>. This energy is positive and equation (41) explains its calculation.

$$E_{adsorption} = E_{surf-i} - E_{surf} - E_i^{gas,ref} \quad (41)$$

With  $E_i^{gas,ref}$  the electronic energy of the species  $i$  calculated from that of its reference in the gas phase,  $E_{surf}$  the electronic energy of the surface alone and  $E_{surf-i}$  the electronic energy of the surface with the adspecies  $i$ . The adsorption energy can be calculated averagely from equation (42), with  $n_i$  the number of adspecies present in the system.

$$\overline{Q}_i = -\frac{1}{n_i}(E_i^{gas,ref} + E_{surf} - E_{surf-i}) \quad (42)$$

For the alumina supported cluster model, the interaction energy between support and platinum cluster was calculated with single point calculations (referred with \*) for the separate cluster and support systems at the geometry of the supported system.

$$E_{interaction} = (E_{Pt_{13}O_n/\gamma-Al_2O_3} - E_{Pt_{13}O_n}^* - E_{\gamma-Al_2O_3}^*) \quad (43)$$

Gibbs free energy was calculated with the following equations, with  $E$  electronic energy,  $S$  the entropies,  $H$  enthalpies,  $P$  the pressure and  $V_m$  the molar volume.

$$G(T, p) = E + H_{trans}(T, p) + H_{vib}(T, P) + H_{rot}(T, p) + PV_m - T(S_{trans}(T, p) + S_{vib}(T, p) + S_{rot}(T, p)) \quad (44)$$

For gas phase species ( $O_2$ ,  $CO$  and  $CO_2$ ), the following equations are used to determine translational and rotational terms. In the case of condensed systems these terms are neglected. Equations (45) to (49) detail each entropic and enthalpic contribution calculations.

$$H_{vib}(T) = N_A \left[ \sum_n \frac{1}{2} h\nu_n + \sum_n \frac{h\nu_n \times \exp\left(-\frac{h\nu_n}{k_B T}\right)}{1 - \exp\left(-\frac{h\nu_n}{k_B T}\right)} \right] \quad (45)$$

$$H_{trans}(T) + H_{rot}(T) + PV_m(T) = 4RT \quad (46)$$

---

<sup>vii</sup> In the case of oxygen adsorption in Chapter 3,  $O_2$  adsorption energy is calculated in place instead of atomic oxygen. Therefore equation (41) is turned into  $Q_{O_2} = E_{surf-O_2} - E_{surf} - E_{O_2}^{gas}$ . In Chapter 6, adsorbed radical gas references were gas radicals.

$$S_{\text{vib}}(T) = N_A k_B \left[ \sum_n \frac{\frac{h c \nu_n}{k_B T} \times \exp\left(-\frac{h \nu_n}{k_B T}\right)}{1 - \exp\left(-\frac{h \nu_n}{k_B T}\right)} - \sum_n \ln\left(1 - \exp\left(-\frac{h \nu_n}{k_B T}\right)\right) \right] \quad (47)$$

$$S_{\text{rot}}(T) = N_A k_B \left( \frac{3}{2} + \ln \left[ \frac{\sqrt{\pi}}{\sigma} \left( \frac{8 \pi^2 k_B T}{h^2} \right)^{\frac{3}{2}} \sqrt{A_e \times B_e \times C_e} \right] \right) \quad (48)$$

$$S_{\text{trans}}(T, p) = N_A k_B \left( \frac{5}{2} + \ln \left( \frac{RT}{P} \left( \frac{2 \pi M k_B T}{h^2} \right)^{3/2} \right) \right) \quad (49)$$

With  $\nu_n$  the vibrational frequencies of the system,  $k_B$  the Boltzmann constant,  $N_A$  the Avogadro constant,  $T$  the temperature,  $h$  the Planck constant and  $M$  the molar weight.  $\sigma$  corresponds to the symmetry number of the system and  $A_e$ ,  $B_e$  and  $C_e$  the moments of inertia according to the eigenaxes of the molecule<sup>viii</sup>.

The determination of adsorption free energy  $G$  used to build the thermodynamic diagrams is detailed in the following equation. The coverage domains reflect the minimum free energy among other coverage systems.

$$G_{\text{adsorption}}(p_{O_2}, T, \theta_{O_2}) = \left( G_{Pt_{13}O_n}(T, \theta_{O_2}) - G_{Pt_{13}}(T) - \frac{n}{2} G_{O_2}(p_{O_2}, T) \right) \quad (50)$$

## 2.4| Micro-kinetic simulations

Building micro-kinetic models for heterogeneous systems is the aim of this work. The Chemkin software was used to simulate micro-kinetics from *ab initio* thermokinetic parameters. This section is a reminder of the rate constant determination using both molecular modelling and estimated methods. The development of a surface reaction generator for oxidation hydrocarbons is also discussed.

### 2.4.1| Micro-kinetics and catalysis

#### 2.4.1.1| Introduction to catalysis kinetics

Identified in the nineteenth century by Berzelius<sup>133</sup>, catalysis knows great progress with Langmuir<sup>134</sup> in the 1910s thanks to the understanding of elementary reaction kinetics. The later corresponds to molecular level reactions. Elementary reactions are generally involving minor changes from the reactants to the products meaning that most of the time one bond is broken and another is formed. These reactions also imply that the

---

<sup>viii</sup> Gas phase entropies and enthalpies have been calculated with online calculator <http://www.colby.edu/chemistry/PChem/scripts/ABC.html>.

changes occurring at the molecular level during the reaction is captured. Fluids elementary reactions involve generally one or two reactants. Indeed the probability that three particles encounter once is low in the medium. In the case of species adsorbed on a solid, third particles are more present, such as a catalyst vacant site.

Catalysis phenomenon can be described by a succession of elementary reactions, starting with adsorption of at least one reactant. It ends with desorption products. The physico-chemical process of heterogeneous catalysis is generalized by the following elementary steps<sup>135</sup>:

- Material transport of the gaseous reactants close to the surface of the catalyst,
- Reactant adsorption on the catalyst,
- Surface reaction that generates the products,
- Product desorption from the surface,
- Product diffusion in the gaseous phase.

Two mechanisms explaining the heterogeneous catalysis of bimolecular reactions are often invoked in the literature (Figure 16). On the one hand the Eley-Rideal mechanism, by which one reactant adsorbs on the surface of the catalyst while the second comes into contact with the first in gas phase. The product formed is then desorbed. On the other hand, the second mechanism is called Langmuir-Hinshelwood and assumes adsorption of two reactants followed by their reaction on the catalyst surface which leads to the formation of adsorbed products.

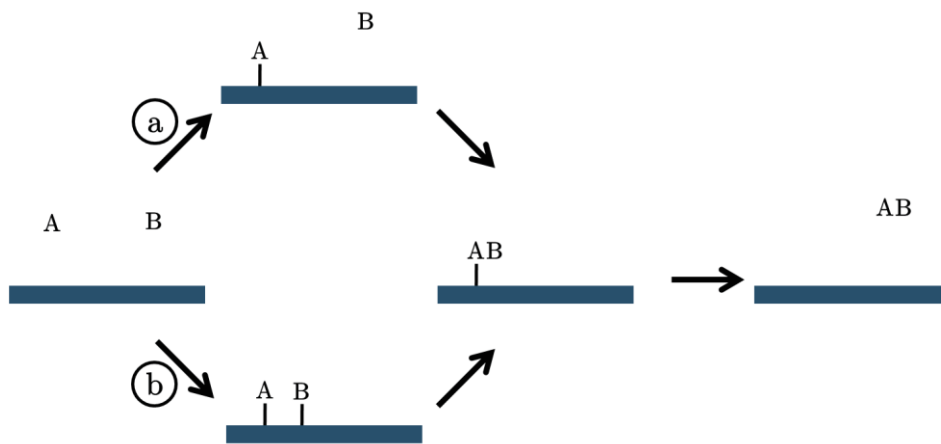


Figure 16: a) Eley-Rideal and b) Langmuir-Hinshelwood mechanisms. Surface diffusion of reactants and products also happens onto the catalyst.

#### 2.4.1.2| Constant rate determination

While the first one happens for highly reactive species in the gas phase such as radicals, the latter is more commonly observed and is the one on which the present study is based on. The interest of working with elementary steps lies in partial orders reaction.

For the following reaction, with  $\nu_i$  the stoichiometric coefficients, reaction rate is  $v_{\text{reaction}}$ , (with  $n_i$  in moles).



$$v_{\text{reaction}} = -\frac{1}{\nu_A} \frac{dn_A}{dt} = -\frac{1}{\nu_B} \frac{dn_B}{dt} = \frac{1}{\nu_C} \frac{dn_C}{dt} \quad (52)$$

The elementary reaction rate is given by the rate constant  $k$ , the reactant  $[i]$  and stoichiometric coefficients.

$$v_{\text{forward}} = k_{\text{forward}} [A]^{\nu_A} [B]^{\nu_B} \quad (53)$$

$$v_{\text{backward}} = k_{\text{backward}} [C]^{\nu_C}$$

In order to determine rate constant  $k$ , Arrhenius<sup>136</sup> gave a first law in 1889, based on the work of Van't Hoff, which describes most of the reactions studied then.

$$k = A e^{-\frac{E_{\text{activation}}}{RT}} \quad (54)$$

This equation is based on experimental data:  $E_{\text{activation}}$  is the activation energy. This is the minimum energy for the reaction to occur. Pre-exponential factor  $A$  is seen as an intrinsic reaction coefficient to experimental conditions. The rate constant expression has a Maxwell-Boltzmann type distribution according to temperature. Altered Arrhenius law are also used. The most common is the Arrhenius-Kooij, involving a temperature dependence of  $A$  and/or activation energy<sup>137</sup>.

$$k = AT^\beta e^{-\frac{E_{\text{activation}}(T)}{RT}} \quad (55)$$

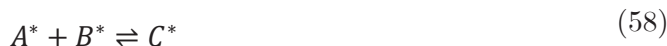
Although empirical, this equation is valid for many reactions. However, it reflects a macroscopic point of view and does not allow interpretation of parameters at the molecular level.

Trautz and Lewis proposed in the 1910s a molecular interpretation of fluid phase chemical kinetics, known as collision theory. It also relies on the activation energy needed for the reaction to occur. Also it allows to calculate pre-exponential factor thanks to molecular parameters. This factor is then interpreted as an average collision frequency between reactants and involves consequently geometry inputs from Vannice<sup>135</sup>. For a gas phase bimolecular reaction, it gives:



$$k_{forward} = N_A \sigma_A \sqrt{\frac{8k_B T}{\pi \mu_{AB}}} e^{-\frac{E_{activation}}{RT}} \quad (57)$$

With reduced mass  $\mu_{AB}$ , cross section  $\sigma_A$  and Avogadro constant  $N_A$ . This approach can be applied to surface reactions, such as the collision of two adsorbed reactant moving freely (in two dimensions) on the catalyst surface.



$$k = 2P_S \sigma_{AB} \sqrt{\frac{\pi k_B T}{2\mu_{AB}}} e^{-\frac{E_{activation}}{RT}} \quad (59)$$

The use of collision theory in real cases fails to represent reactions with complex species. The main hypothesis is the assimilation of reactants to hard spheres with homogeneous reactivity, which is rarely the case. The difference between Arrhenius law pre-exponential factor and collision frequency is integrally attributed to the non-uniformity of reactive molecules. The ratio between the two quantities is called steric factor, and varies considerably (from  $10^1$  to  $10^{-6}$ ). This theory is however used to determine the order of magnitude of a reaction constant, in favorable cases for its application<sup>135</sup>.

#### 2.4.1.3| Transition state theory

The rise of thermodynamics applied to chemical reactions led Eyring, Evans and Polanyi to build the transition state theory (TST)<sup>138-140</sup> by which a reaction rate constant depends on free enthalpy of its transition state, *i.e.* a high energy state by which reactants pass leading to products.

The main hypothesis is that a molecule that reaches the transition state can not go back. A single space movement is responsible for the reaction (passing above an energy barrier)<sup>137</sup>. Particles follow a characteristic movement of classical mechanics, according to a Boltzmann distribution even if the system is not in equilibrium. The tunneling effect that might occur during a reaction is not taken into account. This assumes that reactants can reach the products while going “through” the energy barrier.



$$k = \frac{k_B T}{h} e^{\frac{\Delta S^{TS}}{R}} e^{-\frac{\Delta H^{TS}}{RT}} \quad (61)$$

This theory is successful in understanding phenomena at the molecular level of a wide reaction range. However, it requires perfect knowledge of the geometry as well as transition state thermodynamics. Limitations lie in the core of transition state notion:

this theory assumes that there is only one path from reactants to products, *i.e.* a single transition state. Also TST handles only reactions that passes through as transition state, the free energy of which is higher than reactants or products. Finally, transition state may have a different geometry depending on temperature and environment, this can lead to misestimated reaction parameters considering wide operating conditions<sup>135</sup>.

While Arrhenius law parameters are experimentally determined, those from transition state theory require characterization of an unstable and short-living system. Progresses made over the last twenty years in numerical computation capabilities as well as different mathematical methods in solving the Schrödinger equation for many systems now allows to better estimate thermodynamics of transition states<sup>138</sup>.

Regarding *ab initio* base micro-kinetic schemes (section 2.4.3), *ab initio* determined thermodynamic parameters were used to calculate Arrhenius type rate constant. The averages of  $\Delta S$  and  $\Delta H$  on the 30-730°C (300-1000K) temperature range were took into account. For estimated micro-kinetic (section 2.4.4), *ab initio* electronic energies were used as activation enthalpies and pre-exponential factors were TST estimated. In order to run kinetic schemes to simulate experimental conditions, the Chemkin-Pro software was employed. Its description is displayed in the next section 2.4.2.

## 2.4.2 | Chemkin software

The ANSYS Chemkin-Pro software was used to model some of the thesis experiments and to evaluate the accuracy and robustness of the molecular simulations obtained. The simulations were carried out in zero dimension, that is to say without taking into account spatial constraints in the reactors used. Moreover the calculations were performed in mean field, supposing homogeneous surface and gas. The software uses five main input types (Figure 17): operating conditions, species and reaction data (gas and surface), thermodynamic data (gas and surface), and transport data (gas). The Chemkin DASPK<sup>ix</sup> solver was used with numerical absolute tolerance was set at least to  $10^{-18}$  and relative tolerance to  $10^{-6}$ .

---

<sup>ix</sup> DASPK solver is a differential-algebraic equation solver, *i.e.* containing both differential and polynomial equations. The DASPK solver uses the backward differentiation formulas of orders one through five to solve the a system. Absolute and relative tolerances are dimensionless.

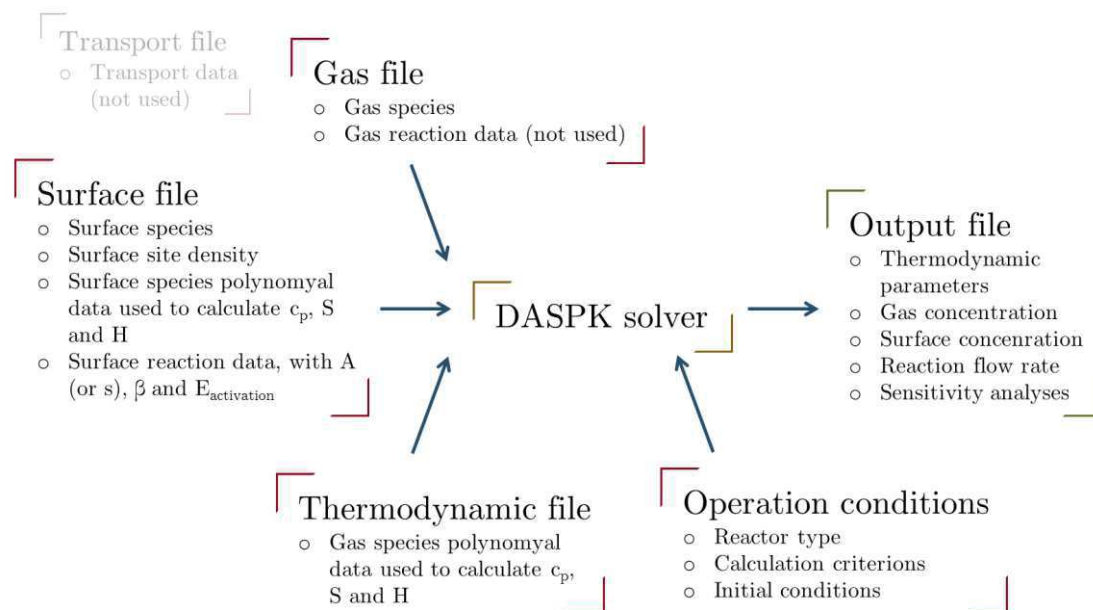


Figure 17: Illustration of Chemkin input and output files.

A continuously stirred-tank reactor (abbreviated CSTR) was used. Reactor Peclet number was much lower than unity. Thiele and mass Biot numbers were found to be also much lower than one, highlighting the occurrence of kinetic regime (Appendices). Platinum densities are determined with respect to the molecular structures. Pt(111) and Pt<sub>13</sub> and are respectively  $2,41 \cdot 10^{-9}$  mol/cm<sup>2</sup> and  $1,54 \cdot 10^{-9}$  mol/cm<sup>2</sup>. The platinum surfaces modelled  $S_{platine}$  depend on the amount of catalyst  $m_{catalyseur}$  of the referent experiment. Equation (62) is applied:

$$S_{platinum} = m_{catalyst} \times w_{Pt} \times \frac{S_{Pt_{13}}}{n_{Pt,surface} M_{Pt}} \quad (62)$$

With  $w_{Pt}$  the platinum mass content of the catalyst,  $S_{Pt_{13}}$  the surface of the Pt<sub>13</sub> model aggregate, number of platinum atoms at the surface  $n_{Pt,surface}$  and the platinum atom mass  $M_{Pt}$ . In the case of platinum aggregates on alumina, kinetic modelling does not take into account the support. In other words, modelling consists of a dense surface of platinum atoms with the reactivity of a dispersed aggregate, only the platinum surface counts.

Only reactions and their surface kinetic data are integrated into the model. Indeed the objective is to observe the surface chemistry of the system. Therefore no gas phase chemistry is present in the model. Indeed the experimental data suggest that no gas phase reaction occurs in operating conditions. Studied reactions are all Langmuir-Hinshelwood types. Kinetic parameters are however generally expressed with Chemkin-Pro by the expression (63).

$$k = AT^\beta e^{-\frac{E_{\text{activation}}(T)}{RT}} \quad (63)$$

With  $A$  the pre-exponential factor translating a probabilistic approach at the molecular scale of the reaction,  $\beta$  the power relative to the temperature and  $E_{\text{activation}}$  the energy required for the reaction to take place. Thermodynamic data are used to calculate the instantaneous temperature of the reactor as well as the kinetic parameters of the backward reaction by the following equation:

$$k_{\text{backward}} = k_{\text{forward}} \times K_{\text{backward}}(T) = \exp\left(-\frac{\Delta_r G_{\text{backward}}}{RT}\right) \quad (64)$$

These data are available in open access for a large number of species in the gas phase, and some surfaces. Yet the peculiarity of the studied surfaces led us to proceed differently.

The temperature of the experiments carried out is regulated. Moreover, no drift to the set point was observed during the experiments, indicating a lack of extreme endo- or exothermic reaction. On the other hand, the calculation of the inverse rate constant by thermodynamics is not used in the models presented here. Indeed all reactions are formulated in both directions with their own kinetic parameters. Finally, transport data of the gas species are not used in the models. Since the gas medium is considered as unreactive and homogeneous, these data are not considered in this work.

In order to evaluate the robustness of the reaction parameters, the raw first-order sensitivity  $S_i$  is reported. It corresponds to the partial derivatives of the reaction flux  $\phi_i$  according to the pre-exponential factor  $A_i$  of each reaction, as displayed in the following equation. Data reported in this work correspond to the ones at the TPD peak temperatures. This sensitivity allows to estimate the reactivity discrepancies of a kinetic model according to slight kinetic parameter shift. Therefore this common tool informs about the stability of a model.

$$S_i(t) = \frac{\partial \phi_i(t)}{\partial A_i} \quad (65)$$

### 2.4.3 | Micro-kinetics and molecular modelling

In the case of kinetic models fully described by molecular simulation, the scheme was composed of few surface reactions. In addition, two formalisms were used in this study according to the two surfaces chosen.

The formalism used to model the kinetics of the Pt(111) surface (shortened by Pt(111) formalism) is classical: a surface site corresponds to one platinum atom of the Pt(111) surface. For instance, the molecular simulation of oxygen adsorbed on Pt(111) shows that it adsorbs in a hollow mode, *i.e.* between three platinum atoms. This is formulated

in the micro-kinetic model that oxygen takes up one site or one atom or three thirds of platinum atoms. In this formalism, one site contains one specie and reactions occur between two adspecies present on distinct sites. The advantage of this approach is the limited number of reactions specified in the model. The disadvantage lies in the rigidity of kinetic parameter expression: Chemkin-Pro software only allows to specify kinetic parameters (equation (63)) that depend linearly on the coverage rate in one or more adsorbed species.

With regard to the  $\text{Pt}_{13}/\gamma\text{-Al}_2\text{O}_3$  surface, the micro-kinetic formalism (abbreviated thereafter  $\text{Pt}_{13}$  formalism) is more detailed. One site is in fact an aggregate of 13 platinum atoms, on which many species are able to adsorb, as molecular simulations suggest. To benefit from the precision of the data collected by the molecular simulation, reactions are duplicated at all coverage rates. This provides a considerable number of reactions, which are not all studied by molecular simulation. The missing data are interpolated from *ab initio* investigated systems.

Data obtained by molecular simulation are integrated in the micro-kinetic models by the thermodynamic potentials and the calculation of the rate constants of the reactions. Given the following chemical reaction, the thermodynamic potential variations  $\Delta X_r$  of the forward reaction are calculated by equation (67). With X a thermodynamic potential (enthalpy, entropy or free enthalpy).



$$\Delta X_r = X_C - X_B - X_A \quad (67)$$

Reaction rate constants are determined in two different ways in this work. In the case of adsorption reactions or desorption for the backward direction, the general chemical equation is:



Equation (69) reflects the probability of the gaseous species adsorbing to the surface with the sticking coefficient  $s_i$ . A value of 1 implies a collision which is systematically reactive with the surface. The determination of the reaction constant k then depends on the coverage of each species j,  $\theta_j$  already present on the surface of the catalyst, the partial order of the species j,  $\nu_j$ , the total adsorption site number  $\Gamma_{tot}$  and the adspecies molar mass  $M_i$ .

$$k_{adsorption} = s_i \frac{\prod_{j=1} \theta_j^{\nu_j}}{\Gamma_{tot}^m} \sqrt{\frac{RT}{2\pi M_i}} e^{-\frac{E_{adsorption}}{RT}} \quad (69)$$

The three kinetic parameters (equation (63)) for such a reaction are the sticking coefficients, the power applied to the temperature  $\beta$  (here 0.5) and  $E_{adsorption}$ . In

practice, sticking coefficient is an imprecise or unknown parameter for most reactions and depends on multiple molecular scale factors (collision angle, gas pressure, kinetic energy of the particle, etc.). For this kind of reaction, the kinetic data are integrated in the reverse (desorption) reaction by equation (64).

The second case concerns surface reactions (equation (60)). These have been studied by molecular simulation via the NEB method, and transition state thermodynamics is known. The Eyring equation (61) allows to determine the reaction rate.

The three kinetic parameters integrated into the models will follow Arrhenius-Kooij formalism. A Matlab script was used to fit thermodynamic parameters to Chemkin formalism.

#### 2.4.4 | Estimated micro-kinetics

Heavy micro-kinetic models containing hundreds or thousands of reactions are discussed in these section. These later used generally estimated micro-kinetic parameters that are generated by specific codes. Few reaction generator for gas species are currently available as NETGEN<sup>141</sup>, EXGAS<sup>142</sup>, Genesys<sup>143</sup> and Reaction Mechanism Generator<sup>144</sup>. These powerful tools are able to generate reactions as well as their kinetic parameters via preset laws and select reaction of interest given the usefulness of the reaction in a peculiar case study. Yet these codes do not deal with surface reaction, except RMG-cat program that developpment is in progress. This code has yet only been tested on Ni(111) surface recently for methane reforming<sup>145</sup>. This section is therefore devoted to the developpement of this kind of tool that would be usefull for micro-kinetic modelling of hydrocarbon oxidation on platinum surfaces.

Exhaustivity of the data generated by the molecular simulation is limited by its computation time. It is not possible, with current technologies and infrastructures, to simulate hundreds of condensed phase configurations in an automatic way. In order to generate heavy models in adequacy with multi-scale approach, estimated micro-kinetics based on *ab initio* calculations were performed.

Studies on the oxidation of specific hydrocarbons focus on a simplified pattern of reactions built on previous research. This may lead to neglecting other reactions and reaction paths. A systematic process as well as Matlab scripts allows to generate an approximate scheme incrementally (from the smallest to the most complex species). In our case, we have set aside the nitrated and sulfur compounds, whose reactivities are not considered in this study. We focus on  $C_xH_yO_z$  hydrocarbons type. The selected gas species are gathered in Table 6.

Table 6: Selected species for estimated mechanisms used for light hydrocarbons oxidation in Chapter 6.

C <sub>0</sub> species	C <sub>1</sub> species	C <sub>2</sub> species		C <sub>3</sub> species
H <sub>2</sub> – Dihydrogene	CH <sub>4</sub> – Methane	C <sub>2</sub> H <sub>6</sub> – Ethane	C <sub>2</sub> H <sub>4</sub> – Ethylene	C <sub>3</sub> H <sub>8</sub> – Propane
O <sub>2</sub> – Dioxygene	CH <sub>3</sub> OH – Methanol	C <sub>2</sub> H <sub>2</sub> – Acetylene	C <sub>2</sub> H <sub>4</sub> OH – Ethanol	C <sub>3</sub> H <sub>6</sub> – Propene
H <sub>2</sub> O – Water	CH <sub>2</sub> O – Formaldehyde	C <sub>2</sub> H <sub>6</sub> O – Dimethyl ether	C <sub>2</sub> H <sub>4</sub> O – Acetaldehyde	C <sub>3</sub> H <sub>4</sub> – Propyne
H <sub>2</sub> O <sub>2</sub> – Hydrogen peroxide	CH <sub>2</sub> O <sub>2</sub> – Formic acid	C <sub>2</sub> H <sub>2</sub> O <sub>2</sub> – Glyoxal	C <sub>2</sub> H <sub>2</sub> O <sub>4</sub> – Oxalic acid	
	CO – Carbon monoxide	C <sub>2</sub> H <sub>4</sub> O <sub>2</sub> – Acetic acid	C <sub>2</sub> H <sub>2</sub> O – Cetene	
	CO <sub>2</sub> – Carbon dioxide			

From the selected molecules, we consider adsorbed radical species (in practice, Pt-O, Pt-H or Pt-C bonds are formed, so that the real system is not radicalar) that can appear during a bond breaking reaction. Dehydrogenation, dehydroxylation or the cleavage of a carbon-oxygen double bond are elements that allows to determine potential adspecies. This step is generated automatically by a script that decomposes the initial species (Table 6) and generates an image and an adjacency matrix related to the radical species.

Generated radicals are potentially unstable species, even adsorbed on a surface. Next step consists in potential radicals *ab initio* geometry optimization on Pt(111) surface. The objective were : to determine if the radical was stable without thermal energy<sup>x</sup> and determine its adsorption energy at low coverage on Pt(111). On more than one hundred possible adsorbed radicals, one counts 63 after validation by molecular simulation. For each potential adsorbed radical, several adsorption modes were tested. Only the most stable radicals, *i.e.* with the lowest electronic energy, were kept.

The next step consists in generating all the possible reactions existing between these adsorbed species. A Matlab script was developed from graph theory. Species are

---

<sup>x</sup> Geometry optimizations are performed with VASP without any speed due to thermal energy, thus temperature is 0K.

formalized by an undirected adjacency matrix<sup>xi</sup> (Figure 18(a,b)). The code then goes through all the two-by-two species combinations<sup>xii</sup>. The first step is to diagonally concatenate reactant matrices (Figure 18c) to form a reactant matrix. The script then tries to break all existing links one by one, to create potential products<sup>xiii</sup> (Figure 18d). The last step is to split the products matrix into two product matrices, and verify if these products are part of the original species.

A scheme of possible reactions is obtained from a group of selected species. The reactions (Langmuir-Hinshelwood type) respect the law of mass action. In order to keep only elementary reactions needed for the Chemkin-Pro formalism, a constraint is applied during the search for a reaction. Indeed, "only a destroyed link and a link created" is the criterion for elemental reactions<sup>xiv</sup>. To note that breaking bond of a hollow adsorbed species does account for one bond, for instance.

---

<sup>xi</sup> The aim of this matrix is to translate bonds between atoms. Simple, double or triple bonds will be counted as 1 into the matrix, zero either. Figure 18 (a, b, e, f) illustrates adjacency matrices.

<sup>xii</sup> The script generates only 2 reactants and 2 products at most, without counting free surface sites.

<sup>xiii</sup> The script does not take into account atom valences, electrons nor bond type.

<sup>xiv</sup> An exception exists to this rule. Molecular simulations have shown that close species such as  $\text{CH}_3\text{OH}^*$  and  $\text{CH}_2\text{OH}^*$  have distinct adsorption modes. This leads to the exclusion of the  $\text{CH}_3\text{OH}^*$  to  $\text{CH}_2\text{OH}^*$  deshydrogenation reaction as an elementary rule. Yet it is probable that there is an elementary reaction between the two species *via* a bridged surface intermediate.

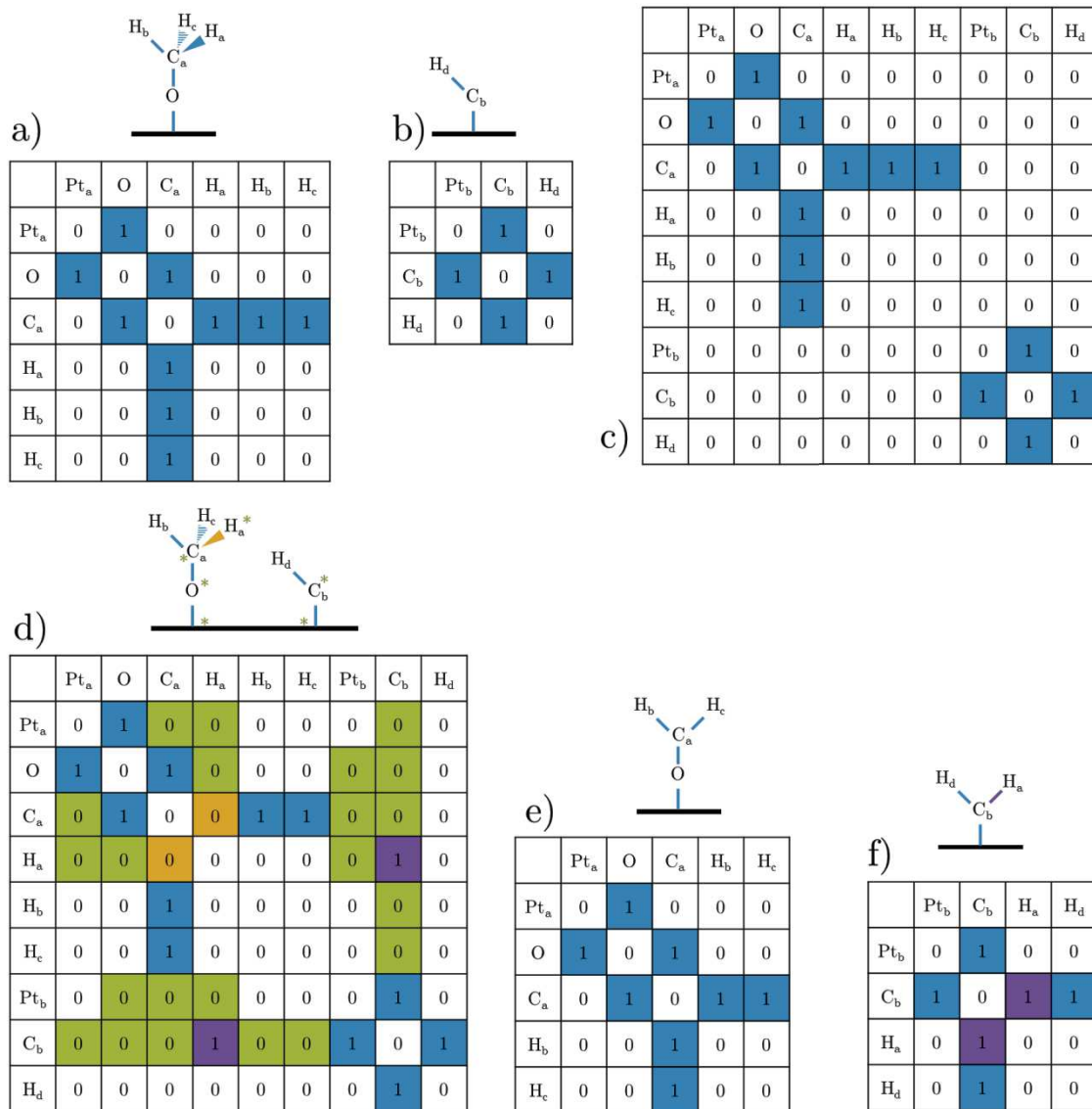


Figure 18: Representations and adjacency matrices associated with the search for reactions between  $\text{CH}_3\text{O}^*$  and  $\text{CH}^*$  adspecies with possible  $\text{CH}_2\text{O}^*$  and  $\text{CH}_2^*$  products. a) and b) represent the reagents and their adjacency matrix with the actual links (in blue). c) is the adjacency matrices of the reactive system. Figure d) shows, from c), the chosen destroyed link (in yellow) and the binding possibility to be created (in green), as well as the selected link created (in purple). e) and f) represent the products and their matrices separated since d).

To build mechanisms involving scarcely known species and reactions, an approximate evaluation of the reaction activation energies is important. Shustorovich and coworkers developed UBI-QEP (for Unity Bond Index-Quadratic Exponential Potential) based on both experimental data and molecular modelling<sup>146,147</sup>. It allows the evaluation of adsorption heats and activation energies between adspecies, from atomic heats of adsorption. This method assumes a purely spherical interaction between two bodies (atoms). The bond index defined by Pauling in 1947 between two bodies is defined by

Equation (70). It defines the order of connection between these two bodies by a Morse type potential.

$$x = e^{-\frac{r-r_0}{a_x}} \quad (70)$$

With  $r$  the inter-atomic distance,  $r_0$  the equilibrium distance and  $a_x$  a constant. The hypothesis of the spherical interaction gives the relation (71).

$$E(x) = D_{AB}(2x - x^2) \quad (71)$$

With  $D_{AB}$  the binding energy at equilibrium. According to the authors, the case of an interaction involving more than two atoms can be handled as several two-body interactions, with the sum of bond index equal to unity. Thus for the adsorption of CO on a metal, one has the CO-metal bond energy.

$$E_{CO-metal} = D_{C-o}(2x_{CO} - x_{CO}^2) + D_{C-metal}(2x_{C-metal} - x_{C-metal}^2) \quad (72)$$

With  $x_{CO}$  and  $x_{C-metal}$  are respectively the bond indexes of C-O and C-M, and  $D_{C-o}$  and  $D_{C-metal}$  binding energies. The order of binding being reduced to 1 according to the UBI-QEP method, we have equation (73)<sup>147,146</sup>.

$$x_{CO} + x_{C-metal} = 1 \quad (73)$$

Resolution of equation (72) leads to expression (74) of the energy of the bond  $E_{CO-metal}$ .

$$E_{CO-metal} = D_{C-o} + \frac{D_{C-metal}^2}{D_{C-metal} + D_{C-o}} \quad (74)$$

Shustorovich *et al.* developed a set of standard solutions for determining molecules heat of adsorption, corresponding to the relationship (75). Since the activation energy of a reaction corresponds to the bonds formation and destruction, UBI-QEP can therefore determine these energies from the heats of adsorption.

$$Q_{CO-metal} = E_{CO-metal} - D_{C-o} \quad (75)$$

In this work, heats of adsorption were determined using *ab initio* calculations. In fact, the UBI-QEP method needs the knowledge of adsorption modes. UBI-QEP adsorption energies have been calculated for methanol, considering distinct adsorption modes (Figure 19). UBI-QEP forecasts molecular modelling adsorption energy of methanol, considering the same adsorption mode. Yet the choice of another mode leads to adsorption energies up to four times stronger than expected. Also molecular modelling

was used to both determine adsorption energies (even for estimated kinetics) and ensure the stability of the adspecie onto the surface.

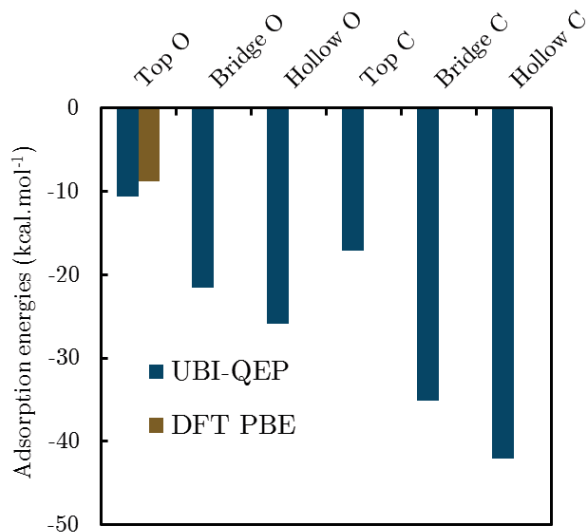


Figure 19: UBI-QEP and DFT adsorption energies of methanol, considering multiple adsorption modes. Molecular modelling only gives top Pt-O bond stable configuration, meaning that the other adsorption modes should be less stabilizing than the top one, whereas UBI-QEP predicts the opposite trend.

Therefore UBI-QEP was used only to determine apparent activation barrier. This calculation is based on adsorption energies. Considering the general surface reaction with reactants A and B that gives AB product, Figure 20a describes a one-dimensional Lennard-Jones potential.

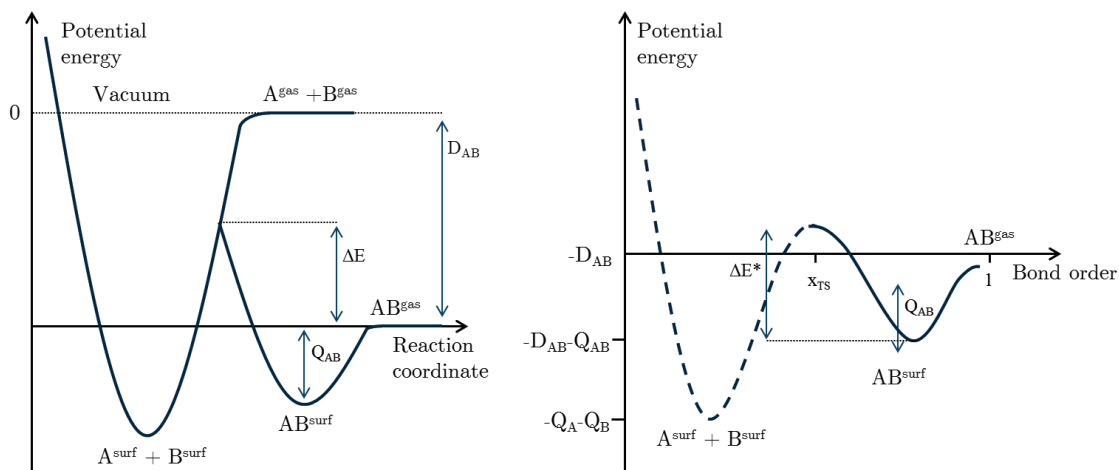


Figure 20 : a) Lennard-Jones one dimensional potential according to one reaction coordinate, that corresponds to the average AB-surface distance, and b) the multi-dimensional unity bond index (UBI) potential diagram. Adapted from Shustorovich and coworkers<sup>146,147</sup>.

The UBI-QEP interaction energy between AB product and the surface is defined the following equation:

$$E_{AB} = D_{AB}(2x_{AB} - x_{AB}^2) + Q_A(2x_A - x_A^2) + Q_B(2x_B - x_B^2) \quad (76)$$

The unity bond index constraint gives the sum of the bond indexes  $x_i$  equal to unity. It leads to the simplified equation (77), that expressed the AB-surface energy only depending on the bond order  $x_{AB}$  that is directly linked to AB distance from the surface.

$$E_{AB} = x_{AB}^2 \left( \frac{Q_A Q_B}{Q_A + Q_B} + D_{AB} \right) + x_{AB} \left( \frac{2Q_A Q_B}{Q_A + Q_B} - 2D_{AB} \right) + \frac{Q_A Q_B}{Q_A + Q_B} - Q_A - Q_B \quad (77)$$

In the case of non-interacting reactive (Figure 20a), the total energy  $E_{A+B}$  is expressed by equation (84). This latter has no bond index conservation imposed because A and B energies are independent. Also for this reason  $x_{AB} = 0$ .

$$E_{A+B} = E_A + E_B = Q_A(2x_A - x_A^2) + Q_B(2x_B - x_B^2) \quad (78)$$

According to Figure 20a, the intersection of these two potential curves appears at the reaction transition state. And because  $x_{AB} = 0$  all along the  $E_{A+B}$  potential curve, it means that the bond index  $x_{AB}$  is equal to zero for the transition state also, therefore giving:

$$E_{AB} = \frac{Q_A Q_B}{Q_A + Q_B} - Q_A - Q_B \quad (79)$$

The activation barrier  $\Delta E_{AB}$  can also be expressed according to  $E_{AB}$ ,  $Q_{AB}$  and  $D_{AB}$ , that gives equation (80), with  $\Delta H_{AB}$  the standard formation enthalpy of the adsorbed specie AB.

$$\Delta E_{AB} = E_{AB} + Q_{AB} + D_{AB} = \frac{Q_A Q_B}{Q_A + Q_B} - Q_A - Q_B + Q_{AB} + D_{AB} = \Delta H_{AB} + \frac{Q_A Q_B}{Q_A + Q_B} \quad (80)$$

Yet this activation barrier is an overestimation, since AB transition state bond distance is finite. Therefore AB transition state bond index is greater than zero,  $x_{TS}$ . This result in a lower energy transition,  $\Delta E^*$ . The true activation barrier need the AB transition state bond index (or AB bond distance) to be calculated. However UBI-QEP does not provide tools to determine it. Instead one will choose the average between the overestimation and a barrierless transition, *i.e.* equation (81).

$$\Delta E^* = \frac{1}{2} \left( \Delta H_{AB} + \frac{Q_A Q_B}{Q_A + Q_B} \right) \quad (81)$$

Shustorovich and coworkers<sup>146,147</sup> developed typical activation barrier equations for dissociative adsorption and surface substitution reactions. Molecular and atomic adsorption is assumed to be barrierless.

# 3| Dissociative adsorption of O<sub>2</sub> on Pt/ $\gamma$ -Al<sub>2</sub>O<sub>3</sub>

Oxygen reactivity toward catalytic surfaces is a prominent topic for oxidation catalysis. The study of oxygen/platinum interaction was therefore the first work of this PhD. This chapter is an adaptation of the following submitted article: *A Multi-Scale Approach to the Dissociative Adsorption of Oxygen on Highly-Dispersed Platinum Supported on  $\gamma$ -Al<sub>2</sub>O<sub>3</sub>*. A. Sangnier, M. Matrat, A. Nicolle, C. Dujardin, C. Chizallet.

## 3.1| Introduction

Platinum is a widely used active phase in heterogeneous catalysis due to its intrinsic activity for hydrogenation/dehydrogenation reactions as well as its redox properties<sup>148–151</sup>. For instance, it is involved in many environmental, refining and petrochemical applications<sup>1,152–155</sup>. Concerning automotive applications, post-treatment devices contain different metals such as rhodium, palladium and platinum enabling the oxidation of hydrocarbons and carbon monoxide into CO<sub>2</sub><sup>6</sup>. Platinum also contributes to the conversion of chemical energy into electricity assisting the hydrogen oxidation to water in fuel cells<sup>4,156–158</sup>. Platinum is also involved into CO conversion to CO<sub>2</sub> and H<sub>2</sub> through the well-known water-gas shift reaction<sup>6</sup>. Recently EU listed platinum as critical material since the supply of the platinum group metals (PGMs) is still relatively concentrated within few countries<sup>159</sup>. The optimisation of high dispersions is a way to reduce practically the use of PGMs.

Understanding the catalyst structuration effect on its reactivity and selectivity is then decisive. In particular, size effects play a huge role in many properties of nanoparticles, with respect to bulk materials<sup>160–163</sup>. These effects are also expected to vary significantly according to the environment of the catalyst, such as the nature of the support or the nature of the gas. For example, the Pt(111) surface is considerably changing in the presence of O<sub>2</sub>, from dissociative adsorption on hollow fcc sites<sup>85,164–167</sup> to PtO<sub>2</sub> layers<sup>168–170</sup>, or, depending on temperature and O<sub>2</sub> partial pressure, to more special

surface structures such as triangles<sup>171</sup>, honeycombs<sup>172</sup> or spoke wheels<sup>173</sup>. A structure effect of platinum for interaction of O<sub>2</sub> is already known: in the case of Pt(321) and Pt(211), the presence of steps or adatoms influences the adsorption of oxygen<sup>174,175</sup>. These atoms facilitate the adsorption at low coverage and lead to higher heats of adsorption than Pt(111).

In the present work, we focus on the interaction of O<sub>2</sub> with the Pt/ $\gamma$ -Al<sub>2</sub>O<sub>3</sub> system, starting from well-dispersed catalysts with subnanometric metallic particle sizes. This is of interest for all the applications where platinum is used in oxidizing environment, such as for oxidation reactions, but also considering that most reduced platinum catalysts were obtained first in an oxidic form, after impregnation, drying and possible calcination. Gamma alumina is a versatile non-reducible support, often chosen at the industrial and laboratory scale for its high surface area and significant surface reactivity<sup>176</sup>, allowing for the dispersion of small metallic particles, if not single atom catalysts<sup>123,177,178</sup>. Our aim is to get an atomic-scale insight in the surface structures described by the ultra-dispersed Pt/ $\gamma$ -Al<sub>2</sub>O<sub>3</sub> system in the presence of O<sub>2</sub>, and in the strength of the corresponding interaction.

*Ab initio* modelling appears as a relevant tool for the investigation of well-dispersed platinum particles on various oxides, in particular  $\gamma$ -Al<sub>2</sub>O<sub>3</sub><sup>9,4,124,179</sup>. Thanks to Density Functional Theory (DFT) calculations, small non-supported aggregates from Pt<sub>2</sub> to Pt<sub>20</sub><sup>180-183</sup> were shown to reconstruct easily upon O<sub>2</sub> adsorption, which makes the adsorption strongly favorable. The preferred adsorption mode on these structures is the bridge one. For particles larger than Pt<sub>35</sub><sup>184,185</sup>, regular facets such as Pt(111) or Pt(100) surfaces can be identified, contrary to the very distorted morphology of the smallest clusters<sup>125,186</sup>. The heat of adsorption of oxygen on the facets is of the same order of magnitude as for the extended surfaces alone. The adsorption of atomic oxygen however appears to be preferred at the intersections of these facets such as edges and corners, thanks to the low-coordinated platinum at edges combined with platinum atoms mobility. Systematic DFT calculations for clusters of variable size show that size effect is substantial for the adsorption of oxygen below about 150 atoms<sup>187</sup>. While many DFT studies deal with the adsorption of oxygen on flat or corrugated platinum surfaces<sup>79,165,166,169,174,188-192</sup>, studies taking into account the support effect on the interaction of oxygen with platinum clusters are much scarcer, and generally concern very small clusters or single atoms, and a single O<sub>2</sub> molecule<sup>180,193-195</sup>. A systematic investigation of the interaction of oxygen with sub-nanometric platinum cluster, typically Pt<sub>13</sub>, supported on  $\gamma$ -Al<sub>2</sub>O<sub>3</sub>, taking into account the effect of O coverage, function of the temperature and O<sub>2</sub> partial pressure, and possible reconstructions, is thus needed. The approach previously undertaken in the case of hydrogen interaction with Pt<sub>13</sub>/ $\gamma$ -Al<sub>2</sub>O<sub>3</sub>, revealing strong reconstructions of the metallic phase and modulation of the metal – support interaction upon variation of the H coverage<sup>123,126</sup>, is worth being extended to oxygen.

In the present work, we propose to combine *ab initio* periodic calculations and O<sub>2</sub> Temperature-Programmed Desorption (TPD) measurements, the respective consistency of which will be evaluated thanks to kinetic modelling, based on the *ab initio* data, through a multi-scale simulation approach. While such an approach turned out to be successful in the case of oxygen desorption from Pt(111)<sup>174</sup> and for many other chemical systems<sup>82,83,87-95</sup>, it was never demonstrated for the interaction of oxygen with the ultra-dispersed Pt/ $\gamma$ -Al<sub>2</sub>O<sub>3</sub> system so far. First, a systematic structural investigation is provided for O<sub>2</sub> dissociative adsorption on Pt<sub>13</sub>/ $\gamma$ -Al<sub>2</sub>O<sub>3</sub>(100), for a number of oxygen atoms per cluster ranging from 1 to 32, thanks to *ab initio* molecular dynamics. Our own calculations on the Pt(111) surface allow the comparison with highly dispersed platinum using the same approach. Thermodynamic and kinetic data are extracted from these *ab initio* models, which allows us to build a kinetic model to simulate the TPD experiments. This multiscale approach a full assignment of the experimental feature in terms of particle size and oxygen coverage.

## 3.2| Experimental results

### 3.2.1| Experimental protocol

The TPD experiments were performed with a Micromeritics (Autochem II 2920) set-up. The oxygen release was quantified with a mass spectrometer (Pfeiffer QMS 200). Experiments consisted into three steps with a total gas flow set to 50 mL.min<sup>-1</sup>: (i) a pre-treatment step at 600°C during five hours with helium enables to remove adsorbed water as well as to clean the surface from adspecies present on the catalyst and on the metal oxide; (ii) a contact step with O<sub>2</sub> (mixture of 5% v/v O<sub>2</sub>/He) during one hour at 100°C; (iii) finally, the release of molecular oxygen is followed during the increase of temperature with a ramp of 5 °C.min<sup>-1</sup> using helium as carrier gas.

The temperature and duration of the pre-treatment step were optimized after analysis of the behaviour of the 1 wt % Pt/ $\gamma$ -Al<sub>2</sub>O<sub>3</sub> material (Appendix A.2). The mass spectrometry signals of O<sub>2</sub> for alumina alone was moreover deduced from that of the catalysts obtained with the same treatment conditions, to extract the contribution of the metallic particles alone.

### 3.2.2| O<sub>2</sub>-TPD experiments

For the 1 wt % Pt/Al<sub>2</sub>O<sub>3</sub> catalyst, O<sub>2</sub> desorption is detected mainly at 504°C and 757°C (Figure 21). The peaks deconvolution with a Gaussian fit allows to put into evidence a shoulder at 835°C (Figure 81 and Figure 82 in appendices). The main peak is shifted to 710°C on the 0.3 wt % Pt/Al<sub>2</sub>O<sub>3</sub> catalyst while shoulders are detected at 515°C and 931°C. In quantitative terms, the system with the lowest Pt content (0.3 wt% Pt) leads to an enhancement of the highest temperature peak and a decrease of

the lower temperature peak as compared to the system with the highest Pt content (1 wt%).

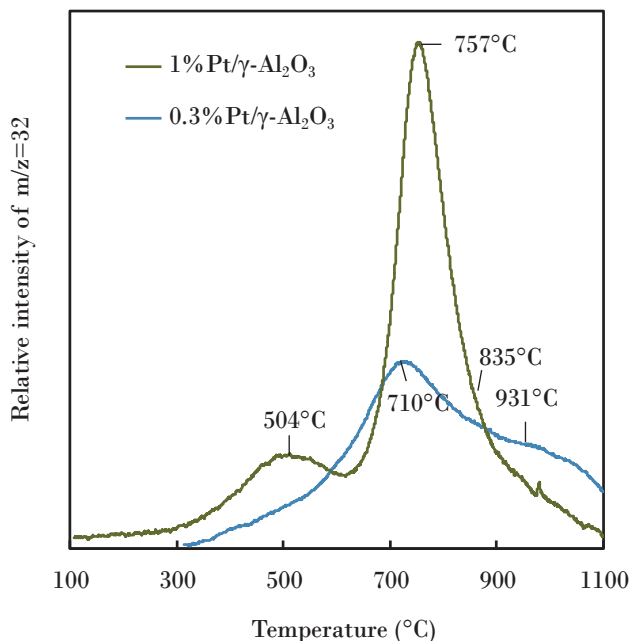


Figure 21 : Relative intensity of oxygen ( $m/z=32$ ) during the Temperature-Programmed Desorption with the 0.3 wt % and 1 wt % Pt/ $\gamma$ -Al<sub>2</sub>O<sub>3</sub> catalysts.

Parker *et al.* report the TPD of O<sub>2</sub> on Pt(111) with different initial oxygen coverages<sup>196</sup>. They show that for coverages lower than 0.2ML, only one peak appears around 460-540°C. A second peak at 400°C is noticed for higher oxygen coverages and a third one lies at 120°C for initial oxygen coverages above 0.5ML. No desorption is reported above 680°C. For stepped surfaces<sup>197</sup> a similar pattern is observed with peaks lying between 300°C and 600°C, with two peaks close to 400°C and 500°C. Our results show that desorption of oxygen on highly dispersed platinum particles supported on alumina occurs on a completely different range of temperature. This suggests that the platinum dispersion has a huge impact on oxygen interaction with platinum, thus on O<sub>2</sub> desorption profile. The shift of O<sub>2</sub> desorption peaks towards high temperature can be associated with stronger interactions between oxygen and platinum atoms in the case of highly dispersed platinum particles on alumina. In previous reports dealing with more or less dispersed Pt/Al<sub>2</sub>O<sub>3</sub> catalysts, the main desorption peaks appeared below 500°C, but temperatures higher than 700°C were generally not sampled<sup>198-200</sup>.

### 3.3| *Ab initio* simulation of oxygen adsorption reactions

*Ab initio* electronic structures calculations were undertaken on Pt<sub>13</sub>O<sub>n</sub>/γ-Al<sub>2</sub>O<sub>3</sub> model to simulate the behavior of highly dispersed platinum. Pt(111) was also considered to

compare with the behavior of large particles or ideal metal surfaces. It also provides a good reference case (Appendix A.4).

### 3.3.1| Adsorption of atomic oxygen

The 13-platinum atoms particle model is supported on a (100) gamma alumina surface model<sup>125</sup>. The particle is composed of two layers of platinum atoms, among which 12 atoms out of 13 are *a priori* accessible to external molecules. This corresponds to a theoretical dispersion of 0.92. This small particle implies a non-regular surface on which no typical extended surface emerges.

Due to the absence of symmetry, each platinum atom and thus each site has a unique behavior. First, we simulated about 60 potential adsorption sites for oxygen (top, bridge and hollow sites) by geometry optimisation. Among the simulated configurations, some of them evolved into more stable ones. The adsorption energies obtained are summarized in Figure 22. Their average, by adsorption mode (as detailed below) is given in Table 7. Some of these structures are shown in Figure 5.

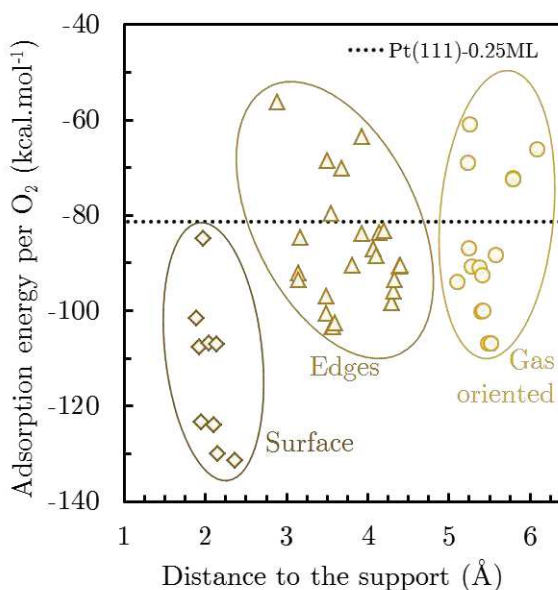


Figure 22 : Adsorption energies per  $O_2$  for a single O atom on the supported  $Pt_{13}$  cluster, as a function of the distance to the support compared to  $Pt(111)$ -0.25 ML. The distance to the support corresponds to the difference between oxygen and mean aluminum of the first alumina layer z coordinates.

From Figure 4, three groups emerge according to their distance from the support. A first group, close to alumina (from 1 to 2.5 Å) is composed of the more stabilizing sites for atomic oxygen. This group corresponds to non-expected adsorption sites that involve the alumina support. Figure 23d shows one of these structures, with the oxygen bonded to one platinum and one aluminum atom. Such site is hereafter named bimetallic bridge. The bimetallic hollow site (Figure 23e) is composed of two platinum

atoms and one aluminum. These peculiar sites which involve the support stabilize drastically the adsorbed oxygen atoms. Two bimetallic hollow sites and two bimetallic bridge sites stand out by their heat of adsorption over  $-120 \text{ kcal.mol}^{-1}$ , compared to the average  $-90 \text{ kcal.mol}^{-1}$  for typical sites.

Table 7: Average adsorption energy per  $\text{O}_2$ , at low oxygen coverage.

Adsorption mode	Adsorption mode	$E_{\text{adsorption}} \text{ (kcal.mol}^{-1}\text{)}$
Pt <sub>13</sub> O – this work	top	-89.8
	bridge	-83.9
	hollow	-87.7
	bimetallic bridge (Al,Pt)	-108.1
	bimetallic hollow (Al,2Pt)	-122.8
Pt(111) – this work	0.25ML	-81.3
Pt(111) <sup>165</sup>	0.25ML fcc hollow	-47.5
Pt(111) <sup>166</sup>	0.25ML fcc hollow	-69.6
Pt(321) <sup>174</sup>	near-edge fcc hollow	-67.2
Non supported Pt <sub>x</sub> O <sub>x</sub> <sup>182</sup>	Top	-75.2 (x=1)
	Top, bridge	-79.4 (x=2)
	Bridge	-79.8 (x=3)
	Bridge	-88.4 (x=4)
	Bridge	-86.8 (x=5)
	Top, bridge	-112.6 (x=10)
Non supported Pt <sub>13</sub> <sup>181</sup>	top	-60.9

The second group of sites, exhibiting a distance to the surface between  $2.5 \text{ \AA}$  and  $4.4 \text{ \AA}$  involves two layers of platinum. They correspond to oxygen atoms adsorbed on the edges of the cluster. The adsorption energies are dispersed (from  $-60$  to  $-100 \text{ kcal.mol}^{-1}$ ) but they are significantly less negative in average as compared to the first group. The third group includes the farthest sites, *i.e.* located on the top of the particle (gap with the second group:  $0.75 \text{ \AA}$ ). The oxygen atoms are oriented to the gas phase (Figure 23a to 5c). The adsorption energy range does not differ significantly from the second group. These data illustrate the significant promoting effect of the support.

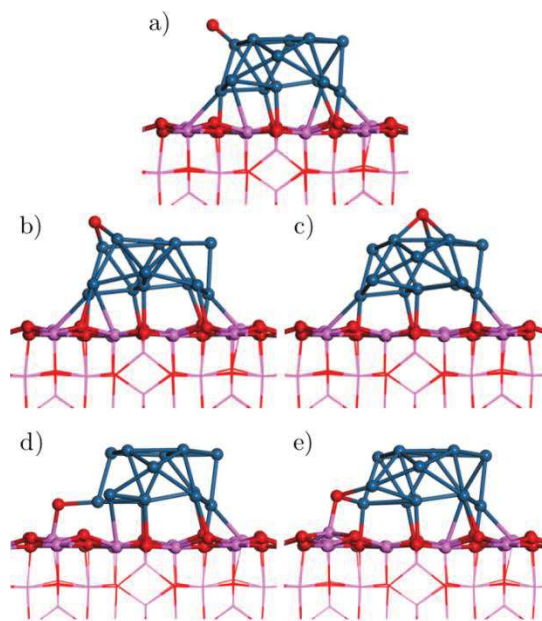


Figure 23 : Illustration of top (a), bridge (b) and hollow (c) typical sites with bimetallic (Al, Pt) bridge (d) and hollow (Al, Pt, Pt) sites (e). Platinum atoms are in blue, alumina in pink and oxygen in red.

The adsorption energies (in absolute value) at low coverage on Pt(111) are much lower than most of the  $\text{Pt}_{13}\text{O}$  adsorption energies (Table 7 and Appendix A.4). However the Pt(111) system with 0.25ML of oxygen exhibits a similar adsorption energy ( $-81.3 \text{ kcal.mol}^{-1}$ ) with respect to the particle traditional sites (edges and gas oriented). This tends to indicate that at low oxygen coverage the main factors determining reactivity are the nature of the support and its interaction with platinum. Mihai *et al.*<sup>200</sup> experimentally quantified the heat of adsorption of  $\text{O}_2$  on poorly dispersed Pt/ $\text{Al}_2\text{O}_3$  catalysts (dispersion: 0.12), and obtained values close to  $-70 \text{ kcal/mol}$ , close to single crystal experiments<sup>201</sup>, showing that the support effects becomes substantial only for highly dispersed catalysts, such as the one considered in the present work.

Also adsorption energies on the supported cluster are of the same order of magnitude as non-supported nano-oxides ( $n_{\text{Pt}} < 13$ ) studied by Schneider *et al.*<sup>182</sup> At this scale, the bridge adsorption mode is clearly preferred. The case of non-supported  $\text{Pt}_{13}$  as investigated by Zhang *et al.*<sup>181</sup> is the exception with two top oxygen atoms, with an adsorption energy close to Pt(111) one. This supports the idea that alumina support favors oxygen adsorption.

### 3.3.2| Evolution of adsorption properties with O coverage and cluster structuration

Higher oxygen coverages were then investigated. Molecular dynamics was used systematically from  $\text{Pt}_{13}\text{O}_2$  to  $\text{Pt}_{13}\text{O}_{32}$  to identify stable configurations (Appendix A.1).

The energetic feature of the most stable systems found is shown in Figure 6. The structure of the systems exhibiting a significant stability domain is depicted in Figure 25, whereas all the discussed structures are reported in Appendix A.5.

For all coverages, the bridge adsorption mode is preferred for oxygen on the particle. In the case of bimetallic sites, the bridge mode is still represented but the bimetallic hollow site (2 platinum, one aluminum) dominates. From two oxygen atoms adsorbed, the cluster gradually reconstructs. Two-layers-like structures (noticed TL) are the most stable up to 12 oxygen atoms, deviating however strongly from the initial one (without oxygen). Therefore the 13 platinum atoms become all accessible for  $n > 10$ , the single initially occluded atom being displaced in such a way by oxygen that it becomes accessible. At higher oxygen coverages, the particles from  $\text{Pt}_{13}\text{O}_{18}$  to  $\text{Pt}_{13}\text{O}_{26}$  exhibit a fully reconstructed hemispheric shape, referred to hereafter as HM. Within this structure, platinum atoms are tetra- and pentavalent. The oxygen atoms are interspersed between the platinum ones. This increases the volume of the cluster up to 290% (volume of the platinum polyhedra of  $84.1 \text{ \AA}^3$  for  $\text{Pt}_{13}$  to  $201 \text{ \AA}^3$  for  $\text{Pt}_{13}\text{O}_{24}$ ). The transition between these two cluster shapes (two-layers and hemispheric) appears for intermediate coverages between 14 and 16 oxygen atoms, with a smooth energetic transition (Figure 24).

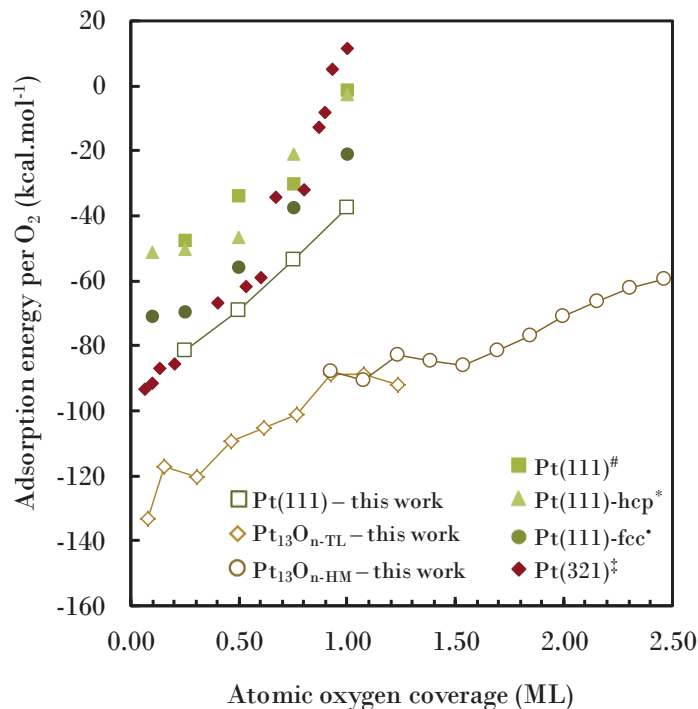


Figure 24 : Mean adsorption energies of  $\text{O}_2$  according to the oxygen coverage for supported  $\text{Pt}_{13}\text{O}_n$  structures and  $\text{Pt}(111)$ . <sup>#</sup>Légaré<sup>165</sup>, <sup>\*</sup>Pang *et al.*<sup>166</sup>, <sup>‡</sup>Schneider and coworkers<sup>174</sup>.

Finally, the structures at very high coverage, starting from  $\text{Pt}_{13}\text{O}_{26}$ , show the disintegration of the hemispheric shape by adsorption of additional oxygen atoms in top

mode. This comes along with the segregation of a few platinum atoms. Non-dissociated  $O_2$  molecules can also be distinguished at high coverages. Although a reconstruction was also observed upon exposure to hydrogen<sup>126,123</sup>, the latter is very different in nature with respect to the one calculated here for oxygen: the bilayer cluster transforms into a cuboctahedron from 20 hydrogen atoms per cluster, with loss of covalent bonding with the support. Such a difference in the response of the cluster shape and interaction with the support in  $H_2$  versus  $O_2$  atmosphere is also at the origin of drastic variations of the stability of Single Atom Catalysts depending on the atmosphere<sup>202</sup>.

The evolution of the average adsorption energy according to oxygen coverage (Figure 6) decreases (in absolute value) continuously in a quasi-linear way. These values contrast significantly with the ones reported with extended surfaces as  $Pt(111)$ <sup>166,165</sup> and  $Pt(321)$ <sup>174</sup>. The cluster shows a huge capacity of stabilizing oxygen atoms on it.

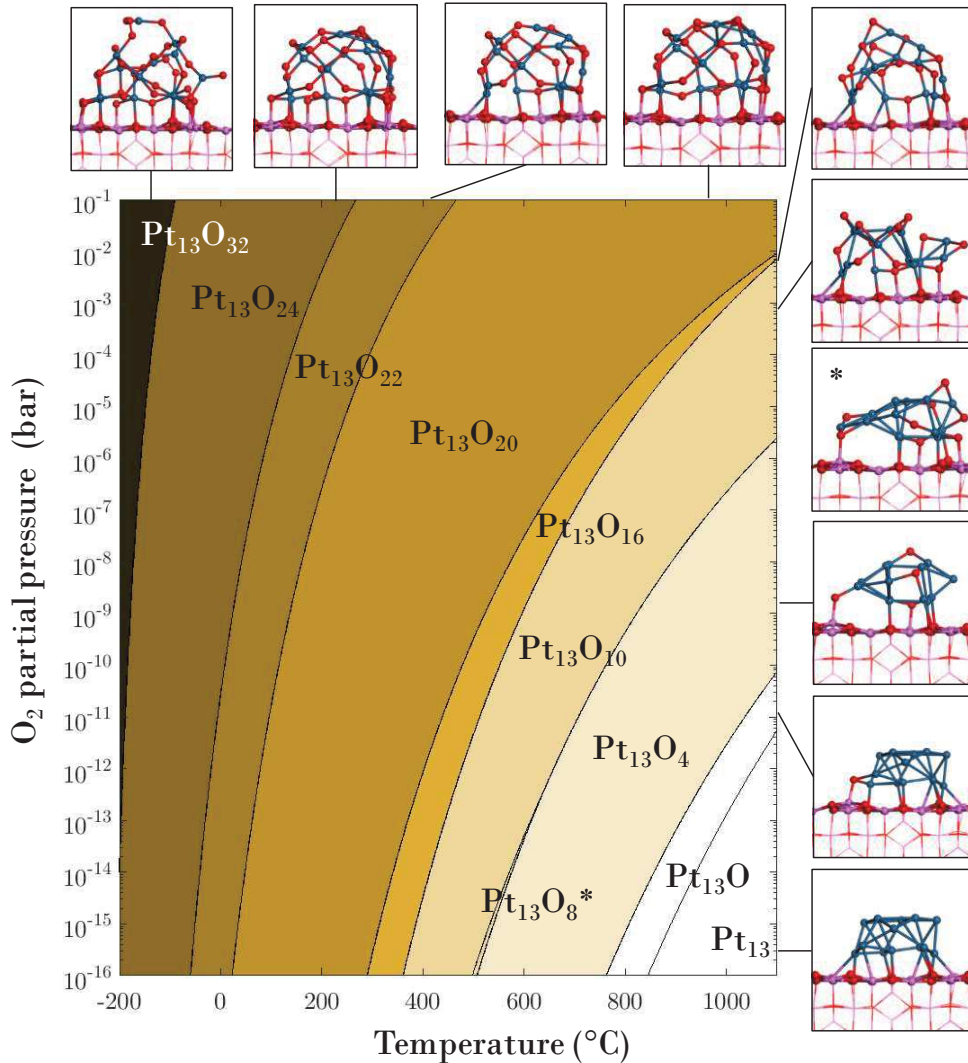


Figure 25 : Phase diagram for supported  $Pt_{13}O_n$  according to temperature and partial pressure of oxygen. The structures of the systems exhibiting a significant stability domain are also depicted (side views).

A ( $P_{O_2}$ , T) phase diagram was built thanks to entropy and enthalpy obtained with *ab initio* structures (Figure 25). Contrary to the case of Pt(111) (Figure 84 in appendices), the diagram for supported Pt<sub>13</sub> only shows a very small stability domain for zero oxygen coverage. This means that the cluster is always oxidized for realistic oxygen partial pressures, in the absence of reducing agent. The diagram is mainly occupied by the high coverage hemispheric structures, having 16 to 24 oxygen atoms.

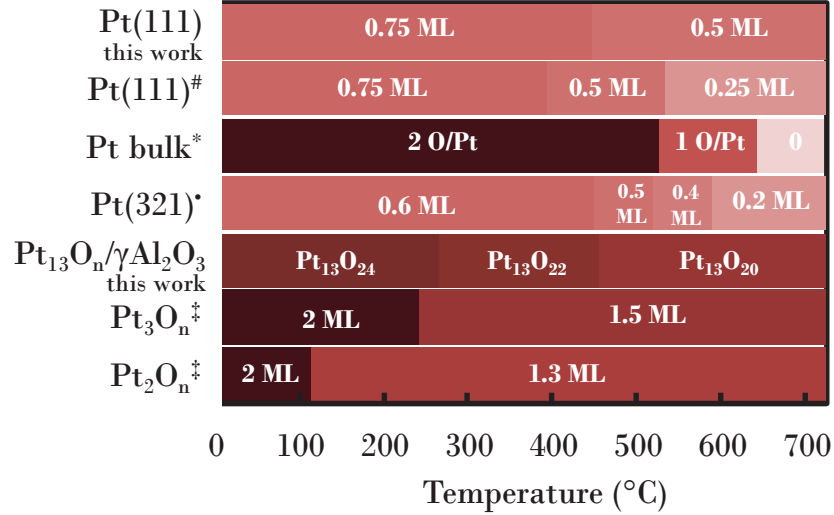


Figure 26 : Comparison of platinum-oxygen phase diagrams at  $P_{O_2}=0.1$  bar according to the nature of the surface. #Légaré<sup>165</sup>, \*Phase diagram of the bulk platinum in presence of only O<sub>2</sub> by HSC Chemistry data, •Schneider and co-workers<sup>174</sup>, ‡Schneider and coworkers<sup>182,183</sup>.

Figure 26 summarizes the phase diagrams reported in the literature for a common partial pressure of O<sub>2</sub> of 0.1 bar. The capacity of the 13-platinum cluster to hold oxygen is of the same order of magnitude as the non-supported Pt<sub>2</sub> and Pt<sub>3</sub> particles studied by Xu and coworkers<sup>182,183</sup>. This is much higher than the extended surfaces capacity in this condition, but closer to the bulk capacity. The high dispersion, the ductility of the platinum clusters and the energetics of oxygen adsorption sites are directly related to the capacity of holding such a quantity of oxygen, even at high temperature. Moreover, the stoichiometry of the supported cluster is close to PtO<sub>2</sub> in these pressure conditions, over a large range of temperature.

The platinum/alumina interaction energy is globally strengthening as the oxygen coverage increases (Figure 27a). The opposite trend was noticed on Pt<sub>13</sub>H<sub>n</sub> structures<sup>126,202</sup>, with an unhooking of the cluster from the support. The impact of the metal/support interaction on the related bond length is not strong (Figure 27b).

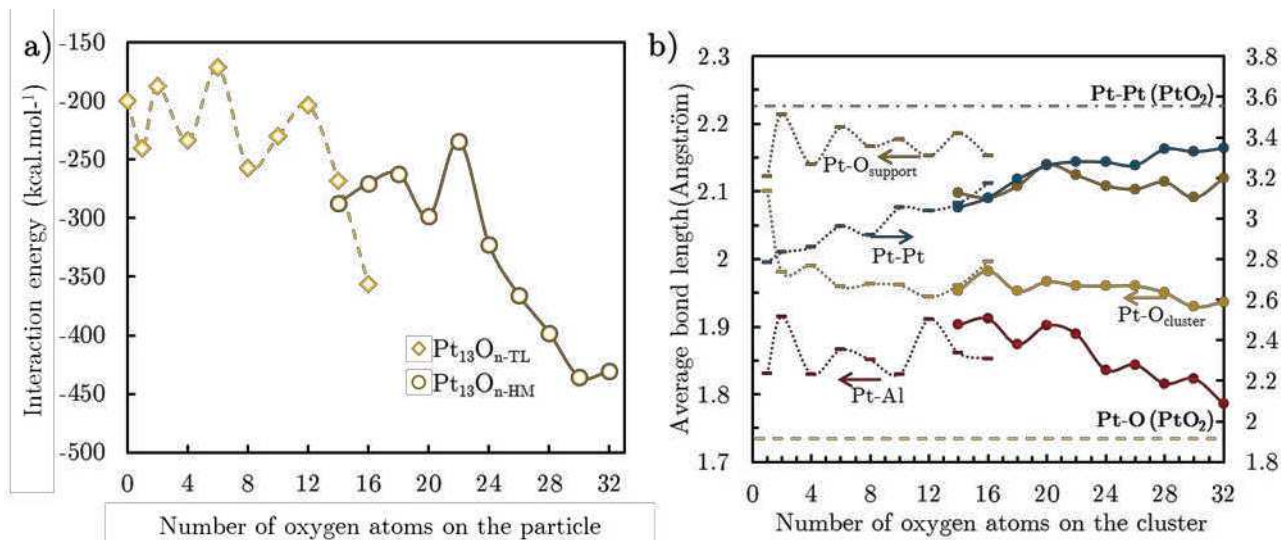


Figure 27 : (a) Interaction energy between the alumina support and the oxidized platinum clusters. (b) Average Pt-Pt, Pt-O<sub>support</sub> and Pt-O<sub>cluster</sub> bond lengths, and minimum Pt-Al length as a function of oxygen coverage. The maximal bond lengths were set to 3.8 Å for Pt-Pt and 2.5 Å for other bonds. Dotted lines corresponds to the two-layers structures whereas plain lines are hemispheric structures data.

Indeed, the average lengths of Pt-Al and Pt-O<sub>support</sub> bonds do not vary by more than 5%. The single trends that can be seen is the shortening of the Pt-O<sub>support</sub> bonds from the bi-planar to the hemispheric structures, in line with the strengthening of the interaction. Moreover a substitution of Pt-Al by Al-O<sub>cluster</sub> bonds occurs with increasing oxygen coverage (Appendix A.5). Likely, the strongest cluster/support interaction comes from those additional Al-O<sub>cluster</sub> bonds. The Pt-Pt length increases with oxygen coverage from about 2.8 Å to 3.4 Å. This represents a 20% rise. The Pt<sub>13</sub>O<sub>14</sub> and Pt<sub>13</sub>O<sub>16</sub> structures that coexists in the two structure types show that the Pt-Pt bonds are slightly shorter for the hemispheric cluster shape than for two-layers structure.

To further investigate the impact of oxygen coverage on charge transfer, the Bader partial charges were computed for platinum and oxygen on the cluster (Figure 28). The oxygen charge remains almost constant with oxygen coverage (between -1 and -0.5), close to the oxygen Bader charge of PtO<sub>2</sub> oxide. However the charge of platinum is increasing almost linearly with coverage, starting from a Pt<sup>0</sup> to a 1.2 electron-depleted platinum for very high oxygen coverage, quite close to a kind of PtO<sub>2</sub> charge.

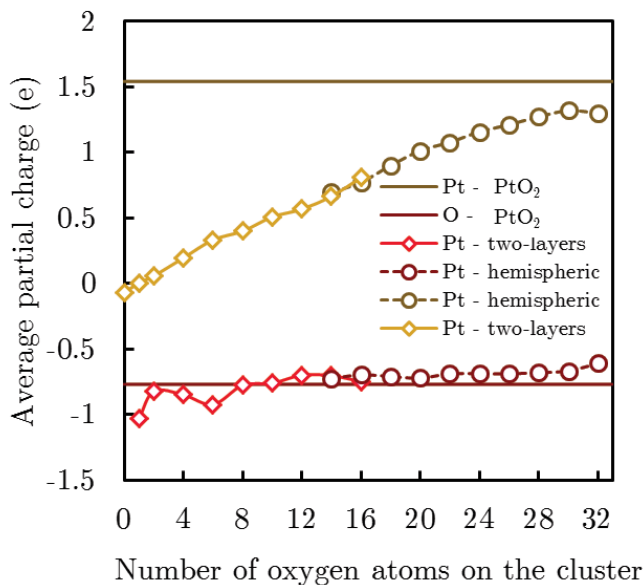


Figure 28 : Mean Bader charge per Pt (blue) and cluster O (red) atoms. The cross-shaped dots represent the two-layers structures while the full dots stand for hemispheric structures.

The smooth transition noticeable from two-layers to hemispheric structures emphasizes the blurred energetic transition discussed previously, showing also that Bader charges are mainly dominated by the stoichiometry of the supported oxide, more than by the morphology. Note that the total charge of the cluster (platinum plus oxygen) remains very close to zero, showing a very weak charge transfer with the support for particles holding oxygen, contrary to what was reported in the presence of hydrogen as adspecies<sup>126</sup>.

### 3.3.3 | Activation energy for the dissociation of $O_2$

Potential energy surfaces and transition states for  $O_2$  dissociation were determined on  $Pt_{13}/\gamma-Al_2O_3$  model, in comparison with Pt(111). For the supported cluster, three coverages were investigated: (1) the dissociation of  $O_2$  on a reduced particle (from 0 to 2 oxygen atoms per cluster), (2) with an intermediate coverage on a two-layers cluster structure (from 8 to 10 oxygen atoms per cluster) and (3) on a high oxygen coverage cluster with an hemispheric shape (from 22 to 24 oxygen atoms per cluster). For Pt(111), two energetic pathways were investigated: the dissociation of  $O_2$  on a reduced surface and another one with an initial 0.5 ML atomic oxygen coverage. On the later structure, the dissociation leads to a 1 ML oxygen coverage. In all cases, this evaluation was performed using the most stable final state. The energy paths are summarized in Figure 29, key-structures (including transition structures) being shown in Appendix A.6. The later corresponds to the O-O bond elongation. Adsorption of a non-dissociated  $O_2$  is energetically favored, more strongly on the clusters than on Pt(111). Notably, on

Pt(111), the molecular adsorption of  $O_2$  is more favorable on the reduced surface, whereas the reverse trend is observed for the cluster, with more negative energies in the case of the oxidized cluster.

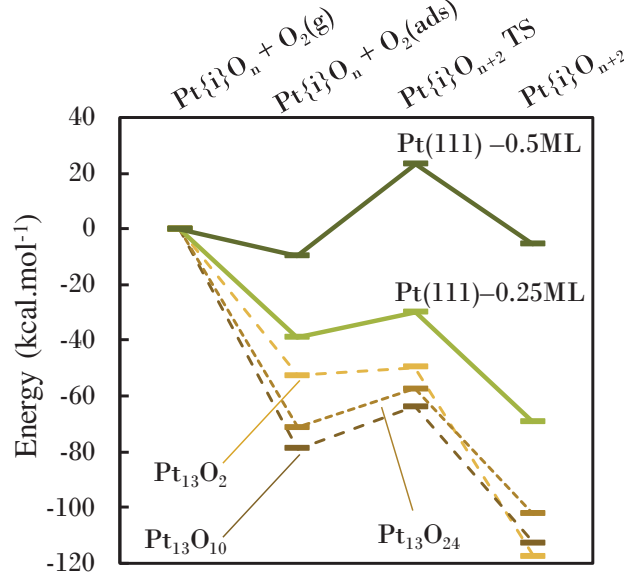


Figure 29 : Dissociation barriers from initial state  $Pt_{13}O_n$  to  $Pt_{13}O_{n+2}$ , and  $Pt(111)O_n$  to  $Pt(111)O_{n+2}$ . The energies are displayed relatively to each initial state energy.

The dissociation barriers from adsorbed  $O_2$  (forward and backward) are given in Table 8. Fu *et al.* report a similar behavior with a O-O bond scission with a  $8.8 \text{ kcal.mol}^{-1}$  barrier on a reduced surface of Pt(111)<sup>189</sup>. A  $8.3 \text{ kcal.mol}^{-1}$  barrier is calculated for the low coverage dissociation on Pt(111). It reaches  $32.5 \text{ kcal.mol}^{-1}$  for the medium coverage. Consequently, the atomic oxygen coverage has a significant inhibiting effect on  $O_2$  dissociation for Pt(111). For the supported  $Pt_{13}$  cluster, a  $3 \text{ kcal.mol}^{-1}$  barrier for the reduced particle is obtained while the one with a medium coverage is about  $15 \text{ kcal.mol}^{-1}$ , despite the same two-layers structure. On the contrary, no significant influence of the cluster structuration (HM versus TL) is noticed as the activation energy found for  $Pt_{13}O_{24}$  formation is almost equivalent to that of  $Pt_{13}O_{10}$ . Note that Zhang and coworkers<sup>181</sup> found an activation energy of  $10 \text{ kcal.mol}^{-1}$  on a non-supported  $Pt_{13}$  reduced particle, within the interval we find here.

Table 8: Dissociation and association barriers for  $O_2$  dissociation on Pt(111) and  $Pt_{13}O_n$  cluster

Reaction	Dissociation barrier ( $\text{kcal.mol}^{-1}$ )	Association barrier ( $\text{kcal.mol}^{-1}$ )
$Pt(111) + O_2(g) \rightarrow Pt(111)-0.25ML$	8.3	67.7
$Pt(111)-0.25ML + O_2(g) \rightarrow Pt(111)-0.5ML$	32.5	48.9
$Pt_{13} + O_2(g) \rightarrow Pt_{13}O_2$	3.0	47.8

$\text{Pt}_{13}\text{O}_8 + \text{O}_2(\text{g}) \rightarrow \text{Pt}_{13}\text{O}_{10}$	15.1	39.2
$\text{Pt}_{13}\text{O}_{22} + \text{O}_2(\text{g}) \rightarrow \text{Pt}_{13}\text{O}_{24}$	13.8	45.0

To conclude, the *ab initio* investigations of supported  $\text{Pt}_{13}\text{O}_n$  clusters reveals a very strong affinity of the catalytic system for oxygen, leading to highly oxidized stoichiometry, the dependence of which is elucidated as a function of the temperature and  $\text{O}_2$  pressure. The metal/support interaction is strengthened upon oxidation thanks to Platinum-Oxygen-Aluminum bridges. A reconstruction takes place, from a biplanar-like morphology at low coverage, to hemispherical shapes at high coverage. Dissociation barriers of  $\text{O}_2$  were also determined and significantly depend on the oxygen coverage. It is now worth analyzing the macroscopic consequences of such microscopic features, which is done thanks to multi-scale kinetic modelling.

### 3.4| Kinetic modelling of $\text{O}_2$ -TPD

Detailed kinetic models were developed to deduce the expected TPD profile from *ab initio* calculations (Appendix A.7), together with the definition of the surface species present throughout the TPD. The kinetic model analysis is performed on several key parameters in order to evaluate its ability to simulate the TPD. A brute force sensitivity analysis of  $\text{O}_2$  peaks with respect to the sticking coefficients as well as on the uncertainty on free energy is performed. Then, the scheme structure is evaluated by considering two distinct mechanisms involved at medium coverages to assess their impact of TPD behavior.

The reaction mechanisms was built by including successive dissociative adsorption reactions of one molecule of  $\text{O}_2$  according to equations (82) and (88). Each direct and reverse reactions are listed, up to 32 oxygen atoms for  $\text{Pt}_{13}$  and 1 ML (monolayer) for Pt(111).



To account for coverage dependent dissociation energy, a linear law was applied to the dissociation energies found for Pt(111), whereas piecewise linear trends were applied to the three *ab initio* dissociation energies investigated on the  $\text{Pt}_{13}$  cluster (section 3.3.3).

Few studies investigated the sticking coefficient of  $\text{O}_2$  on Pt(111)<sup>85,203,204</sup>, however it was shown to vary strongly with  $\text{O}_2$  partial pressure and temperature. No temperature deviation from the setpoint were detected experimentally implying that the endothermic effect due to desorption may be neglected.

### 3.4.1 | Impact of the dispersion on O<sub>2</sub>-TPD

The most stable structures determined by *ab initio* calculations for each oxygen coverage were used to build the present kinetic mechanism. To represent the complex transition between the two-layers (TL) and hemispheric (HM) structures, two structures were considered for Pt<sub>13</sub>O<sub>14</sub> and Pt<sub>13</sub>O<sub>16</sub> with their own kinetic parameters. To correctly depict this transition, two reversible surface reactions were implemented to connect one structure to the other. The rate constants of these reactions are not thermo-consistent and only the activation energies come from *ab initio* data, the pre-exponential factors were set to 10<sup>11</sup> s<sup>-1</sup> as recommended for non-rotating and non-mobile adspecie by Dumesic *et al.*<sup>137</sup>

An important parameter likely affected by Pt dispersion is the sticking coefficient (equation 6). Ertl *et al.* investigated it on Pt(111) in vacuum conditions<sup>85</sup>. They found that it depends on the collision angle with the surface, the oxygen coverage and the temperature, and is of the order of 10<sup>-2</sup>. Therefore, several coefficients were attempted in this work for the Pt<sub>13</sub> mechanism, starting from a trial value of 10<sup>-2</sup>.

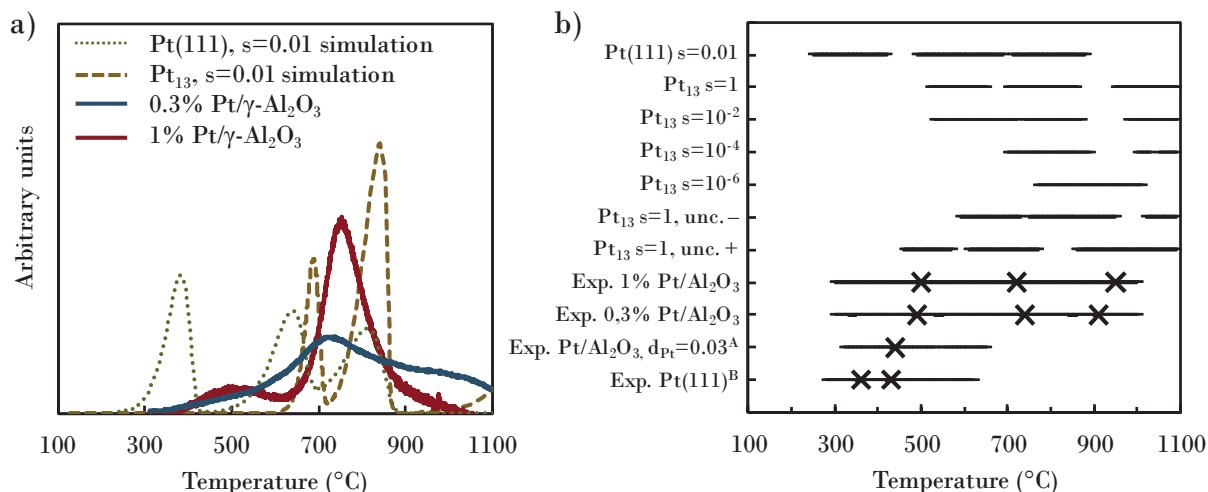


Figure 30 : (a) Predicted O<sub>2</sub> concentration profile during O<sub>2</sub>-TPD with Pt(111) and Pt<sub>13</sub>, with TPD experiments on highly-dispersed Pt/γ-Al<sub>2</sub>O<sub>3</sub>. (b) Impact of sticking coefficient and of a typical errors ( $\pm 3.6$  kcal.mol<sup>-1</sup> for enthalpies and  $\pm 3.6$  cal.mol<sup>-1</sup>.K<sup>-1</sup> for entropies) on Pt<sub>13</sub> kinetic model with a 5°C.min<sup>-1</sup> temperature ramp and starting with the Pt<sub>13</sub>O<sub>20</sub> structure. The O<sub>2</sub>-TPD experiments of <sup>A</sup>Olsson *et al.*<sup>199</sup> and <sup>B</sup>Parker *et al.*<sup>196</sup> are also reported. The lines represent the range of occurrence of O<sub>2</sub> release and the crosses the associated rate-of-desorption maxima.

Figure 30 shows the simulations of the O<sub>2</sub>-TPD experiment with Pt(111) and Pt<sub>13</sub> kinetic models with a sticking coefficient of 10<sup>-2</sup> for all reactions. The Pt<sub>13</sub> simulation exhibits two successive desorption peaks at 686°C and 839°C corresponding to the transition from Pt<sub>13</sub>O<sub>20</sub> to Pt<sub>13</sub>O<sub>16-TL</sub> and then to Pt<sub>13</sub>O<sub>4</sub> respectively. These peaks lie in

the temperature ranges of the main experimental TPD peak, above 700°C. In the case of the Pt(111) simulation, three peaks are obtained (at 384°C, 639°C and 814°C for  $s=10^{-2}$ , corresponding to 0.75ML  $\rightarrow$  0.50ML  $\rightarrow$  0.25ML  $\rightarrow$  0ML respectively). The desorption is here centered around 600°C.

Experimental TPD of Olsson *et al.*<sup>199</sup> (poorly dispersed supported catalysts) and Parker *et al.*<sup>196</sup> (Pt(111)) show respectively one and three peaks on the same temperature range from 300°C to 600°C. The temperature ramp applied in their studies are quite different (40°C.min<sup>-1</sup> and 8°C/s respectively) and may impact O<sub>2</sub>-TPD shape. In contrast, the O<sub>2</sub> adsorption kinetic parameters of Deutschmann<sup>205</sup> were implemented in our own kinetic model, which leads to a broad signal from 100°C to 1100°C with a simulated ramp of 5°C.min<sup>-1</sup>.

The sticking coefficient is typically measured at very low pressure ( $< 0.1$  atm) which is not representative of the thermodynamic conditions of the TPD experiment. Several studies<sup>85,203,204</sup> put forward that for Pt(111) surface, the O<sub>2</sub> sticking coefficient lies around 10<sup>-2</sup>. For Pt(111) stepped surfaces<sup>206,207</sup>, the coefficients were higher and around 10<sup>-1</sup> but the sites were quickly saturated. Considering the peculiar structure of Pt<sub>13</sub> cluster, we varied the sticking coefficient of O<sub>2</sub> from 1 to 10<sup>-6</sup>. Even though the sticking coefficient is expected to decrease with  $\theta_{O_2}$ , it was assumed to be independent of oxygen coverage, for the sake of simplifying the analysis of its impact on desorption. According to the present model, the first two O<sub>2</sub> peaks start to merge for sticking probabilities lower than the threshold value of 10<sup>-2</sup> (Figure 12-b). A slight shift towards higher temperatures is observed for the last peak.

The estimation of enthalpies and entropies from *ab initio* calculations can also lead to an error for methodological reasons. To estimate the consequences of typical errors, we built two kinetic models that lower or enhance the reactivity. The sticking coefficient of O<sub>2</sub> was set to 1. The model that enhances the kinetic (named Pt<sub>13</sub> unc. + on Figure 12b) is built so that 3.6 cal.mol<sup>-1</sup>.K<sup>-1</sup> are added to each  $\Delta_r S_{desorption}$  and 3.6 kcal.mol<sup>-1</sup> are removed to  $E_{dissociation}$  and  $\Delta_r H_{desorption}$ . In that case a 60°C peak shift is noticed. The Pt<sub>13</sub> unc. – model displays two merged peaks at low temperature and a 70°C shift to higher temperatures.

From our analyses, one can conclude that all desorptions are simulated above 500°C with the Pt<sub>13</sub> model, in line with the highest temperature peaks recorded experimentally for both 1% and 0.3% Pt/ $\gamma$ -Al<sub>2</sub>O<sub>3</sub> ultra-dispersed catalysts. The lower temperature peaks are better explained by our Pt(111) *ab initio* kinetic model, suggesting that the biggest particles are at the origin of these peaks. The Pt<sub>13</sub> model remains too discrete with respect to the experiments, with two sharp peaks (686°C and 839°C) surrounding the experimental main large peak (757-710°C, depending on the sample). This suggests that considering a single cluster size, initial morphology and support orientation is an oversimplified description of the system. However the main

trends are captured, which is clearly impossible with an ideal surface model such as Pt(111).

### 3.4.2 | Reaction paths analyses

As the current model is able to reproduce TPD experiment correctly at high temperatures, we may perform path analyses to interpret the model behaviour at high temperatures. The logarithm of the rate constants taken at the temperature of the peaks are reported in Figure 31a. It shows that the preferential path goes through  $\text{Pt}_{13}\text{O}_{16}\text{-TL}$  that is the predominant structure between  $630^\circ\text{C}$  and  $810^\circ\text{C}$ . The rate constants are sufficiently high to desorb more oxygen via the reaction between  $\text{Pt}_{13}\text{O}_{16}\text{-HM}$  and  $\text{Pt}_{13}\text{O}_{14}\text{-HM}$ . The preferred path engages then both  $\text{Pt}_{13}\text{O}_{14}\text{-TL}$  and  $\text{Pt}_{13}\text{O}_{14}\text{-HM}$  to  $\text{Pt}_{13}\text{O}_{12}$ .

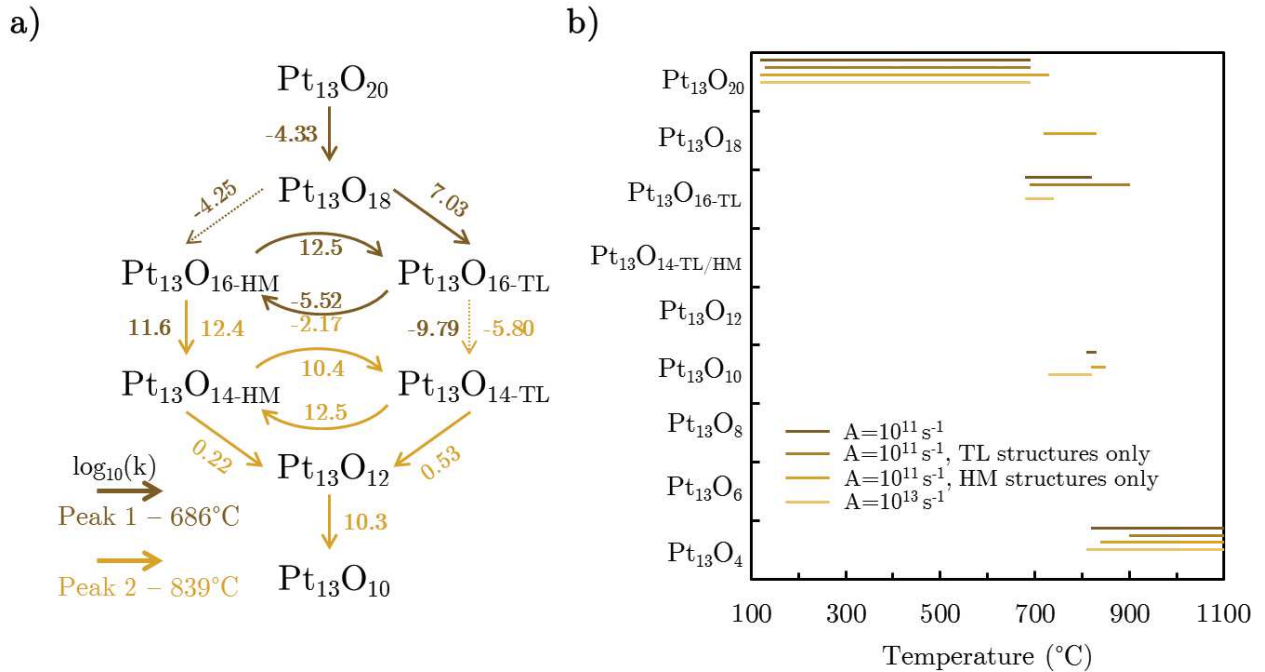


Figure 31 : (a) Logarithm of the rate constants (in s-1) at the peak temperature for  $\text{Pt}_{13}\text{O}_n$  kinetic mechanism. The sticking coefficient of  $\text{O}_2$  is  $10^{-2}$ . (b) Predominant surface species during TPD experiments with distinct scheme structure. The impact of the pre-exponential factor of the two surface reaction A is studied as well as the two paths involving  $\text{Pt}_{13}\text{O}_n\text{-TL}$  or  $\text{Pt}_{13}\text{O}_n\text{-HM}$  independently. The sticking coefficient of  $\text{O}_2$  is  $10^{-2}$ . The reference scheme is the darker one.

The pre-exponential parameters of  $\text{Pt}_{13}\text{O}_{22}$  reduction to  $\text{Pt}_{13}\text{O}_{20}$  appear by far as the most important ones for  $\text{O}_2$  concentration prediction, the sensitivity being 40 times higher than that of the  $\text{Pt}_{13}\text{O}_{18}$  to  $\text{Pt}_{13}\text{O}_{16}\text{-HM}$  reaction. This sensitivity is however significant only between  $310^\circ\text{C}$  and  $380^\circ\text{C}$ , before the first desorption peak occurs. This suggests that some  $\text{Pt}_{13}\text{O}_{22}$  may appear at low temperature and desorbs at lower temperature than the first observed peak.

In order to evaluate the impact of the four structures for  $n=14$  and  $16$ , the TPD was predicted with only TL structures or HM structures using two distinct schemes. The predominant species are displayed in Figure 31b, as a function of the temperature. First and foremost, the major species remains  $\text{Pt}_{13}\text{O}_{20}$  up to the same temperature for the common scheme and the TL one. The desorption of  $\text{O}_2$  from this species is predicted to occur at higher temperature for HM model than for TL model. While the TM model proceeds mainly through  $\text{Pt}_{13}\text{O}_{16\text{-TL}}$ , the HM scheme predicts a direct desorption from  $\text{Pt}_{13}\text{O}_{18}$  to  $\text{Pt}_{13}\text{O}_{10}$ .

Also the impact of the pre-exponential factor set for the surfaces reactions has been assessed by tuning it to  $10^{13} \text{ s}^{-1}$  instead of  $10^{11} \text{ s}^{-1}$ . Figure 31b displays the same predominance of  $\text{Pt}_{13}\text{O}_{20}$ , but the temperature scale with  $\text{Pt}_{13}\text{O}_{16\text{-TL}}$  is shorter and the desorption to  $\text{Pt}_{13}\text{O}_{10}$  occurs at lower temperature. One can thus confirm that increasing  $A$  facilitates the surface reaction between the two  $\text{Pt}_{13}\text{O}_{16}$  structures.

Finally, one may compare the stability domains given by the kinetic model (Figure 13b) and from the *ab initio* thermodynamic diagram (Figure 7). Trying to depict the species appearing in the course of the TPD by a single  $\text{O}_2$  partial pressure and by an equilibrium situation is not possible, as we should have a large kinetic stability domain for  $\text{Pt}_{13}\text{O}_8$  in any case, before reaching  $\text{Pt}_{13}\text{O}_4$ . This shows that kinetic limitations play a strong role in TPD, which cannot be described by a simple thermodynamic diagram.

Considering the temperature ranges of  $\text{O}_2$  desorption, the multi-scale approach which relies on *ab initio* calculations for microkinetic model development provides a consistent model. In addition, the kinetic analyses offers an unrivalled mean to interpret the features of the experimental  $\text{O}_2$ -TPD. It highlights the effect of complex systems involving different cluster geometries which tends to be more realistic. In addition, the kinetic analysis demonstrates that both cluster morphologies (two-layers and hemispherical) must be considered for  $\text{O}_2$  desorption.

### 3.5 | Conclusion

In the present work, we have presented a multi-scale approach applied to oxygen adsorption on highly dispersed  $\text{Pt}/\gamma\text{-Al}_2\text{O}_3$ , combining TPD experiments, *ab initio* and kinetic modelling. High temperature desorption were observed experimentally, suggesting that much stronger interactions exist between oxygen and  $\text{Pt}_{13}$  clusters than for extended surfaces. The *ab initio* electronic calculations of a 13-platinum cluster supported on alumina shows that the support is involved for the most stable adsorption sites. A morphology change is observed according to oxygen coverage, with a low coverage structure characterized by two parallel layers of platinum and an hemispherical shape at high coverage. *Ab initio* thermodynamic data allows to build a phase diagram that shows a highly oxidized cluster for accessible  $\text{O}_2$  pressure and

temperature. The same study was applied to the Pt(111) surface. Kinetic schemes were then set up to simulate TPD experiments using Pt<sub>13</sub> and Pt(111) *ab initio* simulated thermokinetic parameters. Despite some uncertainties on sticking coefficient and desorption free energies barriers, the two models suggest that the experimental low temperature desorption is in agreement with some peak of the Pt(111) simulated TPD, characteristic of large particle with regular facets, whereas high temperature desorption is clearly the contribution of small platinum particles.

Finally this work highlights the reactivity of oxygen on highly dispersed platinum supported on alumina. Several computed thermochemical data such as the heat of adsorption and the achievable oxygen coverage thoroughly differ from well-known extended surfaces. The temperature-programmed desorption of O<sub>2</sub> and the related kinetic simulations demonstrate similar desorption temperature ranges that again consolidate the approach of coupling the experimental and modelling work. The model established herein could be implemented in the future for highly dispersed platinum catalysis mechanism in oxidant media, such as oxidation of carbon monoxide into CO<sub>2</sub>. Some in-depth work would be needed regarding kinetic parameters such as the sticking probability. Also it is shown that a special attention has to be made to account for the structural dimension of modelled systems and its translation in the kinetic scheme. Yet complex *ab initio* models, including a support, an anisotropic catalyst structure and a large oxygen coverage range among others, are herein shown to be relevant when integrated in a kinetic scheme according to the conducted O<sub>2</sub>-TPD experiments.

# 4| Carbon monoxide adsorption on Pt/ $\gamma$ -Al<sub>2</sub>O<sub>3</sub>

This chapter tackles the adsorption of carbon monoxide on highly dispersed alumina supported platinum catalyst. This study is currently adapted as an article. The work undertaken by Mathilde Iachella at IFP Energies nouvelles allows to initiate this study. Some of the presented work were done with and by Eric Genty, post-doctoral researcher at UCCS laboratory. This is the case for experimental characterisation of carbon monoxide adsorption/reaction: (i) the heat of adsorption determination, (ii) the temperature programmed desorption and (iii) reaction.

## 4.1| Introduction

Carbon monoxide is a major concern for its toxicity and production. It mainly comes from all combustion processes, as these later are often incomplete and CO is close in structure to the final product CO<sub>2</sub><sup>6</sup>. The harmfulness of the molecule concerns all animals that uses hemoglobin<sup>13</sup> (*i.e.* vertebrate that includes all mammals). This compound is more hazardous as it is colorless and odorless for humans. In the case of combustion engine, aftertreatment of the exhaust gas including CO is performed thanks to heterogeneous catalysis<sup>6,22</sup>. In automotive steady state conditions, the temperature is high enough to have a suitable carbon monoxide conversion for emission in the atmosphere according to the standards. However, during the cold start and especially on aged catalysts, CO conversion can drop down. Most of the time, noble metals are used in these kind of devices such as platinum, rhodium and palladium<sup>6,22</sup>. It is well-known that Pd-based catalysts are the most active phase for CO oxidation. Yet carbon monoxide adsorption is relevant on platinum phase, in particular on highly dispersed material that can show a divergent behavior compared to extended surfaces<sup>160,161,208</sup>. Characterizing the interaction of CO with platinum, both from a qualitative (adsorption mode) and quantitative (interaction strength, CO coverage) is needed to better control its reactivity.

The interaction of CO with platinum extended surfaces have been experimentally studied for the past 30 years considering numerous techniques<sup>84,96,209–217</sup>. The Pt(111) surface was studied at first by LEED<sup>84</sup> and allows to determine the top position as the preferred one at low coverage (below 0.33ML). That is confirmed by Steininger *et al.*<sup>212</sup> using vibrational analysis. Carbon monoxide adsorbs following regular patterns that change according to temperature, partial pressure of CO and the surface. At higher coverage, the top and bridge position are in competition<sup>213</sup>. A vibrational shift is observed for linear adsorbed CO according to the structuration of the catalyst<sup>218–220</sup>. In addition, the characterisation of carbon monoxide affinity towards Pt/Al<sub>2</sub>O<sub>3</sub> material has been investigated via Adsorption Equilibrium InfraRed (AEIR) spectroscopy to quantify CO heats of adsorption according to several adsorption modes. The team of Bianchi<sup>104–106,108,109,221,222</sup> investigated numerous carbonyls adsorption modes using this technique on Pt/Al<sub>2</sub>O<sub>3</sub>. They determined linear and multibounded heat of adsorption and demonstrated that no significant dispersion impact occurs for linear species in the 0.44–0.75 dispersion range<sup>221</sup>. The influence of pre-oxidised catalyst also highlighted a peculiar 2120cm<sup>-1</sup> vibration modes<sup>223</sup> attributed to platinum depleted linear site (oxidised Pt<sup>2+</sup>). Also Temperature Programmed Desorption (CO-TPD) has been performed on both extended surfaces<sup>96,210,224</sup> and dispersed platinum supported on alumina<sup>209</sup>, that converge to a global desorption of CO below 500°C. Alumina is by the way a material of large prominence in heterogeneous catalysis. Its major use in industrial process as a support for noble metal catalysis in general is explained by a high surface area<sup>121</sup>, high temperature stability and an ability to stem catalyst sintering<sup>123,194</sup>.

Useful information can also be obtained from *ab initio* calculations. By standard Density Functional Theory (DFT) calculations, the preferred adsorption mode is the hollow one, slightly more favoured than the top mode. Yet mainly this latter is experimentally observed<sup>96</sup>. This is due to CO adsorption misestimation on hollow site with the GGA approach<sup>225,226</sup>. Indeed, the hollow mode was found more stable than the top mode on Pt(111) using the PBE exchange-correlation functional, and adsorption energies are overestimated<sup>227</sup>. This contradiction is named as the “CO puzzle” by Feibleman<sup>226</sup> and is not exclusive to platinum surfaces<sup>227,228</sup>. The problem is solved using the Random Phase Approximation (RPA)<sup>229</sup>, however the calculation time needed is hardly affordable.

Considering carbon monoxide as a key molecule in oxidation chemistry, the study of its adsorption on Pt/ $\gamma$ -Al<sub>2</sub>O<sub>3</sub> is of great interest. Indeed gamma alumina is used in many industrial applications. Prior works dealt mainly with extended surfaces<sup>230,231,162,232,233</sup> and scarcely on dispersed ones<sup>208,234</sup>, yet carbon monoxide adsorption may exhibit peculiar reactivity on a dispersed and supported catalyst. In the present work, we unravel therefore the interaction of CO with highly dispersed Pt/ $\gamma$ -Al<sub>2</sub>O<sub>3</sub> systems over a large range of CO coverage, by combining: (i) AEIR spectroscopy and CO

Temperature Programmed Desorption experimental measurements, (ii) *ab initio* calculations of the structures, stability and vibrational feature of adsorbed CO, (iii) *ab initio* based kinetic modelling of the CO-TPD profiles. This multi-scale approach has been recently experienced for CO oxidation on highly dispersed platinum supported on amorphous alumina<sup>162,82,208</sup>, but remains scarce for CO adsorption.

## 4.2| *Ab initio* simulation of carbon monoxide adsorption

The adsorption of one CO has been investigated on numerous sites to identify preferential adsorption modes. Then a study with increasing CO coverage reveals substantial cluster deformations.

### 4.2.1| Adsorption of a single carbon monoxide molecule

The adsorption of one carbon monoxide on the platinum particle has been investigated at first and every typical adsorption sites (top, bridge and hollow sites) were set as initial guesses. Only one alumina-engaged site was detected as final state that heat of adsorption rises at  $-70 \text{ kcal.mol}^{-1}$  with one Al-O bond (Figure 32).

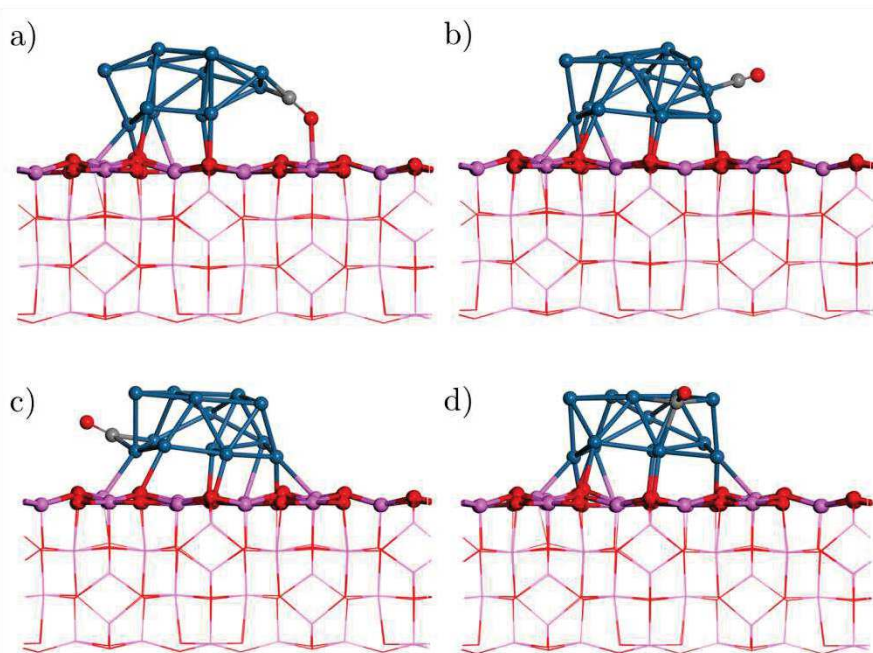


Figure 32: Illustrations of the single carbon monoxide adsorption modes found. The a) most strongly adsorbed and only alumina engaged site and b) top, c) bridge and d) hollow typical sites.

Average adsorption energy of CO are displayed in Figure 33. The hollow site is the less attractive to CO, compared to bridge and top sites. The evolution of heat of adsorption of carbon monoxide follows a similar trend as the one related to oxygen adsorption. The difference lies in the amount of alumina-engaged probed sites, that are hardly represented for CO. The comparison with extended surfaces is not straightforward due to the CO puzzle<sup>226</sup>. In fact the same level of theory (GGA PBE) than this work shows a preferred hollow adsorption mode<sup>230</sup> while experimental results tends to bring the top mode out for low CO coverage<sup>211,235</sup>.

The work by Kresse and coworkers<sup>229</sup> demonstrate that the CO adsorption energy is overestimated using common DFT GGA functionals and Random Phase Approximation (RPA) handles the description of the C-O bond well. Thus the adsorption energy on supported platinum cluster seems to be stronger than Pt(111) top site for CO adsorption for a same level of theory. The revised PBE (RPBE) on Pt(332)<sup>231</sup> also shows top adsorption mode on both terraces and edges with similar adsorption energy than on Pt(111) as previously discussed. One GGA PBE calculation was made on Pt(111) at 0.25ML CO coverage (Figure 92a in appendices) and exhibits a close adsorption energy compared to Schimka *et al.*<sup>229</sup>

This suggests that edges and small particles do not have the same reactivity regarding to CO. Considering Pt<sub>38</sub> and Pt<sub>55</sub> non-supported particles<sup>234</sup>, a significant gap also appears against extended surfaces.

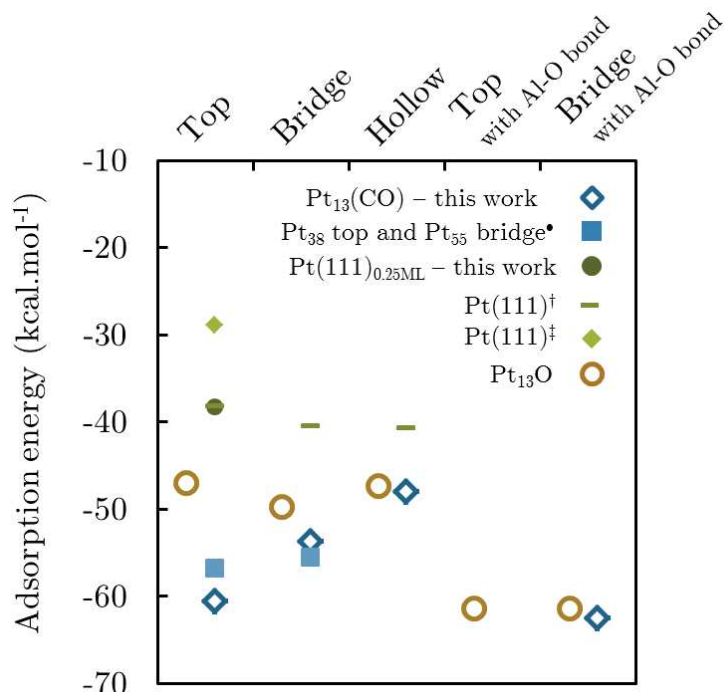


Figure 33: Comparison of the average adsorption energies of one adsorption of CO and atomic oxygen on the Pt<sub>13</sub> cluster and Pt(111). The work on non-supported cluster Pt<sub>38</sub>

and Pt<sub>55</sub> from •Johnston<sup>234</sup> *et al.* is stated. *Ab initio* data are reported for Pt(111) by † Dupont *et al.*<sup>230</sup> (GGA PBE) and ‡ Schimka *et al.*<sup>229</sup> (RPA).

#### 4.2.2 | Adsorption of CO at higher coverages

The adsorption of more than one CO was undertaken on the Pt<sub>13</sub>/γ-Al<sub>2</sub>O<sub>3</sub> model through molecular dynamics to identify stable configurations (Figure 93 in appendices). The Pt<sub>13</sub>(CO)<sub>m</sub>/γ-Al<sub>2</sub>O<sub>3</sub> structures are displayed in Figure 98 in appendices with a number of CO (m) of 2, 3 and three by three up to 24. Some of these structure are represented later, in Figure 36. Regarding frequencies calculations, few imaginary frequencies were found for some structure and are gathered in Table 28 (Appendices).

The sole adsorption mode found below 6 carbon monoxide molecules is the top one with a  $O - \widehat{C} - Pt$  angle close to 180°. The bridge sites appears from Pt<sub>13</sub>(CO)<sub>9</sub>/γ-Al<sub>2</sub>O<sub>3</sub> and is concomitant to disaggregation of the platinum cluster. This trend is noticeable on Figure 34 that displays the average distance of Pt atoms to the support with minima and maxima distances. From 1 to 6 carbon monoxide, the averages are close to 0.3 with almost the same extreme Pt-support distances.

Structures with 9 and 12 carbon monoxide molecules have the same minima than the low coverage structures, while their average and maxima are increasing of about 30%. This is typical of a disaggregation of the cluster as platinum are pushed upwards while some Pt atoms are still hooked to the support. The Pt<sub>13</sub>(CO)<sub>12</sub> structure should be considered with care as two of the adsorbed CO lead to atomic adsorption (Figure 99 in appendices).

For the Pt<sub>13</sub>(CO)<sub>15</sub>/γ-Al<sub>2</sub>O<sub>3</sub> structure, the minimal Pt-support distances are at least doubled. This expresses the uplift of the cluster away from the surface. Figure 36 and Figure 98 in appendices also show that some carbon monoxide are interspersed between the support and the platinum atoms, and seems to prevent the cluster from total unhooking. The adsorption mode population in Figure 100 displays that above Pt<sub>13</sub>(CO)<sub>15</sub>/γ-Al<sub>2</sub>O<sub>3</sub>, adsorption mode with CO linked to the surface. These intersped species are mostly four CO molecules, at 50% in dicarbonyl form and common top/bridge modes for the remaining 50%.

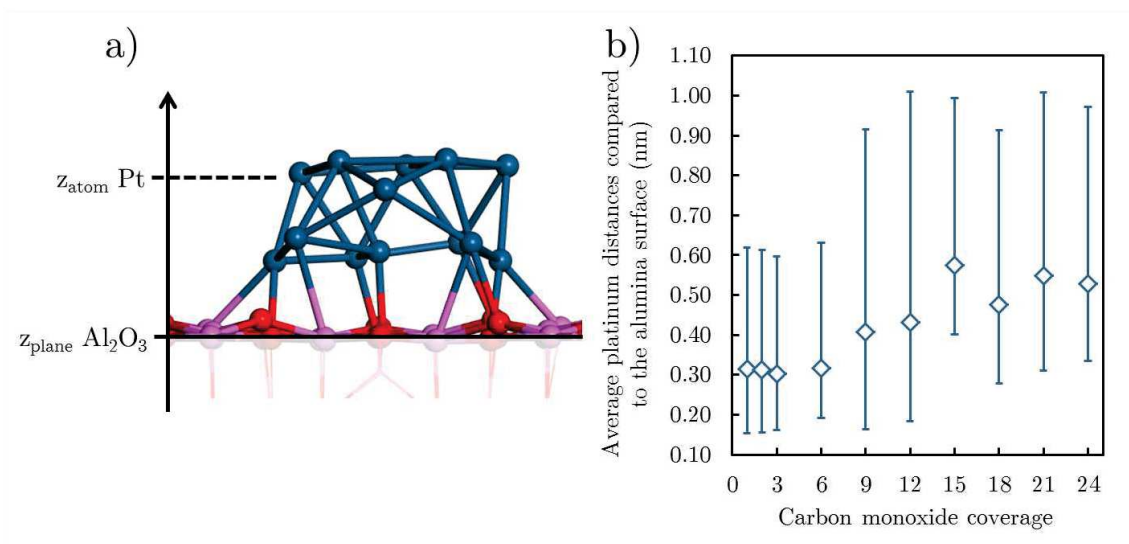


Figure 34: a) Determination of the distance of platinum atoms from the support and b) average distance to the support of the 13 platinum of the cluster according to CO coverage. The bars corresponds to minima and maxima values.

This is confirmed by the interaction energy between the cluster and the support (Figure 35a) which is still favourable to the cluster hooking. A completely different trend happened for the cluster covered by oxygen, where a strengthening of this interaction with increasing oxygen coverage is observed. Despite disaggregation and a uplift of the cluster, a total unhooking can be excluded according to the cluster energies found for non-supported structures (Figure 91 and Figure 101 in appendices).

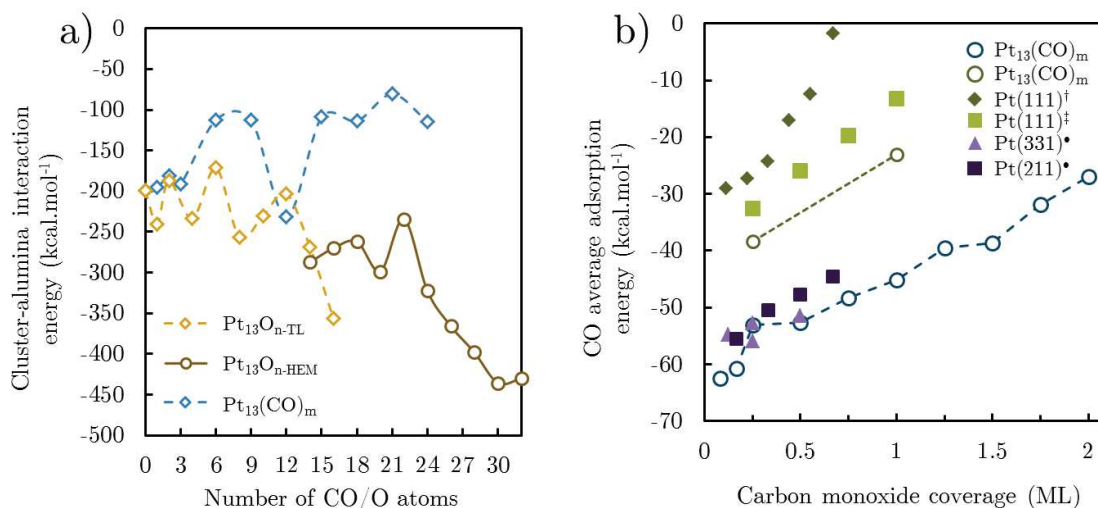


Figure 35: a) Electronic interactions between the alumina and the cluster in presence of oxygen and CO. b) Mean adsorption energy of CO according to the carbon monoxide coverage for  $\text{Pt}_{13}(\text{CO})_m$  and Pt(111) structures. One monolayer in the present work corresponds to  $\text{Pt}_{13}(\text{CO})_{12}$  structure, as 12 platinum are initially at the cluster surface.

The work of †Allian *et al.*<sup>162</sup> (RPBE) and coworkers, ‡Shan *et al.*<sup>233</sup> (RPBE) and •Orita and Inada<sup>232</sup> (PBE) for stepped surfaces are also reported.

Figure 35b displays the average heat of adsorption as a function of the carbon monoxide coverage. One can note that the average adsorption energy increases almost linearly for highly dispersed platinum cluster, revealing almost constant repulsion between CO molecules. The work of Allian *et al.*<sup>162</sup> and Shan *et al.*<sup>233</sup> on Pt(111) with GGA RPBE functionals reveal completely different values of adsorption energies, weaker by at least 50%. Few calculation undertook on the Pt(111) surfaces, *i.e.* at 0.25ML and 1 ML (Figure 92a-b) displayed stronger adsorption energies compared to literature. However the values for stepped Pt(331) and Pt(211) surfaces<sup>232</sup> are quite similar to the ones on supported clusters at low CO coverages. Indeed these surfaces cannot hold as much adspecies as the Pt<sub>13</sub> particles. These adsorption energies appears very similar to the ones of atomic oxygen on the same supported particles<sup>236</sup>.

A thermodynamic diagram (Figure 36) was built to elucidate the dependence of the coverage on temperature and CO partial pressure. A wide domain is dedicated to clean Pt<sub>13</sub> supported clusters, starting at 400°C for  $p_{\text{CO}} = 10^{-4}$  bar and more. Carbon monoxide coverage increases gradually up to the most covered Pt<sub>13</sub>(CO)<sub>24</sub> structure. However 1.5 monolayer (corresponding to 18 CO molecules per cluster) is barely reached at ambient temperature and structure from 0 to 1 ML (below 12 CO molecules) occupy the largest part of the diagram. A STM study of CO high covered Pt(111) surface conducted by Longwitz *et al.*<sup>237</sup> allows to emphasize on these data. They performed an ambient determination of CO coverage on a  $10^{-9}$  to  $10^3$  Torr range of CO partial pressure. The extreme operating points displayed respectively 0.50 and 0.70 monolayer coverage, linearly increasing on the logarithmic pressure range. In these conditions, the Pt<sub>13</sub> model exhibits respectively 0.75 to 1.25 ML, with a transition at  $9.10^{-7}$  bar. Considering Figure 36, imaginary frequencies were found for some Pt<sub>13</sub>(CO)<sub>m</sub> structures were treated as real ones ( Table 28 in appendices). Another treatment was performed in order to evaluate entropy alteration impact on the phase diagram. This peculiar treatment consisted in setting all frequencies below to  $50\text{cm}^{-1}$  to this value (Figure 94 in appendices). Differential phase diagram demonstrates that almost no significant changes happened (Figure 95 in appendices). Entropy differences are less than  $4\text{ cal.mol}^{-1}.\text{K}^{-1}$  per adsorbed CO.

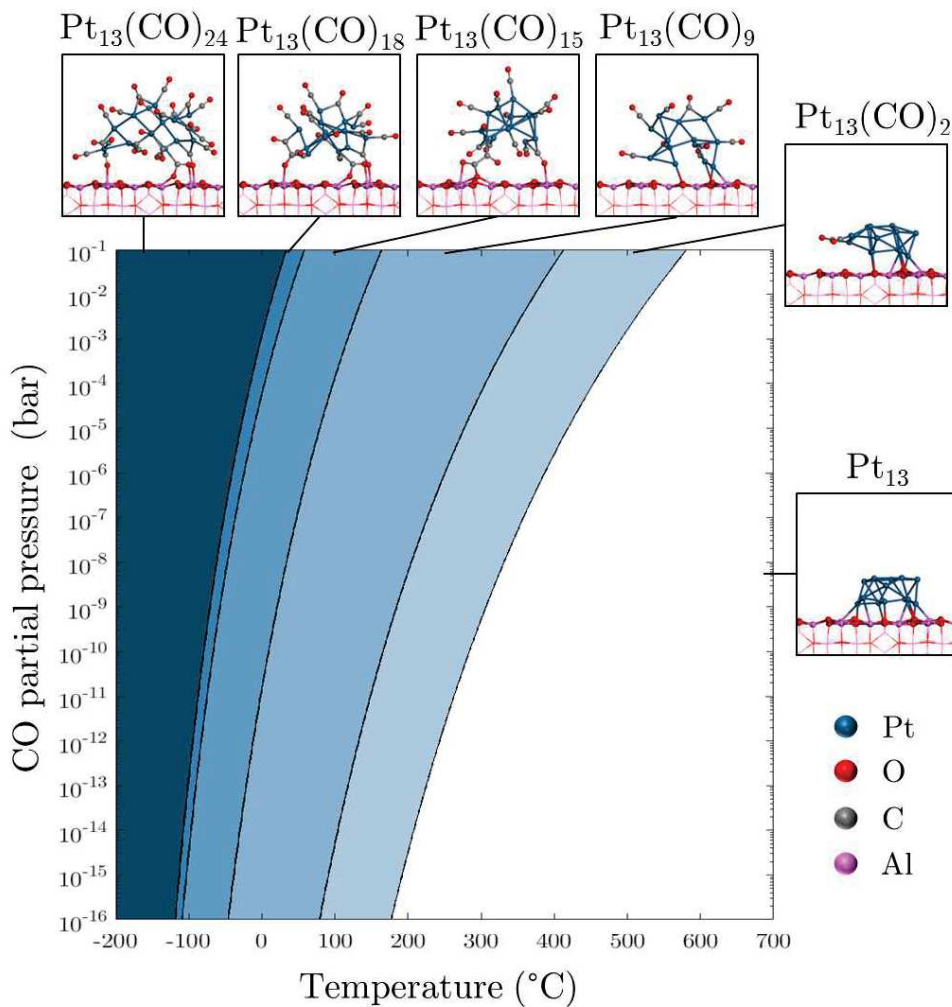


Figure 36: Phase diagram of supported  $\text{Pt}_{13}(\text{CO})_m$  structures according to temperature and partial pressure of CO. The structures of the systems exhibiting a significant stability domain are also depicted (side views).

Finally Bader charges of the cluster elements have been determined (Figure 102). No significant charge transfer between adsorbed CO to platinum can be seen with increasing coverage except for the  $\text{Pt}_{13}(\text{CO})_{12}$  for which atomic adsorption occurs. The carbon charge is lower than the one for CO gas, while the oxygen follow the opposite trend. This suggests that electrons are delocalized from C to O when CO adsorption on Pt occurs. Regarding the total charge of the adsorbed CO, a slight back-donation of the platinum to CO happen, with almost no impact of the CO coverage.

To summarize this molecular modelling investigation, the top and bridge site are the preferred structures for highly dispersed  $\text{Pt}_{13}(\text{CO})_m$  systems supported on alumina, respectively below 9 CO and above 18 CO coverage. The adsorption energies significantly differ from the one obtained for Pt(111) flat surface, however corrugated Pt(331) and Pt(211) are quite close to dispersed  $\text{Pt}_{13}(\text{CO})_m$  data. Above the monolayer of CO, desaggregation and uplift of the cluster happen. A total unhooking of the CO

covered cluster is however not favorable. However at the highest CO coverage, no platinum-alumina bond remains and some adsorbed CO molecules migrate between the alumina support and the platinum cluster.

In order to characterise the adsorption of carbon monoxide on pre-oxidized catalyst, few calculations were undertaken on previously determined  $\text{Pt}_{13}\text{O}_n/\gamma\text{-Al}_2\text{O}_3$ <sup>236</sup>. The two structures in Figure 37 exhibits the adsorption of one carbon monoxide on respectively 4O and 22O adsorbed cluster. For the  $\text{Pt}_{13}\text{O}_4(\text{CO})$ , the adsorption site of CO has been chosen as the most favourable site for the  $\text{Pt}_{13}(\text{CO})/\gamma\text{-Al}_2\text{O}_3$ . The co-adsorption of carbon monoxide and atomic oxygen has also been tested on Pt(111), with a 0.25ML coverage for each specie (Figure 92c). These structures will be discussed afterwards with DFT/experiments comparison.

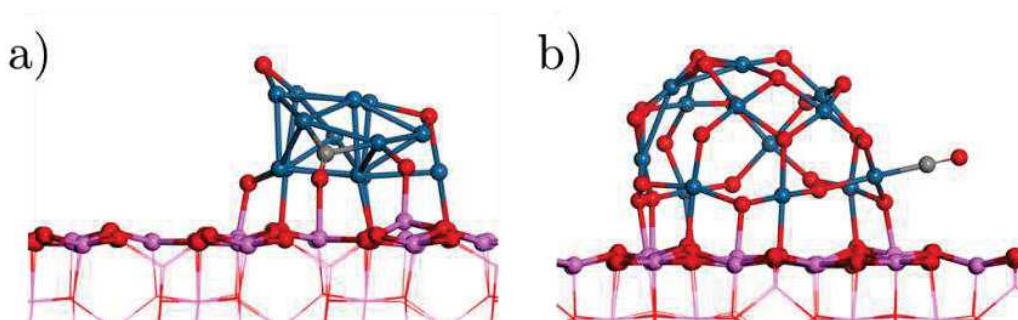


Figure 37: Illustrations of a)  $\text{Pt}_{13}\text{O}_4(\text{CO})$  and b)  $\text{Pt}_{13}\text{O}_{22}(\text{CO})$  structures.

### 4.3| Determination of experimental CO vibration frequencies and heats of adsorption

In order to experimentally evaluate the reactivity of a highly dispersed platinum catalyst supported on alumina, the determination of CO vibration frequencies and heats of adsorption by the AEIR method have been performed. This work has been done on both reduced and oxidized catalyst, that might affect the nature of adsorbed species. Regarding experimental studies, adsorption modes are named differently compared to molecular modelling. Figure 38 explained that experimental linear adsorption modes corresponds to top modelled adsorption. Indeed the  $\text{Pt}-\widehat{\text{C}}-\text{O}$  angle is close to a flat angle. Molecular bridge and hollow sites are gathered in a multibonded B/3FC notation.

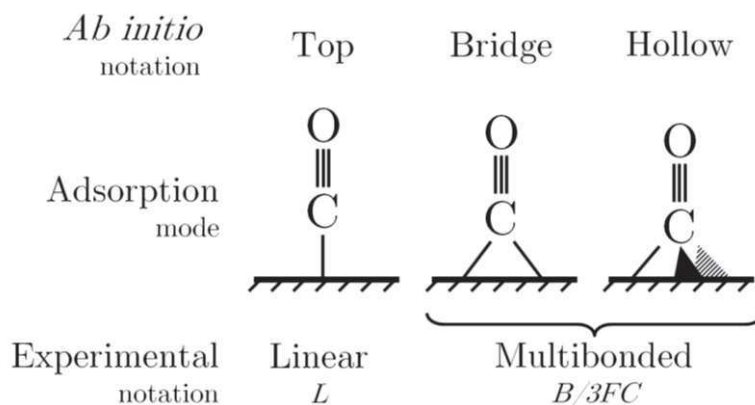


Figure 38: Experimental and molecular modelling correspondence between adsorption mode notations

#### 4.3.1| Influence of Pt oxidation state on the IR spectra of adsorbed CO species

Infrared spectra of 1% wt Pt/Al<sub>2</sub>O<sub>3</sub> materials are displayed in Figure 39. The catalysts were in contact with 0.3% CO/He gas flow at 25°C. The highest band is observed at 2068 cm<sup>-1</sup> for the two materials that corresponds to linearly adsorbed (L, equivalent to top sites) carbon monoxide<sup>219</sup>. In addition, two other shared bands are noticed at 1882 and 1832 cm<sup>-1</sup> attributed to multi-bounded (B/3FC) CO species. The main difference between oxidized and reduced catalyst lies in the 2120 cm<sup>-1</sup> band only observed for the oxidized one. Thanks to Bianchi and coworkers, it has been attributed to electron depleted Pt<sup>2+</sup>, that must be an oxidized platinum due to experimental emergence conditions<sup>223</sup>.

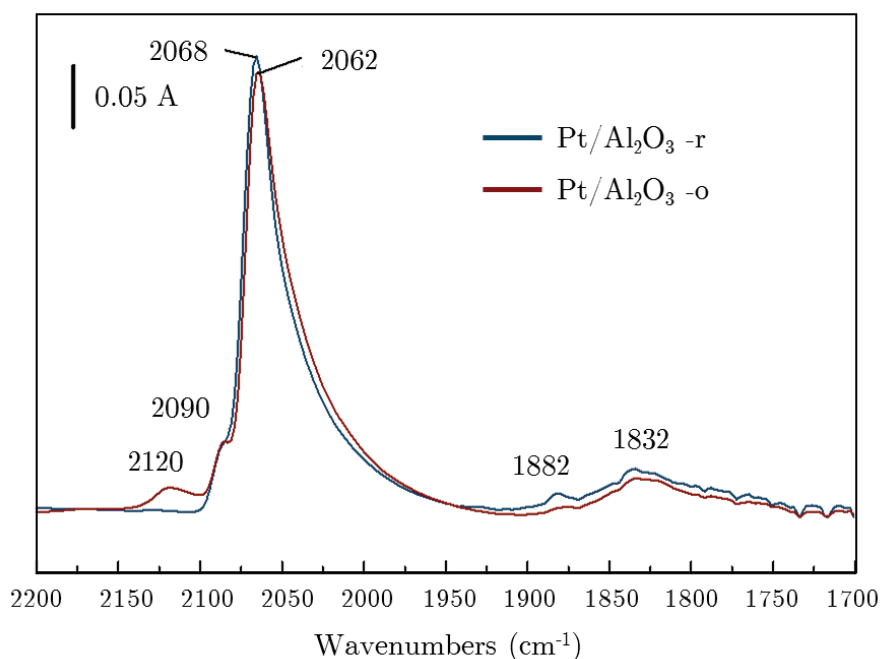


Figure 39: AEIR spectra during CO adsorption at 25°C on reduced catalyst (black line) and oxidized catalyst (red line).

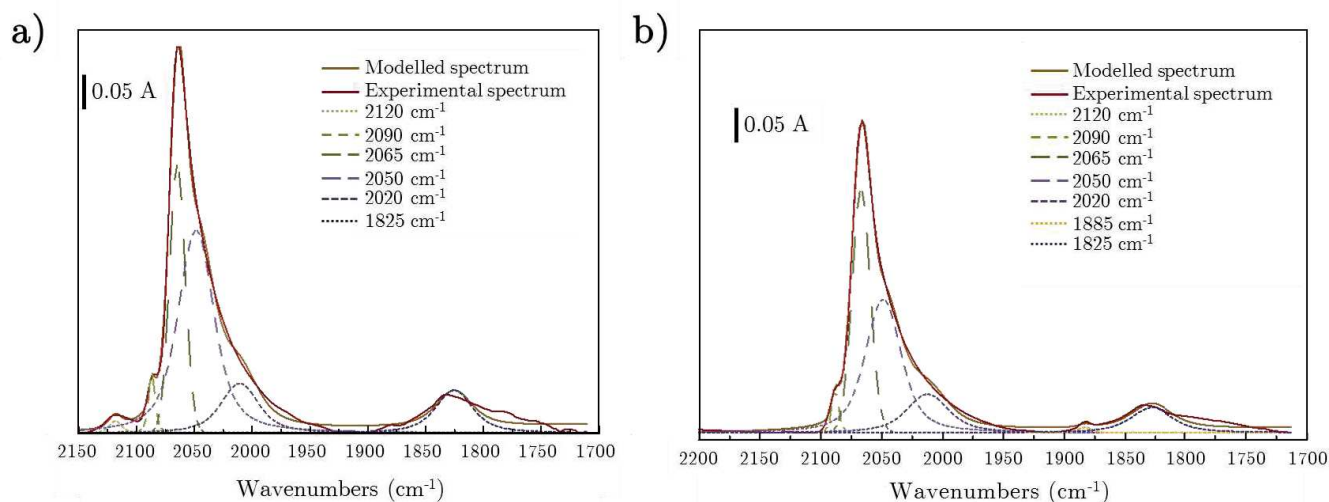


Figure 40: AEIR spectra band deconvolution for the (a) oxidised and the (b) reduced sample Pt/ $\gamma$ -Al<sub>2</sub>O<sub>3</sub>.

The band deconvolution (Figure 40) of these two spectra have been performed. The band assigned to linear carbonyls is composed of four components at 2090, 2065, 2050 and 2020 cm<sup>-1</sup>. It seems that platinum oxidation state does not influence the CO vibration wavenumber for this specific ensemble of bands. The presence of four components is explained by the difference of Pt adsorption site. Prior works identified 2070 cm<sup>-1</sup> as adsorption on Pt steps and 2090 cm<sup>-1</sup> on terraces<sup>238</sup>. The two lower bands might corresponds to peculiar Pt sub-nanometric particle surfaces<sup>218</sup>.

Infrared bands obtained for bridged (B) and threefold coordinated CO (3FC)<sup>239</sup> lie at 1885 cm<sup>-1</sup> and 1825 cm<sup>-1</sup> respectively. The first one has successfully been deconvoluted for the reduced catalyst. It is not the case for the oxidized material but one can see that the global spectra holds it. Bourane *et al.* demonstrated that increasing catalyst mass allows the decomposition of the 3FC/B region into three contributions with a band at 1800 cm<sup>-1</sup><sup>219,239</sup>. These adsorption modes are less intense for oxidized material.

The experiment was reproduced at various temperatures (Figure 41a). The bands previously observed are varying with temperature. Considering linear species, a decrease of the band intensity with increasing the temperature of adsorption is observed. This indicates a drop of concentration of linear CO species at the catalyst surface. The same behaviour is noticed for the bridged and the threefold coordinated species, down to zero intensity reached at 290°C. The observation is in adequacy with the work performed by Bourane *et al.*<sup>239</sup>. Notably, the weaker intensity of the IR band concerning the B and 3FC species compared to the linear species does not imply a lower amount of this specie. Indeed the extinction absorption coefficient ( $\epsilon$ ) is different for the linear and B/3FC CO species<sup>220</sup>. A shift of the bands toward lower wavenumbers with increasing temperature is also visible. This alteration can be due to platinum surface reconstruction.

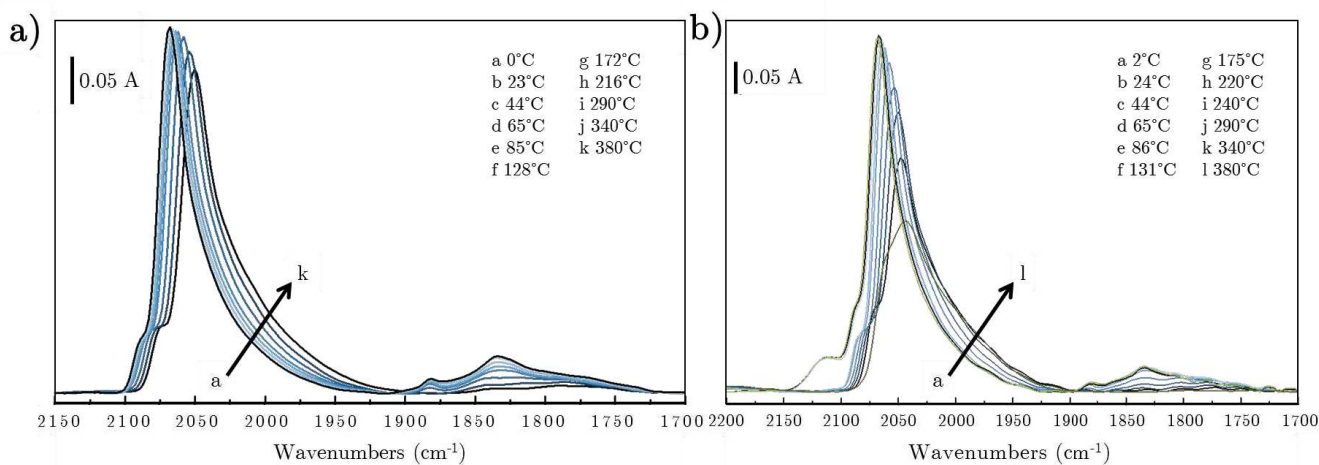


Figure 41: (a) AEIR spectra during the adsorption of 0.3%CO/He on reduced sample and (b) oxidized sample. Some spectrum overlap.

Concerning the oxidized sample (Figure 41b), the difference lies again in the 2120cm<sup>-1</sup> band. This band is observed up to 86°C. At higher temperature, in addition to CO desorption, the intensity decrease implies the reaction of CO (Figure 103 in appendices) with adsorbed oxygen and the reduction of Pt<sup>2+</sup> into Pt<sup>0</sup>. Yet it is not clear if 2120 cm<sup>-1</sup> CO or another linear specie close to Pt<sup>2+</sup> site reacts. The intensity of the other bands is quite stable until 86°C. Then CO conversion into CO<sub>2</sub> occurs by means of the oxygen adsorbed on the Pt nanoparticles (Figure 103 in appendices). A similar behaviour is

observed for multibonded species. These bands are not observed at temperatures higher than 290°C.

#### 4.3.2| Heat of adsorption of the linear and bridged CO species on the two catalysts

To determine the heat of adsorption of the adsorbed CO species, the AEIR method (Adsorption Equilibrium Infrared spectroscopy method) was used<sup>104–109</sup>. This methodology is explained in section 2.2.3. Experimental data and fitting models are reported in Figure 42. Related carbon monoxide heat of adsorption are gathered in Table 9.

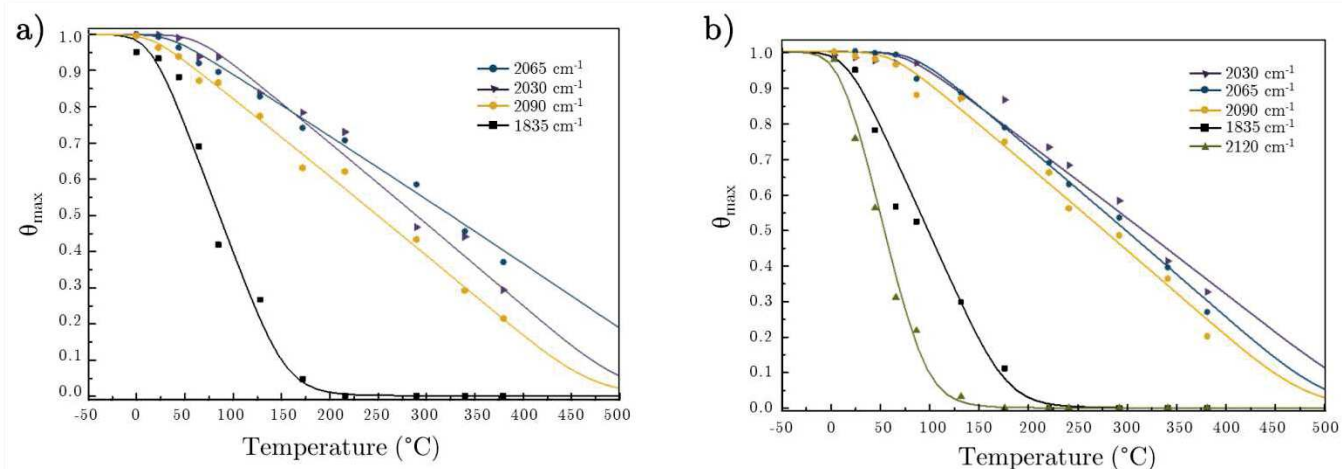


Figure 42: Evolution of the coverage of linear and bridged CO species for the reduced sample (a) and the oxidized catalyst (b). Comparison of experimental data (symbols) and theoretical curves (lines).

Table 9: Heats of adsorption of each species for the two catalytic materials

IR band		1wt.% Pt/Al <sub>2</sub> O <sub>3</sub> -r		1wt.% Pt/Al <sub>2</sub> O <sub>3</sub> -o	
		E <sub>0</sub> (kcal.mol <sup>-1</sup> )	E <sub>θ<sub>max</sub></sub> (kcal.mol <sup>-1</sup> )	E <sub>0</sub> (kcal.mol <sup>-1</sup> )	E <sub>θ<sub>max</sub></sub> (kcal.mol <sup>-1</sup> )
1835 cm <sup>-1</sup>	3 FC	-20.3	-13.1	-21.6	-13.1
2030 cm <sup>-1</sup>	CO(L) on Pt sub-nanometric particles	-39.4	-15.5	-41.8	-16.3
2065 cm <sup>-1</sup>	CO(L) on Pt steps	-41.8	-14.6	-39.4	-16.7
2090 cm <sup>-1</sup>	CO(L) on Pt terraces	-37.5	-13.1	-38.2	-15.5
2120 cm <sup>-1</sup>	CO on Pt <sup>2+</sup>	-	-	-17.2	-12.9

CO linear heat of adsorption (2030, 2065 and 2090  $\text{cm}^{-1}$ ) lie in the same range of values with an  $E_0$  around  $-40 \text{ kcal.mol}^{-1}$  and  $-14 \text{ kcal.mol}^{-1}$  at maximum coverage. The data are similar to the literature albeit quite higher than the present work<sup>106,108,221,222</sup>. This difference can be due to Pt dispersion. In addition the fit might lead to some differences. Concerning the B and 3FC species, the values are lower than the linear species and are similar to the literature data<sup>239</sup>. No significant difference has been noticed between reduced and oxidized samples. This suggests that CO is not influenced by pre-adsorption of oxygen on the catalyst. This is in adequacy with the observations of Bourane *et al.*, that observed the co-adsorption of  $\text{O}_2$  does not modify CO heat of adsorption<sup>239</sup>. Regarding the band at  $2120 \text{ cm}^{-1}$ , its values are close to the B and 3FC species. The decrease of the CO coverage at low temperature could be explained by its oxidation by the oxygen adsorbed on Pt, following a Langmuir-Hinshelwood mechanism<sup>222</sup>.

To conclude, linear species are close, in frequencies and heat of adsorption, to each other so that their structural distinction is not straightforward. However bridge and multibounded species offers a distinct data that can be easily identified. The  $2120\text{cm}^{-1}$  band already discovered by Bianchi and coworkers has been recorded only for oxidized catalyst and thus express an adsorption mode linked to oxidized platinum.

## 4.4 | Comparison of experimental and DFT data

The experimental data previously reported are directly compared to the *ab initio* investigations through CO vibration wavenumbers and enthalpic heat of adsorption. Specific identified frequencies are reported for  $\text{Pt}_{13}(\text{CO})_{3,9,15}$ , Pt(111) and oxidized structures. In a second step, the kinetic modelling of CO adsorption/desorption reactions via *ab initio* data is performed. This kinetic models allow to compare experimental and simulated carbon monoxide temperature programmed desorption.

### 4.4.1 | At thermodynamic equilibrium

Enthalpic heat of adsorption have been determined for both experimental and modelling means. Experimental AEIR methods allowed to determined CO heats of adsorption for somme infrared bands. The enthalpic range, from  $0\vartheta_{\text{max}}$  to  $\vartheta_{\text{max}}$  is reported in Figure 45. The related *ab initio* data have been also calculated on a  $30^\circ\text{C}$ - $500^\circ\text{C}$  temperature range, respectively  $T_{\text{min}}$  and  $T_{\text{max}}$  in Figure 45. These two ranges are compatible as experimental results demonstrated that CO is fully desorbed beyond  $500^\circ\text{C}$ .

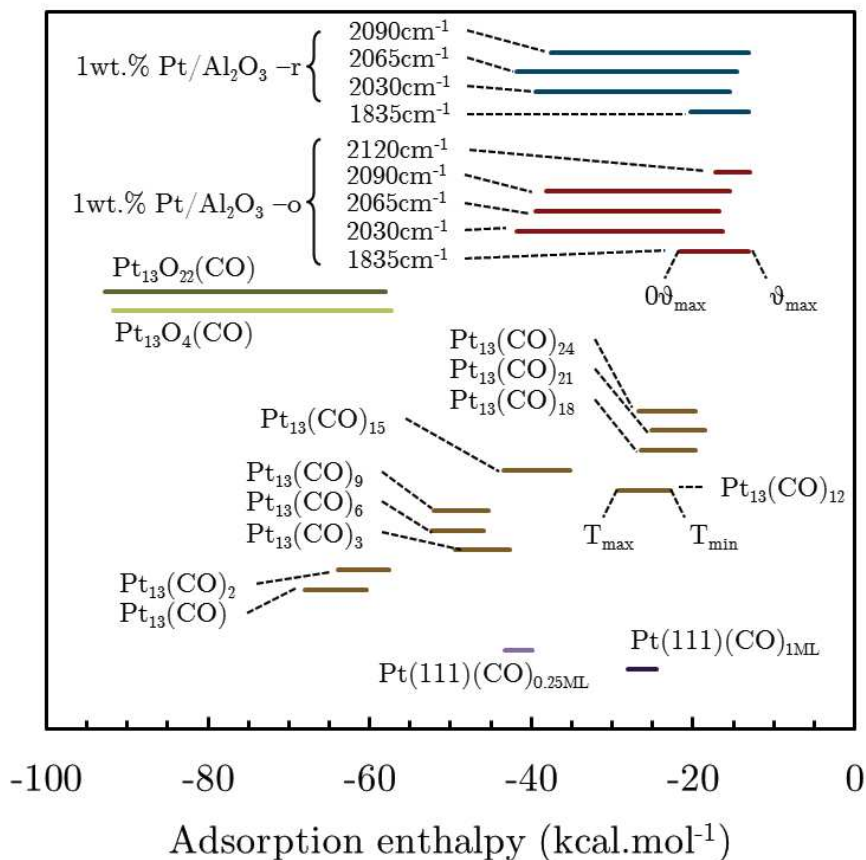


Figure 43: Experimental and calculated CO enthalpic heats of adsorption compared to DFT adsorption enthalpy. For  $\text{Pt}_{13}(\text{CO})_m$  with  $m > 1$  and  $\text{Pt}(111)_{1\text{ML}}$  structures, mean enthalpies are displayed.

*Ab initio*  $\text{Pt}_{13}(\text{CO})_m$  structures occupy a large heat of adsorption range from  $-70 \text{ kcal.mol}^{-1}$  to  $-20 \text{ kcal.mol}^{-1}$ . Although low covered structures are far from experimental findings, one can observe that highest CO covered structures ( $m > 15$ ) correspond to fully covered  $\text{Pt}/\gamma\text{-Al}_2\text{O}_3$ , whatever the experimental oxidation state or adsorption mode. This suggests that experimental  $\vartheta_{\text{max}}$  is higher than one monolayer. Moreover  $\text{Pt}(111)_{1\text{ML}}$  heat of adsorption lies from  $-30$  to  $-25 \text{ kcal.mol}^{-1}$ , that does not corresponds to experimental fully covered range. Considering  $\text{Pt}(111)_{0.25\text{ML}}$  structure, heat of adsorption is in adequacy with low covered experimental data for linear vibration modes.

Regarding multibonded modes, they are not isolated in any *ab initio* structures. Yet the more bridge containing structures are  $\text{Pt}_{13}(\text{CO})_m$  with  $m > 15$ , from 0.3 to 0.5 in proportion (Figure 100 in appendices). That would explain the significant shift between these structures and the other  $\text{Pt}_{13}(\text{CO})_m$  ones. Also one can note that  $\text{Pt}_{13}(\text{CO})_{15}$  heat of adsorption is lower than  $\text{Pt}_{13}(\text{CO})_{12}$ . This is due to CO decomposition into atomic carbon and oxygen for two carbon monoxide in the structure (Figure 99 in appendices).

Therefore  $\text{Pt}_{13}(\text{CO})_{12}$  heat of adsorption does not only correspond to CO adsorption enthalpy. Considering oxidized structures  $\text{Pt}_{13}\text{O}_{22}(\text{CO})$  and  $\text{Pt}_{13}\text{O}_4(\text{CO})$ , they lie out of the range, far from the  $2120\text{cm}^{-1}$  heat of adsorption range corresponding to electron depleted platinum  $\text{Pt}^{2+}$ . This suggests that *ab initio* structures are not representative from this peculiar site.

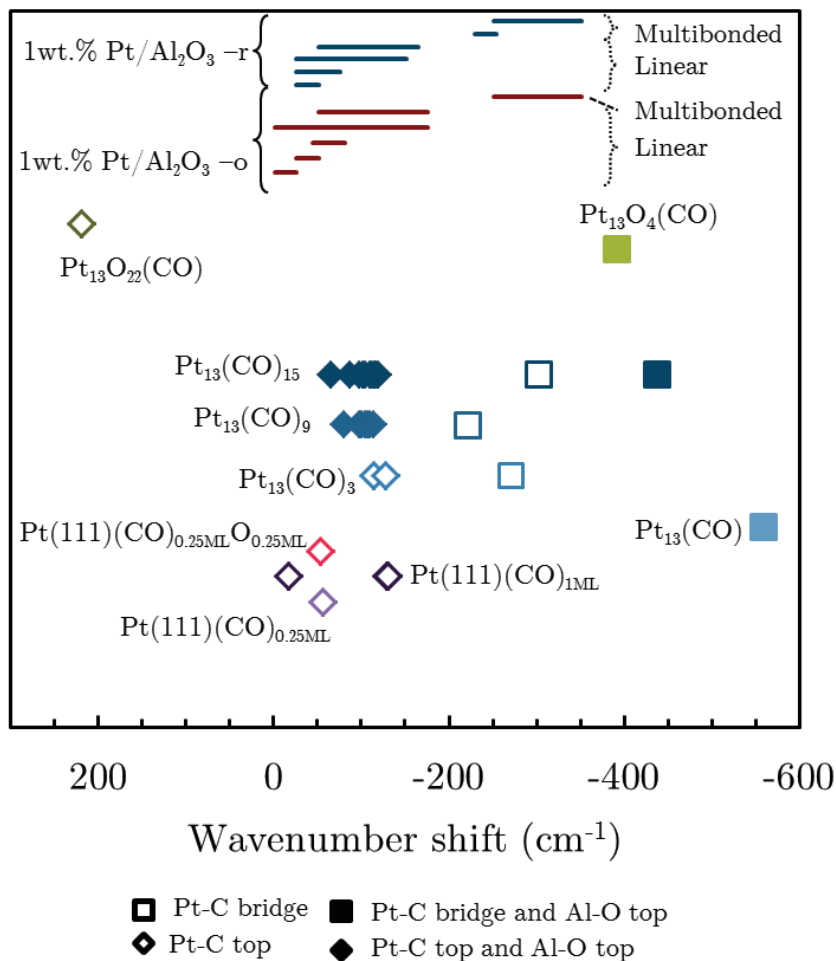


Figure 44: Experimental and calculated C-O bond vibration wavenumber normalized to gas CO ( $2126\text{cm}^{-1}$  found by *ab initio* calculation).

The comparison of CO vibration has been made through shifted wavenumbers values (Figure 44). Indeed the performed *ab initio* calculations has led to harmonic frequencies. In order to remove the anharmonic contributions of experimental data, equation (35) was applied (section 2.3.2.6.) and were turned into wavenumbers. Experimental vibration ranges displayed in Figure 40 were adapted in Figure 44. *Ab initio* determined frequencies were identified at their related CO vibration mode. Considering the comparison between experimental linear modes and *ab initio* top sites, every modelled wavenumber is in the experimental range. One can observe that Pt(111) wavenumber shifts are close to zero than  $\text{Pt}_{13}(\text{CO})_m$  structures. Bianchi<sup>221</sup> has

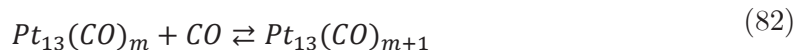
demonstrated that linear adsorbed CO vibrations is shifted towards lower wavenumbers with decreasing size particle. This shift was evaluated at  $19 \text{ cm}^{-1}$  on a 0.44-0.75 dispersion range. This assumption is in adequacy with the reported data. Both platinum bridged and platinum-alumina adsorption sites (plain and empty squares) exhibits significantly distinct wavenumbers compared to top adsorption modes. They are close to experimental ranges of reduced and oxidised catalysts. Finally the oxidized top adsorbed CO on the  $\text{Pt}_{13}\text{O}_{22}$  adsorbed structures exhibits and out of the range wavenumber ( $2340\text{cm}^{-1}$  in absolute).

The comparison of CO vibration wavenumbers and enthalpic heats of adsorption are globally congruent between molecular modelling and experimental data. Both  $\text{Pt}_{13}(\text{CO})_m$  and Pt(111) structures display in-range CO heats of adsorption. Below  $\text{Pt}_{13}(\text{CO})_{15}$ , structures exhibit very strong CO enthalpies that are not recorded with experimental data. It may be due to a scarce number of these sites for which infrared intensity would be too low to be recorded. Also DFT misestimation energy for uncountered on flat surface<sup>226</sup> for this kind of system may overestimate CO adsorption. Regarding vibration wavenumbers, linear and top modes are in excellent adequacy. The distinction between flat and dispersed platinum surfaces is significant enough for *ab initio* data and is in accordance with previously demonstrated shift with platinum dispersion. Multibonded adsorption modes are close to experimental data though more shifted for alumina bonded species. Yet purely platinum bridge adsorbed CO are representative of this vibrations. Finally, the oxidised species, vibration wavenumber and heat of adsorption data suggest that these structures are not representative of the experimental oxidised catalyst. Therefore the experimental catalyst may be more CO covered than expected.

#### 4.4.2 | CO-TPD and micro-kinetic modelling

To further the comparison between DFT calculations and experimental findings, a Temperature Programmed Experiment has been undertaken combined with micro-kinetic modelling. This later is based on *ab initio* supported  $\text{Pt}_{13}(\text{CO})_m$  results to determine the rate constant of desorption. To highlight key reactions, a sensitive analysis was done at simulated peak temperatures.

Since the  $\text{Pt}_{13}(\text{CO})_m$  *ab initio* structures were investigated three-by-three, the thermodynamic data obtained by *ab initio* investigations were interpolated by piecewise linear patterns (Figure 96 in appendices) to a kinetic mechanisms using Chemkin Pro formalism. These mechanism was based on molecular CO barrierless adsorption reactions following equation (82).



Experimental Temperature Programmed Desorption (Figure 45a) shows a 260°C desorption temperature range, from 70°C up to 330°C, with no thin distinct peaks. A shoulder is visible at 70°C, followed by a steep increase of CO release with a maximum of 500 ppm at 103°C. A local maximum is reached at 144°C discerned from the first peak by a slight dip. Then a mild decrease begins up to 330°C. Concerning oxidation during the experiment, mass spectrometer signal shows a small release of CO<sub>2</sub> close to 100°C. Few oxygen may have remained on the cluster or close to it on the support, through hydroxyl groups, and oxidized at low temperature.

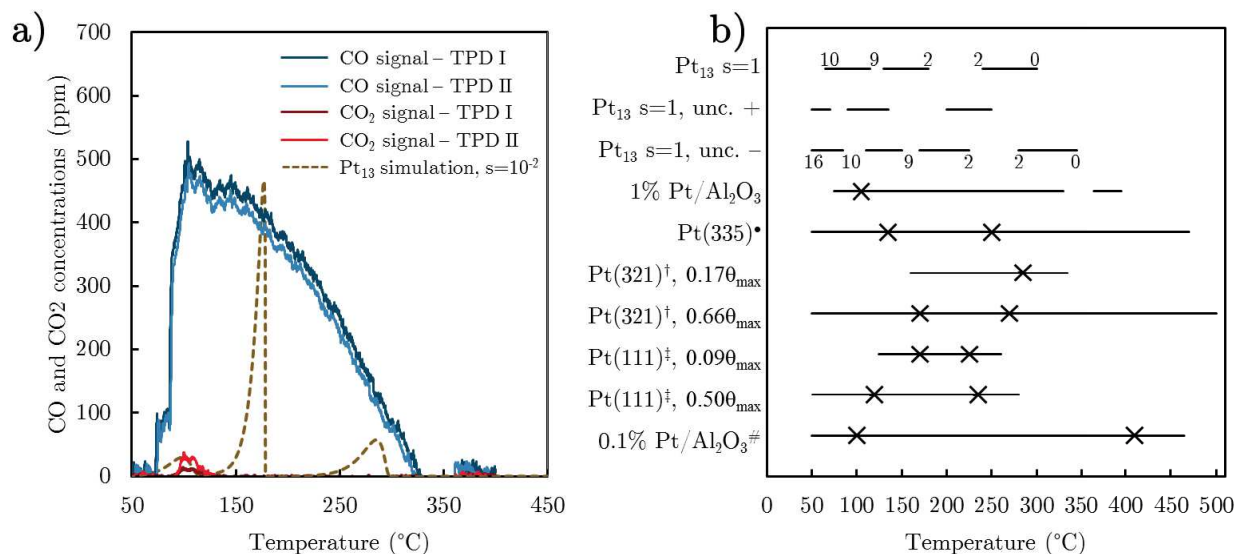


Figure 45: (a) TPD-CO simulation with Pt<sub>13</sub>(CO)<sub>m</sub> mechanism and relative intensity of CO (m/z=28) during the Temperature-Programmed Desorption on highly-dispersed 1 wt. % Pt/γ-Al<sub>2</sub>O<sub>3</sub>. CO<sub>2</sub> release (m/z=44) is also shown. (b) Impact *ab initio* typical error ( $\pm 3.6$  kcal.mol<sup>-1</sup> for enthalpies and  $\pm 3.6$  cal.mol<sup>-1</sup>.K<sup>-1</sup> for entropies) on Pt<sub>13</sub>(CO)<sub>m</sub> kinetic model with a 5°C.min<sup>-1</sup> temperature ramp. Experimental TPD of <sup>•</sup>Di Maggio<sup>224</sup> (10°C/s rate), <sup>†</sup>Gland and McClellan<sup>210</sup> (10°C/s) and <sup>‡</sup>Ertl *et al.*<sup>96</sup> (15°C/s) are reported. For alumina supported platinum, the TPD of <sup>#</sup>Herz and McCreedy<sup>209</sup> with a 0.90 Pt dispersion is displayed.

Extended surfaces show same experimental temperature ranges although depending on their initial CO coverage. Considering Pt(335) stepped surface<sup>224</sup>, CO desorbs on a wide range that cover the one of this work, similarly at Pt(321)<sup>210</sup> with 0.66θ<sub>max</sub> initial CO coverage. However starting from 0.17θ<sub>max</sub>, the temperature range lies from 150°C to 330°C, that constitute the high part of our TPD-CO. The Pt(111)<sup>96</sup> surface exhibits lower desorption temperature, from 50°C to 280°C. That range represent the low temperature one of our experiment. One can conclude that platinum particles shows similar reactivity to CO adsorption from both flat and corrugated surfaces.

It should be noted that temperature rates are significantly different compared to this work. The high heat speed might be not representative of thermal equilibrium states during TPD. Thus CO desorption end temperature could be overestimated. Also one can see that stepped surfaces as Pt(335) and Pt(321) starts almost 100°C before Pt(111) surface, similarly as platinum particles.

Herz and McCready<sup>209</sup> used a 55°C.min<sup>-1</sup> heat speed on a 0.9 platinum dispersed catalyst supported on alumina. Figure 45 report a wide desorption range, however the major desorption appears focused around the first peak, that appears at a similar temperature than our work.

Regarding micro-kinetic modelling of the TPD experiment (Table 29 for typical reaction parameters, in appendices), a wide range of sticking coefficient has been investigated. This parameter is not well estimated as it represents a reactive collision probability, that depends on diverse parameter such as temperature, partial pressure, tilt angle for instance. King and Shigeishi<sup>215</sup> recorded a 0.67 probability on Pt(111) at 30°C and low CO partial pressure (10<sup>-8</sup> Torr), and decrease down to 0.14 at 220°C. Ertl<sup>96</sup> and Hayden<sup>216</sup> reported similar data. Despite these high values and considering the peculiar Pt<sub>13</sub>(CO)<sub>m</sub> particle shape, it can considerably vary.

Hence several micro-kinetic models were tested to evaluate, the impact of the sticking probability. The modelling of the CO flow before TPD gives a Pt<sub>13</sub>(CO)<sub>10</sub> and Pt<sub>13</sub>(CO)<sub>11</sub> surface species mix with respectively 0.63 and 0.37 ratios. Figure 45b displayed the following TPD modelling. A three peaks desorption is observed in the fully integrated in the temperate range of experimental TPD. The main peak is the second one passing from Pt<sub>13</sub>(CO)<sub>9</sub> to Pt<sub>13</sub>(CO)<sub>2</sub> structure. Carbon monoxide sticking coefficient *s* has been evaluated over a 1 to 10<sup>-6</sup> range, 10<sup>-2</sup> by 10<sup>-2</sup> (Figure 104 in appendices). No impact on CO release has been detected down to 10<sup>-4</sup>, and slightly at 10<sup>-6</sup>. Therefore the sticking coefficient is considered to have no effect on carbon monoxide desorption. .

*Ab initio* typical error was evaluated through two models. The variation from the main model (with *s*<sub>CO</sub>=1) of ± 3.6 kcal.mol<sup>-1</sup> for desorption enthalpies and ± 3.6 cal.mol<sup>-1</sup>.K<sup>-1</sup> for entropies was done in such way that a model fully enhance desorption while the other one dampen it (respectively named unc. + and unc. -). While surface species conditions were the same for the unc. + model than the main one, the model that moderate the desorption starts with a Pt<sub>13</sub>(CO)<sub>16</sub> structure. Indeed this model is favourable to a deeper CO adsorption by lowering activation barriers. Therefore the simulated adsorption step, prior TPD simulation, gives this higher covered structure. A four peak desorption is thus observed for this model, starting from 50°C up to almost 350°C, widening the range to +40°C compared to experiment. The simulated TPD with the facilitating model appears to end 50°C earlier than the main one. In view of this

complete study, the modelled desorption is almost covered by the temperature range of experimental desorption.

Finally a brute-force sensitive analysis was performed on the model with  $s_{\text{CO}}=10^{-2}$  to assess the propensity of each double-sided reactions to deviate regarding their pre-exponential factor. Figure 46 report the normalized sensitivity toward gas CO at the temperatures of the peaks. Only the second peak reactions are sensible, mainly through the  $\text{Pt}_{13}(\text{CO})_6$  to  $\text{Pt}_{13}(\text{CO})_4$  reactions. Hence each reaction from  $\text{Pt}_{13}(\text{CO})_9$  to  $\text{Pt}_{13}(\text{CO})_2$  is significantly sensitive.

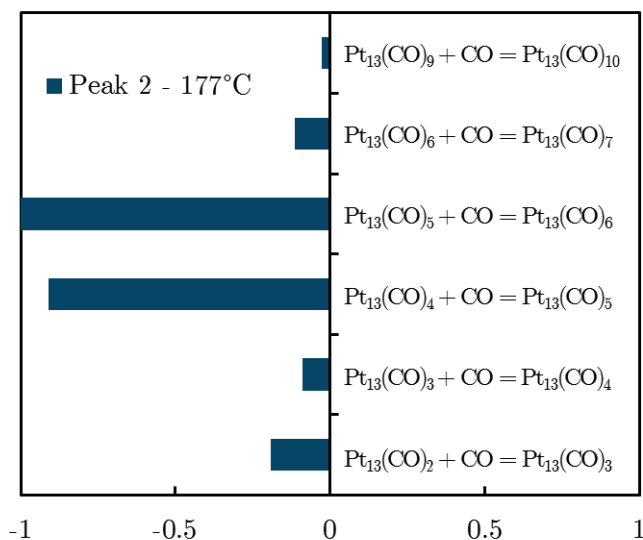


Figure 46: Relative sensitivities of the pre-exponential factors relative to CO at the peak temperatures for the most sensitive two-sides reactions for the  $\text{Pt}_{13}(\text{CO})_m$  kinetic mechanism with transition structures. The CO sticking coefficient is  $10^{-2}$ .

To outline experimental and DFT comparison, both direct comparison of CO vibration wavenumber and adsorption enthalpy are congruent. Carbon monoxide adsorption phenomenon is handled on a reduced catalyst. Yet *ab initio* data about oxidised cluster model did not correspond to experiments. This suggests that the chosen models are not representative of the experimental surface state, that may be more covered in CO molecule. Experimental and simulated Temperature Programmed Desorption are in adequacy according to temperature range. Typical *ab initio* error and uncertainty on the CO sticking coefficient have been scanned with several kinetic model versions, and demonstrated that few desorption temperature shift occurs. However the whole broad desorption peak is not handled by simulated TPD. This may be due to the site diversity that is not represented for a given CO-covered structure. This would be handled therefore with more probed *ab initio* models integrated at the kinetic model.

## 4.5| Conclusion

In this chapter, the multi-scale approach was applied to carbon monoxide adsorption on highly dispersed Pt/ $\gamma$ -Al<sub>2</sub>O<sub>3</sub>. This approach used experimental TPD and AEIR method, *ab initio* calculations on Pt<sub>13</sub>(CO)<sub>m</sub>/ $\gamma$ -Al<sub>2</sub>O<sub>3</sub> and Pt(111) surface models combined with kinetic modelling of CO desorption. Carbon monoxide desorption was observed at low temperature all at once, indicating low adsorption interactions with highly dispersed platinum. Few dispersion impact is therefore noticed as identical desorption temperature on both flat and stepped extended surfaces was observed. Solid infrared characterisation allows to distinguish multiple linear and multibounded adsorption modes. AEIR determined heat of adsorption ranges are close to prior data.

*Ab initio* investigations on the platinum cluster representative of the experimental catalytic material. The adsorption of one CO demonstrated that top sites are the most stable ones, and that very few interactions exist with the alumina support. Considerable cluster reconstruction is observed with increasing CO coverage. The formation of other species, especially dicarbonyl is noticed. Disaggregation and uplift from the support are reported, while adspecies are interspersed between alumina and platinum cluster. Thermodynamic parameter determinations allow to develop a phase diagram of pure CO adsorption. Mildly covered structures are observed between 25°C and 500°C, considering a CO partial pressure of 0.01 bar. Carbon monoxide clean surface is easily achievable compared to oxygen adsorption diagram. *Ab initio* data have been directly compared to experimental ones through CO vibration wavenumbers and adsorption enthalpy. These data are congruent in both vibration and enthalpy for the reduced catalyst. The experimental data on the oxidised catalyst are close to the reduced ones. Yet *ab initio* related models did not reproduce experimental observations, that may be due to a representativity issue.

Molecular modelling of Pt<sub>13</sub>(CO)<sub>m</sub>/ $\gamma$ -Al<sub>2</sub>O<sub>3</sub> structures allows to build kinetic schemes in order to simulate CO-TPD experiments. As previous oxygen desorption simulation, some uncertainties on CO sticking coefficient exist. Yet it does not significantly impact desorption on the large probed range. Desorption enthalpies and entropies uncertainties were also evaluated. Simulation agrees with experimental TPD, as the whole models set displays simulated discrete peaks in the range of the experimental broad desorption.

Finally this work has brought new information on CO adsorption/desorption phenomenon on highly dispersed platinum supported on alumina. Platinum dispersion as few impact considering experimental temperature desorption range and modelled adsorption enthalpies. Like in chapter 3, carbon monoxide adsorption study allows to demonstrate that the multiscale approach is versatile and can be extended to multiple molecular phenomena. The high level of detail committed in modelling investigation and the accordance of experimental material and modelled surfaces might play a major role

in the capability of the multi-scale approach. The two developed adsorption models are ready-to-use bases in order to study carbon monoxide oxidation, in the next chapter. In a greater extent CO adsorption kinetic modelling is a key feature towards every deep oxidation catalysis process, and can therefore be used for future works.

# 5| Carbon monoxide oxidation on Pt/ $\gamma$ -Al<sub>2</sub>O<sub>3</sub>

## 5.1| Introduction

Carbon monoxide oxidation represents the next step after oxygen and carbon monoxide adsorptions. As the simplest oxidation reaction, it has been studied since one century. The common accepted reaction pathway follows a Langmuir-Hinshelwood mechanism<sup>240-244</sup>, with adsorption of reactants in the first steps. Oxidation takes place at the surface and adsorbed CO<sub>2</sub> is then desorbed. It has also been demonstrated that CO inhibits the reaction while O<sub>2</sub> has a promoting effect<sup>241,244-247</sup>.

Although the reaction is molecularly simple, the sensitivity of the reaction toward metal dispersion is a controversial topic with opposite conclusions. Gracia and coworkers discussed this point<sup>248</sup> based on experimental and modelling works. Considering multiple sites such as step, edges, corners and planar surfaces, multiple reactivities can be attributed<sup>249,250,162</sup>. Also the proportion of sites varies with particle size. Small particles below 20Å contain a higher percentage of corner platinum atoms than 50Å particles or a Pt(111) single crystal. This variation affects CO oxidation. It has been shown that CO oxidation occurs more easily on flat surfaces<sup>251</sup> than stepped surfaces<sup>252</sup>. This is attributed to higher adsorption energies at corner and edges implying that reactants must face an additional energy toward CO oxidation. However this theory does not cover some works and discussions are still ongoing<sup>231,253,254</sup>.

Carbon monoxide oxidation displays a particular behavior as experimental oscillations of CO<sub>2</sub> gas fraction have been recorded for sufficiently dispersed materials. This phenomenon is explained *via* dynamic depleted and rich oxygen zones on the catalyst<sup>255,256</sup> due to adsorption competition between oxygen and carbon monoxide. Therefore spatial oscillations of adspecies are observed onto the catalyst surfaces<sup>257</sup>. Also two regimes have been elucidated during CO oxidation, leading to hysteresis between ignition and extinction temperature<sup>247,258-260</sup>. A low activity regime is recorded

at low temperature while a high regime is observed at high temperature, with efficient CO conversion. The regime differences are not well explained and can be attributed to O/CO coverage ratio or slight temperature release during oxidation<sup>261</sup>. Finally the water gas shift equilibrium that uses CO and water to produce CO<sub>2</sub> and H<sub>2</sub> can be active and thus share a reactant and products with CO oxidation<sup>81,262</sup>. A competition occurs between CO oxidation and water reduction.

This work aimed at bringing new information on CO oxidation sensibility towards highly dispersed platinum catalyst and initial oxidation state of platinum. The multiscale approach developed so far is here used to fundamentally study CO oxidation. Highly dispersed platinum over alumina catalyst is an catalyst surface in that case.

The multi-scale approach used here needs to restrain the study to few parameters. Indeed the work will be focused on the accuracy between kinetic models developed from the *ab initio* Pt<sub>13</sub>/γ-Al<sub>2</sub>O<sub>3</sub> structure and our own experiments that engage a 0.98 platinum dispersion catalyst. The level of detail in kinetic models will be also discussed.

Experimental Temperature Programmed Reaction (TPR) of CO were performed on both pre-oxidized and pre-reduced catalysts using both continuous ramps and plateau. Global kinetic parameters such as CO and O reactions partial orders and activation energies were determined.

Following the previous chapters, *ab initio* co-adsorption of CO and atomic oxygen has been modelled. The Pt<sub>13</sub>O<sub>n</sub>(CO)<sub>m</sub> structures were used as initial states toward CO oxidation. The common indicators, such as adsorption energies, metal support interactions or the establishment of phase diagram used in the previous chapters were also benchmarked.

The study focuses first on the kinetic model development considering the transition states obtained for several structures. Then, thermokinetic datasets are considered in order to characterise the CO<sub>2</sub> adsorption and CO oxidation. Finally, the TPR experiments are simulated and enabled to discuss the global kinetic parameter effect.

## 5.2| Experimental oxidation of CO

To quantify the global kinetics of CO oxidation on highly dispersed platinum supported on alumina, Temperature Programmed Reaction (TPR) of CO were carried out on the 1 wt. % Pt/γ-Al<sub>2</sub>O<sub>3</sub> catalyst investigated in the previous chapters. This experiment was performed with mass spectrometer analysis, used to determine CO conversion rates and *operando* IR solid spectroscopy for adspecies investigations. The TPR was performed starting from both pre-reduced and oxidated catalyst. In addition to the CO light-off, global oxidation data as partial orders and activation energy were determined.

### 5.2.1 | Light-off measurement

Oxidation of CO has been performed using the micro-reactor (section 2.2.2.1) with a 12.1 mg catalytic material and a total gas flow set to  $12 \text{ mL}\cdot\text{min}^{-1}$ . The gas flow was composed of CO (1000ppm),  $\text{O}_2$  (10.0%) and completed with helium. For the oxidated catalyst ( $\text{Pt}/\gamma\text{-Al}_2\text{O}_3\text{-o}$ ), a first step of one hour at  $25^\circ\text{C}$  was set so that the solid was in equilibrium with gas phase. Then a temperature ramp was applied with a 15 minutes plateau to stabilize the output gas flow. The average CO conversion of the plateau was calculated. Finally CO oxidation during temperature ramp decrease was also recorded. In this case CO conversion was determined continuously (Figure 47). A pre-reduced material  $\text{Pt}/\gamma\text{-Al}_2\text{O}_3\text{-r}$  was also tested, with a reduction step set at  $300^\circ\text{C}$  during 5 hours in 5%  $\text{H}_2/\text{He}$  gas flow (1000ppm). For this catalyst, CO conversion was determined per plateau.

The oxidation spreads from  $55^\circ\text{C}$  to  $225^\circ\text{C}$  for the oxidated catalyst. The phenomenon starts  $20^\circ\text{C}$  later for the reduced one. The temperature at 50% CO conversion ( $T_{50\%}$ ) rises at  $150^\circ\text{C}$  for the first one and  $163^\circ\text{C}$  for the second. A shift is visible between the three experiments, with a  $15^\circ\text{C}$  shift at 50% conversion. Salomon and coworkers<sup>244</sup> recorded a  $30^\circ\text{C}$  to  $40^\circ\text{C}$  hysteresis for this conversion rate with a poly-dispersed  $\text{Pt}/\text{Al}_2\text{O}_3$  catalyst and identical gas flow conditions.

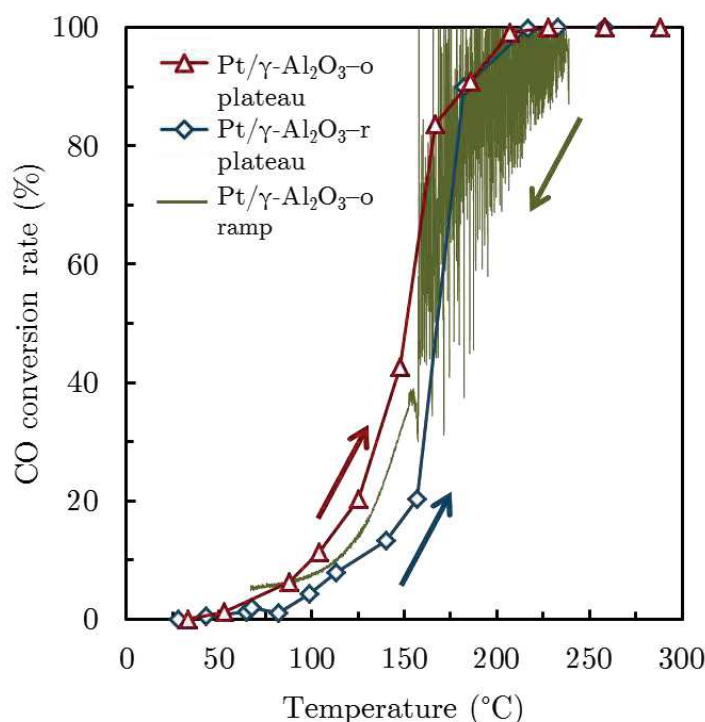


Figure 47: Carbon monoxide Temperature Programmed Desorption on  $\text{Pt}/\gamma\text{-Al}_2\text{O}_3\text{-o}$  and  $\text{Pt}/\gamma\text{-Al}_2\text{O}_3\text{-r}$  (1000ppm CO, 10%  $\text{O}_2$ ).

The carbon dioxide production oscillation phenomenon is observed beyond 40% CO conversion up to total oxidation, with decreasing amplitude. It has been observed many times by Sales<sup>242</sup> and more recently by Grunwaldt *et al.*<sup>263</sup>. They demonstrated that oscillations occur for nanoparticles (1-2 nm) starting at 106°C (20% CO conversion) for 0.63 dispersed Pt/Al<sub>2</sub>O<sub>3</sub><sup>263</sup> (Table 10). Prior carbon monoxide TPR realised on distinct platinum dispersion catalysts demonstrate that this dispersion delays oxidation T<sub>50%</sub> towards higher temperatures.

Table 10: Carbon monoxide oxidation characteristics on Pt/Al<sub>2</sub>O<sub>3</sub> in excess of oxygen compared to carbon monoxide. The CO oxidation temperature range as well as T<sub>50%</sub> is presented. Dispersion were determined using \*hydrogen chemisorption titration.

Material	Gas flow	T <sub>50%</sub> (%)	Temperature range (°C)	Dispersion
1% Pt/Al <sub>2</sub> O <sub>3</sub> -o	1000 ppm CO 10% O <sub>2</sub>	150°C	55 – 225	0.90*
1% Pt/Al <sub>2</sub> O <sub>3</sub> -r		163°C	75 – 220	
2.9% Pt/Al <sub>2</sub> O <sub>3</sub> <sup>108</sup>	1% CO 10% O <sub>2</sub>	137	120 – 180	0.55
3.8% Pt/Al <sub>2</sub> O <sub>3</sub> <sup>263</sup>	1000 ppm CO 10% O <sub>2</sub>	106	50 – 140	0.63*
2.0% Pt/SiO <sub>2</sub> <sup>248</sup>	1% CO 10% O <sub>2</sub>	172	124 – /	0.8*

In order to determine the CO oxidation pathways, *in operando* infrared spectroscopy has been used during CO TPR. The experimental work was mainly performed by Eric Genty at UCCS laboratory (Université de Lille) and it enables finding hydroxylated intermediates<sup>103</sup>. While hydrogen-carbonate species have been uncovered for low CO conversion, thanks to hydroxyl adspecies from the support, two pathways are forecast for high CO conversion. These latters go through formates or carbonates, respectively by OH\* and adsorbed oxygen. These data will be discussed in further section 5.3.3 with related *ab initio* calculations.

### 5.2.2 | Global kinetic parameters

Partial order toward CO and O<sub>2</sub> have been determined in close conditions of TPR experiment on Pt/γ-Al<sub>2</sub>O<sub>3</sub>-o at 120°C (7% CO conversion). Figure 48a summarizes the conditions applied to partial order determination. Carbon monoxide inhibits its own oxidation with a partial order of -0.57, while O<sub>2</sub> concentration has almost no impact with less than 0.02. The inhibitor effect of CO has already been noticed<sup>250,264,265</sup> (Table 11). Concerning oxygen impact on CO oxidation, it is known as a promoter, yet its large excess in the present work demonstrates that in oxidant gas media, and for the

highly dispersed catalyst we are considering here, O<sub>2</sub> does not influence CO oxidation. This latter is indeed in large excess (10%) compared to CO.

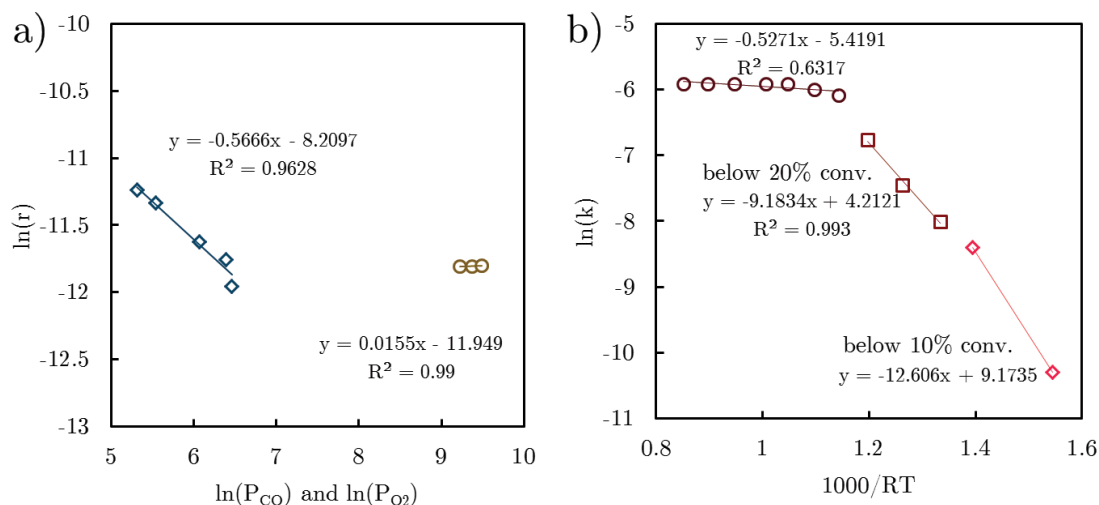


Figure 48: a) O<sub>2</sub> and CO partial order during CO oxidation on pre oxidised catalyst Pt/ $\gamma$ -Al<sub>2</sub>O<sub>3</sub>-o and (1000ppm CO, 10% O<sub>2</sub>), and b) Apparent activation energy determination of CO oxidation on Pt/ $\gamma$ -Al<sub>2</sub>O<sub>3</sub>-o in kcal.mol<sup>-1</sup>, calculated below 10% and 20% CO conversion.

Table 11: Partial order and activation energies previously obtained for CO oxidation.

Material	CO content (ppm)	O <sub>2</sub> content (%)	Temperature (°C) and conversion rate (%)	CO partial order	O <sub>2</sub> partial order
Pt/ $\gamma$ -Al <sub>2</sub> O <sub>3</sub> - o	1000	10%	120°C, 7%	-0.57	0.02
2.0% Pt/Al <sub>2</sub> O <sub>3</sub> <sup>264</sup>	10000	1.0%	120-160°C	-0.53	0.70
1.6% Pt/Al <sub>2</sub> O <sub>3</sub> <sup>250</sup>	10000	3.0%	180°C, 6-14%	-0.50	0.74
Pt/SiO <sub>2</sub> <sup>265</sup>	3000	1.0%	64-180°C	-0.2	0.90

Activation energy has also been determined at low CO conversion on Pt/ $\gamma$ -Al<sub>2</sub>O<sub>3</sub>-o (Figure 48b), determined between 60°C and 230°C. The activation energy lies at 9.2 kcal.mol<sup>-1</sup> below 20% CO conversion and 13 kcal.mol<sup>-1</sup> below 10%, that congruent with previously performed studies, though in the lower range. In similar conditions, Boubnov *et al.*<sup>263</sup> found a 18.2 kcal.mol<sup>-1</sup> activation barrier on a 3.8% Pt/Al<sub>2</sub>O<sub>3</sub> with 0.63 platinum dispersion, and 13.9 kcal.mol<sup>-1</sup> with the a 0.06 dispersed Pt/Al<sub>2</sub>O<sub>3</sub> material. Ertl and Eiswirth<sup>259</sup> found a 8.2 kcal.mol<sup>-1</sup> activation on Pt(110) cristalline surface (Table 13). The data of Gracia *et al.*<sup>248</sup> suggest that on Pt/SiO<sub>2</sub>, activation energy increases with platinum dispersion. Yet data on Pt/Al<sub>2</sub>O<sub>3</sub> are not corroborating this trend.

Table 12: Partial order and activation energies previously obtained for CO oxidation.

Catalyst	Dispersion	Apparent activation energy (kcal.mol <sup>-1</sup> )
1 wt. % Pt/ $\gamma$ -Al <sub>2</sub> O <sub>3</sub> -o	0.90	9.2 (below 20% conversion) 13 (below 10% conversion)
3.8% Pt/Al <sub>2</sub> O <sub>3</sub> <sup>263</sup>	0.63	18.2
	0.06	13.9
Pt(110)	-	8.2
2.0% Pt/SiO <sub>2</sub> <sup>248</sup>	0.29	13.1
	0.63	17.2
	0.76	22.0

Experimental TPR of CO was performed on both pre-reduced and pre-oxidised 1% wt. Pt/ $\gamma$ -Al<sub>2</sub>O<sub>3</sub> catalyst. A shift is observed on the light-off curves that may be an influence of the initial catalyst oxidation state. Indeed CO conversion for the reduced catalyst happens slightly at higher temperature than the pre-oxidised one. This may be due to a lack of adsorbed oxygen at the beginning of the pre-reduced catalyst TPD. The carbon dioxide production oscillations have been recorded for every experimental TPD, indicating that the material undergoes spatial surface heterogeneities through O/CO coverage discrepancies, that allows conversion fluctuations. Oxidation temperature is corroborated by close works. Also oscillations are recorded for high conversion rates and small hysteresis cycle is noticed. Concerning reactant partial orders, O<sub>2</sub> is present in a too large excess to determine the well-known promoting effect. However CO negative partial order is correctly forecast<sup>250,264</sup>.

### 5.3| Molecular modelling of CO oxidation

In order to investigate numerically the CO oxidation, a non-exhaustive set of co-adsorbed Pt<sub>13</sub>O<sub>n</sub>(CO)<sub>m</sub> structures were calculated *ab initio*, as a bridge between extreme Pt<sub>13</sub>O<sub>n</sub> and Pt<sub>13</sub>(CO)<sub>m</sub> structures. Atomic oxygen, CO and CO<sub>2</sub> adsorption energies were determined and compared with existing data. The search for CO oxidation transition states has been performed. Also, according to experimental infrared data<sup>103</sup>, some Pt<sub>13</sub>O<sub>n</sub>(CO)<sub>m</sub>H<sub>2</sub>O structures were calculated to evaluate energetics of these pathways.

### 5.3.1 | Co-adsorption of O and CO on Pt<sub>13</sub>/γ-Al<sub>2</sub>O<sub>3</sub>

To handle CO oxidation on the Pt<sub>13</sub>/γ-Al<sub>2</sub>O<sub>3</sub> model, co-adsorption is the first step to deal with. According to the most stable Pt<sub>13</sub>O<sub>n</sub> and Pt<sub>13</sub>(CO)<sub>m</sub> structures found *via* the thermodynamic diagrams<sup>xv</sup> (respectively in sections 3.3.2 and 4.2.2), initial guesses were investigated (*i.e.* Pt<sub>13</sub>O<sub>10</sub>(CO)<sub>9</sub>, Pt<sub>13</sub>O<sub>10</sub>(CO)<sub>15</sub> and Pt<sub>13</sub>O<sub>16</sub>(CO)<sub>9</sub>). Also as oxygen is predominant in oxidant media, two additional guess structures with one CO were investigated (Pt<sub>13</sub>O<sub>4</sub>(CO) and Pt<sub>13</sub>O<sub>22</sub>(CO)). Although the latter ones were effectively the final states, the three others underwent spontaneous CO desorption and CO<sub>2</sub> formation during geometry optimisation. This suggests that an overall coverage of 24 and more adspecies is hard to reach. The maximum coverages obtained are 23 for 0 K optimisations.

These calculations lead, without using molecular dynamics (not performed in the present section for the sake of time), to the systems displayed in Figure 49. The configurations found for the cluster reveal huge differences except for Pt<sub>13</sub>O<sub>4</sub>(CO) and Pt<sub>13</sub>O<sub>22</sub>(CO) that are close to their related Pt<sub>13</sub>O<sub>n</sub> systems. For Pt<sub>13</sub>O<sub>16</sub>(CO)<sub>7</sub> the cluster is still quite compact and keeps a hemispheric shape. This is not the case for Pt<sub>13</sub>O<sub>10</sub>(CO)<sub>9</sub> and Pt<sub>13</sub>O<sub>8</sub>(CO)<sub>11</sub> that spread over the alumina surface.

To probe adsorption energies of atomic oxygen and CO adsorption energies, respectively one O and one CO have been removed from the structure, then submitted to a new geometry optimisation. These ones correspond to the potential atoms engaged in transition state search, as seen afterwards. These structures are displayed in Figure 105 and Figure 106 in appendices.

---

<sup>xv</sup> The considered structures in phase diagrams lie beyond 0°C, on the full range of calculated O<sub>2</sub>/CO partial pressures.

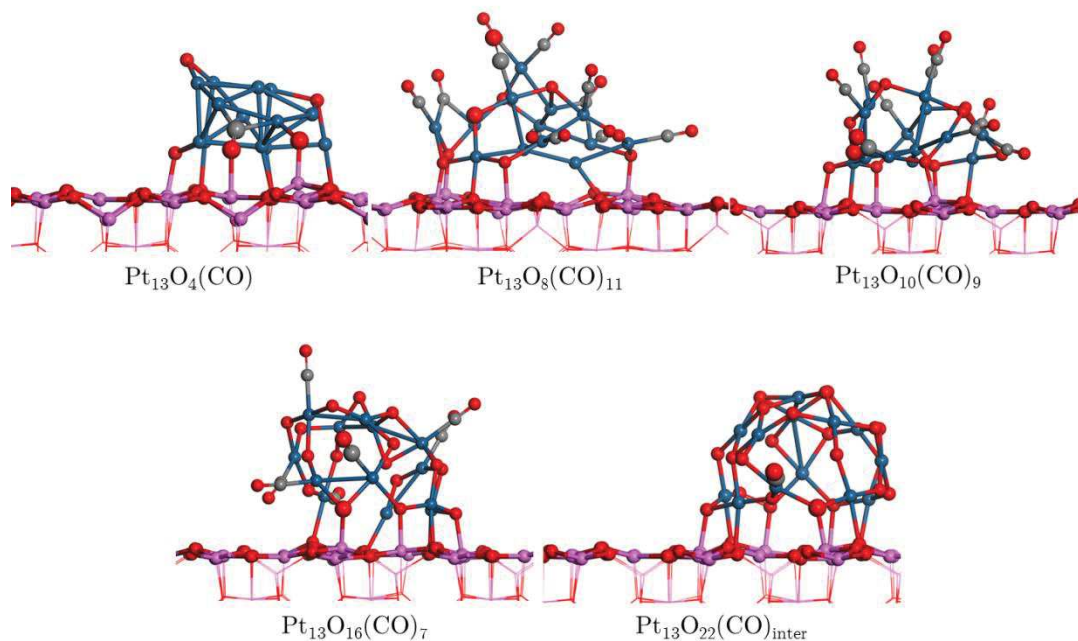


Figure 49: Illustrations of co-adsorbed  $\text{Pt}_{13}\text{O}_n(\text{CO})_m$  structures, with potential atomic oxygen and adsorbed CO as bigger atoms.

Prior graphs were turned into 3D plots ( $E_{\text{adsorption}} = f(\theta_{\text{O}}, \theta_{\text{CO}})$ ) to emphasize multiple coverage impact. The thin plate spline<sup>xvi</sup> interpolation method was used *via* the Matlab software. Figure 50 records adsorption energy of O in such format. The adsorption of one CO leads to less stable adsorption sites for oxygen. This is significant for  $\text{Pt}_{13}\text{O}_4(\text{CO})$ . For intermediate coverages at the center of the graphics a weakening of at least  $20 \text{ kcal.mol}^{-1}$  is observed. Yet for highly covered CO structures, the trend is not clear as the cluster is disaggregating due to CO molecules.

---

<sup>xvi</sup> Thin plate spline is a spline-based method to interpolate and extrapolate data. Splines are functions defined piecewise by polynomials. The particularity of thin plate splines are the inter- and extrapolation smoothing.

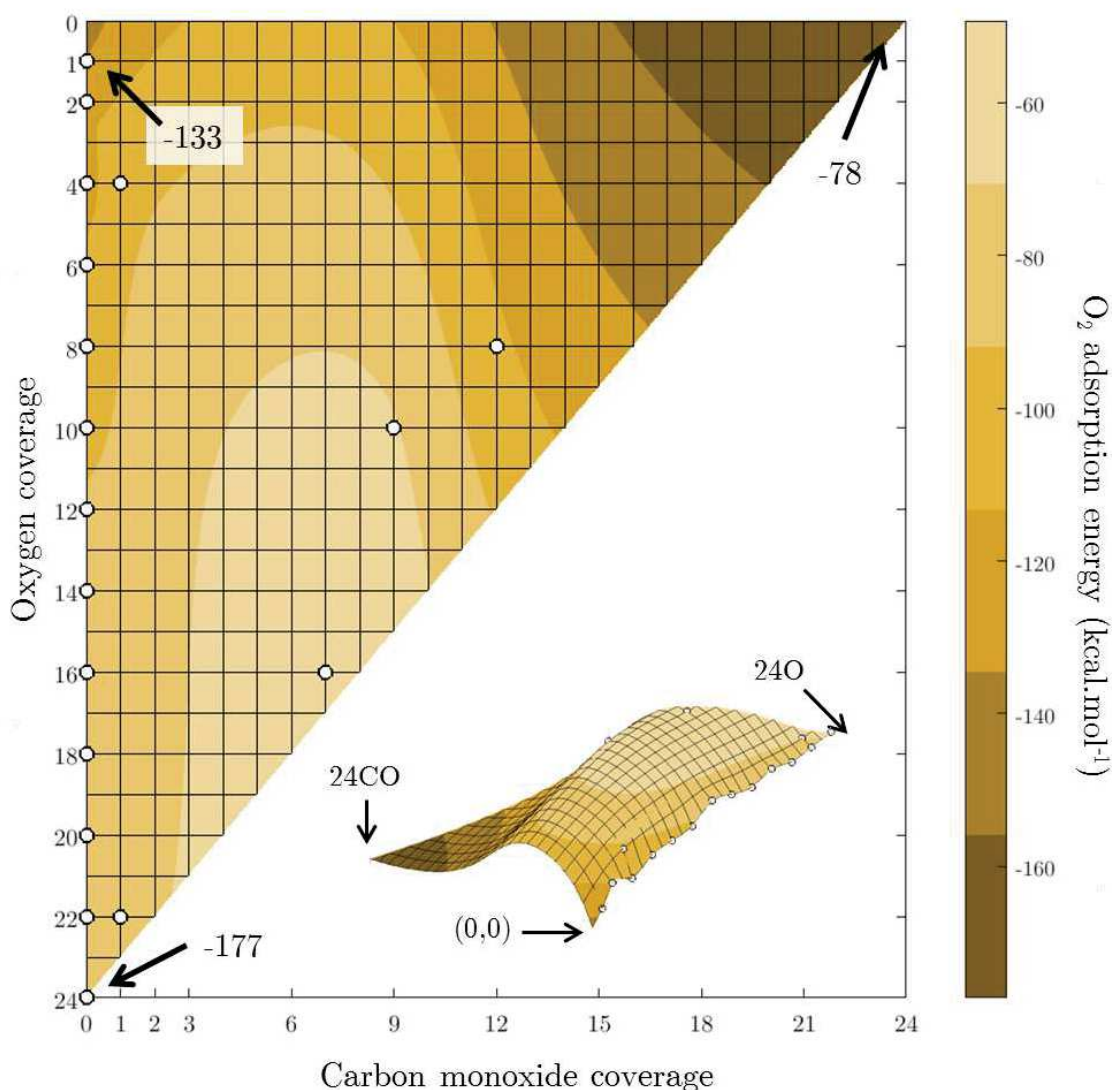


Figure 50: Atomic oxygen adsorption electronic energy per  $\text{O}_2$  according to CO and oxygen coverage. The  $\text{Pt}_{13}\text{O}_n$  data derive from Figure 24 in Chapter 3. Other energies are calculated according to  $\text{Pt}_{13}\text{O}_n(\text{CO})_m$  and the related  $\text{Pt}_{13}(\text{CO})_m$  structure, following equation (42). Interpolation is a thin-plate spline made by Matlab.

In the same way, Figure 51 draws the CO adsorption energies with  $\text{Pt}_{13}\text{O}_n(\text{CO})_m$  data. Considering  $\text{Pt}_{13}\text{O}_4(\text{CO})$  and  $\text{Pt}_{13}\text{O}_{22}(\text{CO})$  that represent the simplest cases, huge differences exist for the adsorption of one carbon monoxide. It seems that the latter is optimal when the cluster is clean. Co-adsorption has a dramatical effect even with few oxygen atoms, however a plateau is reached, which does not depends on the morphology of the oxidized cluster. With four or twenty oxygen on the cluster, no significant difference appears. In particular the adsorption mode that engages the surface for  $\text{Pt}_{13}\text{O}_4(\text{CO})$ . This plateau is extended for light CO coverage by the value of  $\text{Pt}_{13}\text{O}_{16}(\text{CO})_7$ . Concerning  $\text{Pt}_{13}\text{O}_8(\text{CO})_{11}$  and  $\text{Pt}_{13}\text{O}_{10}(\text{CO})_9$ , these two structures exhibit

similar energy, but these data are significantly different from the  $\text{Pt}_{13}(\text{CO})_m$  curve and the plateau.

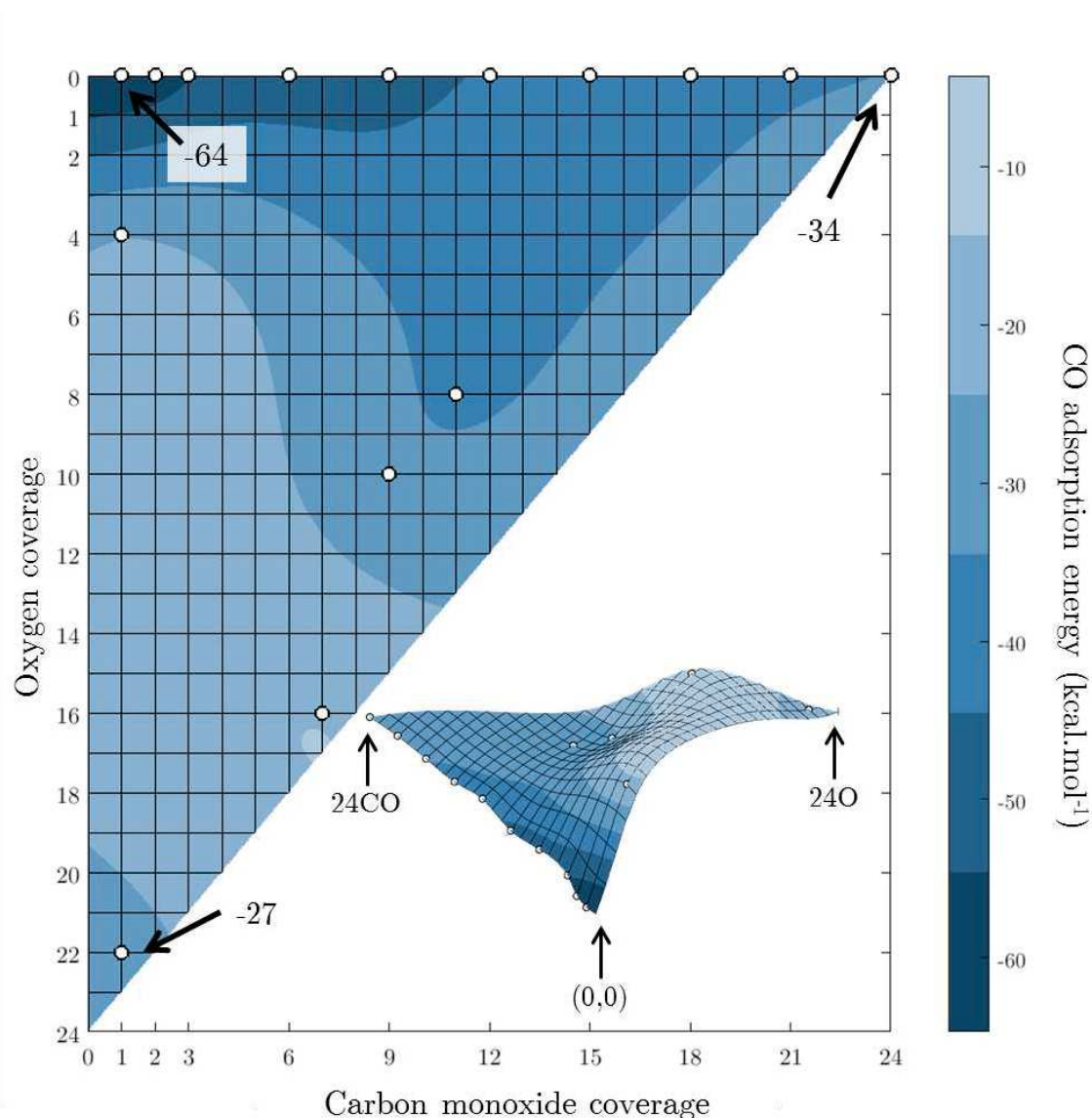


Figure 51: Carbon monoxide adsorption electronic energy according to CO and oxygen coverage. The  $\text{Pt}_{13}(\text{CO})_m$  data derive from Figure 35b in Chapter 4. Other energies are calculated according to  $\text{Pt}_{13}\text{O}_n(\text{CO})_m$  and the related  $\text{Pt}_{13}\text{O}_n$  structure, following equation (42). The interpolation between data points is thin-plate spline.

The metal-support interaction is also impacted by co-adsorption (Figure 52). Our previous work has demonstrated that it strengthens with increasing oxygen coverage while slightly weakening with carbon monoxide coverage (Figure 35a). Starting from  $\text{Pt}_{13}\text{O}_n$  data, adding CO to the system weakens the metal-support interaction whatever the oxygen coverage, up to a ridge reached between  $\text{Pt}_{13}\text{O}_n(\text{CO})_6$  and  $\text{Pt}_{13}\text{O}_n(\text{CO})_9$ . With more carbon monoxide, the interaction seems to strengthen again. Although lack of molecular dynamics does not allow to display the most stable structure. Metal-

support interaction for  $\text{Pt}_{13}\text{O}_n$  demonstrates that discrepancies appear even with well optimized structures. Therefore metal-support interaction is not so dependent on cluster shape, but more on adsorbed species.

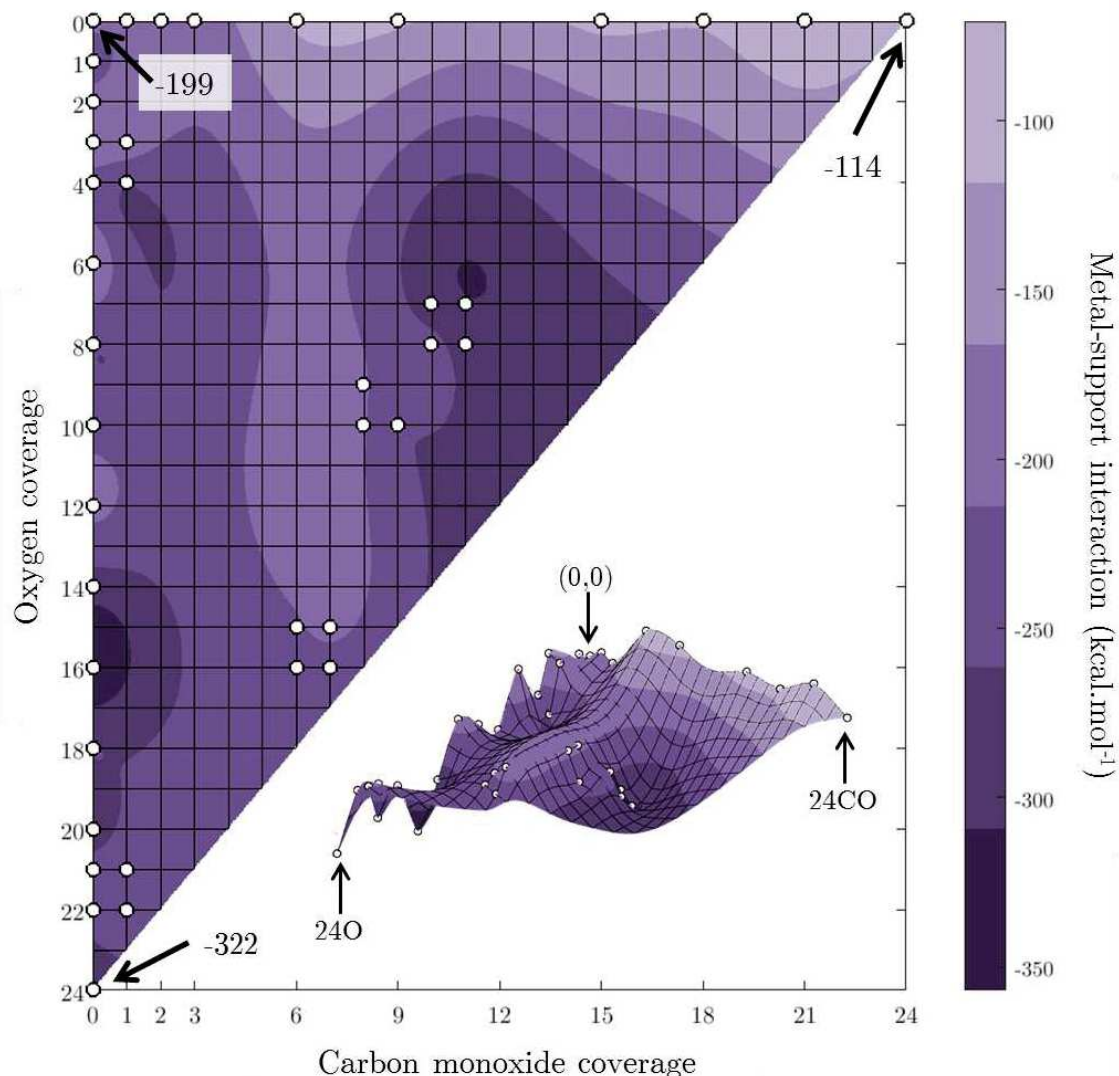


Figure 52: Metal support interaction according to CO and oxygen coverage. The  $\text{Pt}_{13}(\text{CO})_m$  data derive from Figure 27a in Chapter 3 and Figure 35a in Chapter 4 for  $\text{Pt}_{13}\text{O}_n$  ones. Co-adsorbed structure interactions are calculated according to equation (44). The interpolation between data points is thin-plate spline.

Also a non-exhaustive  $(p_{\text{O}_2}, p_{\text{CO}}, T)$  thermodynamic diagram has been built to evaluate the stability domain of co-adsorbed species but also the competition between fully oxygenated and CO-adsorbed clusters. Figure 53 illustrates the diagram with a fixed CO partial pressure of 0.1 bars. One can realize that the identical  $\text{Pt}_{13}\text{O}_n$  structures are found in yellow at the right bottom corner corresponding to the highest temperature and  $\text{O}_2$  partial pressure.

At the opposite,  $\text{Pt}_{13}(\text{CO})_m$  structures appear at low  $\text{O}_2$  partial pressure, with typical temperature range found in chapter 4. The co-adsorbed structures are represented by  $\text{Pt}_{13}\text{O}_{22}(\text{CO})$  and  $\text{Pt}_{13}\text{O}_{11}(\text{CO})_8$ . The latter occupies a small domain between  $\text{Pt}_{13}\text{O}_n$  and  $\text{Pt}_{13}(\text{CO})_n$  which is congruent with co-adsorption phenomenon. On the contrary,  $\text{Pt}_{13}\text{O}_{22}(\text{CO})$  domain supersedes mainly the  $\text{Pt}_{13}\text{O}_n$  ones, with a major border with oxygenated cluster only. This is explained by the large stability conferred to  $\text{Pt}_{13}\text{O}_{22}$  structure on which the CO has been added, whereas  $\text{Pt}_{13}\text{O}_{11}(\text{CO})_8$  has not endured molecular dynamics. One can conclude that this diagram is not fully representative of co-adsorption domains for this reason. Yet it can be assumed that every  $\text{Pt}_{13}\text{O}_n(\text{CO})$  would replace almost every  $\text{Pt}_{13}\text{O}_n$  structures in this diagram. For larger number of CO-adsorbed  $\text{Pt}_{13}\text{O}_n(\text{CO})_m$  domains are difficult to predict. However, it can be assume that  $\text{Pt}_{13}\text{O}(\text{CO})_m$  domains would mostly be present at mild temperature and  $\text{O}_2$  partial pressure.

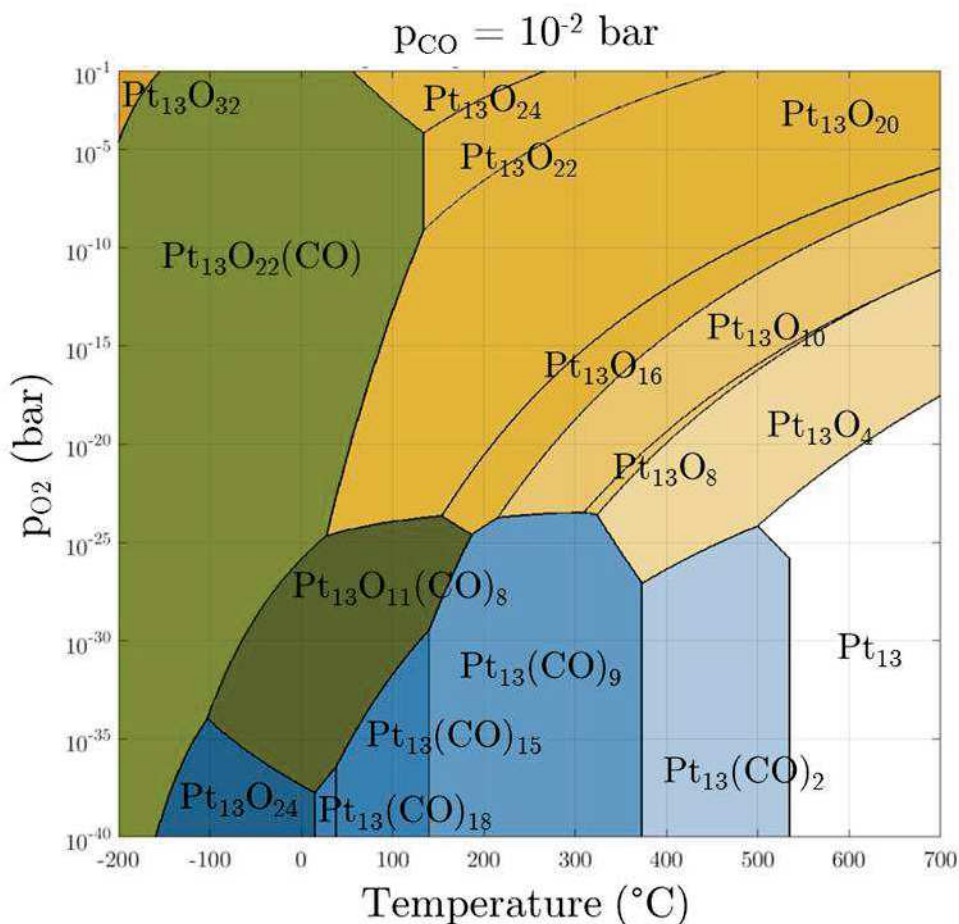


Figure 53: Thermodynamic diagram ( $p_{\text{O}_2}, p_{\text{CO}}, T$ ) with a fixed CO partial pressure of 0.1 bars.

Although Figure 53 is representative to common  $\text{O}_2/\text{CO}$  oxidation conditions, Figure 107 in appendices displays this diagram for other CO partial pressures. One can see

that even at  $p_{\text{CO}}=10^{-20}$  bar, the  $\text{Pt}_{13}\text{O}_{22}(\text{CO})$  already occupies the diagram that is likely related to  $\text{Pt}_{13}\text{O}_n$ . The  $\text{Pt}_{13}(\text{CO})_m$  structures appear at low  $\text{O}_2$  partial pressure close to  $p_{\text{CO}}=10^{-10}$  bar as well as  $\text{Pt}_{13}\text{O}_{11}(\text{CO})_8$ . These domains will continuously substitute the prior  $\text{Pt}_{13}\text{O}_n$  structures with increasing CO partial pressure.

We finally considered the Bader charges (section 2.3.2.4.) with respect to O and CO coverages, in Figure 111a-e (Appendices). The cleanest clusters  $\text{Pt}_{13}\text{O}_2$  and  $\text{Pt}_{13}(\text{CO})$  appear as the minimum charge point, whatever the element. Considering the carbon charge (Figure 111a), except for low coverages a plateau below one electron is clearly observed with almost no impact of coverage. In the case of CO oxygen in Figure 111d, almost every structures exhibits a plateau at a bit more than one electron depleted. The charge for the whole CO molecule (Figure 111c) is almost -0.1 electron. Thus few donation appear between CO and platinum. Yet a slight impact of oxygen coverage is noticed as  $\text{Pt}_{13}\text{O}_{22}(\text{CO})_m$  structures show a +0.1 electron charge.

Considering the atomic oxygen charge (Figure 111b), a slight decrease is observed with increasing CO coverage. Platinum charge (Figure 111e) is the most variable one from -0.1 to +1.1 electron. This variation clearly depends mainly on oxygen coverage. A trend is noticeable according to CO coverage, but with lower amplitude: the Bader charge between  $\text{Pt}_{13}\text{O}_n(\text{CO})_m$  structures and their  $\text{Pt}_{13}\text{O}_n$  relatives does not show significant variation.

In conclusion, the electronic behaviour of the platinum cluster is mainly affected by oxygen coverage. The impact of carbon monoxide is limited to the presence or not of the molecule on the surface. Indeed discrepancies appears only between almost clean surface and the rest. Also few crossed influences are recorded: adsorption of CO does not dramatically change the Bader charge of adsorbed oxygen and *vice versa*.

### 5.3.2 | Carbon monoxide oxidation on $\text{Pt}_{13}/\gamma\text{-Al}_2\text{O}_3$

Based on the previous calculations performed, this section focuses on CO oxidation leading to  $\text{CO}_2$ . The formation mechanism of a unique carbon dioxide on the particle thanks to atomic oxygen and adsorbed CO is performed. This  $\text{CO}_2$  was searched from initial guesses built from  $\text{Pt}_{13}\text{O}_n(\text{CO})_m$  structures, so that two structures constitute a pair of initial and final states of CO oxidation. Note that the work of Vajda *et al.*<sup>208</sup> on  $\text{Pt}_{10}\text{O}_2(\text{CO})_7/\alpha\text{-Al}_2\text{O}_3$  cluster demonstrates that oxidation *via* non-dissociated  $\text{O}_2$  is preferred, with the formation of the intermediate  $\text{OOCO}$  adsorbed specie and carbonate as possible a dead-end reaction. As all our starting state exhibit dissociated  $\text{O}_2$  only, we did not investigate this possibility.

The structures with adsorbed  $\text{CO}_2$  are gathered in Figure 109 (appendices). Among the five tested structures,  $\text{Pt}_{13}\text{O}_{21}(\text{CO}_2)$ ,  $\text{Pt}_{13}\text{O}_3(\text{CO}_2)$  and  $\text{Pt}_{13}\text{O}_9(\text{CO})_8(\text{CO}_2)$  display a carbon dioxide close to the surface. The latter is bonded in different manners but exhibits Al-O bonds for all three. For  $\text{Pt}_{13}\text{O}_{15}(\text{CO})_6(\text{CO}_2)$  and  $\text{Pt}_{13}\text{O}_{10}(\text{CO})_7(\text{CO}_2)$ ,

carbon dioxide lies far from the surface and the typical adsorption mode is found – top Pt-C and top Pt-O, agreeing with literature<sup>230,266</sup>. Table 13 gathers the electronic adsorption energies of the five probed structures as well as data of the literature. One can observe that every electronic adsorption energy is unfavoured toward adsorption and therefore promote desorption. The work of Vajda *et al.*<sup>208</sup> on both non supported and alumina supported Pt<sub>10</sub> clusters provides a 37 kcal.mol<sup>-1</sup> adsorption energy at low coverage, *i.e.* with one CO and O<sub>2</sub> molecule onto platinum. This value is far from our low coverage calculated structure Pt<sub>13</sub>O<sub>3</sub>(CO<sub>2</sub>). Yet large discrepancies appear regarding CO<sub>2</sub> adsorption mode. Concerning the Pt<sub>13</sub> cluster, adsorption of CO<sub>2</sub> is made by a Pt-C bond and two O-Al ones. This peculiar bonds that engage alumina as an adsorption site is a propable stabilisator of the CO<sub>2</sub> adsorption. Regarding the work of Vajda *et al.*<sup>208</sup>, CO<sub>2</sub> is not properly adsorbed on the surface but in a O=O-C-O complex form that is not observed in our calculations. This complex is also found by Allian *et al.* on Pt<sub>201</sub> non supported cluster. Again this conformation gives a large value of CO<sub>2</sub> desorption. Yet Dupont, Jugnet and Loffreda<sup>230</sup> found a 9.2 kcal.mol<sup>-1</sup> with a typical adsorption site with one oxygen and carbon atoms adsorbed onto platinum.

Table 13: Carbon dioxide adsorption characteristics on Pt<sub>13</sub>O<sub>n</sub>(CO)<sub>m</sub> structures. Electronic adsorption energy and adsorption modes are gathered.

Structure	Electronic adsorption energy (kcal.mol <sup>-1</sup> )	Adsorption mode	Bond lengths (Å)
Pt <sub>13</sub> O <sub>3</sub> (CO <sub>2</sub> )	-29	C bonded to Pt 2 O bonded to Al	Pt-C: 1.98 Al-O: 1.92 Al-O: 2.08
Pt <sub>13</sub> O <sub>21</sub> (CO <sub>2</sub> )	11	C bonded to Pt O bonded to (Al,Pt)	Pt-C: 1.99 Al-O: 2.08 Pt-O: 2.11
Pt <sub>13</sub> O <sub>7</sub> (CO) <sub>10</sub> (CO <sub>2</sub> )	33	C bonded to Pt O bonded to Pt	Pt-C: 1.92 Pt-O: 2.03
Pt <sub>13</sub> O <sub>9</sub> (CO) <sub>8</sub> (CO <sub>2</sub> )	22	C bonded to Pt O bonded to Pt	Pt-C: 2.07 Pt-O: 2.14
Pt <sub>13</sub> O <sub>15</sub> (CO) <sub>6</sub> (CO <sub>2</sub> )	18	C bonded to Pt O bonded to Pt	Pt-C: 2.07 Pt-O: 2.06
Pt <sub>10</sub> O(CO)/α-Al <sub>2</sub> O <sub>3</sub> <sup>208</sup>	37	O=O-C-O complex	-
Pt <sub>201</sub> <sup>162</sup>	57	O=O-C-O complex	-
Pt(111) <sup>230</sup>	9.2	C bonded to Pt O bonded to Pt	Pt-C: 2.10 Pt-O: 2.12
Pt <sub>10</sub> <sup>208</sup>	37	O=O-C-O complex	-

Carbon dioxide adsorption energy has been evaluated as a function of CO and O coverage (Figure 54). Despite the low number of probed structures, a plane trend according mainly to CO coverage appears. It seems that CO<sub>2</sub> adsorption is favorable

only for the  $\text{Pt}_{13}\text{O}_4(\text{CO}_2)$  ( $-29 \text{ kcal.mol}^{-1}$ ) structures as the other data are positive. Loffreda and coworkers<sup>230</sup> report on Pt(111) and bimetallic Pt-Sn crystals positive values from 8.3 to 11  $\text{kcal.mol}^{-1}$ .

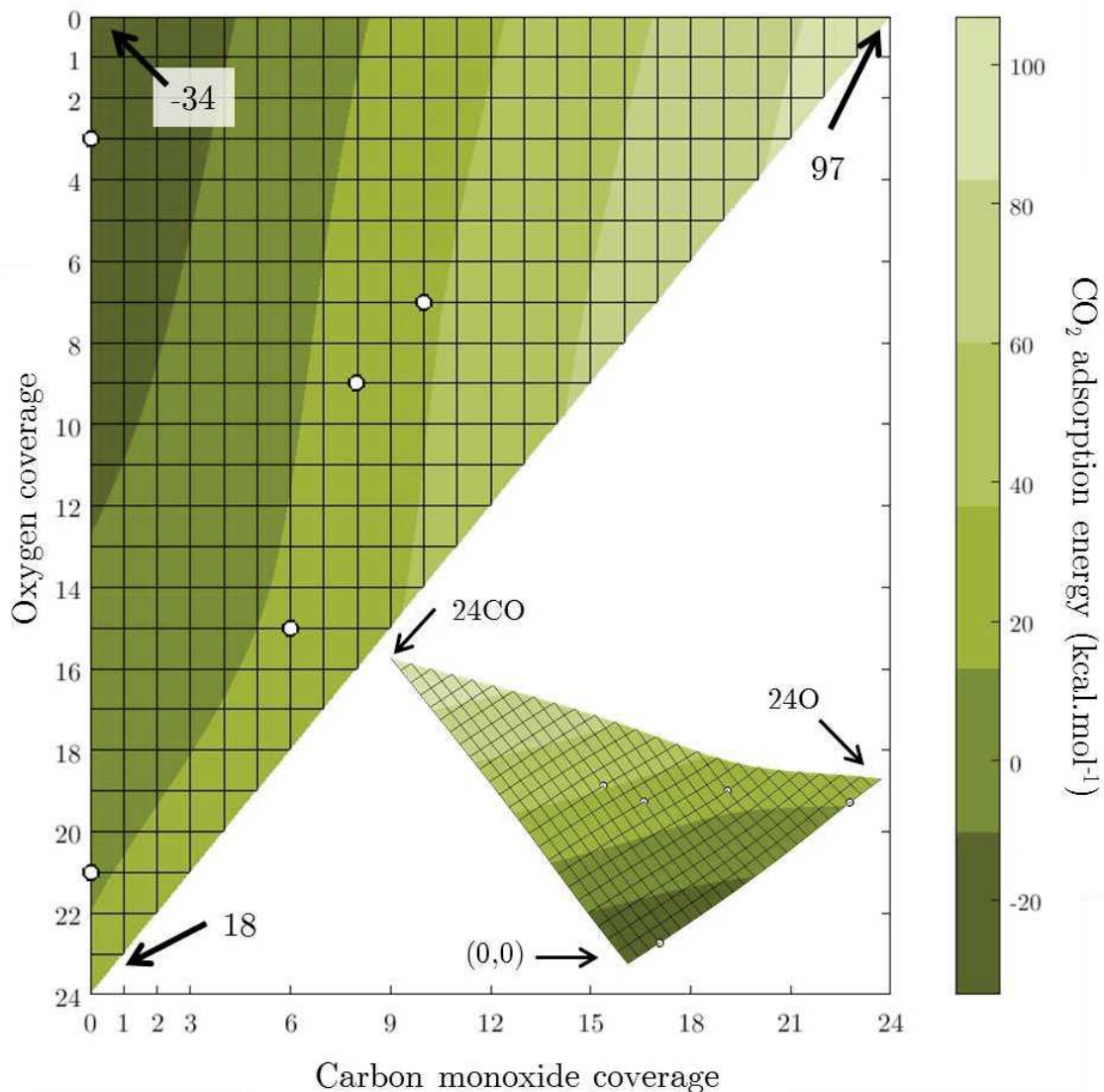


Figure 54: Carbon dioxide adsorption electronic energy according to CO and oxygen coverage. The adsorption energies were calculated according to equation (41). The interpolation between data points is thin-plate spline.

Transition states relative to CO oxidation have been searched for all five configurations. Only two transition structures were found, Table 14 displays  $\text{Pt}_{13}\text{O}_{16}(\text{CO})_7^\ddagger$  and quasi-TS  $\text{Pt}_{13}\text{O}_4(\text{CO})^\ddagger$  characteristics. For other investigated stoichiometries, optimisations after transition structure search failed. This was mainly observed by too many imaginary frequencies. The electronic activation energies for both systems are extremely similar, and very close to  $\text{Pt}_{10}\text{O}(\text{CO})/\alpha\text{-Al}_2\text{O}_3$ <sup>208</sup>.

Table 14: Data on the transition states found for CO oxidation. Electronic oxidation energy and structural information are displayed

Structure	Forward/backward electronic oxidation energy (kcal.mol <sup>-1</sup> )	O...C=O distance	Imaginary frequency	Vibration mode
Pt <sub>13</sub> O <sub>4</sub> (CO) <sup>‡</sup>	11.8/34.9	2.026 Å	44 cm <sup>-1</sup>	Pt <sub>13</sub> deformation
			320 cm <sup>-1</sup>	O...C=O elongation
Pt <sub>13</sub> O <sub>16</sub> (CO) <sub>7</sub> <sup>‡</sup>	12.0/36.7	1.898 Å	232 cm <sup>-1</sup>	O...C=O elongation
Pt <sub>10</sub> O(CO)/α-Al <sub>2</sub> O <sub>3</sub> <sup>208</sup>	14			
Pt(111) <sup>230</sup>	18.9/22.8	1.98 Å	302 cm <sup>-1</sup>	O...C=O elongation
Pt <sub>10</sub> <sup>208</sup>	14		-	
Pt <sub>55</sub> <sup>266</sup>	28.0 to 35.1	1.9 to 2.1 Å		-
Pt <sub>147</sub> <sup>266</sup>	7.83 to 43.4			-
Pt <sub>1</sub> /FeO <sub>x</sub> <sup>267</sup>	18.2/22.8	1.26 Å		-

The Pt(111) surface<sup>230</sup> oxidation energy is slightly higher than small clusters<sup>208,267</sup> supported or not. The work of Dobrin<sup>266</sup> demonstrates that CO oxidation activation barrier can be wide due to O/CO coverage, up to four times the value reported in the present work. In fact small clusters with tens of atoms display the lowest electronic oxidation of CO. The single atom catalyst Pt<sub>1</sub>/FeO<sub>x</sub><sup>267</sup> leads even to a higher energy, although the support is different.

The saddle point corresponds to a 1.9 to 2.0 Å distance between atomic oxygen and carbon from CO. That is the typical distance of every surface. Yet a spurious imaginary frequency remains for Pt<sub>13</sub>O<sub>4</sub>(CO)<sup>‡</sup> that corresponds to cluster deformation.

### 5.3.3 | Impact of adsorbed water

To complete the study and investigate the water influence on CO oxidation, preliminary calculations with alumina hydroxyls were undertaken. Indeed the presence of hydrogen-carbonates and formates according to solid IR spectroscopy might play a role in oxidation<sup>103</sup>.

Adsorption of dissociated water has been intended at first, close and far from the cluster (in Appendices Figure 112a, and Figure 114(a,b) Figure 115(a,b)). Adsorption

energies in Table 15 are different, depending on their distance to the cluster. Indeed adsorbed water far from Pt<sub>13</sub> is dissociative with -22 kcal.mol<sup>-1</sup> average adsorption energy. When close to the cluster, energy drops down (in absolute value) to around -16.2 kcal.mol<sup>-1</sup> and H<sub>2</sub>O is mainly in its molecular form<sup>xvii</sup>. One can see that dissociated water adsorbed far from the cluster has an adsorption energy identical to alumina alone<sup>268</sup>, while close adsorbed water seems less stable due to platinum aggregate.

Table 15: Adsorption energies of water on alumina on initial and final structures. The symbol \* indicates dissociated water into H\* and HO\*. Illustrations of the structures are visible in Figure 112(b,c), Figure 114(a,b) and Figure 115(a,b) in appendices.

Structure	Adsorption energy of water (kcal.mol <sup>-1</sup> ) and their site	
	H <sub>2</sub> O on Al <sub>2</sub> O <sub>3</sub> (close)	H <sub>2</sub> O on Al <sub>2</sub> O <sub>3</sub> (far)
Pt <sub>13</sub> O <sub>16</sub> (CO) <sub>7</sub>	-17.6 (Al <sub>IV</sub> -μ <sub>1</sub> )	-21.1* (Al <sub>I</sub> -μ <sub>1</sub> )
Pt <sub>13</sub> O <sub>15</sub> (CO) <sub>6</sub> (CO <sub>2</sub> )	-16.2 (Al <sub>IV</sub> -μ <sub>1</sub> )	-20.7* (Al <sub>I</sub> -μ <sub>1</sub> )
Pt <sub>13</sub> O <sub>22</sub> (CO)	-14.8* (Al <sub>I</sub> -μ <sub>1</sub> )	-24.3* (Al <sub>I</sub> -μ <sub>1</sub> )
Dissociative adsorption on (100) Al <sub>2</sub> O <sub>3</sub> <sup>268</sup>	25.3* (Al <sub>I</sub> -μ <sub>1</sub> )	

Adsorption of water has also been intended on the cluster, Figure 114c illustrates water adsorption only on the cluster while Figure 114d is relative to one OH\* on the cluster and one H\* on alumina. Their adsorption energy are significantly different, respectively of -32.4 and 24.1 kcal.mol<sup>-1</sup>. In addition, the cluster suffers large distortion due to OH\* adsorption and consequently these data are complex to apprehend.

In order to investigate CO oxidation in presence of water, *ab initio* calculations of probable intermediate structures have been performed. Calculations were undertaken starting from the structures presented in Table 15 with H<sub>2</sub>O adsorbed on Al<sub>2</sub>O<sub>3</sub> close to the platinum cluster. These structures are illustrated in appendices. Intermediates such as formates (Figure 112a and Figure 114e), carbonates (Figure 114f) and hydrogen-carbonates (Figure 115c) have been found.

Two possible reaction paths have been deduced from experiments and *ab initio* energetics. The first path (Figure 55a) starts with the direct adsorption of OH\* onto CO\* to form a carboxylate, from which an hydrogen-carbonate is formed. Finally the dehydroxylation of the molecule to alumina adsorbed OH\* leads to CO<sub>2</sub>. The second one on Figure 55b goes through the formation of a formate on the cluster by breaking the O-H bond and creating a bond with adsorbed CO. The hydrogen recovery by one

---

<sup>xvii</sup> The initial guesses all start with dissociated water: OH\* and H\*.

atomic oxygen on the cluster allows the formation of  $\text{CO}_2$ , with  $\text{OH}^*$  migration to the surface.

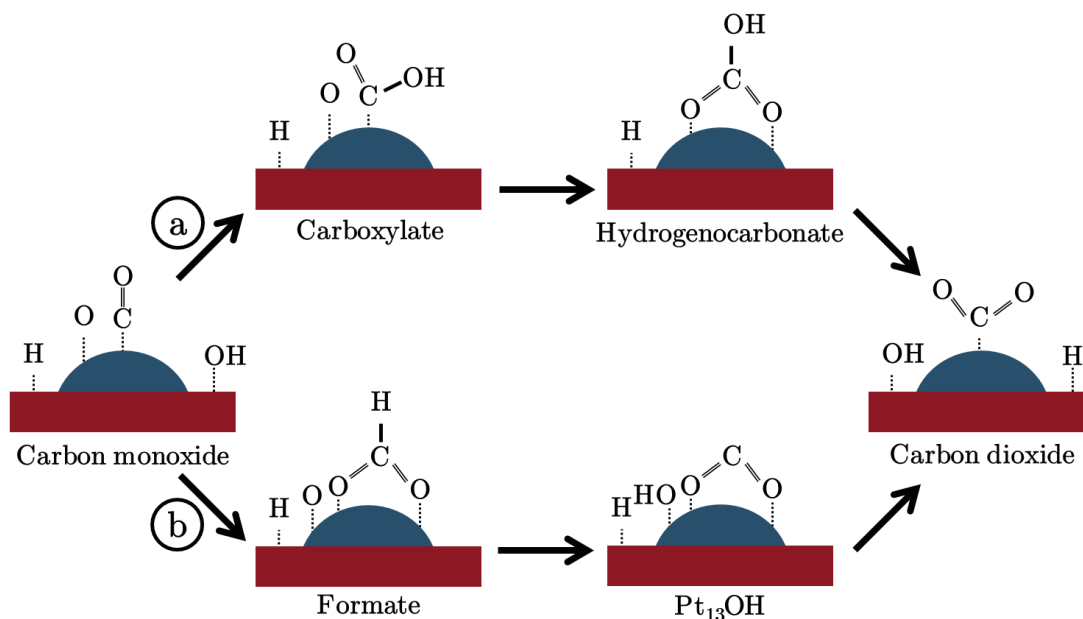


Figure 55: Scheme of the two possible hydroxyl assisted pathways according to *ab initio* calculated structures. The first pathway (a) pass through carboxylate adspecies thanks to OH migration from the alumina to the cluster. The second one leads to formate by the mean of hydroxyl O-H bond break. The adsorption modes displayed here are not representative.

Electronic energies of the previous systems are illustrated Figure 56, with an offset with respect to initial states. The  $\text{Pt}_{13}\text{O}_{16}(\text{CO})_7$  and  $\text{Pt}_{13}\text{O}_{22}(\text{CO})$  have been used to simulate these intermediates. For the first system, one can see that carboxylate structure as  $15 \text{ kcal.mol}^{-1}$  higher energy than the initial step. This mean an energetic barrier to get over. Note the latter is an underestimation of the true barrier, as the transition structures were not determined. However the few configurations gathered on  $\text{Pt}_{13}\text{O}_{22}(\text{CO})$  system give a barrierless pathway (from the point of view of reaction intermediates) straight from initial to final states. Conversely this structure has a high electronic barrier ( $25 \text{ kcal.mol}^{-1}$ ) while  $\text{Pt}_{13}\text{O}_{16}(\text{CO})_7$  structure is energetically favourable towards formate pathway. Therefore the formation of these species is possible from O/CO/OH adsorbed systems. As a future work, the use of NEB method would allow to determine activation barrier.

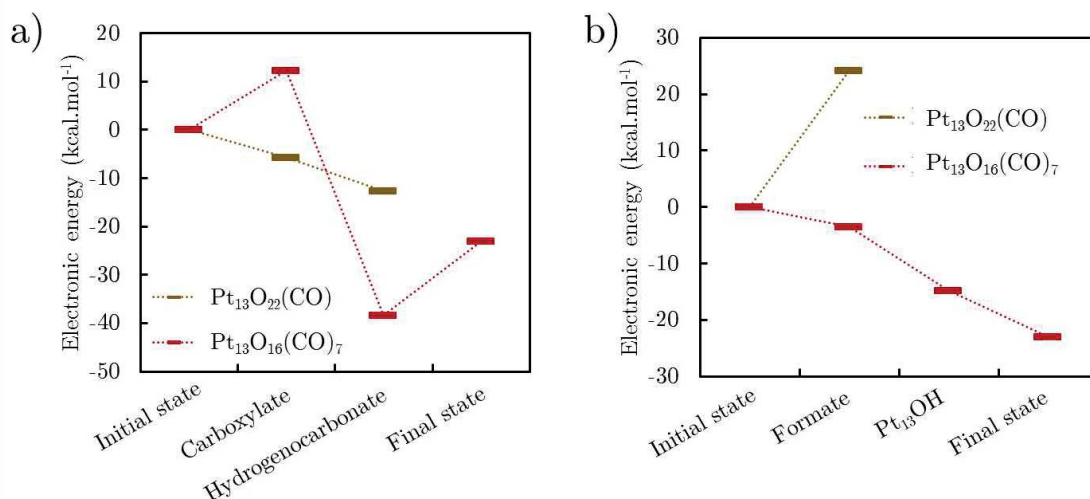


Figure 56: Electronic energies of initial, final and intermediate systems corresponding to a) the formate path (Figure 55) and b) the carboxylate path. Energy of the initial state is set to zero.

To conclude on *ab initio* modelling, the few structures probed suggest that all energetics depends on both oxygen and CO coverages. These structures allows to uncover adsorption peculiarities. Indeed the CO adsorption energy might be quite constant for highly covered structures. Carbon dioxide adsorption is however mainly unfavourable whatever the coverage, with a quite linear trend. In any case a great number of O/CO co-adsorbed systems would bring finer trends. Interestingly, these calculations support a minimum energy for specific CO coverages on the metal support interaction. Carbon dioxide adsorption has also been investigated on close O/CO covered Pt<sub>13</sub> surfaces. Except for the Pt<sub>13</sub>O<sub>3</sub>(CO) structure that alumina is engaged in adsorption site, all the electronic adsorption energies do not favor CO<sub>2</sub> adsorption. Regarding CO oxidation, the two transition states found lead to similar electronic oxidation barriers despite huge structural differences. The electronic energies are in the range of prior DFT studies on both flat surfaces and platinum clusters. Yet CO oxidation electronic energies found are the lowest on Pt<sub>13</sub> and Pt<sub>10</sub> clusters, supported or not.

Carbon monoxide oxidation was then simulated according to kinetic models that hold previously investigated *ab initio* data. Therefore experimental TPR will be compared to simulated ones. Considering that oxygen and carbon monoxide adsorptions reactions are parts of the global phenomenon of CO oxidation, the previously developed kinetic models were used. Also the exhaustivity of the multi-scale method with few *ab initio* structures probed has led to discuss the level of complexity of the developed kinetic models.

## 5.4| Micro-kinetic modelling of CO oxidation

As experimental work leads to global kinetics indicator such as  $T_{50\%}$  or activation energies, *ab initio* based micro-kinetic modelling of CO oxidation can be evaluated. Only  $\text{Pt}_{13}\text{O}_n(\text{CO})_m(\text{CO}_2)$  structure energetics is implemented in the model and the role of hydroxyls on alumina will not be discussed in this part. To handle the oxidation kinetics itself, several kinetic parameters sets were tested (Table 16).

The determination of CO oxidation enthalpies from the two previous structures  $\text{Pt}_{13}\text{O}_4(\text{CO})^\ddagger$  and  $\text{Pt}_{13}\text{O}_{16}(\text{CO})_7^\ddagger$  has led to distinct oxidation enthalpies, whereas electronic energies were found close (Table 30). Therefore distinct kinetic models have been built with their own CO oxidation reactivities. Also  $\text{CO}_2$  desorption enthalpies have been calculated. In the case of unfavored  $\text{CO}_2$  adsorption electronic energies, this data led to barrierless  $\text{CO}_2$  desorption.

- The first ones, called “molecular” (MOL) was performed with few reactions. They consist in pure *ab initio* thermodynamics, invariant according to O/CO coverages. Only  $\text{CO}_2$  adsorption reaction and CO oxidation are tested here.
- To evaluate the impact of  $\text{O}_2$  and CO adsorption, “desorption” (DES) models were built. The O/CO desorption kinetics depends respectively on  $\theta_{\text{O}}$  and  $\theta_{\text{CO}}$ . The data used for CO oxidation and  $\text{CO}_2$  desorption is the same as MOL model.
- The variation of  $\text{CO}_2$  desorption has then been made. On the basis of DES models, “variation” (VAR) models use oxygen coverage dependent  $\text{CO}_2$  desorption thermodynamics. As usual, a sticking coefficient study has been performed to benchmark the impact of this factor.
- Finally “complex” (CPX) models handle a double dependence of all adsorption/desorption reactions according to  $\theta_{\text{O}}$  and  $\theta_{\text{CO}}$  were made as a higher level of detail.

Table 16: Kinetic model characteristics according to reaction type and coverage dependences.

Kinetic model	Kinetic parameters		
	O/CO adsorption/desorption	$\text{CO}_2$ adsorption/desorption	CO oxidation
Molecular (MOL)	None	$\Delta_{\text{r}}X_{\text{des CO}_2} = \Delta_{\text{r}}X_{\text{Pt}_{13}\text{O}_4\text{CO}}$ or	$\Delta_{\text{r}}X_{\text{oxy CO}} = \Delta_{\text{r}}X_{\text{Pt}_{13}\text{O}_4\text{CO}}$ or $\Delta_{\text{r}}X_{\text{oxy CO}} = \Delta_{\text{r}}X_{\text{Pt}_{13}\text{O}_{16}(\text{CO})_7}$
Desorption (DES)	$\Delta_{\text{r}}X_{\text{des.O and CO}} = f(\theta_{\text{O or CO}})$	$\Delta_{\text{r}}X_{\text{des CO}_2} = \Delta_{\text{r}}X_{\text{Pt}_{13}\text{O}_{16}(\text{CO})_7}$	
Variable (VAR)		$\Delta_{\text{r}}X_{\text{des CO}_2} = f(\theta_{\text{O}})$	
Complex	$\Delta_{\text{r}}X_{\text{des.O and CO}} = f(\theta_{\text{O}}, \theta_{\text{CO}})$	$\Delta_{\text{r}}X_{\text{des CO}_2} = f(\theta_{\text{O}}, \theta_{\text{CO}})$	

(CPX)			
-------	--	--	--

Except for MOL “molecular” models, kinetic parameters interpolations have been made to deal with every coverage from 0 to 24 adspecies. Indeed as  $\text{Pt}_{13}\text{O}_n$  and  $\text{Pt}_{13}(\text{CO})_m$  structures were respectively studied two-by-two and three-by-three, piecewise linear interpolations were performed on desorption enthalpy and entropy. Consequently for each  $(n_{\text{O}}, m_{\text{CO}})$  surface species, four two-side reactions can occur:  $\text{O}_2$ ,  $\text{CO}$  and  $\text{CO}_2$  adsorption/desorption and  $\text{CO}$  oxidation (Figure 57). According to *ab initio* investigations, the kinetic models handle all surface species with less than 23 adspecies on the cluster. To verify the coherence of the models,  $\text{O}_2$ -TPD and  $\text{CO}$ -TPD were performed in the same conditions than previous simulations (respectively Figure 30 and Figure 45) and similar results were found (Figure 116 in appendices). Reaction fluxes complete the analysis to understand in detail the drivers of these kinetics.

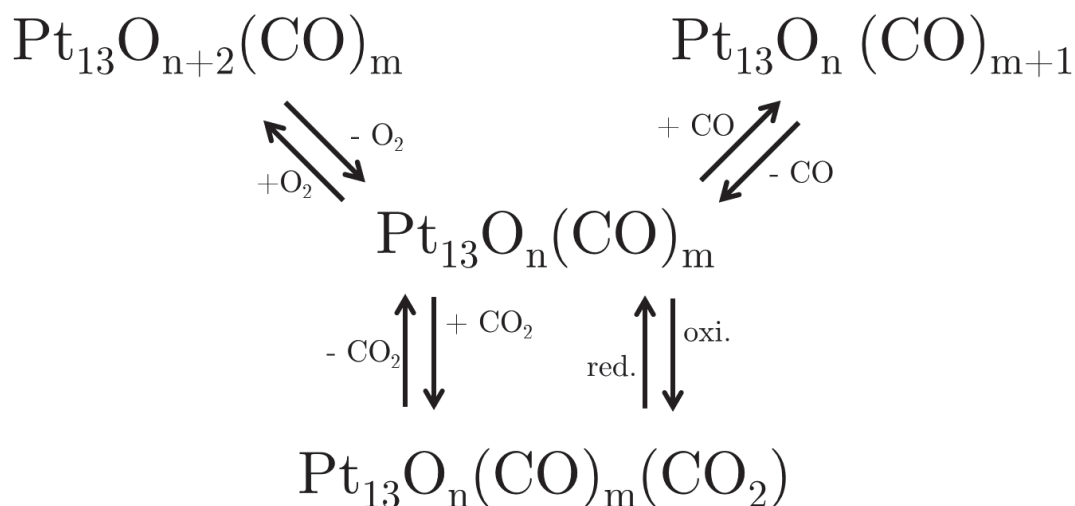


Figure 57: Illustration of the kinetic-type reactions engaged in DES, VAR and CPX models, with a given  $\text{Pt}_{13}\text{O}_n(\text{CO})_m$  surface specie.

#### 5.4.1| MOL and DES models: sole oxidation micro-kinetics

“Molecular” (MOL) models are the simplest ones developed in this chapter. Indeed a focus is made on the *ab initio* data determined for  $\text{CO}$  oxidation. Two “molecular” models were developed. They are named after the previously found transition states. Figure 58 illustrates  $\text{CO}_2$  gas fraction production through temperature. The maximum  $\text{CO}_2$  release temperature is considered as a good indicator of the  $T_{50\%}$ .

As  $\text{Pt}_{13}\text{O}_4(\text{CO})$  structure leads to an additional imaginary frequency, two processes were performed to determine thermodynamic parameters. In one case the imaginary

frequency was assumed as a real one ( $\text{Pt}_{13}\text{O}_4(\text{CO})$ -eq model, Table 31 in Appendices). In another case, every frequencies below  $50\text{cm}^{-1}$  were to this maximum value ( $\text{Pt}_{13}\text{O}_4(\text{CO})$ -eq model, Table 32 in Appendices). The oxidation simulation of the two models exhibit no significant discrepancies. Therefore only one model represents  $\text{Pt}_{13}\text{O}_4(\text{CO})$  reactivity. For this model, the desorption occurs on a  $60^\circ\text{C}$  temperature range. Moreover the model handles correctly well the present experimental work that  $T_{50\%}$  rises at  $157^\circ\text{C}$  (Figure 47).

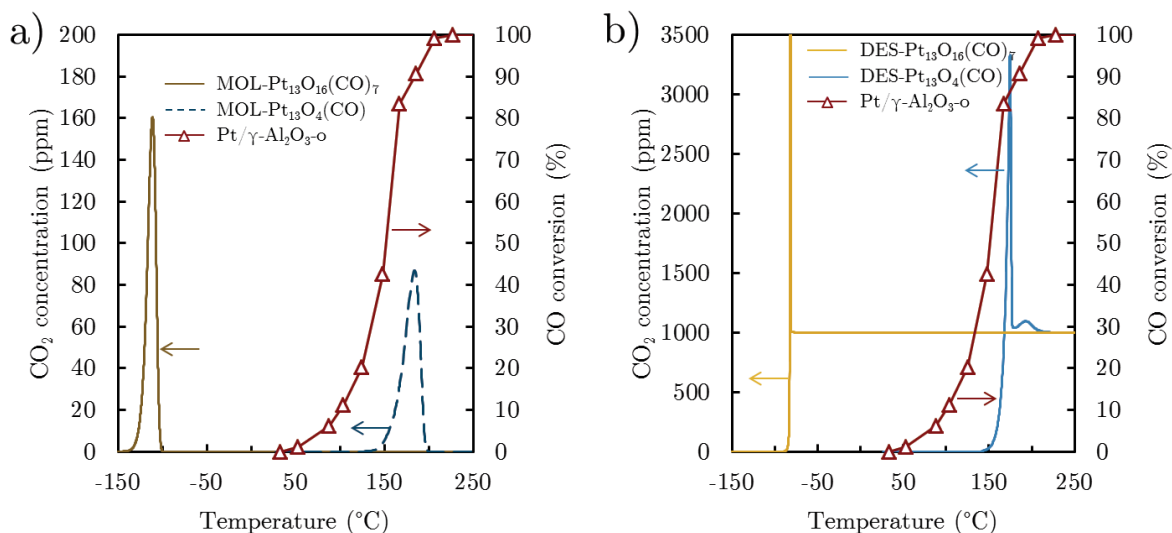


Figure 58: Carbon dioxide gas fraction outlet of the MOL and DES models of CO TPR simulations. For the molecular models, the initial surface specie was the reduced one. Desorption models Temperature windows were adapted to observe the  $\text{CO}_2$  release, keeping a  $5^\circ\text{C}\cdot\text{min}^{-1}$  ramp. Other initial conditions calculation are displayed in Script 1 (appendices).

This is not the case of  $\text{MOL-Pt}_{13}\text{O}_{16}(\text{CO})_7$  that leads to a  $-111^\circ\text{C}$  temperature. This is due to a lower oxidation activation energy of  $10.5\text{ kcal}\cdot\text{mol}^{-1}$  (Table 33 in appendices). One can also noticed that  $\text{CO}_2$  desorption is barrierless. This indicates that  $\text{Pt}_{13}\text{O}_{16}(\text{CO})_7$  kinetics is not representative of real surface species.

To be representative of the whole phenomenon, one needs to add the kinetics of adsorption/desorption of  $\text{O}_2$ ,  $\text{CO}$  and  $\text{CO}_2$ . The “desorption” (DES) models have been built in this way with kinetic parameters presented in previous chapters. Also  $\text{O}_2$  adsorption reactivity is the same whatever the  $\text{CO}$  coverage is and *vice versa*. Concerning  $\text{CO}_2$  adsorption/desorption, the reactivity is identical to the MOL models with only one reaction.

First the one hour adsorption flow with the corresponding experimental conditions is simulated for the clean  $\text{Pt}_{13}$  surface. Applied conditions are a  $300\text{K}$  constant temperature and  $1000\text{ ppm CO}$ ,  $10\% \text{ O}_2$  and the rest of helium. This simulation allows to determine the surface species in equilibrium with the gas mixture. In a second step,

the simulation of the TPR is performed with the given species at surface initial conditions.

In the case of the DES-Pt<sub>13</sub>O<sub>4</sub>(CO), the initial surface specie is mainly Pt<sub>13</sub>O<sub>12</sub>(CO)<sub>10</sub>. As oxydation appears at very low temperature for DES-Pt<sub>13</sub>O<sub>16</sub>(CO)<sub>7</sub>, the simulation starts at -250°C and Pt<sub>13</sub>(CO)<sub>23</sub> specie is predominant there. Yet a 5°C.min<sup>-1</sup> temperature ramp is kept. This is due to dissociative adsorption activation energy of O<sub>2</sub> that stems atomic oxygen adsorption at this temperature.

Compared to the MOL model, DES-Pt<sub>13</sub>O<sub>16</sub>(CO)<sub>7</sub> has a T<sub>50%</sub> of -82°C. This confirms that the reactivity held in MOL-Pt<sub>13</sub>O<sub>16</sub>(CO)<sub>7</sub> is not representative at the starting temperature. Figure 119 (Appendices) illustrates the surface species at several temperatures during CO oxidation. It goes from Pt<sub>13</sub>(CO)<sub>23</sub> to mainly Pt<sub>13</sub>O<sub>3,4,5</sub> through Pt<sub>13</sub>O<sub>2,3,4,5</sub>(CO)<sub>m</sub> species.

#### 5.4.2| VAR and CPX models: CO<sub>2</sub> desorption dependence

So far carbon dioxide adsorption/desorption reactions used only one kinetic set for every O/CO coverages. In order to evaluate the impact of a variable CO<sub>2</sub>, the thermodynamics found by *ab initio* have been interpolated according to oxygen coverage (Figure 121 in appendices). This leads to the “Variable” (VAR) models.

Carbon dioxide concentration during TPR simulation is displayed for this model in Figure 59. One can see that T<sub>50%</sub> for the Pt<sub>13</sub>O<sub>16</sub>(CO)<sub>7</sub> reactivity rises now at 85°C. This suggests that CO<sub>2</sub> desorption kinetic parameters play a major role in CO oxidation temperature range. In this case, T<sub>50%</sub> shifted from DES model up to 160°C, closer to the experimental value than for the Pt<sub>13</sub>O<sub>16</sub>(CO)<sub>7</sub> MOL model.

This is explained by less favorable CO<sub>2</sub> desorption enthalpies (Figure 121 in appendices). Indeed, at -250°C, the initial temperature, Pt<sub>13</sub>O(CO)<sub>23</sub> is found to be predominant. At this temperature, the entropy for CO<sub>2</sub> desorption reaction is high which leads to fast reactions. However, its related enthalpy is high also. This is directly related to the temperature shift in CO<sub>2</sub> release, and T<sub>50%</sub> is significantly increased. Thus surface species changes with increasing temperature to Pt<sub>13</sub>O<sub>8</sub>(CO)<sub>15</sub> at 30°C. At this point, CO<sub>2</sub> desorption is barrierless though entropy has decreased (Figure 121). The CO<sub>2</sub> release starts around this temperature. Indeed, in terms of temperature and surface species, the systems lie in the same conditions than model VAR-Pt<sub>13</sub>O<sub>4</sub>(CO) detailed afterwards. Only CO<sub>2</sub> oxidation reactivity changes. As the latter is facilitated for Pt<sub>13</sub>O<sub>16</sub>(CO)<sub>7</sub> *ab initio* structure, the T<sub>50%</sub> appears earlier than for Pt<sub>13</sub>O<sub>4</sub>(CO).

Concerning Pt<sub>13</sub>O<sub>4</sub>(CO) reactivity, T<sub>50%</sub> is close to 120°C. This temperature shifted down to 40°C below the equivalent “desorption” model. This is due to the kinetic model differences in itself. Indeed the MOL and DES-Pt<sub>13</sub>O<sub>4</sub>(CO), the addressed CO<sub>2</sub>

desorption data are the one of *ab initio*  $\text{Pt}_{13}\text{O}_4(\text{CO})$  for every surface species present in the model. This desorption parameters include an activation barrier for the  $\text{CO}_2$  to desorb. However in the VAR models,  $\text{CO}_2$  desorptions enthalpy is varying with oxygen coverage. Desorption enthalpy is barrierless for  $\text{Pt}_{13}\text{O}_{7-17}(\text{CO})_m$  surface species, that allows  $\text{CO}_2$  to desorb lower in temperature than MOL and DES- $\text{Pt}_{13}\text{O}_4(\text{CO})$  models. This indicates that  $\text{CO}_2$  desorption kinetic parameters influence significantly oxidation temperatures. Initial and final states are equivalent, from balanced O/CO structures to fully oxidized  $\text{Pt}_{13}$  structures. Reaction fluxes also follow the same pattern as the “Desorption” model (Figure 118 and Figure 123 in appendices).

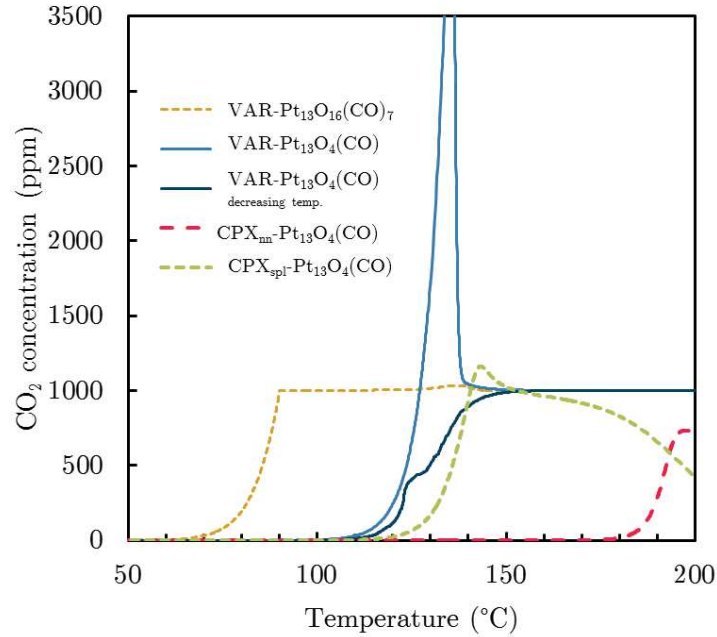


Figure 59: Carbon dioxide outlet gas fraction with VAR and CPX models during CO TPR simulations. Temperature windows were adapted to observe the  $\text{CO}_2$  release, keeping a  $5^\circ\text{C}\cdot\text{min}^{-1}$  ramp. The main initial surface specie is  $\text{Pt}_{13}\text{O}_{12}(\text{CO})_{10}$ . Other initial conditions calculation are displayed in Script 1 (appendices).

In order to evaluate the ability to reproduce the experimental hysteresis, a decreasing TPR was simulated with VAR- $\text{Pt}_{13}\text{O}_4(\text{CO})$ . As seen on Figure 59, the beginning of the transition is less abrupt than in ascendent temperature. Also a difference in  $T_{50\%}$  is noticeable with less than a  $10^\circ\text{C}$  gap, that corresponds to the present experimental set of TPR. However Salomons and coworkers<sup>244</sup> show that the inverse happens: CO oxidation lasts longer at low temperature with decreasing temperature.

One final variation consists in a multiple dependence of adsorption reaction parameters such as  $\Delta_r X = f(\theta_o, \theta_{CO})$ . These “Complex” (CPX) models were built thanks to nearest neighbor and thin plate splines interpolations (respectively  $\text{CPX}_{mn}$  and  $\text{CPX}_{spl}$ ). An illustration of these extrapolations is displayed in Figure 60. Therefore the  $\text{CPX}_{mn}$  model only used *ab initio* determined thermodynamics, but reactivity changes is abrupt

from one coverage to another. For the thin-plate spline interpolation, most of the data are extrapolated with curvilinear trends and smooth transitions between coverage vicinal structures.

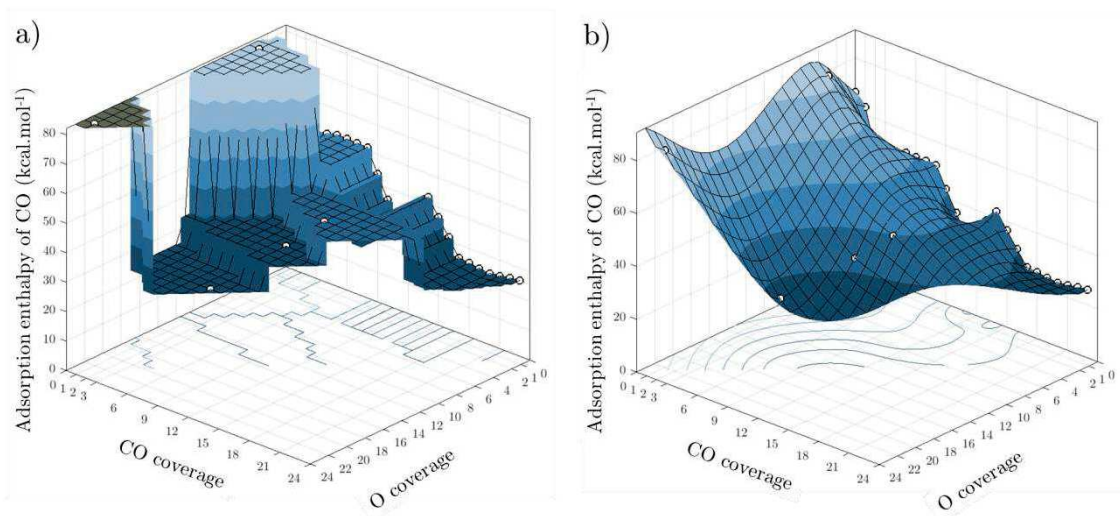


Figure 60: Illustration inter- and extrapolation of the extrapolation used to determine  $\text{Pt}_{13}\text{O}_n(\text{CO})_m$  thermodynamic parameters used to calculate kinetic parameters. The case of CO desorption enthalpy is illustrated here with a) nearest neighbor and b) thin spline plates extrapolation.

While  $\text{CPX}_{\text{spl}}$  simulation has a  $T_{50\%}$  of  $135^\circ\text{C}$ , close to prior data,  $\text{CPX}_{\text{nn}}$  model exhibits a  $193^\circ\text{C}$   $T_{50\%}$ . This highlights that interpolation method plays a huge role in this multi-scale work. Also one can see that for both model, a decrease of  $\text{CO}_2$  production at higher temperatures appears, due to CO desorption from the surface. This is not visible for the experimental probed temperatures.

In order to evaluate the sticking coefficients of  $\text{O}_2$ , CO and  $\text{CO}_2$ , simulation of altered  $\text{VAR-Pt}_{13}\text{O}_4(\text{CO})$  model have been performed. Sticking coefficients were changed from 1 to  $10^{-4}$  separately (Figure 61). One can see that lowering any sticking coefficient shifts oxidation to higher temperatures. A  $10^\circ\text{C}$  shift of the oxidation  $T_{50\%}$  is noticed for the lowered  $s_{\text{CO}}$  and  $s_{\text{O}_2}$  models. In the case of lowered  $s_{\text{CO}_2}$ , oxidation happens twice. Indeed lowering the  $\text{CO}_2$  sticking coefficient leads to lower the desorption reaction rate, calculated by thermo-consistency. Therefore  $\text{CO}_2$  molecules desorbs slower than other models. Assuming that CO oxidation happens on the same surface species highlighted in Figure 122 (Appendices) and considering  $\text{CO}_2$  desorption kinetic parameters interpolation for this model (Figure 121 in appendices), the first peak corresponds to  $\text{CO}_2$  barrierless desorption on  $\text{Pt}_{13}\text{O}_n(\text{CO})_{8-10}$  species while the second has a  $80 \text{ kcal.mol}^{-1}$  desorption energies on highly oxidised final species. This peak deconvolution is therefore observable only due to  $\text{CO}_2$  desorption rate lowering. Oxidation temperature range reaches  $65^\circ\text{C}$  versus  $35^\circ\text{C}$  for the  $\text{VAR-Pt}_{13}\text{O}_4(\text{CO})$  reference model.

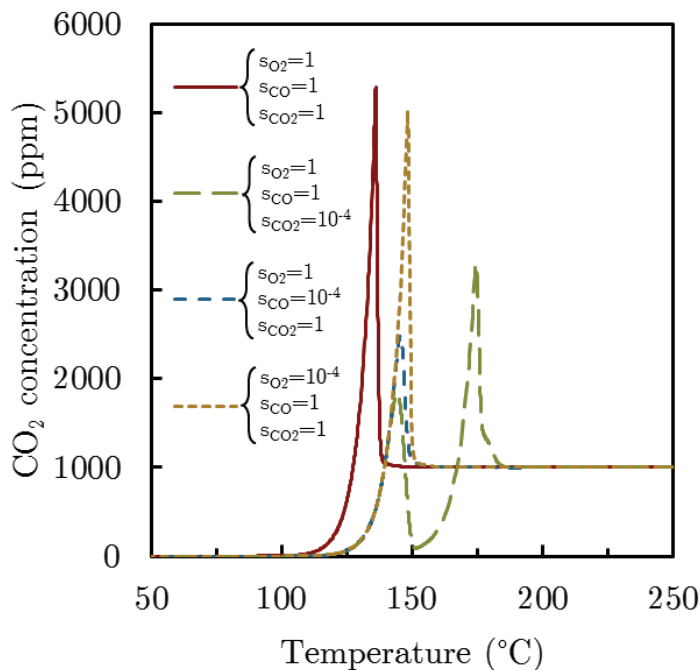


Figure 61: CO<sub>2</sub> desorption of simulated CO-TPR using VAR kinetic parameter sets with sticking coefficient variations. The main initial surface specie is Pt<sub>13</sub>O<sub>12</sub>(CO)<sub>10</sub>. Other initial conditions calculation are displayed in Script 1 (appendices). Sticking coefficient were changed from 1 to 10<sup>-4</sup> one at a time.

Carbon dioxide gas fraction of the VAR-Pt<sub>13</sub>O<sub>4</sub>(CO) models with altered sticking coefficients. Temperature ramp is 5°C.min<sup>-1</sup>. Other initial conditions calculation are displayed in Script 1 (appendices).

Thanks to the “variable” and “complex” models, the determination of carbon monoxide apparent activation energy have been performed as for experimental data (Table 17). It appears that simulated activation energies are several times higher than experimental determinations<sup>248,108</sup>. All the simulated ones are comprised between 40 and 60 kcal.mol<sup>-1</sup>, with very close data for the same CO<sub>2</sub> reactivity of Pt<sub>13</sub>O<sub>4</sub>(CO) models: VAR-Pt<sub>13</sub>O<sub>4</sub>(CO) and CPX<sub>spl</sub>. Yet only CO oxidation reaction kinetic parameters are identical between these two models. This may suggest that apparent activation energy is mostly led by CO oxidation reactions.

Table 17: Experimental and simulated apparent activation energies for CO-TPR according to VAR-Pt<sub>13</sub>O<sub>4</sub>(CO) and CPX<sub>spl</sub> kinetic models.

Experimental/Simulated TPR	Model/Catalyst	Apparent activation energy (kcal.mol <sup>-1</sup> )
Experimental	1% wt. Pt/γ-Al <sub>2</sub> O <sub>3</sub> -o,	9.2 (below 20% conversion) 13 (below 10% conversion)

	d=0.90	
	3.8% Pt/Al <sub>2</sub> O <sub>3</sub> <sup>263</sup> , d=0.63	18.2
	2.0% Pt/SiO <sub>2</sub> <sup>248</sup> , d=0.76	22.0
Simulation	VAR-Pt <sub>13</sub> O <sub>16</sub> (CO) <sub>7</sub>	39.6
	VAR-Pt <sub>13</sub> O <sub>4</sub> (CO)	61.0
	CPX <sub>spl</sub>	58.3

To conclude, CO oxidation micro-kinetics modelling is not straightforward as multiple parameters must be taken into account. Adsorption steps are of major concern as it draws the initial surface species as a first step. Here, one can see that for Pt<sub>13</sub>O<sub>4</sub>(CO) models that starts at ambient temperature, balanced O/CO structures are obtained and lead to highly oxidized species as expected by previous simulations. This *ab initio* reactive model is by the way more congruent than Pt<sub>13</sub>O<sub>16</sub>(CO)<sub>7</sub> as T<sub>50%</sub> is constantly close to experimental values. Also the latter is not representative of O/CO coverage rate encountered from ambient to oxidation temperatures. The impact of interpolating kinetic parameters from *ab initio* data has a great influence on T<sub>50%</sub> higher temperatures, but not significant on apparent activation energies. Finally, reaction fluxes analyses demonstrate that Pt<sub>13</sub> most solicited species are Pt<sub>13</sub>O<sub>n</sub> ones with few carbon monoxide adsorbed.

## 5.5| Conclusion

Oxidation of carbon monoxide on highly dispersed Pt/ $\gamma$ -Al<sub>2</sub>O<sub>3</sub> was investigated in this chapter. The multi-scale approach used for chapters 3 and 4 was altered in order to adjust to the complexity of CO oxidation. Experimental TPR experiments were carried out, as well as *ab initio* modelling of co-adsorbed Pt<sub>13</sub>O<sub>n</sub>(CO)<sub>m</sub>/ $\gamma$ -Al<sub>2</sub>O<sub>3</sub>, oxidized and alumina hydrated structures. Several kinetic schemes were built based on adsorption previously computed data and oxidation ones.

CO oxidation TPR experiments allows to determine T<sub>50%</sub> mid-oxidation temperature, CO and O reaction partial orders, and global activation energy. Data were found close to prior works with similar operating conditions and surface dispersion. Specific points about CO oxidation were observed, as: (i) CO<sub>2</sub><sup>gas</sup> production oscillations and (ii) oxidation hysteresis between extinction and ignition conversion dataset. A noticeable effect of catalyst oxidation state has been revealed.

Few *ab initio* calculations of co-adsorbed structures, undertook on the basis of earlier developed Pt<sub>13</sub>O<sub>n</sub>/ $\gamma$ -Al<sub>2</sub>O<sub>3</sub> and Pt<sub>13</sub>(CO)<sub>m</sub>/ $\gamma$ -Al<sub>2</sub>O<sub>3</sub> systems, demonstrates that

adsorption energetics is impacted by both O/CO coverages. Carbon monoxide adsorption is quite homogeneous for highly covered structures, while oxygen adsorption energy demonstrates significant dependency. Carbon dioxide adsorption is unfavoured, yet clear linear trend according to O/CO coverages is noticed. The merged phase diagram of oxygen and carbon monoxide adsorption, implemented with co-adsorbed energetics, demonstrates that oxidized structures are more stable than carbonylated ones. Regarding oxidation transition states, oxidation electronic barriers are found identical and close to prior studies. However, oxidation entropies and enthalpies are clearly distinct.

Considering that few *ab initio* structures were probed, and that oxidation kinetics implies reactant adsorption, several kinetic schemes were built with increasing complexity. Isolated oxidation kinetics of  $\text{Pt}_{13}\text{O}_4(\text{CO})$  system exhibits oxidation temperature close to experimental TPR. Adsorption kinetics plays demonstrates that balanced O/CO coverage structures are predominant at initial TPR conditions. The hysteresis between CO ignition and extinction is however not captured. For highly detailed schemes, the thermodynamic interpolation and discretisation method is a major element. Smooth and continuous interpolations are observed to be congruent with experiments. Moreover  $\text{Pt}_{13}\text{O}_{16}(\text{CO})_7$  based schemes demonstrates that structure representativity and oxidation kinetics is of major concern, much more than kinetic scheme complexity.

Finally this work highlights the reactivity of highly dispersed platinum supported on alumina. Several computed thermochemical data such as the heat of adsorption and the achievable oxygen coverage thoroughly differ from well-known extended surfaces. The temperature-programmed desorption of  $\text{O}_2$  and the related kinetic simulations demonstrate similar desorption temperature ranges that again consolidate the approach of coupling the experimental and modelling work. The model established herein could be implemented in the future for highly dispersed platinum catalysis mechanism in oxidant media, such as oxidation of carbon monoxide into  $\text{CO}_2$ .

The engaged level of detail, especially for *ab initio* and kinetic modelling is a key to reproduce experimental observations. Some of the developed schemes are congruent with experimental TPR, yet few CO oxidation features have not been handled. This is the case of  $\text{CO}_2^{\text{gas}}$  production oscillations. This phenomenon is not accessible in our approach as Chemkin software does not take into account surface coverage inhomogeneities. Monte-Carlo kinetic simulation would be a convenient tool for this application. To go further carbon oxidation is known to be impacted by platinum dispersion, although it is not well understood. This study aimed only at CO oxidation on highly dispersed platinum surface. Yet the multi-scale approach can be addressed to other platinum dispersion, particularly flat and stepped extended surfaces.





# 6| Light hydrocarbons oxidation

## 6.1| Introduction

The multiscale modelling approach has been used so far to study peculiar reactions, one kind at a time. The high level of details of oxygen adsorption study in chapter 3 allows to handle the oxidation state of a surface. The study of the adsorption of carbon monoxide has contributed to understand the phenomenon on the highly dispersed Pt/ $\gamma$ -Al<sub>2</sub>O<sub>3</sub> catalyst. The next stage consisted in the reaction of the two adspecies toward the oxidation of CO into CO<sub>2</sub>, with a deep kinetic investigation. This approach gave fruitful results and led to a higher level of knowledge of the fundamental phenomena studied.

However the previous chapters have hardly addressed hydrocarbon oxidation. Only CO oxidation has been handled which is not representative of an engine exhaust gas. The multiscale approach is ideal to go further into hydrocarbon oxidation. Interestingly the exhaust gas is substantially changing, affected by fuel composition as well as different combustion systems. Therefore the versatility of the multiscale approach is convenient for this kind of system.

Handling hydrocarbon oxidation reactivity in a kinetic scheme is not trivial. Considering gas phase hydrocarbon oxidation this has already been made, yet solely for fuel surrogates comprising usually up to four compounds. Those models operate hundreds of molecules and radicals and thousands of reactions. For instance, the oxidation of butane is modelled by the kinetic schemes of Healy *et al.*<sup>269,270</sup> and consists in 238 species for 1328 reactions. Yet combustion reactions do not take into account surface as reactive medium. Moreover two points add complexity to surface kinetic schemes: (i) one can assume that some radicals that are unstable in gas phase might exist on a surface and (ii) different adsorption modes are considered as different radicals. Therefore the numbers of reactions and species increase dramatically.

In any case, the use of a reaction generator has demonstrated significant advantages to create consistent kinetic schemes. Some automated procedures have been developed such as NETGEN<sup>141</sup>, Reaction Mechanism Generator<sup>144</sup> or Genesys<sup>143</sup>. However they only deal with gas phase reactions. Surface considerations are not taken into account. Only the in-progress code RMG-cat<sup>145</sup> tackles at surface reaction, and has been used so far for steam reforming on Ni(111).

Nevertheless some light hydrocarbon oxidation kinetic schemes have been developed, essentially on the Pt(111) surface. Vlachos *et al.*<sup>80</sup>, deal with the oxidation of methane, with a so-called zero-dimension mechanism. The components are reduced to 7 molecules that can be adsorbed, and interact through 31 reversible reactions. Deutschmann<sup>205</sup> also developed a mechanism for C<sub>1</sub> hydrocarbons, with 25 species and 88 reactions. Here the gas phase diffusion to the solid is taken into account as well as the heat transfer. One key point lies in the optimisation of the model, that development aimed at fitting to methane oxidation experimental data.

Finally, the mechanism of Lindstedt *et al.*<sup>271</sup> tackles the dehydrogenation of C<sub>2</sub> hydrocarbons with the laws of transport and heat, including 44 species and 271 reactions. The surface scattering of species is represented here as a reaction with its own kinetic parameters. These studies are limited to reaction paths elucidated experimentally. The first two studies favor the oxidation of methane by successive dehydrogenations then by carbon oxidation to CO and CO<sub>2</sub>. Gas phase oxidation reactions are also present. The third study focuses mainly on the catalytic dehydrogenation of ethane into ethylene onto platinum.

Deutschmann uses only experimental data for activation energies. Vlachos and Lindstedt used atomic adsorption heats from both DFT and experiments. Molecular adsorption heats are generated by the UBI-QEP method. Vlachos uses coverage coefficients applicable to the adsorption energies of atomic adspecies from both experimental and DFT data. Then these coefficients are used to determine the heats of molecular adsorption. This allows to calculate (also by UBI-QEP), activation energies with covered species dependencies. Vlachos team has also determined energy dependencies toward H, O, OH and CO surface species.

Regarding experimental data on related hydrocarbon oxidation, Vlachos model manages to reproduce selectivity of CO over a limited temperature range. However the model is not able to handle the conversion of methane and the production of hydrogen by steam reforming. The Deutschmann model does not fully capture the temperature variations implied by the surface reactivity. Methane light-off is however correct, but the experimental data concern a single ratio of methane/air. The conclusions focus solely on heat transfer and the diffusion phenomenon from the gas phase to the solid phase. The Lindstedt<sup>271</sup> mechanism is capable of simulating hydrocarbons conversion such as ethane, methane, ethylene and CO.

This chapter aims at the transposition of the prior developed multiscale approach for light hydrocarbons oxidation. Indeed the considerable amount of species and reactions impose to alter the method to large systems. At first, the radicals and molecules *ab initio* modelling has been performed on Pt(111) as a simpler surface model than Pt<sub>13</sub>/γ-Al<sub>2</sub>O<sub>3</sub>. It allows to consider only one kind of adsorption site per adspecies, due to the symmetry of the surface. Species from C<sub>0</sub> to C<sub>2</sub> were exhaustively considered, with few C<sub>3</sub> non oxygenated radicals. Also only electronic energy determination has been undertaken, that leads to estimated micro-kinetic parameters. Molecular modelling data allows to draw adsorption energy trends according to adsorption modes.

The development of an automated script was needed to (i) set all the surface reactions and (ii) address their unique kinetic parameters. This reaction generator is detailed in chapter 2, section 2.4.4. In order to represent light hydrocarbons from the Diesel exhaust line, methanol and propene were chosen. Oxidation of CO/methanol and CO/propene mixtures were also performed as carbon monoxide is a prominent gas in Diesel exhaust. Regarding experimental oxidation, the Temperature Programmed Reaction (abbreviated TPR) of methanol and propene were performed on highly dispersed platinum catalyst. The impact of carbon monoxide addition to the inlet gas mixture was also evaluated.

## 6.2 | Oxidation experiments

In order to tackle light hydrocarbon oxidation on platinum surface, TPR of methanol and propene were performed using the micro-reactor set-up. In addition different concentrations of carbon monoxide were added to the gas mixtures to evaluate its impact on methanol and propene oxidation. Activation energies were determined to address a quantitative data to this impact. For these experiments the 1% wt. Pt/γ-Al<sub>2</sub>O<sub>3</sub> catalyst was used.

### 6.2.1 | Oxidation of methanol

#### 6.2.1.1 | Global kinetics

Methanol oxidation with 0ppm, 800ppm and 2000ppm of CO were performed from 20°C to 225°C. The operating conditions are gathered in Table 18. A total flow rate of 30 mL.min<sup>-1</sup> was used to ensure a sufficient flow to the mass spectrometer. Dioxygen is in excess with 8.0 vol. %. Micro-gas chromatography was used to determine methanol and CO conversion.

Table 18: Operating conditions for pure methanol and methanol/CO mixtures oxidation experiments.

Total flow (mL.min <sup>-1</sup> )	30.0	Catalyst mass (mg)	12.7
------------------------------------	------	--------------------	------

CH <sub>3</sub> OH rate (ppm)	3500	GHSV (h <sup>-1</sup> )	86000
CO rates (ppm)	0.0 800 2000	Temperature slope (°C.min <sup>-1</sup> )	2
O <sub>2</sub> rate (%)	8.0		

The conversion of methanol is displayed in Figure 62a. The temperature at 50% conversion,  $T_{50\%}$ , is used as the main temperature indicator. Methanol  $T_{50\%}$  rises at 131°C, on a 175°C wide temperature range. Lin *et al.*<sup>272</sup> reported a  $T_{50\%}$  of 110°C for similar operating conditions (0.37 wt. % Pt/Al<sub>2</sub>O<sub>3</sub> with unknown dispersion, 2000ppm CH<sub>3</sub>OH and 20% O<sub>2</sub>, with a GHSV of 50000 h<sup>-1</sup>). The authors have also studied the impact of methanol and O<sub>2</sub> concentrations on boron nitride supported catalyst. Methanol has no significant effect on its own oxidation in the 1000ppm to 3000ppm range. However O<sub>2</sub> is found to have a negative effect from 5% to 80% volume concentration, that shifts  $T_{50\%}$  up to 10°C higher.

In the case of methanol/CO mixtures TPR, carbon monoxide displays a significant effect on methanol oxidation. Activation energy of methanol oxidation changes drastically with CO addition, from 15 kcal.mol<sup>-1</sup> to 37kcal.mol<sup>-1</sup> with 800ppm CO and 70kcal.mol<sup>-1</sup> with 2000ppm CO. Conversion occurs within a narrower range of temperature. The  $T_{50\%}$  has no significant variation either with or without carbon monoxide. Yet the threshold effect has not been captured, and must lie between 0 and 800ppm CO concentration. Therefore CO has a considerable effect on methanol oxidation.

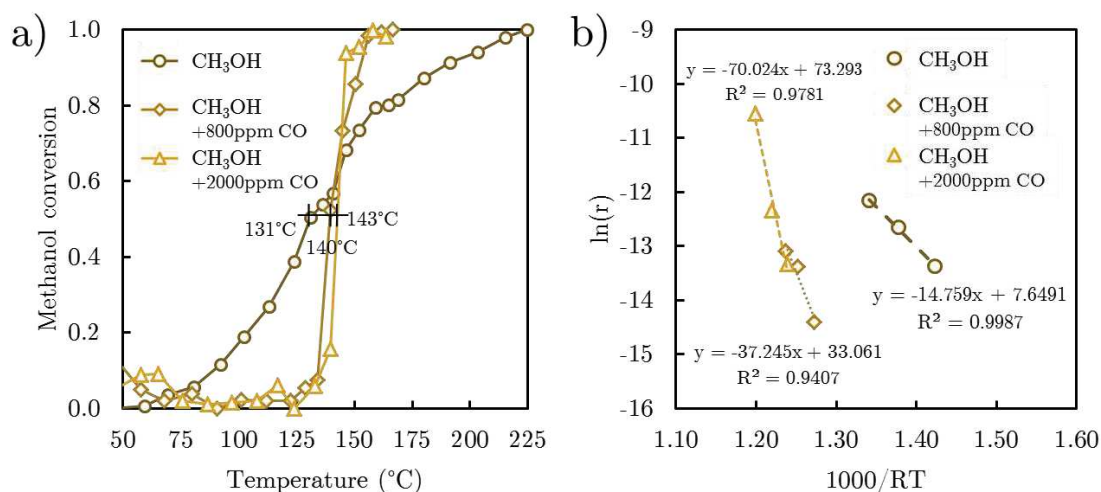


Figure 62: Experimental temperature programmed reaction of methanol/CO mixtures, using a 2°C.min<sup>-1</sup> temperature ramp and 3500ppm CH<sub>3</sub>OH (8% O<sub>2</sub>). a) Methanol conversion with distinct CO concentrations and b) related methanol oxidation activation energies determination, in kcal.mol<sup>-1</sup>.

Methanol also impacts carbon monoxide oxidation (Figure 63a). Activation energy of CO oxidation increases, from 10.6 to 63.2 kcal.mol<sup>-1</sup>. The T<sub>50%</sub> of CO oxidation alone (undertook in chapter 2, 1000ppm CO) lies at 155°C, with a 175°C wide oxidation range. This range gets thinner to 100°C and 50°C with respectively 0.22 and 0.57 CO:methanol ratios. Therefore CO oxidation occurs on a narrower range as CO:methanol ratio increases. Regarding CO oxidation T<sub>50%</sub>, the methanol impact is not clear as carbon monoxide concentration inhibits its own reactions. Indeed CO inlet concentrations are different for the three TPR.

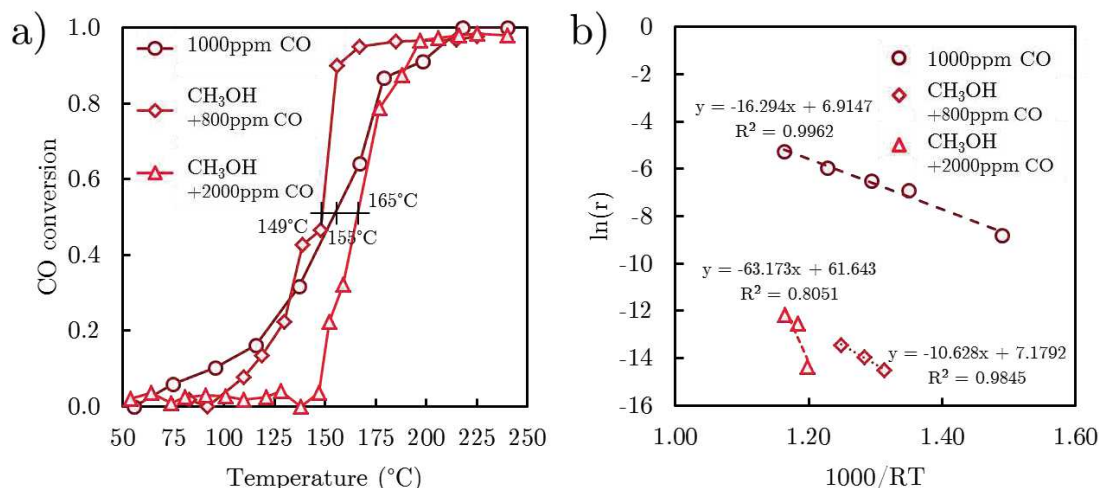


Figure 63: Experimental data about temperature programmed reaction of methanol/CO mixtures, using a 2°C.min<sup>-1</sup> temperature ramp and 3500ppm CH<sub>3</sub>OH. a) CO conversion with distinct methanol concentrations and b) related CO oxidation activation energies determination.

Moreover carbon dioxide concentration oscillations are observed at the reactor outlet *via* mass spectrometer analyses, only with CO containing mixtures. This suggests that only carbon monoxide oxidation is the source of these oscillations. Yet no quantitative study has been performed as oscillation frequency is too high to be detected by micro gas chromatography.

Activation energies of all TPR have been determined for CO and methanol conversion rates below 20%. Data are displayed in Figure 62b for methanol and Figure 63b for CO. A linear trend is recorded according to CO/methanol ratio (Figure 64) on the 0-0.6 ratio range. Indeed in this case with 3500ppm CH<sub>3</sub>OH, every 100ppm CO added to the inlet mixture leads to increase the methanol oxidation activation energy by 3 kcal.mol<sup>-1</sup>. Carbon monoxide activation energies also exhibits an increasing trend. Yet on the ideal case of pure CO, *i.e.* with an infinite CO/methanol ratio, the activation energy lies at 11 kcal.mol<sup>-1</sup>. Moreover as carbon monoxide inhibits its own oxidation, the contribution of methanol is not directly observable with these experiments.

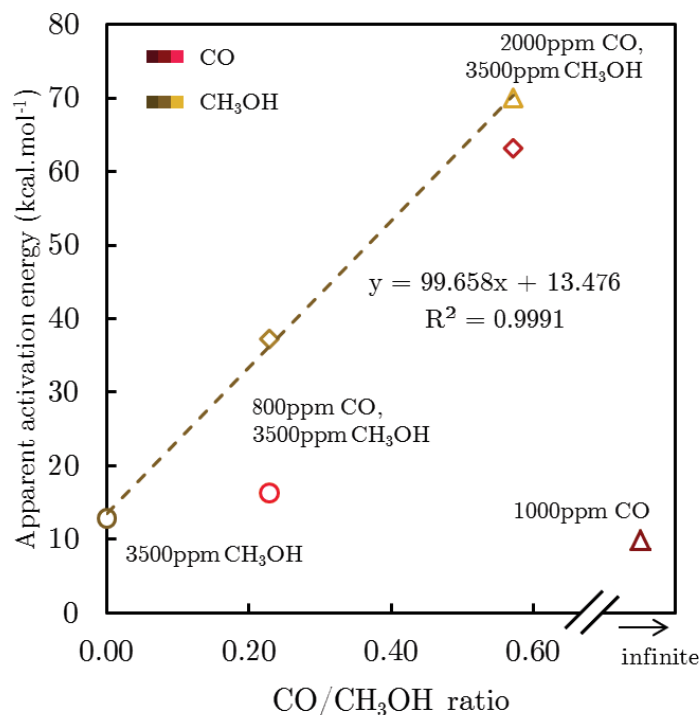


Figure 64: Activation energies of methanol/CO mixture oxidation according to CO/CH<sub>3</sub>OH ratio. Methanol activation energies are set in brown, while CO ones are in red. Linear characteristics of the methanol activation energies trend are displayed. The inlet gas mixtures are also reminded.

#### 6.2.1.2| *In operando* IR spectroscopy

Infrared spectroscopy allows to observe adsorbed species on the catalyst during the TPR. Spectra were probed through TPR experiments, at different temperatures. In order to determine bond vibration frequencies, Table 19 gathers the main observed wavenumbers and their related bond vibration according to prior studies<sup>273,274</sup>.

Table 19: Determination of solid IR vibrationnal modes during methanol oxidation according to literature<sup>273,274</sup>.

Catalyst	Assignments	Vibrational modes	Wavenumbers /cm <sup>-1</sup>	
			Literature	This study
Al <sub>2</sub> O <sub>3</sub>	Bridging methoxy <sup>273</sup>	$\nu_{C-O}$	1098	-
		$\delta_{CH_3}$	1200	-
		$\delta_{CH_3}$	1458	1452
		$\delta_{CH_3}$	1472	1469
		$\nu_{CH_3}$	2844	2842
		$\nu_{CH_3}$	2955	2948
		$\nu_{CH_3}$	2970	2999

Al <sub>2</sub> O <sub>3</sub>	Formate <sup>274</sup>	$\nu_{(s)}\text{OCO}$	1380	1378
		$\nu_{(as)}\text{OCO}$	1595	1597
		$\delta_{\text{CH}}$	1395	1396
		$\nu_{\text{CH}}$	2905	2908
		$\nu_{(a)}\text{OCO} + \delta_{\text{CH}}$	2970	2998
Al <sub>2</sub> O <sub>3</sub>	Formaldehyde <sup>274</sup>	$\delta_{\text{CH}}$	1280	-
		$\delta_{\text{CH}}$	1490	1470
		$\nu_{\text{C=O}}$	1695	1679
Mg vanadate	Free carboxylate COO <sup>-</sup> /acetate <sup>273</sup>	$\nu_{(as)}\text{OCO}$	1590	1597
		$\nu_{(s)}\text{OCO}$	1420	-

In order to evaluate IR absorption variations, differential spectra were calculated. It consist in subtracting absorption spectrum at low temperature T<sub>l</sub> to the consecutive spectrum at higher temperature T<sub>h</sub>. Consequently the catalyst and gas contributions to IR absorption are removed by subtraction. In this kind of analysis, a negative band indicates that a IR absorbant surface specie concentration is increasing. Figure 128 (Appendices) displays differential spectra for each methanol oxidation mixture.

Typical raw infrared absorption spectra are displayed in Figure 65 for pure methanol and Figure 66 with 800ppm CO mixture oxidation. Regarding oxidation of methanol without carbon monoxide, the main adsorbed species are the bridging methoxy adsorbed radical and formate species with typical bands at 1189, 1451, 1468, 2825, 2947, 2960 cm<sup>-1</sup> and 1377, 1396, 1597, 2907, 2998 cm<sup>-1</sup> respectively (Table 19). The presence of adsorbed water (around 1657 cm<sup>-1</sup>) at low temperature cannot be rule out. The hydroxyl groups of alumina becomes perturbed by adsorption of methoxy adsorbed radical, formate or water in line with the broad signal around 3400 cm<sup>-1</sup><sup>122</sup>. Additional bands are observed at 1334 and 1632 cm<sup>-1</sup> which can be assigned to carbonate species ( $\Delta\nu$  around 300 cm<sup>-1</sup>).

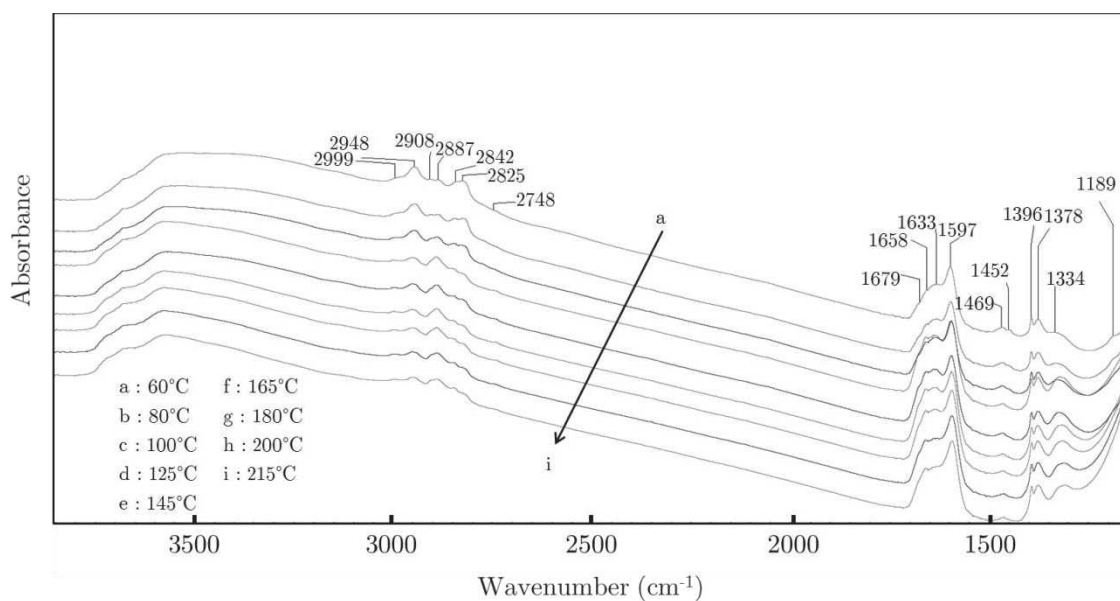


Figure 65: Solid infrared absorbance spectra during methanol oxidation (3500ppm, 8% vol. O<sub>2</sub>) according to temperature.

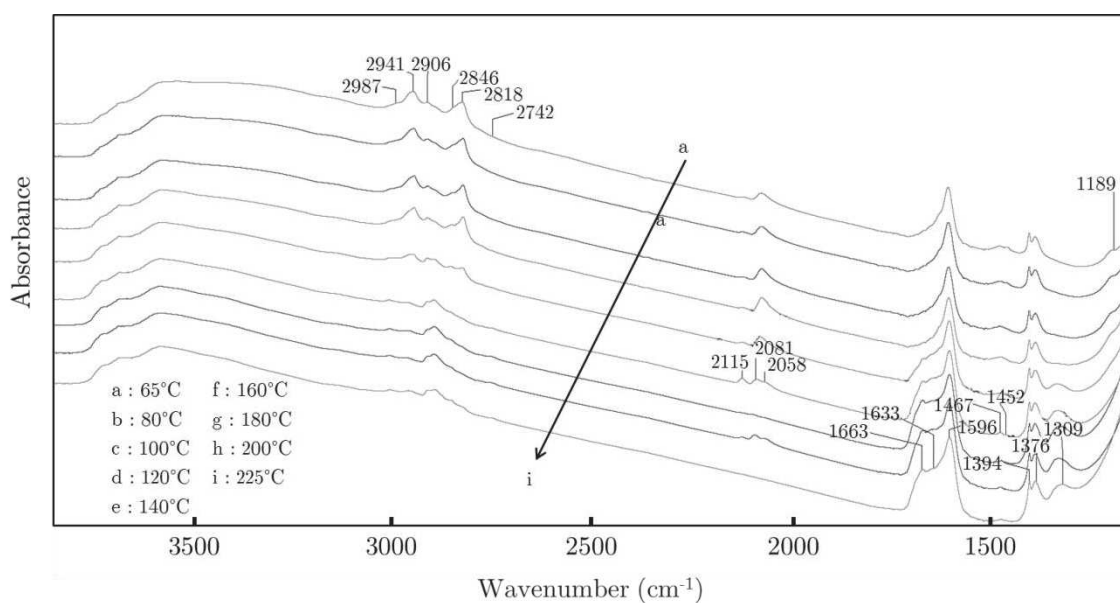


Figure 66: Solid infrared absorbance spectra during methanol/CO mixture oxidation (3500ppm, 800ppm CO, 8% vol. O<sub>2</sub>) according to temperature.

The differential spectra mainly put into evidence the development of carbonate species (1670-1325 cm<sup>-1</sup>) at the expense of methoxy adsorbed radical species (2960-2840 cm<sup>-1</sup>). Further increase of the signals related to formate species is also observed above 100°C.

In the presence of the methanol with 800ppm CO mixture (Figure 66), similar evolution of adsorbed species is obtained. Additional band from 2130 cm<sup>-1</sup> to 2075 cm<sup>-1</sup> is typical of linear carbonyl species adsorbed on Pt<sup>0</sup> as previously described in Chapter 4. The

intensity of this band decreases between 160°C and 180°C. The development of carbonate species appears delayed towards high temperature in the presence of CO. It should be highlighted that the intermediate formation of adsorbed formaldehyde cannot be observed during the experiments in our conditions.

## 6.2.2 | Oxidation of propene

### 6.2.2.1 | Global kinetics

Temperature programmed reaction set-up used for methanol oxidation was applied to propene oxidation. Oxidation of propene/CO inlet mixture was also undertaken. The specific operating conditions of the experiments are gathered in Table 20. Again, mass spectrometer was used as a highly sampling frequency recorder for both inlet and outlet gas fraction. Micro gas chromatography was used to address a quantitative conversion of CO and propene through temperature. Finally, IR spectroscopy has been used to identify adspecies presence and variations during the oxidation.

Table 20: Operating conditions for propene and propene/CO gas mixture oxidation TPR.

Total flow (mL.min <sup>-1</sup> )	30.0	Catalyst mass (mg)	12.0
C <sub>3</sub> H <sub>6</sub> rates (ppm)		GHSV (h <sup>-1</sup> )	91000
Without CO	3300		
With CO	1800		
CO rate (ppm)	1000	Temperature slope (°C.min <sup>-1</sup> )	2
O <sub>2</sub> rate (%)	10.0		

Figure 67a displays propene conversion according to temperature, for both propene and CO/propene mixture oxidations. The propene oxidation T<sub>50%</sub> lies at 223°C. In the case of propene/CO mixture, this temperature rises at 265°C. This 42°C shift can be due to the presence of carbon monoxide, or a possible effect of propene on its own oxidation. Indeed propene concentrations are different in the two TPR.

The work of Haneda<sup>275</sup> shows a lower T<sub>50%</sub> close to 170°C for a platinum catalyst on alumina with a dispersion of 0.81 (600ppm C<sub>3</sub>H<sub>6</sub>, 1% O<sub>2</sub>). They also highlighted an inhibitor effect with a decreasing platinum dispersion. One can observe that for propene oxidation, the 100% propene rate conversion is reached at lower temperature than for propene/CO mixture. In this case, oxidation goes on, up to 100°C higher.

Activation energies (Figure 67b) have been determined below 20% propene conversion. The activation energy of propene oxidation lies at 2.9 kcal.mol<sup>-1</sup>. The CO/propene mixture oxidation exhibits an identical propene oxidation activation energy. This suggests no significant effect of the addition of CO, at least for a 2/1 ratio between

propene and CO. Propene concentration has also no impact on its own activation energy.

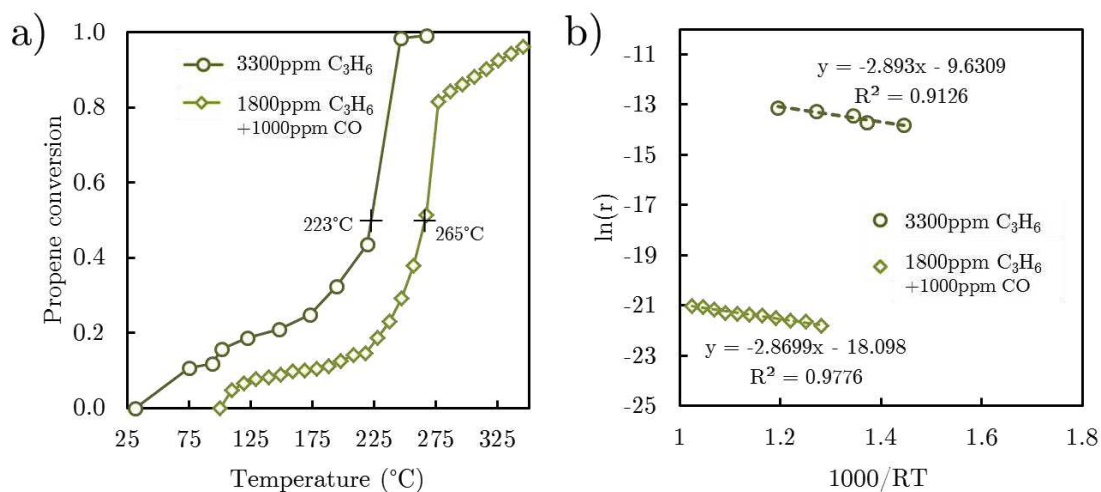


Figure 67: Temperature programmed reaction of the propene/CO mixtures (10% O<sub>2</sub>). a) Propene conversion with and without carbon monoxide and b) related propene oxidation activation energies determination (in kcal.mol<sup>-1</sup>).

Regarding CO conversion for the CO/propene TPR in Figure 68, the oxidation suddenly happens at 270°C. The T<sub>50%</sub> lies at 274°C. As a reminder, the CO conversion for CO oxidation (undertook in chapter 5) exhibits T<sub>50%</sub> equal to 170°C, with a wide oxidation temperature range. It is clear that propene has a considerable impact on CO oxidation. The presence of propene delays the CO oxidation T<sub>50%</sub> by 100°C. No influence of CO concentration can be responsible of this huge discrepancy. Indeed CO concentrations are identical between the two TPR. Interestingly the conversion of CO does not reach 100% on the scanned temperature range. A plateau is reached below 80% CO concentration. To explain this, two conditions have to be fulfilled: (i) propene adsorption is more favourable than CO one at temperature above 270°C, and (ii) the catalytic material quantity is not sufficient to address a full oxidation of propene and CO. Consequently a 100% global conversion is not accessible, that is fully endured by CO oxidation.

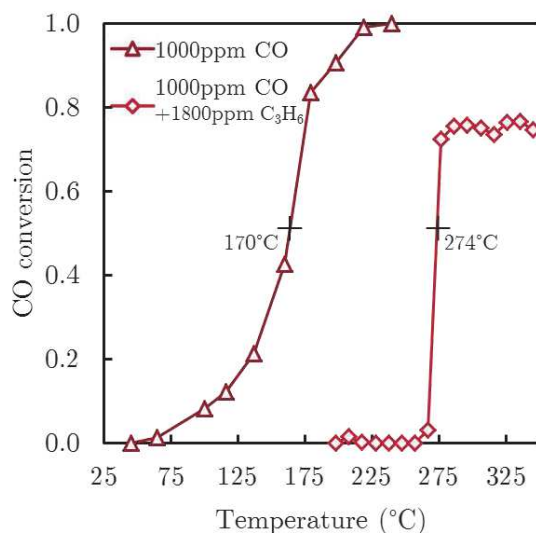


Figure 68: Temperature programmed desorption of the propene/CO mixtures (10% O<sub>2</sub>). Carbon monoxide conversion during TPR of the propene/CO mixture, and CO oxidation alone.

#### 6.2.2.2| *In operando* IR spectroscopy

Infrared spectroscopy was performed on both TPR. Raw infrared spectra through time are displayed in Figure 69 and Figure 70 respectively for propene and propene/CO mixture. The differential spectra are presented in Figure 129 (Appendices). Significant interferences have been recorded for propene oxidation TPR due to reflections between splitted monocristalline windows, that appear in the differential spectra (Figure 129 in appendices).

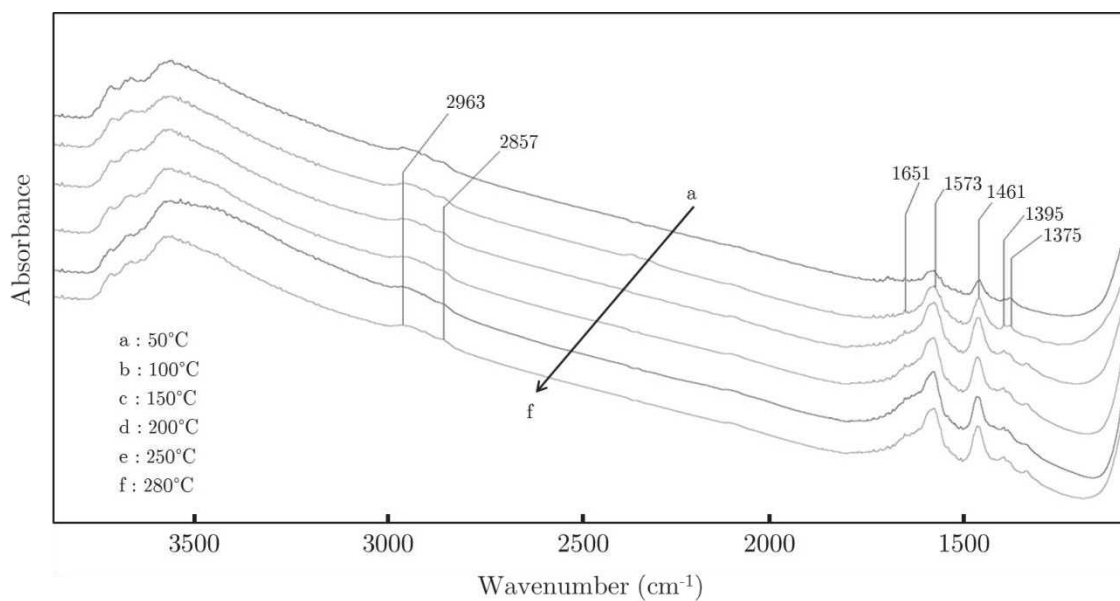


Figure 69: Solid infrared absorbance spectra during propene oxidation (3300ppm C<sub>3</sub>H<sub>6</sub>, 8% vol. O<sub>2</sub>) according to temperature.

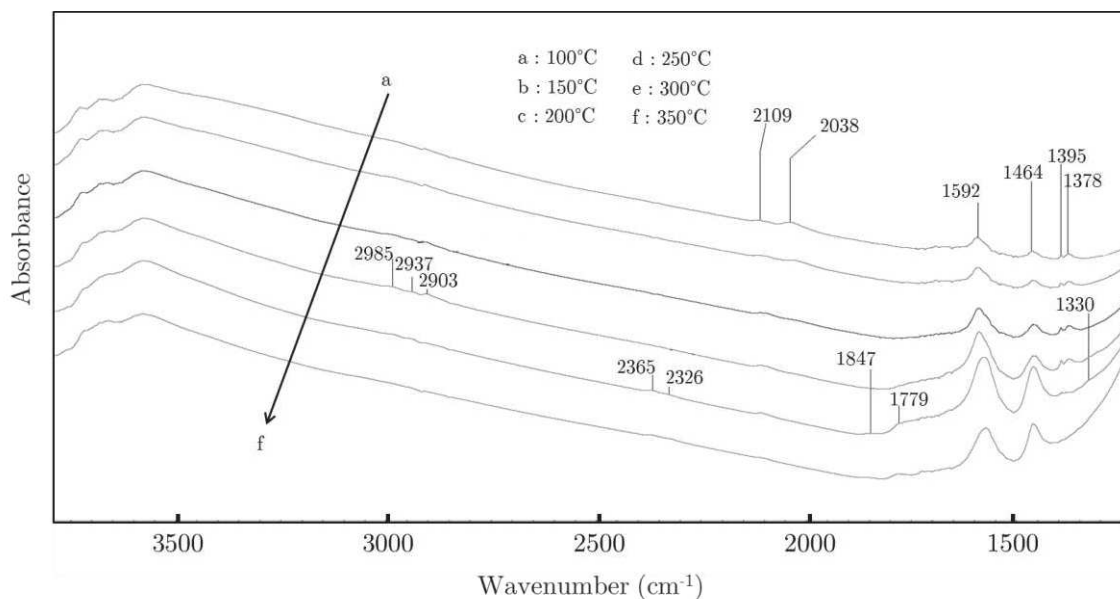


Figure 70: Solid infrared absorbance spectra during propene/CO mixture oxidation (1800ppm C<sub>3</sub>H<sub>6</sub>, 1000ppm CO, 8% vol. O<sub>2</sub>) according to temperature.

The presence of adsorbed water is revealed by the band at 1650 cm<sup>-1</sup> and the broad band related to perturbed hydroxyl species from alumina support (Figure 69). The increase in temperature leads to the desorption of water in agreement with the negative bands at 1650 and 3300 cm<sup>-1</sup> observed on differential spectra. Above 150°C, the intensity of bands related to formate and carboxylate or acetate species increases continuously. Additional band at 1720 cm<sup>-1</sup> develops between 200 and 250°C. The later band can be assigned to C=O stretching vibration of partly oxidized compound.

Regarding propene/CO oxidation at 100°C (Figure 70), the formation of formate species (1378, 1394, 1591cm<sup>-1</sup>) and carbonate species (1464cm<sup>-1</sup>) is observed. Two types of carbonyl species are revealed at low temperature: CO adsorbed on Pt<sup>2+</sup> (2109cm<sup>-1</sup>) and CO adsorbed on Pt<sup>0</sup> (2038cm<sup>-1</sup>). The evolution of adsorbed species shows mainly the increase of IR bands related to formate, carboxylate or acetate species as well as the C=O stretching vibration of partly oxidized compound. Above 300°C the formate species are completely consumed whereas the spectra is mainly dominated by carboxylate or acetate species. In this range of temperature, the CO conversion to CO<sub>2</sub> reaches 75%.

Propene oxidation shares a significant impact of the presence of CO in the inlet mixture. However for propene oxidation, the T<sub>50%</sub> is shifted, conserving identical activation energy. Regarding CO impact on methanol oxidation, the T<sub>50%</sub> does not significantly changes while activation energies are considerably increasing with CO/methanol ratio.

Propene and methanol also influence the oxidation of CO. Thanks to CO temperature programmed reaction performed in chapter 5, this influence has been benchmarked. The presence of propenes delays of 100°C the  $T_{50\%}$  of CO oxidation. Propene is also expected to stem CO adsorption and therefore limits CO oxidation. Regarding methanol impact on carbon monoxide, activation energies increase with CO/methanol ratio. Yet it could be only due to CO inhibition effect on its own oxidation. Methanol as moreover few influence on  $T_{50\%}$  CO conversion.

Infrared spectroscopy allows handle surface phenomena. Methoxy radical is clearly observed for both methanol and methanol/CO mixtures. Infrared spectra during propene and propene/CO oxidation experiments exhibit the presence of hydrogen-containing radicals. The addition of carbon monoxide is clearly visible on the spectra as typical  $2120\text{cm}^{-1}$  to  $240\text{cm}^{-1}$  absorption bands. The presence of formate, carboxylate or acetate are also reported, that may be due to reactions between oxidation intermediates and alumina hydroxyl groupments. Yet accurate identification of oxidation intermediates is not straightforward. Their determination would be of interest regarding reaction path analyses of future simulated hydrocarbon oxidation.

To conclude about experimental oxidation of light hydrocarbons mixtures, the inlet gas composition plays a major role in chemicals oxidation. Large discrepancies have been recorded with a simple set of TPR. This suggests complex adsorption and oxidation effects between hydrocarbons and CO. This experiment set has allowed to draw general conclusion with quantitative indicator variations, such as oxidation  $T_{50\%}$  and activation energies. Surface analysis through IR spectroscopy has brought some key points about potential oxidation intermediates and has allowed to address assumptions for hydrocarbon an CO competition.

### 6.3| Molecular modelling of $\text{C}_0\text{-C}_3$ on Pt(111)

In order to address molecular modelling of light hydrocarbons oxidation, extensive *ab initio* calculations have been performed. Atoms, molecules and radicals from C0 to C3 were modelled in both gas and adsorbed phases. To limit the studied adsorption mode, these compounds were studied on Pt(111) surface. Calculation conditions are detailed in section 2.3. Despite several initial configurations were tested, only one adsorption mode per specie is discussed (the most stable one). Gas phase calculations were performed on atoms, molecules and radicals in order to determine the adsorption energy. This energy is used in order to built the UBI-QEP based kinetic scheme detailed in section 6.4. In gas phase, *ab initio* calculations consisted here in spin-polarized 0K geometry optimizations to evaluate species energetics. Surface species calculations also consist in 0K geometry optimizations. Consequently electronic adsorption energies of atoms, molecules and radicals were determined. This work

constitutes therefore an updated GGA-PBE database about adsorbed radicals on Pt(111).

### 6.3.1| Atomic and molecular adsorption

Investigations started with atoms and selected molecules adsorption at low coverage, *i.e.* one atom or molecule per Pt(111) box. Adsorption modes found for H, O and C atoms are respectively top and hollow fcc. Adsorption energies are close to the highest estimations from previous works (Figure 71). Hydrogen adsorption energy lies at  $-73$  kcal.mol<sup>-1</sup> (according to atomic gas phase hydrogen). Prior GGA and B3LYP calculations provided a value around  $-62$  kcal.mol<sup>-1</sup>. For oxygen, the range is wider from  $-70$  kcal.mol<sup>-1</sup> to  $-107$  kcal.mol<sup>-1</sup>. GGA PBE functional calculations constitute the stronger adsorption energies of the literature. These recent works corroborate our calculation. Concerning carbon atom, few GGA PW91 exhibit similar energies than the present work with  $-168$  kcal.mol<sup>-1</sup>. B3LYP data are much lower but might neglect long interaction energies as they were obtained on cluster models, displaying only three slabs and no periodicity.

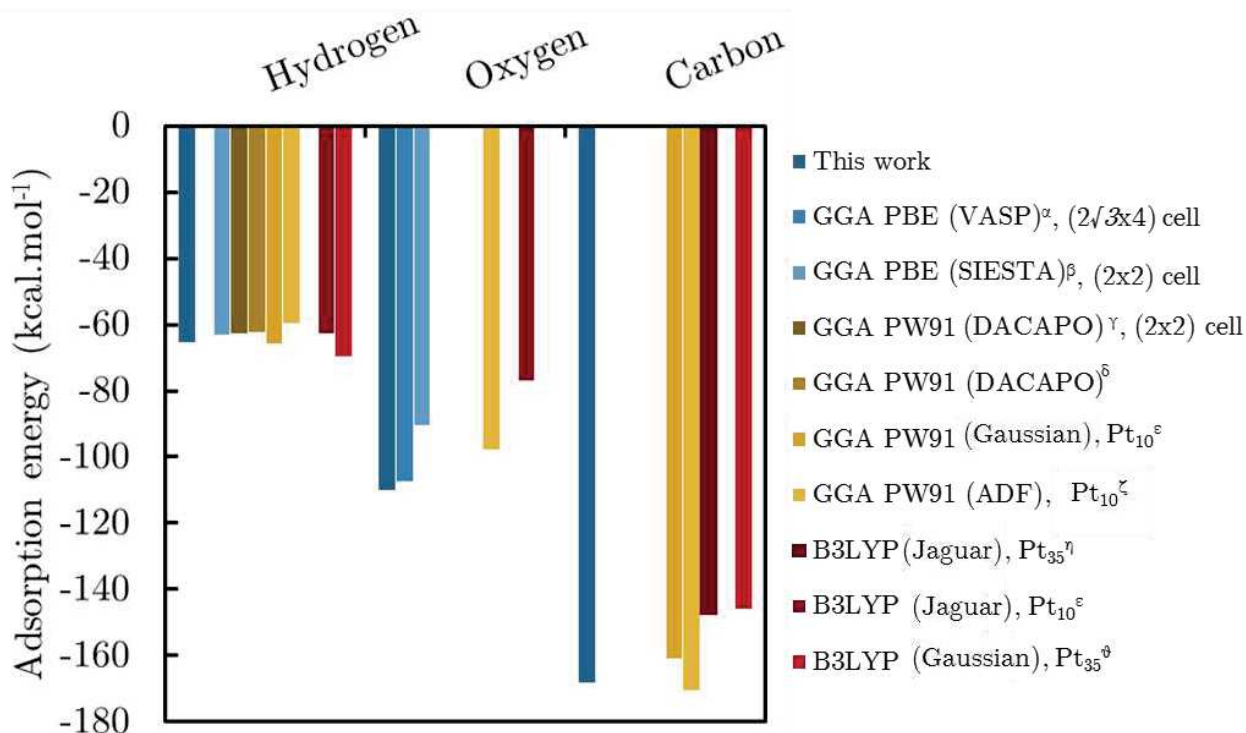


Figure 71: Adsorption energies for atoms on Pt(111) with one radical per cell. For GGA PBE, the work of <sup>α</sup>Qiang *et al.*<sup>276</sup> and <sup>β</sup>Stamatakis *et al.*<sup>277</sup> are reported. PW91 functional has been used by <sup>γ</sup>Ferrin *et al.*<sup>278</sup>, <sup>δ</sup>Mavrikakis *et al.*<sup>279</sup>, <sup>ε</sup>Psofogiannakis *et al.*<sup>280</sup> and <sup>ζ</sup>Chak-Tong *et al.*<sup>281</sup>. Pt(111) surface was modelled *via* clusters using B3LYP functional in <sup>η</sup>Goddard *et al.*<sup>282</sup>, <sup>θ</sup>Jacob *et al.*<sup>283</sup> and <sup>ε</sup>Psofogiannakis *et al.*<sup>280</sup>.

Selected C<sub>0</sub>-C<sub>3</sub> molecules from Table 6 were evaluated. As suggested by previous studies, dihydrogen is not stable on Pt(111) and undergoes a dissociative adsorption<sup>284</sup>, as well as methane<sup>285</sup>. Also propane was not found stable without dissociative adsorption. Molecular adsorption energies are reported in Figure 72. One can see that significant disparities appear according to functionals. The case of carbon monoxide, that is peculiar due to DFT C-O bond misestimation, exhibits a 15 kcal.mol<sup>-1</sup> adsorption energy range. For most of the molecules, adsorption energies are gathered in a range, thinner than 15 kcal.mol<sup>-1</sup>.

One can noticed that dioxygen is one of the most strongly adsorbed molecules among C<sub>0</sub>-C<sub>3</sub> selected species. Only carbon dioxide and oxalic acid have ositive adsorption energies, *i.e.* not favoured on Pt(111).

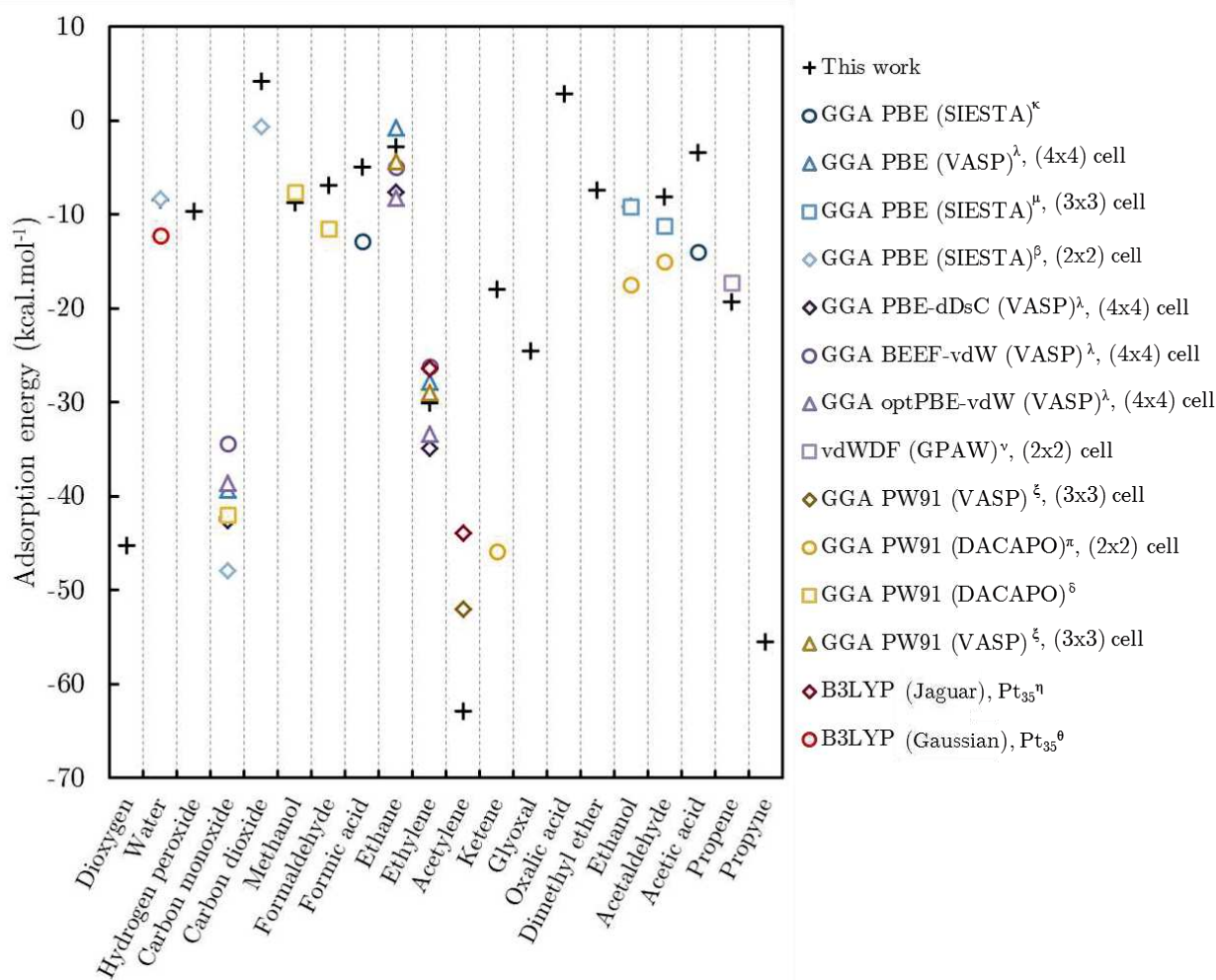


Figure 72: Adsorption energies of C<sub>0</sub>-C<sub>3</sub> selected molecules at low coverage on Pt(111) with one radical per cell. The work of <sup>k</sup>Saliccioli *et al.*<sup>286</sup>, <sup>l</sup>Stamatakis *et al.*<sup>277</sup>, <sup>m</sup>Vlachos *et al.*<sup>287</sup>, <sup>v</sup>Honkala *et al.*<sup>288</sup>, <sup>l</sup>Gautier *et al.*<sup>118</sup>, <sup>δ</sup>Mavrikakis *et al.*<sup>279</sup>, <sup>π</sup>Alcalà *et al.*<sup>289</sup>, <sup>ξ</sup>Aleksandrov *et al.*<sup>290</sup>, <sup>η</sup>Goddard *et al.*<sup>282</sup> and <sup>θ</sup>Jacob *et al.*<sup>283</sup> are reported.

Moreover one can observe that acetylene and ketene adsorption energies lies far from previously determined ones. Concerning ketene, Alcalà and coworkers<sup>289</sup> simulated the molecule on a 2 by 2 two layer Pt(111) unit cell. Favourable lateral interactions between ketene molecules could explain the significant discrepancy. Also no adsorption energies have been found in literature for some molecules. This is the case of hydrogen peroxide, glyoxal, oxalic acid, dimethyl ether and propyne.

### 6.3.2| Adsorption of radicals

From these selected molecules and thanks to an automated code that generates probable radicals from these molecules (detailed in section 2.4.4.), *ab initio* calculations have been performed on Pt(111) adsorbed radicals. More than a hundred C<sub>0</sub>-C<sub>3</sub> radicals were calculated in both spin polarized gas phase and Pt(111) adsorbed states. For some C<sub>1</sub> and C<sub>2+</sub> radicals, three adsorption modes were tested. The one that exhibits the lowest electronic energy was kept. Table 21 gathers the characteristics of these radicals, compared with literature.

Most of the adsorption energies found are close to prior GGA level computed ones. Discrepancies are noticed for H containing species, that might be due to misestimation of Van der Waals contribution by the chosen PBE functional.

Table 21: Characteristics of radical adsorption on Pt(111) determined *via ab initio* molecular modelling on a Pt(111) surface with one radical per cell.

Name	Formula	Adsorption mode	Illustration (appendices)	Adsorption energy (kcal.mol <sup>-1</sup> )	Previous comput. results
Hydroxyl	OH*	O <sub>b</sub>	Figure 130e	-56.7	-47 <sup>283</sup> , -49 <sup>279</sup>
Peroxy	OOH*	O <sub>t</sub>	Figure 131b	-30.9	-24 <sup>283</sup>
Methyl	CH <sub>3</sub> *	C <sub>t</sub>	Figure 132b	-49.6	-45 <sup>279</sup> , -50 <sup>282</sup>
Methylidene	CH <sub>2</sub> *	C <sub>b</sub>	Figure 132c	-98.6	-95 <sup>282</sup> , -104 <sup>291</sup>
Methylidyne	CH*	C <sub>h</sub>	Figure 132d	-158	-146 <sup>282</sup> , -166 <sup>291</sup>
Methoxy	CH <sub>3</sub> O*	O <sub>t</sub>	Figure 133a	-41.1	-36 <sup>279</sup>
Hydromethyl	CH <sub>2</sub> OH*	C <sub>t</sub>	Figure 133d	-49.6	-46 <sup>279</sup>
Hydroxymethylene	CHOH*	C <sub>b</sub>	Figure 133e	-80.4	-75 <sup>279</sup>
Formyl	CHO*	C <sub>t</sub>	Figure 133c	-57.4	-54 <sup>279,286</sup>
Carboxyl	COOH*	C <sub>t</sub> - O <sub>t</sub>	Figure 134d	-58.5	-59 <sup>277</sup> , -62 <sup>286</sup>
Formate	HCOO*	O <sub>t</sub> - O <sub>t</sub>	Figure 134c	-57.8	-56 <sup>277</sup>
-	CCH*	C <sub>t</sub> - C <sub>b</sub>	Figure 135b	-115	-109 <sup>290</sup> , -141 <sup>282</sup>
Dicarbon	CC*	C <sub>t</sub> - C <sub>b</sub>	Figure 135c	-148	-148 <sup>290</sup> , -141 <sup>282</sup>
Vinyl	CHCH <sub>2</sub> *	C <sub>t</sub> - C <sub>b</sub>	Figure 135e	-68	-65 <sup>292</sup> , -72 <sup>290</sup>

Vinylidene	CCH <sub>2</sub> *	C <sub>t</sub> – C <sub>b</sub>	Figure 135f	-105	-94 <sup>292</sup> , -98 <sup>282</sup>
Ethyl	CH <sub>3</sub> CH <sub>2</sub> *	C <sub>t</sub>	Figure 136b	-46	-39 <sup>292</sup> , -46 <sup>282</sup>
Ethylidene	CH <sub>3</sub> CH*	C <sub>b</sub>	Figure 136c	-93	-85 <sup>292</sup> , -90 <sup>282</sup>
Ethylidyne	CH <sub>3</sub> C*	C <sub>h</sub>	Figure 136d	-141	-132 <sup>292</sup> , -134 <sup>282</sup>
Ketenyl	CHCO*	C <sub>t</sub> – C <sub>b</sub>	Figure 136f	-92.5	-91 <sup>289</sup>
-	CCO*	C <sub>t</sub> – C <sub>b</sub>	Figure 137a	-135	-125 <sup>289</sup>
-	COC(H,O)*	C <sub>t</sub> – C <sub>t</sub> – O <sub>t</sub>	Figure 137c	-55.3	
Formylmethylene	CHC(H,O)*	O <sub>t</sub> – C <sub>b</sub>	Figure 137d	-101	
-	C(O,OH)C(O,O)*	O <sub>t</sub> – O <sub>t</sub>	Figure 138a	-46.8	
-	COC(O,OH)*	C <sub>t</sub>	Figure 138b	-58.9	
-	COHC(O,OH)*	O <sub>t</sub> – C <sub>b</sub>	Figure 138c	-77.0	
-	COHC(O,O)*	O <sub>t</sub> – C <sub>b</sub>	Figure 138d	-113	
-	C(O,O)C(O,O)*	O <sub>t</sub> – O <sub>t</sub>	Figure 138e	-147	
-	COC(O,O)*	O <sub>t</sub> – C <sub>b</sub> – O <sub>t</sub>	Figure 138f	-75.0	
Hydroxyethynyl	CCOH*	C <sub>t</sub> – C <sub>b</sub>	Figure 139a	-132	-118 <sup>289</sup>
-	COHCOH*	C <sub>t</sub> – C <sub>b</sub>	Figure 139b	-87.0	
-	COCOH*	C <sub>t</sub> – C <sub>b</sub>	Figure 139c	-86.2	
-	COCO*	C <sub>t</sub> – C <sub>t</sub>	Figure 139d	-192	
-	CC(O,OH)*	C <sub>h</sub>	Figure 139e	-133	
-	CHOCH <sub>3</sub> *	C <sub>b</sub>	Figure 140a	-78.4	
-	COCH <sub>3</sub> *	C <sub>h</sub>	Figure 140b	-76.0	
-	CH <sub>2</sub> OCH <sub>2</sub> *	C <sub>t</sub> – C <sub>t</sub>	Figure 140c	-75.8	
-	CHOCH <sub>2</sub> *	C <sub>t</sub> – C <sub>b</sub>	Figure 140d	-121	
-	CHOCH*	C <sub>b</sub> – C <sub>b</sub>	Figure 140e	-162	
-	CHOC*	C <sub>b</sub> – C <sub>h</sub>	Figure 140f	-177	
Ethoxy	CH <sub>3</sub> CH <sub>2</sub> O*	O <sub>t</sub>	Figure 141b	-40.9	-43 <sup>289</sup>
Acetyl	CH <sub>3</sub> CO*	C <sub>t</sub> – O <sub>t</sub>	Figure 141d	-171.3	
-	CHCH <sub>2</sub> OH*	C <sub>b</sub>	Figure 141f	-98.3	
Formylmethyl	CH <sub>2</sub> C(H,O)*	C <sub>t</sub> – C <sub>t</sub> – O <sub>t</sub>	Figure 141e	-46.2	-54 <sup>289</sup>
Ethylene oxide	CH <sub>2</sub> CH <sub>2</sub> O*	C <sub>t</sub> – O <sub>t</sub>	Figure 142a	-85.3	
-	CHCH <sub>2</sub> O*	C <sub>t</sub> – O <sub>b</sub>	Figure 142b	-135	-71 <sup>289</sup>
1-Hydroxyethyl	CH <sub>3</sub> CHOH*	C <sub>t</sub>	Figure 142c	-56.7	-49 <sup>289</sup>
1-Hydroxyethylidene	CH <sub>3</sub> COH*	C <sub>t</sub>	Figure 142d	-66.9	-80 <sup>289</sup>
1-Hydroxyvinyl	CH <sub>2</sub> COH*	C <sub>t</sub>	Figure 142e	-59.0	-88 <sup>289</sup>
Hydroxyethylene	CH <sub>2</sub> CHOH*	C <sub>t</sub> – C <sub>t</sub>	Figure 142f	-29.2	-33 <sup>289</sup>
2-Hydroxyvinyl	CHCHOH*	C <sub>t</sub>	Figure 143a	-64.7	-86 <sup>289</sup>
Hydroxyacetylene	CHCOH*	C <sub>t</sub> – C <sub>b</sub>	Figure 143b	-69.7	-78 <sup>289</sup>
Hydroxyvinylidene	CCHOH*	C <sub>b</sub>	Figure 143c	-136	-146 <sup>289</sup>
-	CH <sub>3</sub> C(O,O)*	O <sub>t</sub> – O <sub>t</sub>	Figure 143e	-56.5	-52 <sup>286</sup>
-	CH <sub>2</sub> C(O,O)*	O <sub>t</sub> – O <sub>t</sub>	Figure 143f	-66.2	-42 <sup>286</sup>
-	CH <sub>2</sub> C(O,OH)*	C <sub>t</sub> – O <sub>t</sub>	Figure 144a	-47.2	-47 <sup>286</sup>
-	CHC(O,OH)*	O <sub>t</sub> – C <sub>b</sub>	Figure 144b	-99.4	-97 <sup>286</sup>
-	CC(O,OH)*	C <sub>h</sub>	Figure 144c	-133	-133 <sup>286</sup>
Isopropyl	CH <sub>3</sub> CHCH <sub>3</sub> *	C <sub>t</sub>	Figure 145b	-41.1	-41 <sup>291</sup>

-	$\text{CH}_3\text{CCH}_3^*$	$\text{C}_t$	Figure 145d	-78.1	$-85^{291}$
-	$\text{CH}_3\text{CHCH}^*$	$\text{C}_t - \text{C}_b$	Figure 145e	-75.5	
-	$\text{CH}_2\text{CCH}_3^*$	$\text{C}_t$	Figure 145f	-121	
-	$\text{CH}_3\text{CHC}^*$	$\text{C}_t - \text{C}_b$	Figure 146a	-67.1	
-	$\text{CH}_2\text{CCH}_2^*$	$\text{C}_t - \text{C}_t$	Figure 146c	-35.2	

This dataset allows to determine adsorption energy trends according to adsorption mode. For instance Figure 73 presents the Pt-OR adsorbed radicals according to groupment R. One can see that oxygen is the strongest bonded radical. Regarding OH radical, hydrogen weakens the adsorption bond between platinum and oxygen. Considering groupment R of increasing size, the trend is almost linear between O and OOH, with an early plateau with a saturated ethyl groupment. Therefore heavier saturated oxygen adsorbed radicals may display an adsorption energy between -40 and -50 kcal.mol<sup>-1</sup>. Note that such a result may be impacted by the use of non-local exchange correlation functionals, or functionals corrected by a dispersion term. This would be valid for a low covered Pt(111) surface. Considering Pt-O bond length, one can notice that bridge bonds are 10% longer than hollow ones.

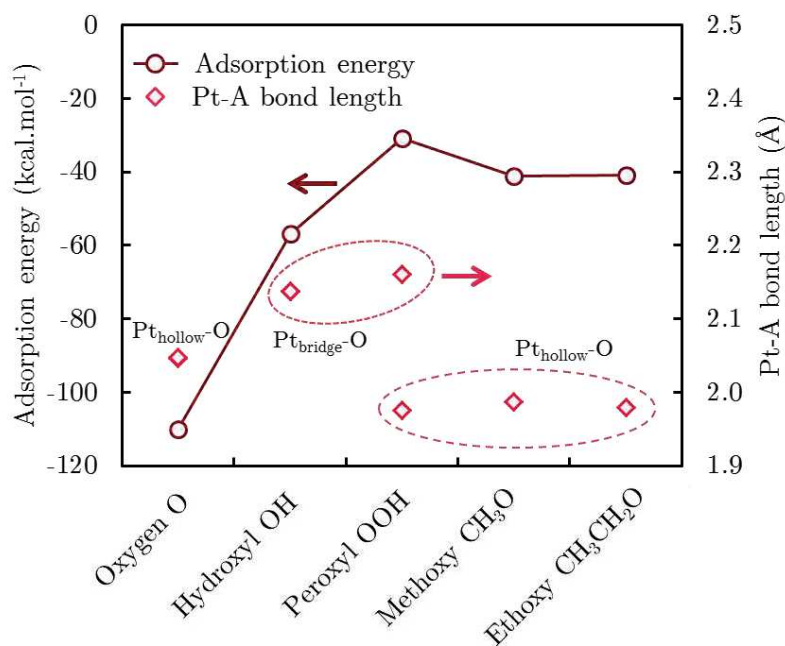


Figure 73: *Ab initio* determined adsorption energies and bond lengths of Pt-OR adsorbed species on Pt(111) with one radical per cell.

Figure 74 gathers the Pt-CR adsorption mode characteristics. One can observe carbon or alkylidyne, in other terms components with the minimal number of hydrogen atoms bonded to the C linked with the surface leads to strong adsorption energy for C<sub>1</sub> and C<sub>2</sub> radicals. For radicals that only lack one hydrogen compared to their related molecules

( $\text{CH}_3$ ,  $\text{CH}_3\text{CH}_2$ ,...), adsorption energy range is narrow and comprised between -40 and -50  $\text{kcal.mol}^{-1}$ . Therefore low dehydrogenated alkanes preferred adsorption mode is Pt-CR with an adsorption energy close to -45  $\text{kcal.mol}^{-1}$ . One can expect that hydrogen saturated heavy alkanes have a typical adsorption energy of methyl, ethyl or isopropyl. For highly dehydrogenated radicals, electronic adsorption energies are very different due to the radical stabilisation onto the surface, but also gas phase radical energy. Yet this energy varies significantly due to radical stability in gas phase.

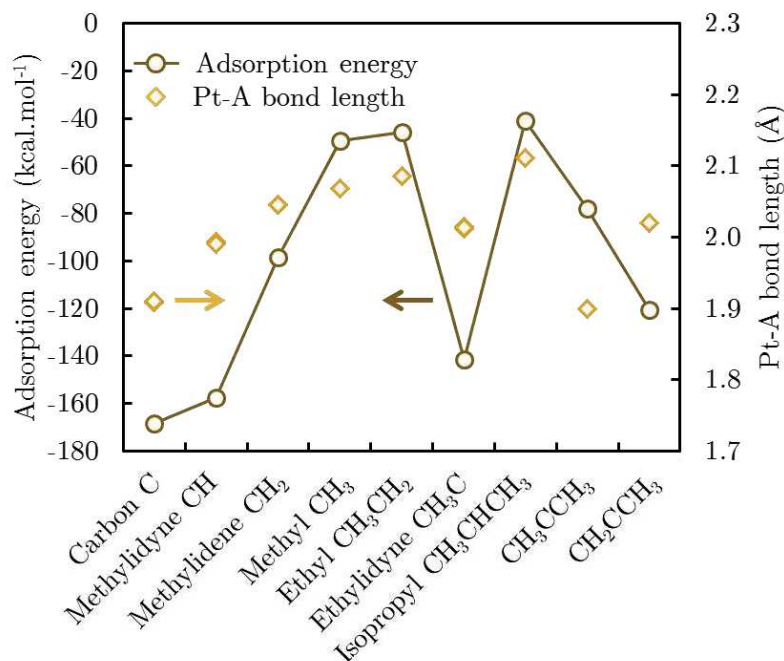


Figure 74: *Ab initio* determined adsorption energies and bond lengths of Pt-CR adsorbed species with one radical per cell.

As a conclusion about *ab initio* calculations, we benchmarked adsorbed  $\text{C}_0\text{-C}_3$  molecules and radicals on Pt(111). The use of PBE functional allows to handle almost a large panel of adspecies, with attenuated discrepancies regarding prior studies with specific functionals. This dataset can be used as a base for many kinetic mechanism that deals with heterogeneous reactions on platinum that involve  $\text{C}_x\text{H}_y\text{O}_z$  species. In order to be representative of oxidizing operating conditions, oxidized Pt(111) surface must be taken into account, at various oxygen coverage and in co-adsorption with the radicals. This may not be done extensively easily. One can assume that calculations of key radicals on oxidised Pt(111) would be used to determine energetic trends according to oxygen coverage, and therefore reduce the number of calculated radicals on oxidised Pt(111).

These data can also be used as a base to forecast high hydrocarbon adsorption energies from the light ones. Trends can help bypassing exhaustive radical calculations for heavy models on Pt(111), which may however be affected by the lack of dispersion corrections. Yet poly-functional radical characteristics are difficult to forecast. Indeed

adsorption modes can be competitive. Also one must take into account stereoisomerism as an impact factor on both adsorption mode and energy. Finally a larger database would allow to draw group contributions.

## 6.4| Preliminary micro-kinetic simulations of methanol oxidation

In order to simulate oxidation TPR of methanol, simulations were performed using a C<sub>0</sub>-C<sub>1</sub> micro-kinetic model. The model was tested with experimental conditions of pure methanol oxidation. Several scheme versions were tested.

The development of a surface reaction generator was required in order to manage the generation including reaction pathways definition as well as kinetic parameter evaluation. This reaction generator is detailed in section 2.4.4. The selected C<sub>0</sub>-C<sub>1</sub> molecules present in section 6.3.1 and *ab initio* determined related radicals of section 6.3.2 constituted the species set used for reaction generation. *Ab initio* electronic adsorption energies found in section 6.3 were used as reaction activation barriers. The pre-exponential factors were evaluated based on the transition state theory estimations from Dumesic<sup>137</sup>, *i.e.* a factor of 10<sup>13</sup> s<sup>-1</sup> for adsorption reactions and 10<sup>11</sup> s<sup>-1</sup> for surface reactions. Adsorption sticking coefficient were set by default to 1. Only activation barriers are thermo-consistent in the schemes according to the UBI-QEP method.

Three successive versions of the C<sub>0</sub>-C<sub>1</sub> micro-kinetic schemes were tested (Cf. Table 22) in order to evaluate successively the impact of various parameters :

- The raw model (RAW), based on previously determined *ab initio* data (section 6.3) with UBI-QEP determined activation energies (section 2.4.4), allows to evaluate the relevance of the automatically generated and non altered scheme.
- The oxygen improved model (OXY), based on the first one with Pt(111) *ab initio* kinetic parameters found in Chapter 3 (oxygen adsorption/desorption from Pt(111), section 3.3.3).
- The methanol improved model (MET), including the OXY subset from which methanol adsorption has been favored.

Table 22: Micro-kinetic characteristics of the C<sub>0</sub>-C<sub>1</sub> models through the three versions (RAW, RED and DES).

Scheme versions	O <sub>2</sub> adsorption reactivity	Methanol desorption reactivity
C <sub>0</sub> -C <sub>1</sub> -RAW Raw	s <sub>O2</sub> =1, E <sub>ads</sub> =0 (dy default)	E <sub>des</sub> =0.9 kcal.mol <sup>-1</sup> A <sub>des</sub> =10 <sup>13</sup> s <sup>-1</sup> (dy default)

C <sub>0</sub> -C <sub>1</sub> -OXY Oxygen improved	s <sub>O2</sub> =0.01, E <sub>ads</sub> =0.8+24.2 kcal.mol <sup>-1</sup>	E <sub>des</sub> =0.9 kcal.mol <sup>-1</sup> A <sub>des</sub> =10 <sup>13</sup> s <sup>-1</sup> (dy default)
C <sub>0</sub> -C <sub>1</sub> -MET Methanol improved	s <sub>O2</sub> =0.01, E <sub>ads</sub> =0.8+24.2 kcal.mol <sup>-1</sup>	E <sub>des</sub> =2 kcal.mol <sup>-1</sup> A <sub>des</sub> =10 <sup>11</sup> s <sup>-1</sup> (dy default)

The simulations were undertaken into two steps: (i) the adsorption simulation of 1 hour at 30°C. Conditions of pure methanol oxidation similar to the experimental one were set, i.e. 1000 ppm of methanol and 8% of O<sub>2</sub> completed with inert gas He. Then (ii) temperature programmed reaction was simulated with the same gas composition and 30°C as the initial temperature. The final temperature simulated is adapted in the simulation in order to speed up the calculation time.

The first micro-kinetic model tested was the raw model (RAW). This model is purely defined by UBI-QEP kinetic parameters. In this model methanol and dioxygen adsorption do not have an electronic barrier. In order to evaluate this raw model, the adsorption simulation step was performed, followed by the oxidation step. Surface species proportions are displayed in Table 23. No free platinum sites are recorded. The surface is full of atomic oxygen. Considering the oxidation step, no reaction occurred in the simulated temperature range, i.e. from 30°C to 280°C. Atomic oxygen is the only recorded surface specie during the whole simulated TPR. This is due to the strong adsorption energy of oxygen on Pt(111) surface. Moreover no dissociation energy has been allocated to O<sub>2</sub> dissociation in this automatically generated model. Therefore oxygen saturates the surface, no methanol is able to adsorb leading to a no reactive system. This means that oxidation would not occur below partial dioxygen desorption.

Table 23: Surface species proportions after a one hour adsorption step (1000 ppm CH<sub>3</sub>OH, 8% O<sub>2</sub>).

Scheme versions	Surface species proportions
C <sub>0</sub> -C <sub>1</sub> -RAW Raw scheme	Oxygen: 1
C <sub>0</sub> -C <sub>1</sub> -OXY Oxygen improved	Platinum sites: 0.66 Oxygen: 0.34
C <sub>0</sub> -C <sub>1</sub> -MET Methanol improved	Methanol: 0.81 Oxygen: 0.19

In order to improve the RAW model, the previously investigated O<sub>2</sub> dissociative adsorption thermodynamic parameters were implemented to generate the “oxygen improved” (OXY) model. This implies an electronic dissociation barrier, that depends

linearly on oxygen coverage (section 3.3.3). The  $O_2$  sticking coefficient was altered to 0.01 according to the literature detailed in Chapter 3<sup>85</sup>. Surface species during the adsorption step with the OXY model is displayed in Figure 75. One can observe that this updated model initiates a partial oxidation of the platinum surface that leads to a surface third-partly covered with atomic oxygen. The rest of the surface constitutes free platinum sites. Except inlet gases, water is recorded at the outlet, *i.e.* less than  $10^{-2}$  ppm.

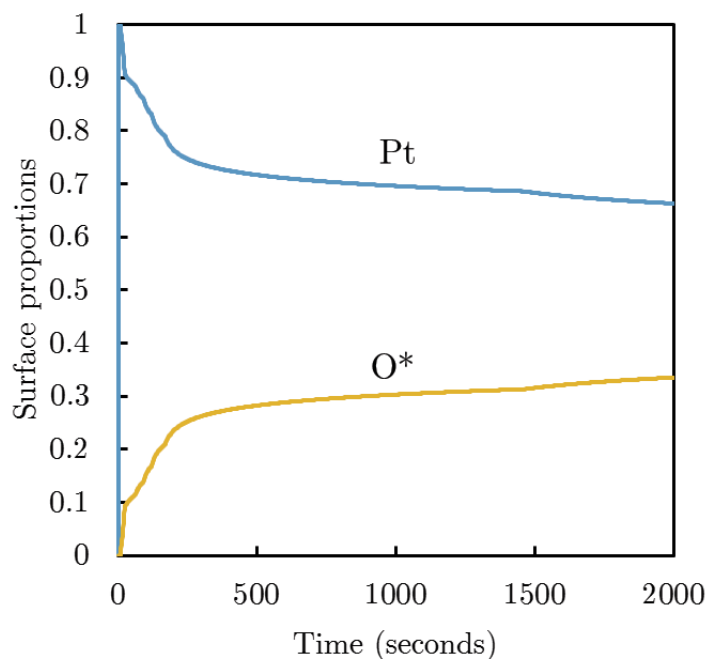


Figure 75: Surface species proportions of the simulated adsorption step of methanol with the OXY micro-kinetic model. Gas inlet consist in 8%  $O_2$  and 1000ppm  $CH_3OH$  at  $30^\circ C$ .

Temperature Programmed Reaction simulation has been performed with the OXY model and the previously discussed surface species proportions. This oxidation produces very few carbon-containing species: formaldehyde and formic acid (Figure 76a). Regarding surface species, free platinum sites and atomic oxygen mainly occupy the surface (Figure 76b). Oxygen surface specie concentration increases with temperature. One can notice that methanol concentration drops with increasing temperature that may be due to slow methanol readsorption. This suggests that methanol desorption energy is weak and therefore desorption is favored compared to adsorption reaction. Methanol adsorption kinetic parameters may be the key reaction for methanol oxidation to occur. Our experiments as well as of the one reported by Lin et al. do not display the formation of such species<sup>272</sup>, but only water and  $CO_2$ .

As  $C_0$ - $C_1$  kinetic models lead to time-consuming simulations, the TPR was not simulated beyond 130°C. Yet few calculations at constant temperature were performed at 280°C, 330°C and 380°C. No oxidation occurred at these temperatures as well.

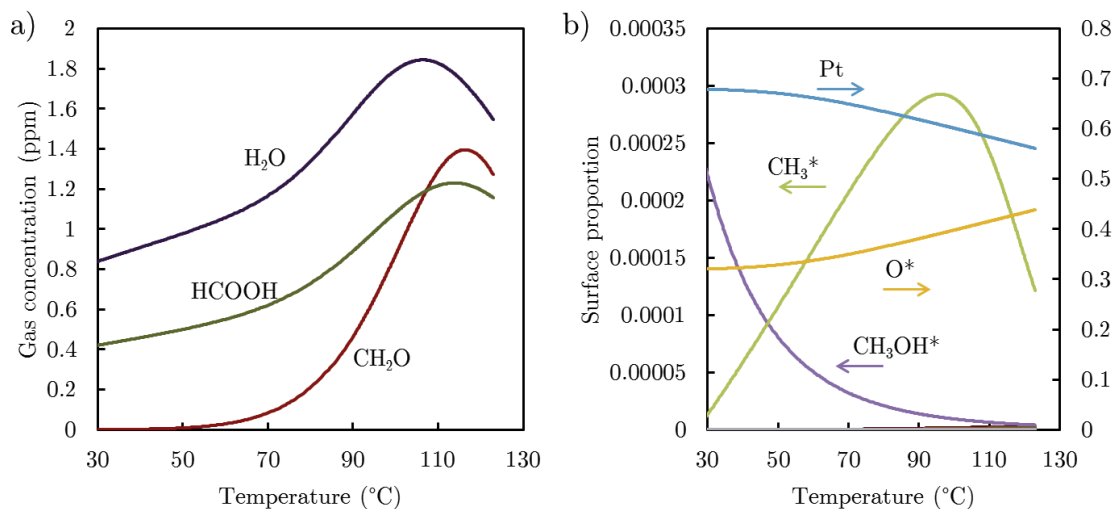


Figure 76: TPR simulation of methanol with the OXY model. Gas inlet consists into 8%  $O_2$  and 1000 ppm of  $CH_3OH$  at 30°C. A 5°C/min ramp is applied. a) Outlet produced gas concentrations and b) surface species proportions.

Finally methanol adsorption reaction has been favored in order to observe its impact on the kinetic scheme and methanol oxidation. The desorption energy has therefore been set at 20 kcal.mol<sup>-1</sup> in place of 0.9 kcal.mol<sup>-1</sup>. The pre-exponential factor has been altered from 10<sup>13</sup> s<sup>-1</sup> to 10<sup>11</sup> s<sup>-1</sup>. This constitutes the MET kinetic model. The adsorption step performed at 30°C with inlet gases 8%  $O_2$  and 1000ppm  $CH_3OH$  has led to a surface fully covered at 19% of atomic oxygen and 81% of undissociated methanol.

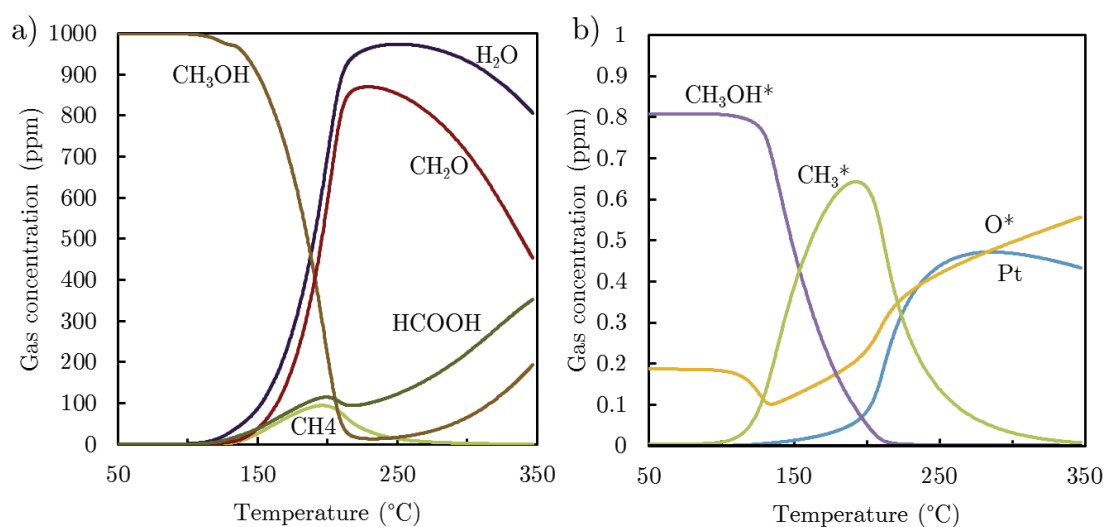


Figure 77: TPR simulation of methanol with the MET model. Gas inlet consist in 8% O<sub>2</sub> and 1000ppm CH<sub>3</sub>OH at 30°C. A 5°C/min ramp is applied. a) Outlet produced gas concentrations and b) surface species proportions. This leads to the RED kinetic model.

This is directly related to the modifications performed from OXY to MET model. TPR from ambient up to 350°C has been simulated with this model (Figure 77). The oxidation of methanol occurs and produces significant amounts of formaldehyde and formic acid into the gas phase (Figure 77a). No CO<sub>2</sub> has been recorded, as well as CO adspecies onto the platinum surface (Figure 77b). The desorption of partially oxidized compounds may be due to favoured desorption of these species. Therefore desorption energies of at least oxygenated hydrocarbons and radicals may be underestimated. This can be explained by the exchange correlation functional PBE used for ab initio calculations. Indeed this functional does not fully take into account dispersive terms that can stabilize molecules and radicals and therefore give stronger adsorption energies.

To conclude about these preliminary results on C<sub>0</sub>-C<sub>1</sub> micro-kinetic simulations, one can notice that multiple parameters need to be taken into account. The raw and purely UBI-QEP estimated model needs to be improved in order to be representative of the experimental results available. The allocated energies play a huge role in the model. The use of enthalpy instead of electronic energies may be a useful improvements for future works, as well as another functional including more precise dispersion terms. The functional PBE-dDsC evaluated by Gautier et. al<sup>118</sup> would be an interesting one, especially for both light and heavy hydrocarbons. Also pre-exponential factors have an impact on simulations. In these models, factors were selected according to transition state theory estimations<sup>137</sup>. This kinetic parameters should be determined and evaluated with care. Vlachos et al.<sup>80</sup> optimized these factors in order to fit experimental oxidation of methane. Lindstet<sup>271</sup> and coworkers used surface modified collision theory laws, that could be implemented in such a multi-scale approach.

## 6.5| Conclusion

We presented here the first steps of applying the previously developed multiscale approach to light hydrocarbons oxidation. Experimental data gathered from the temperature programmed desorption highlighted adsorption and oxidation interferences between carbon monoxide and both methanol and propene. However quantitative descriptors such as oxidation temperature range, T<sub>50%</sub> and oxidation activation energies brought easy-to-compare data with kinetic simulations. Moreover FTIR spectroscopy has provided clues in order to apprehend surface phenomenon, that are directly comparable to simulated surface concentrations.

Prior to the simulation of kinetic scheme, the construction of the scheme is a challenge on itself. The amount of species and reactions is such that automated scripts need to be developed to: (i) generate possible radicals from the degradation of adsorbed molecules, (ii) generate all the possible reactions between adsorbed species with molecularity constraints, and (iii) calculate and address unique kinetic parameters for each reactions. This automatic development was implemented and detailed in section 2.4.4.

In addition and according to the previously developed multiscale approach, kinetic parameters are obtained from *ab initio* calculations. Indeed extensive DFT modelling has been made on C<sub>0</sub>-C<sub>3</sub> molecules and radicals, on a simple Pt(111) clean surface. The versatile PBE functional has been used. This dataset constitutes a recent DFT basis for almost one hundred species adsorbed on platinum. It can therefore be used for multiscale studies of both oxidized and reduced operating conditions. Regarding some adsorption modes, electronic adsorption energy of heavier hydrocarbons can be estimated using trends determined for C<sub>0</sub>-C<sub>3</sub> radicals. This chapter contains therefore the first steps of a proven multiscale method towards larger chemical systems. An open perspective however remains, dealing with the effect of dispersion corrections on the observed trends, expected to be non-systematic between oxygenated and non-oxygenated compounds.

Preliminary simulations of methanol oxidations has demonstrated that a purely UBI-QEP based model is not appropriate and should be improved. The implementation of *ab initio* based data of dissociative adsorption on Pt(111) and changing methanol adsorption kinetic parameters has led to the first methanol oxidation results based on a detailed kinetic and heterogeneous mechanism. Yet the multi-scale approach towards hydrocarbon oxidation requires additional work in order to be representative of oxidation experiments. Two main outlines may be (i) the determination of pre-exponential factors, either by collision theory adapted laws or transition state calculations, and (ii) the use of enthalpy instead of electronic energy as performed by UBI-QEP methodology. Also, the oxygenated versus non oxygenated compounds adsorption competition may change with another exchange correlation functional in the *ab initio* calculations, which may lead to an improvement in terms of adsorption competition between O<sub>2</sub> related compounds and methanol related compounds.



# 7| Conclusions and perspectives

This work has been performed to answer several issues about catalytic oxidation of carbon monoxide and light hydrocarbons especially on highly dispersed platinum supported on alumina: (i) the oxidation state of such surface, (ii) the understanding of CO and HC reactivity using a multi-scale approach, (iii) the differences with ideal extended surfaces as well as (iv) the microscopic behaviour of the adspecie/catalyst/support system were explored.

Diesel engine aftertreatment was used as a case study in terms of operating conditions: temperature, partial pressures and gas composition. In order to reach the objectives of this work, a multiscale methodology was adapted and applied. It combines experiments with *ab initio* molecular modelling and *ab initio*-based micro-kinetic models to shed light on microscopic matter behaviour. Tools and processes have been developed to manage these three very distinct domains.

Chapter 3 was devoted to interactions between atomic oxygen and platinum supported on alumina as well as dissociation of molecular oxygen on the metallic clusters. Experimental O<sub>2</sub>-TPD exhibited higher desorption temperatures than prior studies. Also highly dispersed Pt/ $\gamma$ -Al<sub>2</sub>O<sub>3</sub> was never tested before. Extensive DFT modelling on the model Pt<sub>13</sub>/ $\gamma$ -Al<sub>2</sub>O<sub>3</sub> system, with adsorption of atomic oxygen on a wide range of coverage demonstrated that oxygen binds strongly on the surface, more than on the ideal Pt(111) surface. Also a thermodynamic diagram (p<sub>O2</sub>,T) has demonstrated that with p<sub>O2</sub>=0.1 bar, a high oxygen coverage is reached for this kind of particle. Dissociation of dioxygen onto the cluster is activated with coverage dependent activation barrier. Thermokinetic parameters were thus calculated *ab initio* to implement a DFT-based micro-kinetic model on dissociative-adsorption of O<sub>2</sub>. Simulation of O<sub>2</sub>-TPR in experimental conditions has led to a consistent temperature range according to experiments. Although energetic was accurately defined, a large space of uncharted parameters has to be investigated. This case demonstrated that a deep DFT study on an appropriate surface model is able, when integrated in a micro-kinetic model, to capture the main features of experiments. This study is an accurate base for adsorption and reaction on Pt/ $\gamma$ -Al<sub>2</sub>O<sub>3</sub> in oxidant media.

Carbon monoxide adsorption was studied in Chapter 4. The binding energies between CO and platinum emphasize again strong interactions, although weaker than the one with oxygen. Most of all desaggregation and unhooking of the platinum cluster from the alumina support is recorded. CO-TPD were again performed to evaluate experimental adsorption of carbon monoxide. A wide peak was observed below 350°C. Combined to *operando* IR to record the evolution of surface species, several top and bridge adsorption modes were identified. The comparison of experimental data and *ab initio* model shows some similarities but interfacial (*i.e.* alumina engaged) adsorption modes are difficult to distinguish both in wavenumber and heat of adsorption. The bridge mode is well understood. Yet the oxidized state does not describe well the 2120cm<sup>-1</sup> adsorption mode, suggesting that for CO adsorption on oxydized catalysts, a more exhaustive simulation of the possible O/CO ratio is needed. A micro-kinetic model was also built using the same pattern as the previous one. Again the simulated CO-TPD temperature ranges matched with the experimental one. Yet the modelled simulation exhibits thin discrete peaks, that is not congruent with experiments. Therefore the phenomenon is not completely handled by this model. A larger DFT investigation, with for instance the inclusion of multiple adsorption energies for a given CO coverage structure as well as exploring the adsorption on bigger aggregate would be an interesting point.

Oxidation of carbon monoxide into CO<sub>2</sub> was investigated in Chapter 5. Using the results from the two previous chapters, *ab initio* co-adsorbed systems were studied. This allowed to emphasize the developed indicators (as heat of adsorption, metal/support interaction or Bader charges analyses) on the double dependence of oxygen and carbon monoxide coverages. Adsorption of carbon dioxide was also evaluated. A few transition states of CO oxidation were determined. Activation energies were found close to prior cluster studies. Experimental temperature programmed reactions demonstrated that prior catalyst oxidation state has an impact on CO oxidation. Previous micro-kinetic model of Chapters 3 and 4 about oxygen and CO adsorption were merged with CO oxidation kinetics. This time a considerable parameter space needed to be investigated. Therefore several kinetic models were developed, of increasing complexity. Considering the data obtained on oxidation transition states, kinetic modelling allows to simulate experimental T<sub>50%</sub>. However oxidation temperature range and simulated apparent activation energies suggest that model improvements are required. This may be due to the rougher co-adsorbed states description with respect to O<sub>2</sub> or CO adsorbed state (the later were refined by molecular dynamics whereas the former were not). These three chapters have demonstrated thereby that a deep investigation is required to handle correctly experimental data, and that very simple models using the Pt(111) surface are most of the time non-sufficient. The needed level of detail includes studying all distinct sites, working with several configurations for each operation conditions (for instance, at the same surface species coverage), using long-time molecular dynamics.

The tools necessary to tackle hydrocarbon oxidation using the multiscale approach have been developed: (i) surface reaction mechanism generator to generate exhaustive kinetic schemes and (ii) *ab initio* radical adsorption dataset over more than 80 gas and surface species to allocate activation barrier to these reaction. Preliminary kinetic simulations of methanol oxidation have been performed and exhibits promising data for future works.

This work opens multiple perspectives towards oxidation catalysis in general. The results regarding the platinum surface state in highly dispersed material is a background for any studies considering oxidant media. This is the case for the oxidation of numerous compounds like H<sub>2</sub>, nitrogen and sulphur oxides, that are present in engine exhaust gases. Some key reactions for both light and heavy hydrocarbons can be investigated via DFT modelling, considering highly oxidated platinum clusters. Coming back to the synthesis methods used to prepare the supported heterogeneous catalyst, one may remember that before becoming a reduced nanoparticle, the platinum precursors are deposited in an oxidic form. The calculations performed regarding the interaction of oxygen with platinum clusters are also useful to better understand the activation steps in the course of the preparation of the catalyst<sup>202</sup>.

In a multi-scale approach, the fundamental impact of dopants on the catalysts could be a case study. Indeed chlorine, potassium or even sodium that may be present in the support can alter microscopic material characteristics, such as catalyst/support interaction or adsorption and oxidation activity<sup>107,264,293,294</sup>.

Generating an hydrocarbon oxidation micro-kinetic model on highly dispersed Pt/ $\gamma$ -Al<sub>2</sub>O<sub>3</sub> is arduous giving the multiscale approach developed in this thesis, considering the number of non-equivalent sites on clusters, and the very high number of steps in the reaction network, close to 600 for C<sub>0</sub>-C<sub>1</sub> kinetic scheme, and estimated at 46000 reaction for C<sub>0</sub>-C<sub>3</sub> kinetic scheme with the selected C<sub>0</sub>-C<sub>3</sub> molecules and radicals (section 6.3). We used an ideal surface as Pt(111) as a simpler start in the present work, but limited ourselves to the quantification of the stability of reaction intermediates, without transition state search. This of course opens improvement perspectives. The next step would consist in evaluating major discrepancies with peculiar dispersed or oxidized surfaces for key reactions. Some similarities may be found for typical reactions according to chemical groupments, including the impact of carbon chain length, spatial conformation or surface sites. Therefore an appropriate and controlled level of detail would ensure the multi-scale approach adaptation for heavier kinetic schemes.

Steady state and iterative data analysis data analysis were performed with dedicated tools developed within this study, mainly between DFT and micro-kinetics. In addition, a surface mechanism generator was developed in order to establish large

surface reactions schemes. The reaction generation for catalytic kinetic has barely been developed, due to complex interaction with surface. Currently, the generator develops a scheme according to a selected batch of both gas and surface species. However the development of add-ons with, for instance, the estimation of energetics, the choice of both TST and collision theory determination of rate constants and the reduction of reactions would be interesting perspectives. Therefore an easy generation of micro-kinetic models whatever the surface and species could be considered in surface science.

Conclusions drawn here allows a better apprehension of platinum surface state in oxidant media, as well as carbon monoxide adsorption and oxidation on dispersed catalyst. These points go far beyond depollution catalysis and are of interest for oxidation catalysis in general.

# Appendices

## Appendices A: Dissociative adsorption of oxygen on Pt/ $\gamma$ -Al<sub>2</sub>O<sub>3</sub>

### A.1. Determination of dimensionless quantities of experimental reactor

Thermophysical data were gathered from online [www.engineeringtoolbox.com](http://www.engineeringtoolbox.com), accessed july 31<sup>st</sup> 2018.

Mass transfer Peclet number was determined using equation (83), with  $Re$  the Reynolds number and  $Pr$  the Prandtl number.  $Re$  was determined with prior COMSOL<sup>103</sup> simulation at 0.1 in the reactor cell.

$$Pe = Re \times Pr \quad (83)$$

Prandtl number was calculated with equation (84), with dynamic viscosity  $\mu$  (1.8  $\mu$ Pa.s for air at ambient temperature), specific heat  $c_p$  (1012  $J.kg^{-1}.K^{-1}$  for air) and thermal conductivity  $\lambda$  (24.35  $mW.m^{-1}.K^{-1}$  for air). Prandtl number is  $7.5.10^{-1}$ , therefore Peclet number is  $7.5.10^{-2}$ .

$$Pr = \frac{\mu c_p}{\lambda} \quad (84)$$

Thiele modulus was calculated thanks to equation (85), with reaction rate constant  $k$  that varies between 1 and  $10^{-3} s^{-1}$  for O<sub>2</sub> desorption. Typical concentration  $[A]$  and reaction global order  $n$  (assumed to be unity). Mass diffusion coefficient  $D$  of helium in air is  $2.2 m^2 .s^{-1}$  at 300°C.

$$Pr = L \sqrt{\frac{k[A]^{n-1}}{D}} \quad (85)$$

Characteristic length  $L$  corresponds to equivalent catalyst grain diameter given by equation (86). Considering catalytic material as spheres of 400  $\mu m$  diameter,  $L$  is  $4.10^{-4} m$ . Therefore maximum Thiele modulus value rises at  $2.6.10^{-5}$ .

$$L = \frac{6V}{S} = 6 \frac{\frac{4}{3}\pi r^3}{4\pi r^2} \quad (86)$$

Biot number is determined with equation (87). Convective coefficient of the air  $h$  was set to  $1 \text{ W/m}^2 /\text{K}$ , while typical length  $L_b$  is the ratio between reactor volume and surface (respectively  $283\mu\text{L}$  and  $242 \text{ mm}^2$ ). Thus  $L_b$  is estimated at  $1.17 \cdot 10^{-3} \text{ m}$ . Biot number is then  $4.8 \cdot 10^{-2}$ .

$$Bi = \frac{hL_b}{\lambda} = 2r \quad (87)$$

## A.2. Illustration of a typical velocity-scaled MD run with cluster reconstruction

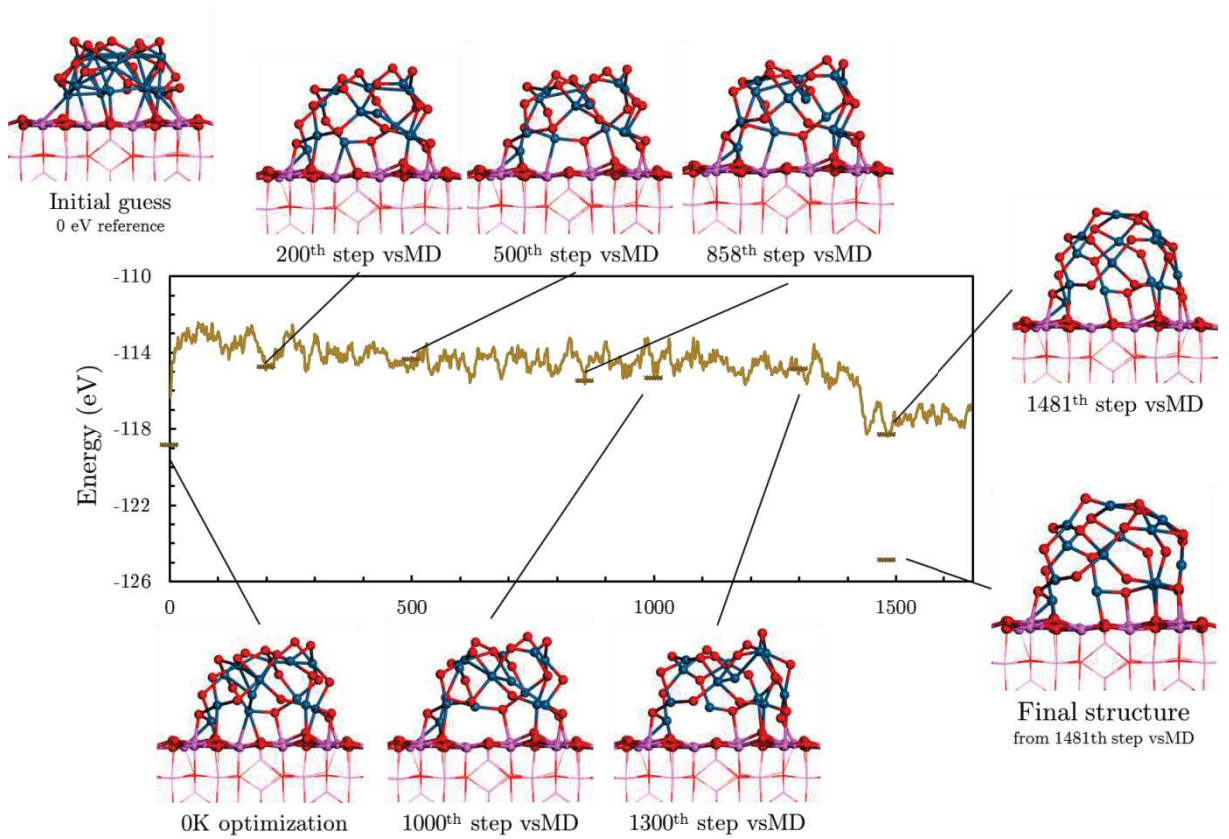


Figure 78: Energies and illustrations of  $\text{Pt}_{13}\text{O}_{20}$  structure through the optimisation process: optimisation – velocity-scaled molecular dynamics at 600K and 5fs. The initial (0K) and final structures were obtained by geometry optimisation (quench for the final structure). Aluminum: purple, oxygen: red, platinum: blue.

### A.3. Optimisation of the TPD protocol

A first set of O<sub>2</sub>-TPD experiments was performed on the 1 wt % Pt/ $\gamma$ -Al<sub>2</sub>O<sub>3</sub> material to investigate the impact of the high temperatures reached in the TPD experiments. The sample underwent dehydrations at 300°C or 600°C before TPD. Water release was observed (Figure 79a) on a large range of temperatures, always starting at the dehydration temperature up to the final one (1100°C). This phenomenon can be attributed to the dehydroxylation of the surface of gamma alumina<sup>121,102,295,296</sup>. Moreover, the expected oxygen release follows a similar trends than water release, with a H<sub>2</sub>O/O<sub>2</sub> ratio of intensities around 100 to 1. This suggests a possible impact of water release on oxygen desorption in a way that is not elucidated. Thus it can perturb the interpretation of the O<sub>2</sub> desorption from the nanoparticles in the case of the supported catalysts. Hence we tried to minimize water release with appropriate dehydration conditions.

Figure 79b illustrates the effect of the duration of the dehydration step on the water release during O<sub>2</sub>-TPD for the 1 wt % Pt/ $\gamma$ -Al<sub>2</sub>O<sub>3</sub> system. The signals related to water are similar after a dehydration of 300°C whatever the dehydration duration (1 or 5 h). Nevertheless there is a significant difference for 600°C dehydration experiments. The intensity of the peaks and their width are weaker after 5h dehydration rather than 1h dehydration. This is in line with the work of Lagauche *et al.*<sup>102</sup> showing that during a TPD most of the water is released before 600°C, but they still found few hydroxyl groups on the surface.

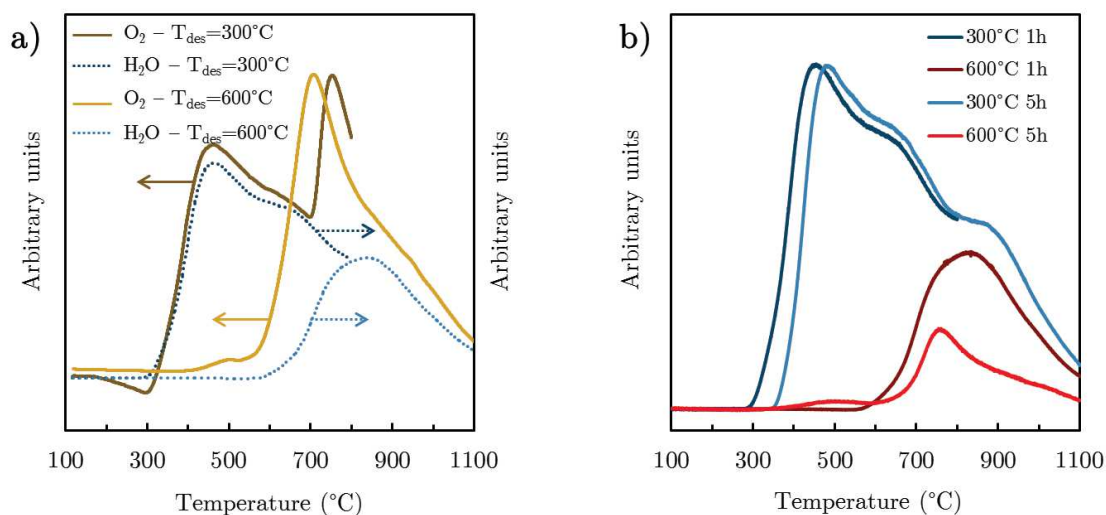


Figure 79: a) Relative signals of oxygen ( $m/z=32$ ) and water ( $m/z=18$ ) during the O<sub>2</sub>-TPD 1 wt % Pt/Al<sub>2</sub>O<sub>3</sub> with a dehydration temperatures of 300°C and 600°C for 1 hour prior to the TPD experiment. b) Relative signals of water ( $m/z=32$ ) during TPD experiments on 1 wt % Pt/Al<sub>2</sub>O<sub>3</sub> according to different dehydration conditions.

In order to obtain a highly dehydrated material to limit the effect of water, a five hours dehydration step at 600°C was selected, prior to TPD (Figure 80). Moreover, the mass spectrometry signals of O<sub>2</sub> for alumina alone were deduced from that of the catalysts obtained with the same treatment conditions. Thus we avoid a possible contribution of O<sub>2</sub> adsorption on alumina.

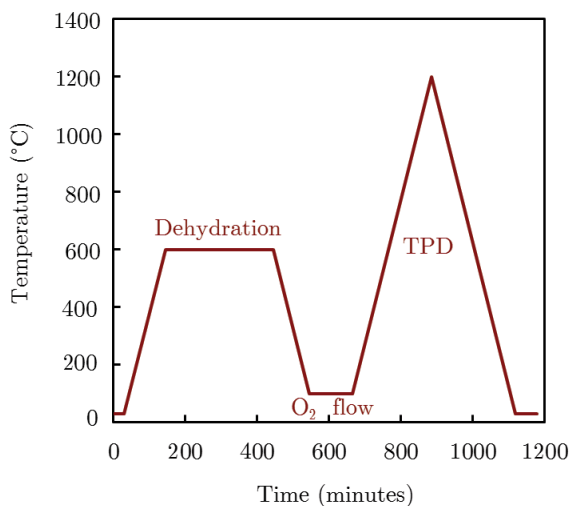


Figure 80: Definitive temperature process during TPD experiments

#### A.4. Deconvolution of the TPD profiles

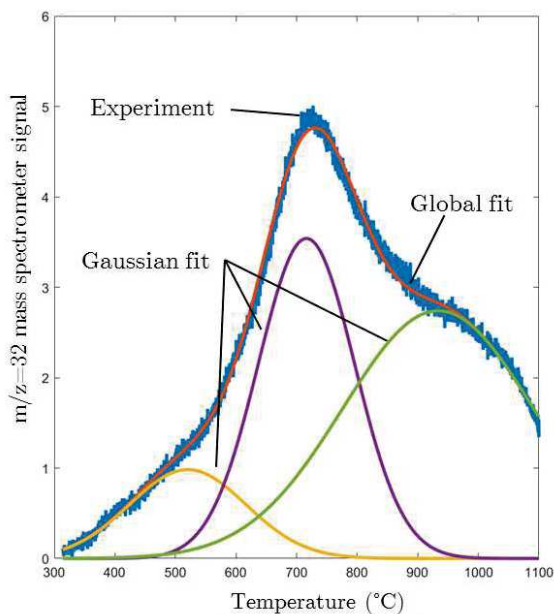


Figure 81: Deconvolution fit of the MS signal  $m/z=32$  recorded during TPD for the 0.3wt % Pt/ $\gamma$ -Al<sub>2</sub>O<sub>3</sub> catalyst using three Gaussian-type fitting curves. The global fit curve is the sum of the three Gaussian curves.

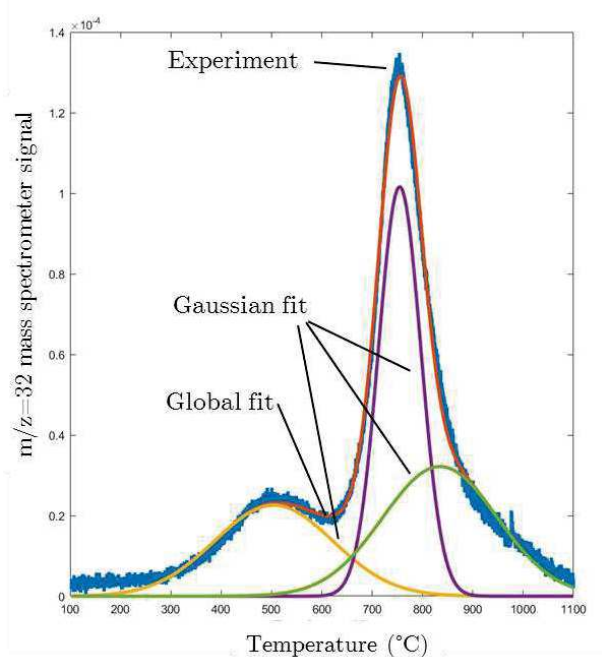


Figure 82: Deconvolution fit of the MS signal  $m/z=32$  for the 1wt % Pt/ $\gamma$ -Al<sub>2</sub>O<sub>3</sub> catalyst using three Gaussian-type fitting curves. The global fit curve is the sum of the three Gaussian curves.

### A.5. Dissociative adsorption of O<sub>2</sub> on Pt(111) investigated by *ab initio* calculations

Pt(111) was considered to account for bigger particles that may be formed during the TPD experiments. It also provides a good reference case. Atomic oxygen coverages from 0 to 1 monolayer were simulated (Figure 83). The well-known p(2x2) periodic surface patterns were calculated<sup>97,196</sup>. The oxygen atoms were found only in fcc hollow site, in agreement with the literature<sup>165,174,189,166</sup>, whatever the coverage. Our adsorption energies (Table 24) are quite close to the ones of Pang *et al.*<sup>166</sup> who uses the same *ab initio* level of theory (GGA PBE). The comparison with older simulations is not easy as the functionals used are different<sup>165</sup>. Stepped surfaces<sup>174,231</sup> show a mildly higher oxygen stability and a slightly larger coverage capacity. These kind of structures are likely to undergo platinum surface reconstruction<sup>190</sup>.

For 0.75ML and 1ML coverages, subsurface oxygen atoms simulations were performed but found energetically unfavored. It is however known that adsorbed oxygen can lead to the formation of an oxide<sup>169,188</sup>. The investigation of such surface structure would require a dedicated study that is beyond the scope of the present work.

The mean adsorption energy (Table 24) was found to get less favorable with increasing oxygen coverage. A thermodynamic diagram was also constructed to evaluate the difference with previous Pt(111) studies (Figure 84) and compare with Pt<sub>13</sub> in a

consistent way. As the adsorption are found more favorable than the one reported by Legaré<sup>165</sup>, the phase diagram induced coverages domain shifted to higher temperature. Our calculations are however close to the latest work of Pang *et al.*<sup>166</sup>

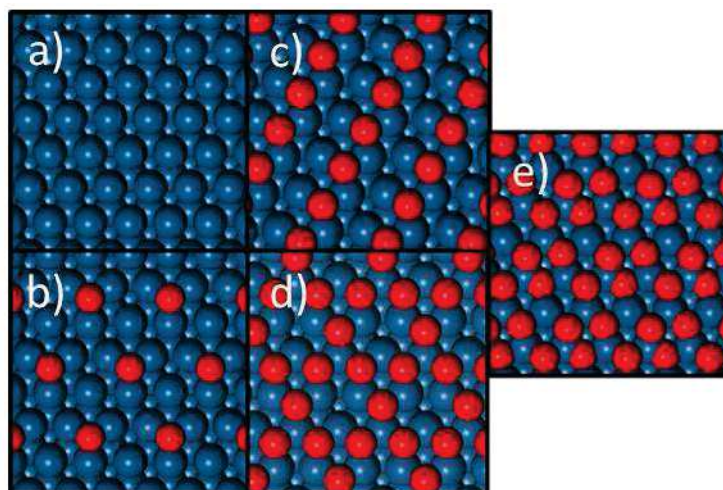


Figure 83: Illustrations of simulated Pt(111)-nO surfaces (top views) with no oxygen (a), 0.25ML (b), 0.5ML (c), 0.75ML (d) and 1ML (e). Platinum atoms are in blue, oxygen in red.

Table 24: Atomic heat of adsorption per O<sub>2</sub> found for Pt(111) systems

Oxygen coverage (ML)	E <sub>adsorption</sub> (kcal.mol <sup>-1</sup> )
0.25	-81.3
0.50	-69.2
0.75	-53.5
1.0	-37.3

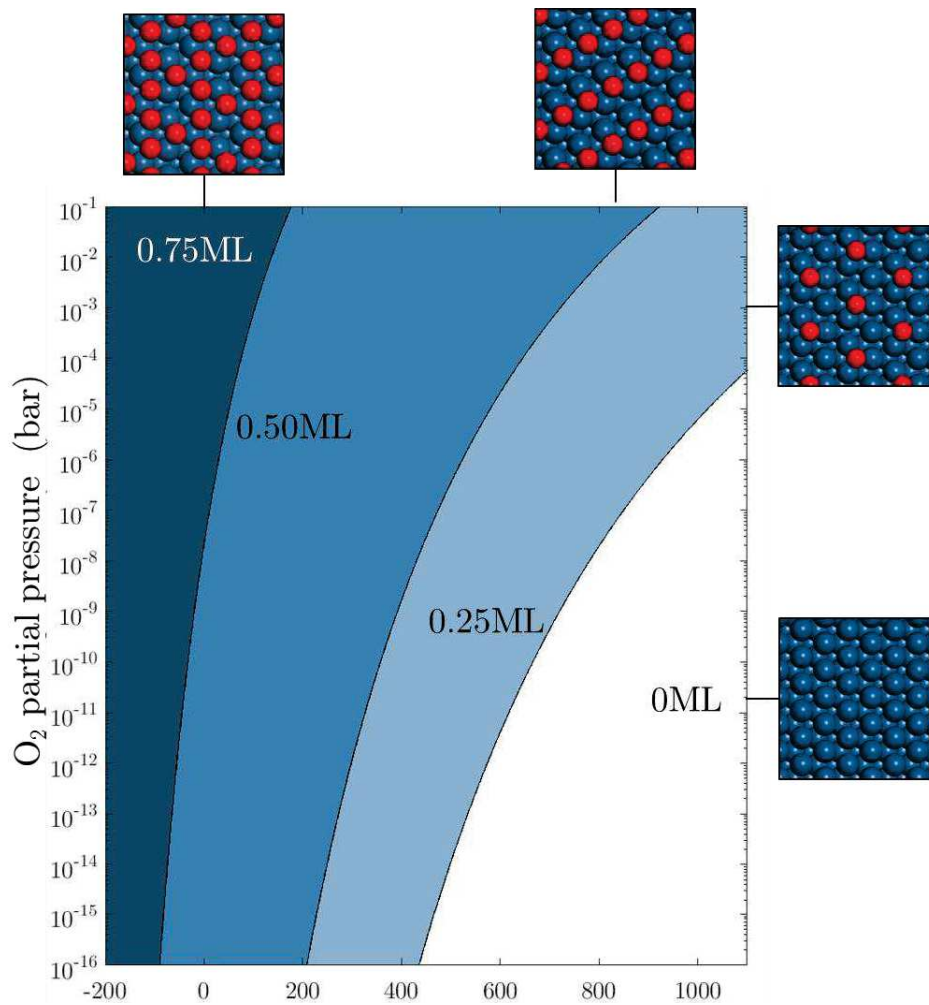


Figure 84: Thermodynamic diagram ( $p_{O_2}, T$ ) for the adsorption of atomic O on Pt(111).

A.6. Most stable structures found for the supported  $\text{Pt}_{13}\text{O}_n$  system from *ab initio* calculations

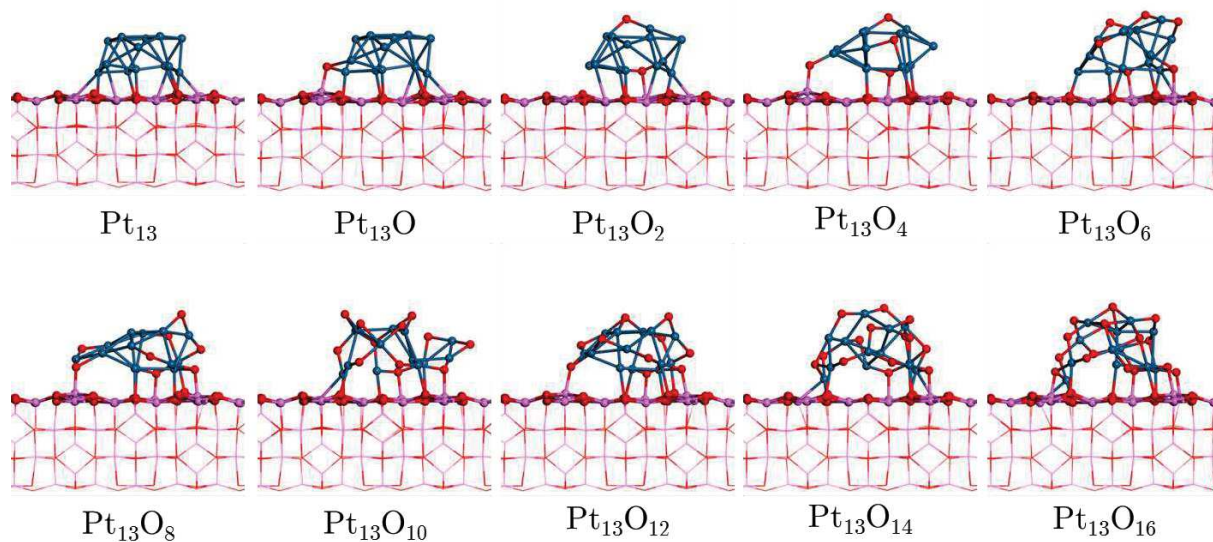


Figure 85: Illustrations of the two-layers  $\text{Pt}_{13}\text{O}_n$  structures (side views).

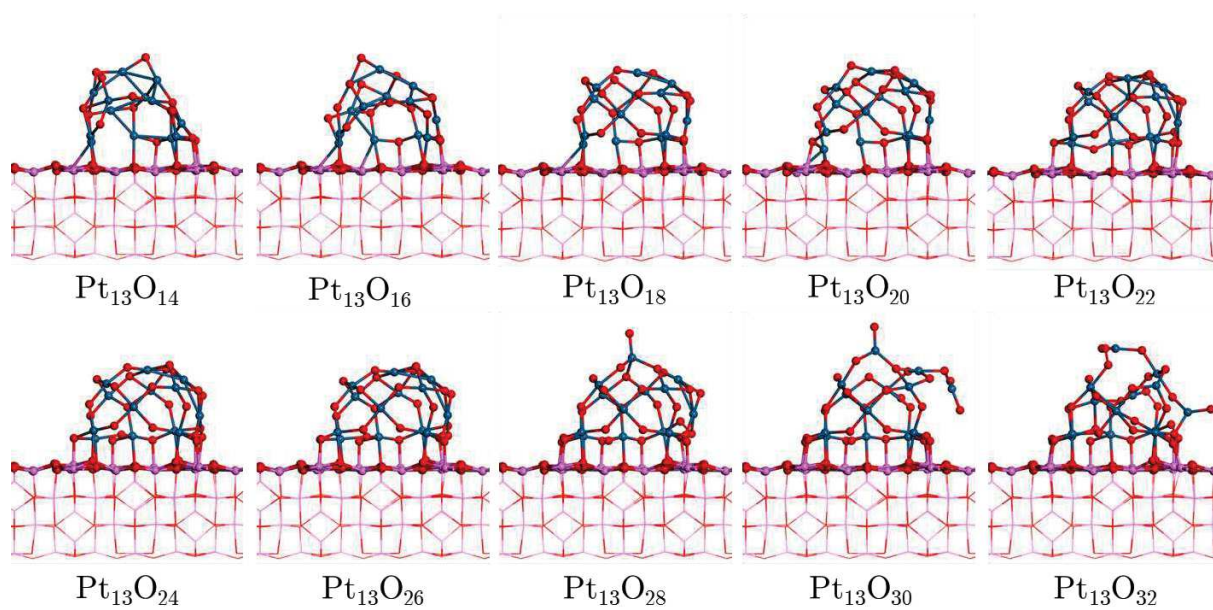


Figure 86: Illustrations of the hemispheric  $\text{Pt}_{13}\text{O}_n$  structures (side views).

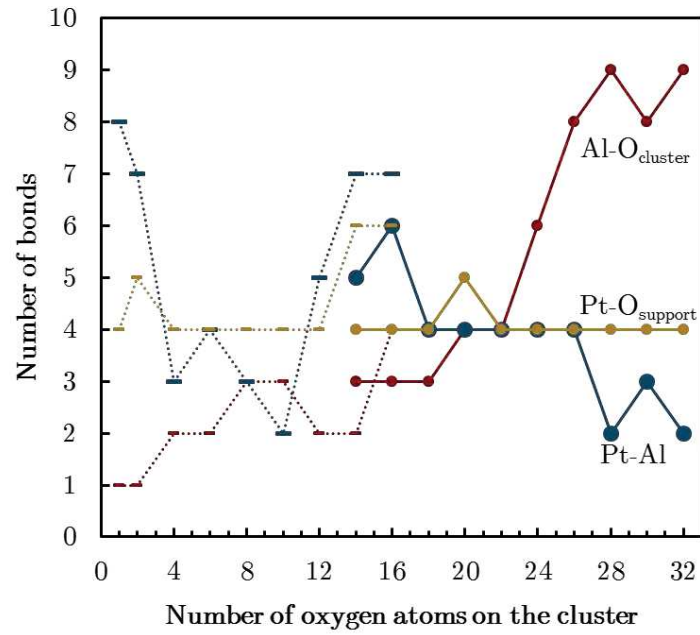


Figure 87: Number of bonds between the cluster and the support (Pt-Al, Al-O<sub>cluster</sub> and Pt-O<sub>support</sub>). The maximum bond length for the count was 2.5 Å. Dotted lines corresponds to the two-layers structures whereas plain lines are hemispheric structures data.

## A.7. Transition structures for the dissociation of O<sub>2</sub>

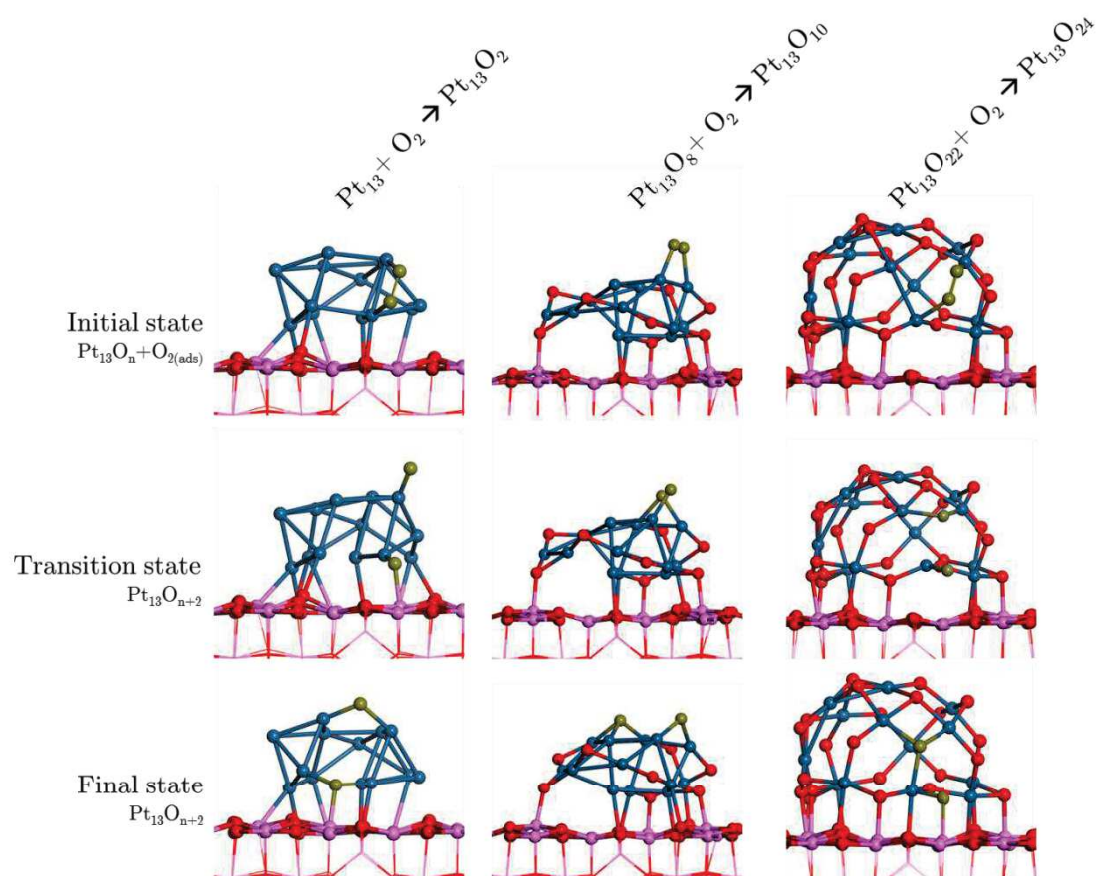


Figure 88: Configurations of initial, transition and final states for the three coverages investigated for dissociation of O<sub>2</sub> on Pt<sub>13</sub>O<sub>n</sub>/γ-Al<sub>2</sub>O<sub>3</sub>. The oxygen atoms engaged in dissociation are set in brown.

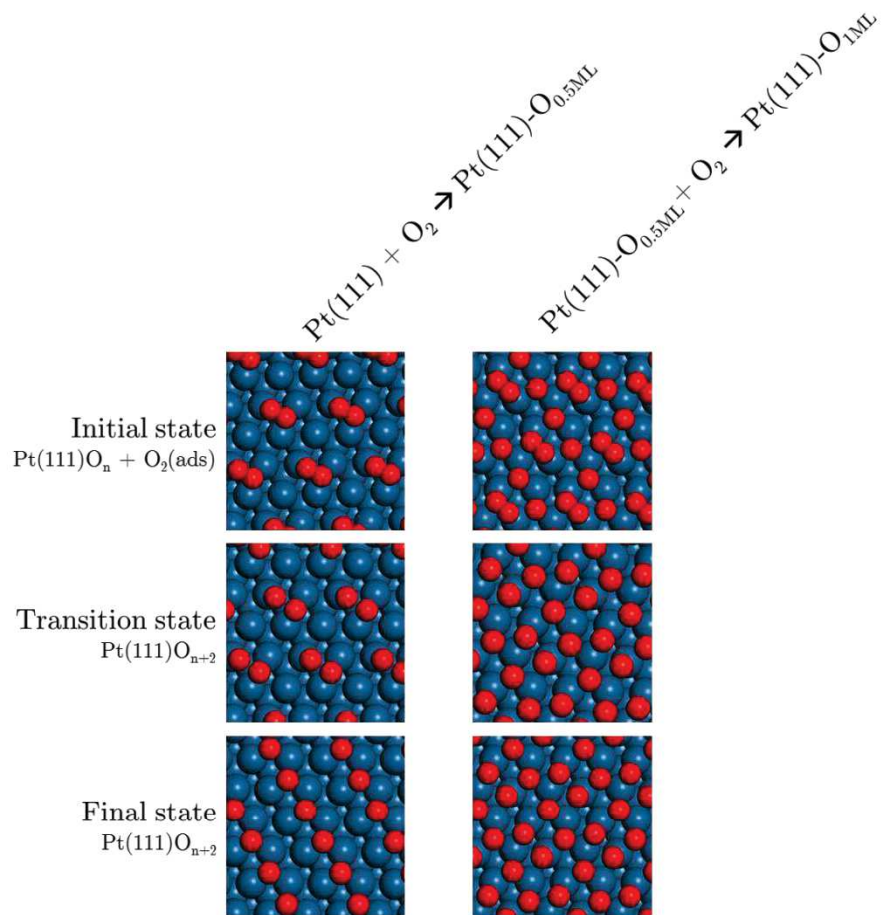


Figure 89: Configurations of initial, transitions and final states for the two coverages investigated for dissociation of  $\text{O}_2$  on  $\text{Pt(111)}$ .

Table 25: Transition state characteristics for  $\text{Pt}_{13}\text{O}_n$  and  $\text{Pt(111)}$  structures.

Transition state	Imaginary frequency ( $\text{cm}^{-1}$ )	O-O bond length ( $\text{\AA}$ )
$\text{Pt}_{13}\text{O}_2$	32	4.26
$\text{Pt}_{13}\text{O}_{10}$	57	3.01
$\text{Pt}_{13}\text{O}_{24}$	118	3.09
$\text{Pt(111)-0.5ML}$	256	1.91
$\text{Pt(111)-1ML}$	109	2.37

## A.8. Kinetic parameters for the $\text{Pt}_{13}\text{O}_n$ model and $\text{Pt}(111)$ model

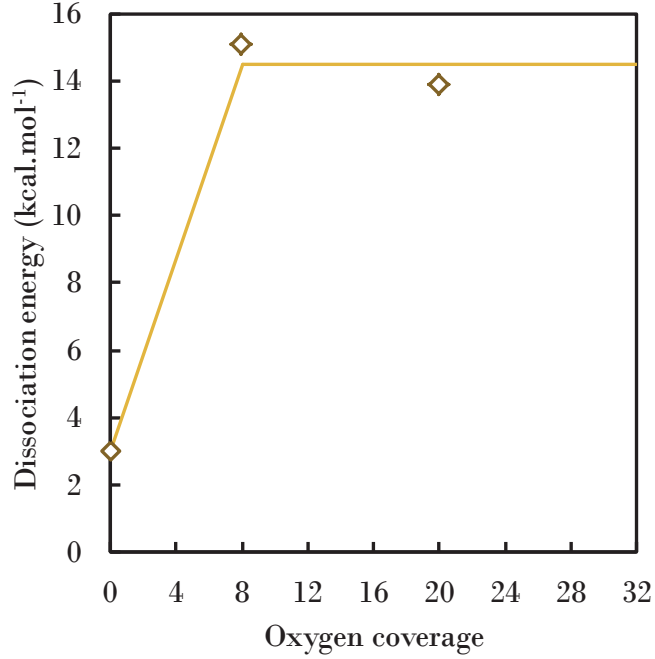


Figure 90: Dissociation activation energy for the supported  $\text{Pt}_{13}$  system. Diamonds are the DFT-determined values, lines are the piecewise linear trends chosen in the kinetic model.

Table 26: Reactions and kinetic parameters of the  $\text{Pt}(111)$  model with a sticking coefficient of 0.01

Reaction	Forward parameters			Backward parameters		
	Sticking coefficient	$\beta$	$E_{\text{dissociation}}$ (kcal.mol <sup>-1</sup> )	Pre-exponential factor (mol.s <sup>-1</sup> .cm <sup>-2</sup> )	$\beta$	$E_{\text{activation}}$ (kcal.mol <sup>-1</sup> )
$\text{O}_2 + 2 \text{ Pt} \leftrightarrow 2 \text{ PtO}$	0.01	0	34.7	4.19E+29	0.5	119
$\text{O}_2 + 2 \text{ PtO} \leftrightarrow 2 \text{ PtO}_2$	0.01	0	85.3	4.19E+29	0.5	128
$\text{O}_2 + 2 \text{ PtO}_2 \leftrightarrow 2 \text{ PtO}_3$	0.01	0	136	8.72E+29	0.5	94.9
$\text{O}_2 + 2 \text{ PtO}_3 \leftrightarrow 2 \text{ PtO}_4$	0.01	0	186	1.04E+30	0.5	104

Table 27: Reactions and kinetic parameters of the  $\text{Pt}_{13}\text{O}_n$  model with a sticking coefficient of 0.01

Adsorption reactions	Forward parameters			Backward parameters		
	Sticking coefficient	$\beta$	$E_{\text{dissociation}}$ (kcal.mol <sup>-1</sup> )	Pre-exponential factor (s <sup>-1</sup> )	$\beta$	$E_{\text{activation}}$ (kcal.mol <sup>-1</sup> )
$\text{O}_2 + \text{Pt}_{13} \leftrightarrow \text{Pt}_{13}\text{O}_2$	0.01	0	2.97	2.80E+18	0.5	119

$O_2 + Pt_{13}O_2 \leftrightarrow Pt_{13}O_4$	0.01	0	5.84	4.01E+18	0.5	128
$O_2 + Pt_{13}O_4 \leftrightarrow Pt_{13}O_6$	0.01	0	8.72	6.48E+18	0.5	94.9
$O_2 + Pt_{13}O_6 \leftrightarrow Pt_{13}O_8$	0.01	0	11.6	4.86E+18	0.5	104
$O_2 + Pt_{13}O_8 \leftrightarrow Pt_{13}O_{10}$	0.01	0	14.5	1.17E+17	0.5	96.5
$O_2 + Pt_{13}O_{10} \leftrightarrow Pt_{13}O_{12}$	0.01	0	14.5	4.20E+18	0.5	40.2
$O_2 + Pt_{13}O_{12} \leftrightarrow Pt_{13}O_{14-TL}$	0.01	0	14.5	2.27E+21	0.5	104
$O_2 + Pt_{13}O_{12} \leftrightarrow Pt_{13}O_{14-HM}$	0.01	0	14.5	2.28E+20	0.5	100
$O_2 + Pt_{13}O_{14-TL} \leftrightarrow Pt_{13}O_{16-TL}$	0.01	0	14.5	3.04E+19	0.5	126
$O_2 + Pt_{13}O_{14-HM} \leftrightarrow Pt_{13}O_{16-HM}$	0.01	0	14.5	1.02E+18	0.5	26.0
$O_2 + Pt_{13}O_{16-TL} \leftrightarrow Pt_{13}O_{18}$	0.01	0	14.5	2.40E+16	0.5	38.8
$O_2 + Pt_{13}O_{16-HM} \leftrightarrow Pt_{13}O_{18}$	0.01	0	14.5	7.13E+18	0.5	99.1
$O_2 + Pt_{13}O_{18} \leftrightarrow Pt_{13}O_{20}$	0.01	0	14.5	2.60E+23	0.5	120
$O_2 + Pt_{13}O_{20} \leftrightarrow Pt_{13}O_{22}$	0.01	0	14.5	1.86E+23	0.5	53.3
$O_2 + Pt_{13}O_{22} \leftrightarrow Pt_{13}O_{24}$	0.01	0	14.5	2.26E+23	0.5	43.7
$O_2 + Pt_{13}O_{24} \leftrightarrow Pt_{13}O_{26}$	0.01	0	14.5	3.41E+23	0.5	21.3
$O_2 + Pt_{13}O_{26} \leftrightarrow Pt_{13}O_{28}$	0.01	0	14.5	2.14E+23	0.5	24.8
$O_2 + Pt_{13}O_{28} \leftrightarrow Pt_{13}O_{30}$	0.01	0	14.5	1.26E+23	0.5	25.4
$O_2 + Pt_{13}O_{30} \leftrightarrow Pt_{13}O_{32}$	0.01	0	14.5	6.70E+23	0.5	31.7
Surface reactions	Pre-exponential factor (s <sup>-1</sup> )	$\beta$	E <sub>activation</sub> (kcal.mol <sup>-1</sup> )	Pre-exponential factor (s <sup>-1</sup> )	$\beta$	E <sub>activation</sub> (kcal.mol <sup>-1</sup> )
$Pt_{13}O_{14-TL} \leftrightarrow Pt_{13}O_{14-HM}$	1E+11	0.5	0	1E+11	0.5	11.0
$Pt_{13}O_{16-TL} \leftrightarrow Pt_{13}O_{16-HM}$	1E+11	0.5	74.6	1E+11	0.5	0

## Appendices B: Carbon monoxide adsorption on Pt/ $\gamma$ -Al<sub>2</sub>O<sub>3</sub>

### B.1. Non supported Pt<sub>13</sub> cluster and Pt(111) extended surface

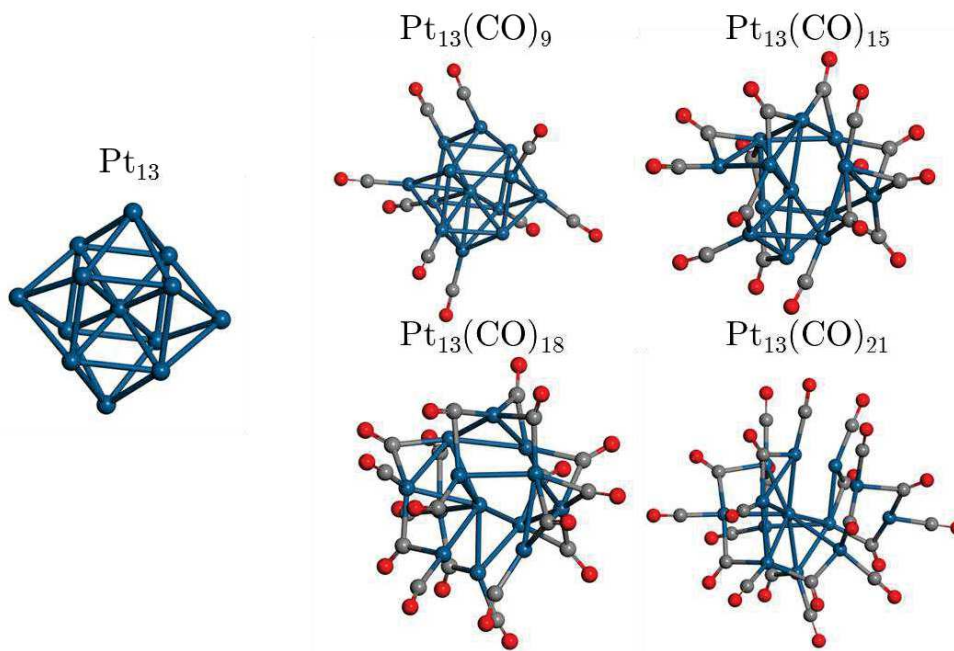


Figure 91: Illustrations of the non-supported Pt<sub>13</sub>(CO)<sub>m</sub> structures. *Ab initio* calculations characteristics were identical to the supported clusters except that Kpoint was set to 5x5x5. The initial guesses were built with a cuboctaedric 13-platinum aggregate (close to Pt<sub>13</sub> final structure in this figure) with top adsorbed CO.

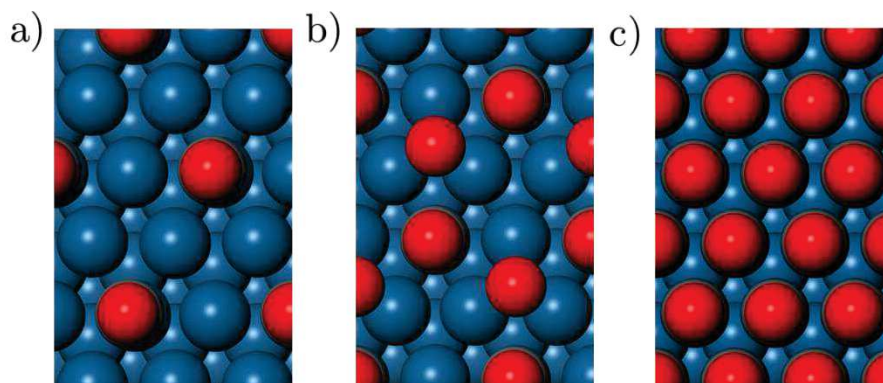


Figure 92: Illustrations of a) Pt(111)(CO)<sub>0.25ML</sub>, b) Pt(111)O<sub>0.25ML</sub>(CO)<sub>0.25ML</sub> and Pt(111)(CO)<sub>1ML</sub>.

## B.2. Illustration of a typical velocity-scaled MD run with $\text{Pt}_{13}(\text{CO})_9$ cluster reconstruction

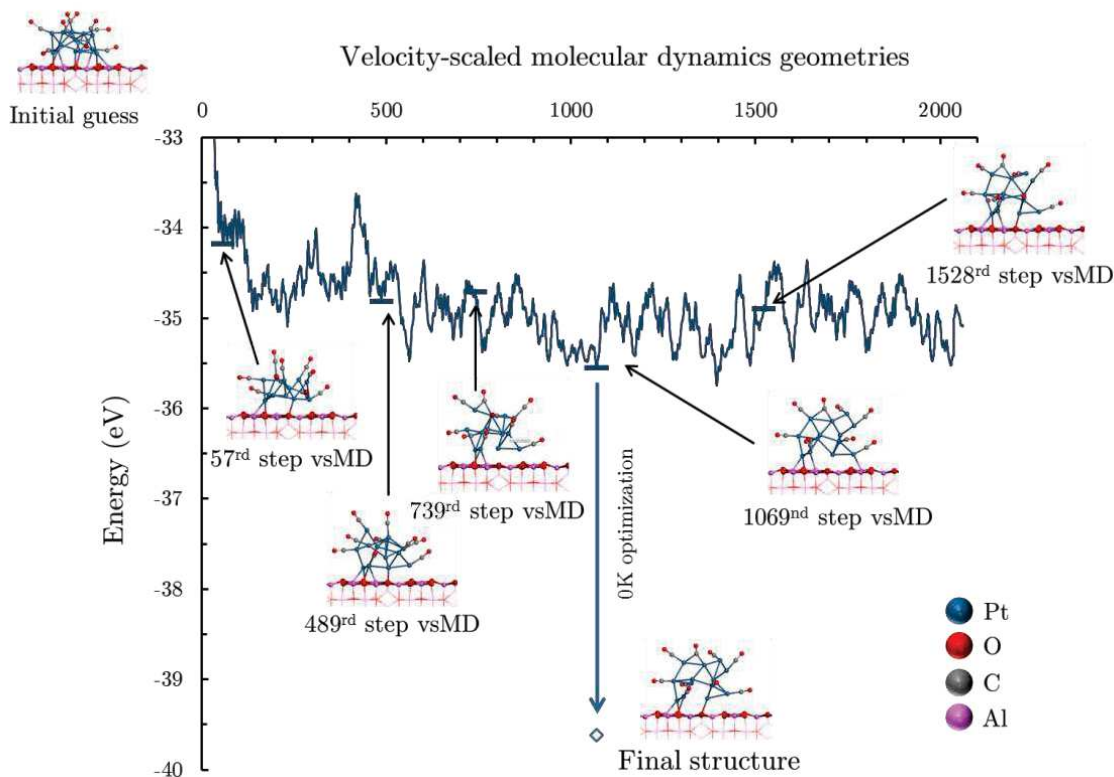


Figure 93: Illustration of the velocity-scaled molecular dynamics of  $\text{Pt}_{13}(\text{CO})_9$

## B.3. Impact of *ab initio* frequencies treatment on adsorption thermodynamic data

Imaginary frequencies were found for some *ab initio* models, after molecular dynamics and geometry optimisation. The frequencies are given in Table 28.

Table 28: Imaginary wavenumbers of the  $\text{Pt}_{13}(\text{CO})_m$  structures

Structures	Wavenumbers ( $\text{cm}^{-1}$ )	Structures	Wavenumbers ( $\text{cm}^{-1}$ )
$\text{Pt}_{13}(\text{CO})$	-	$\text{Pt}_{13}(\text{CO})_{12}$	-
$\text{Pt}_{13}(\text{CO})_2$	6	$\text{Pt}_{13}(\text{CO})_{15}$	17
$\text{Pt}_{13}(\text{CO})_3$	-	$\text{Pt}_{13}(\text{CO})_{18}$	8, 12, 24
$\text{Pt}_{13}(\text{CO})_6$	8, 35	$\text{Pt}_{13}(\text{CO})_{21}$	4, 11, 17, 28

$\text{Pt}_{13}(\text{CO})_9$	-	$\text{Pt}_{13}(\text{CO})_{24}$	8, 11, 30
-------------------------------	---	----------------------------------	-----------

In order to evaluate the impact of low and imaginary frequencies in thermodynamic parameters, a treatment on these frequencies was applied. The treatment consist in setting all the frequencies below  $50 \text{ cm}^{-1}$  to this minimal value. This treatment was applied to the determination of CO adsorption thermodynamic diagram (Figure 94).

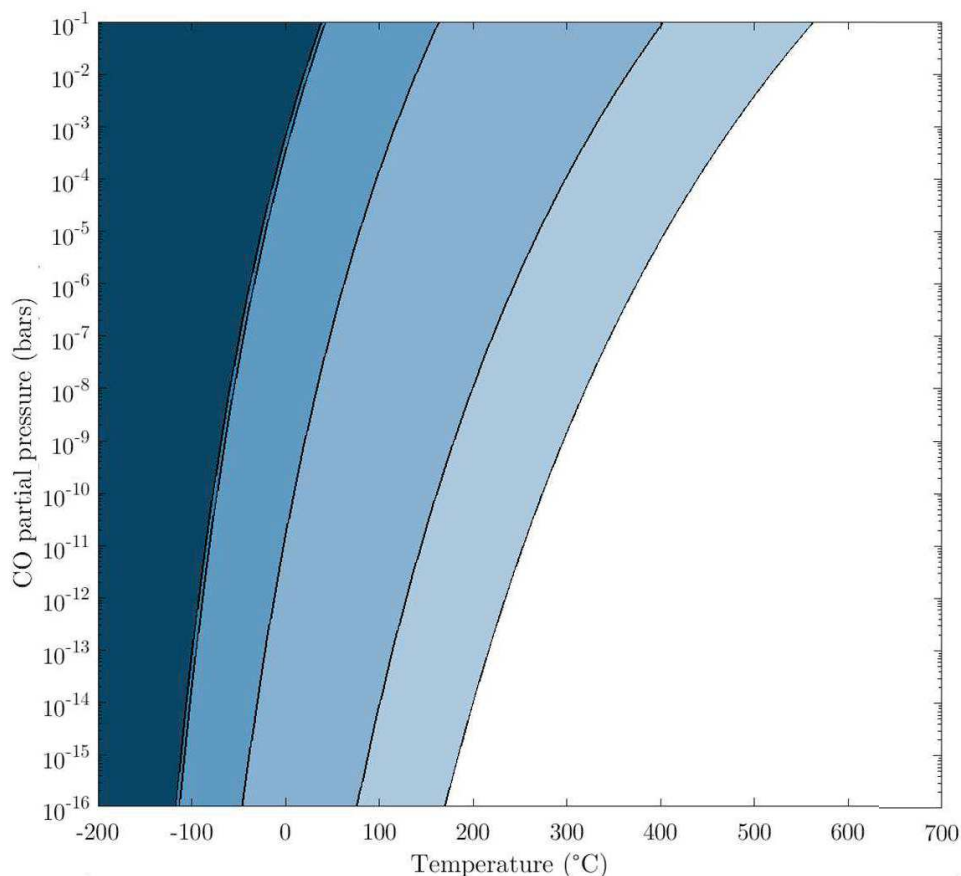


Figure 94: Phase diagram with system entropies calculated with *ab initio* imaginary and real treated frequencies. Colors corresponds to the same species as untreated diagram.

A differential phase diagram was then calculated as the difference between each treated and untreated diagram according to the number of CO adsorbed species (Figure 95). One can observe that the domains of  $\text{Pt}_{13}(\text{CO})_2$  and  $\text{Pt}_{13}(\text{CO})_{18}$  have been diminished for the benefit of vicinal domains. This is indicated by the red-violet pairs of strips. Nonetheless this treatment has few impact on thermodynamic parameters.

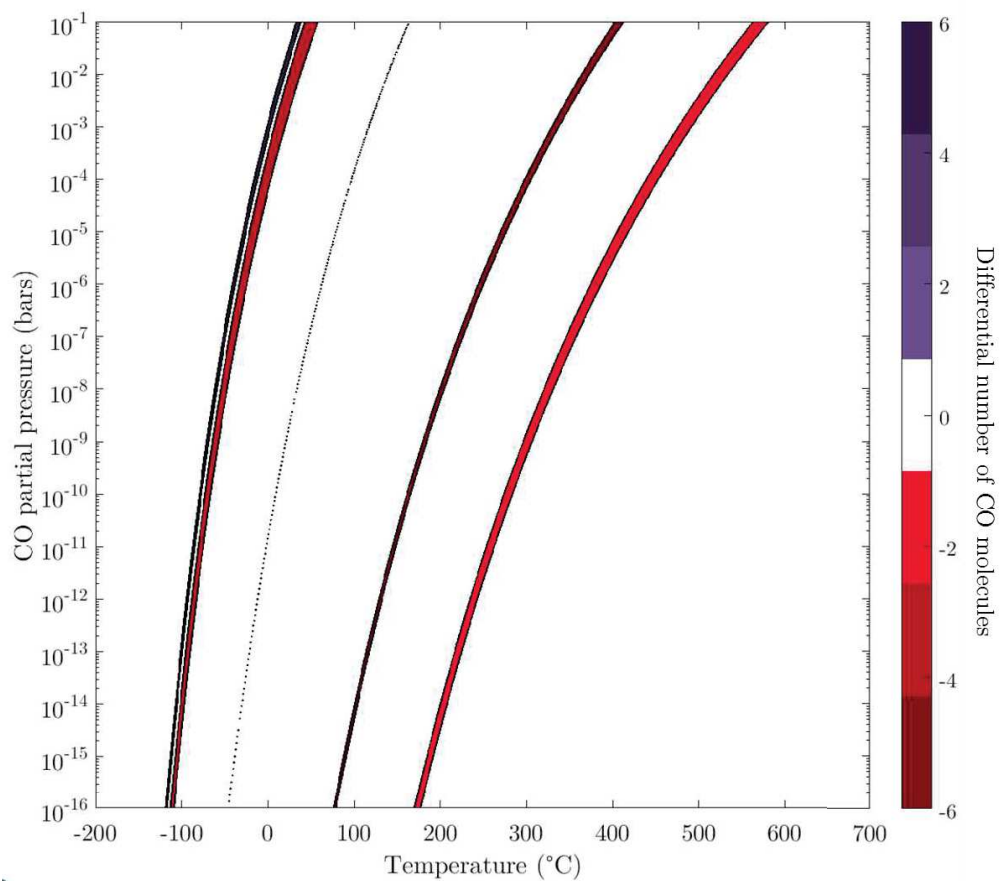


Figure 95: Phase diagram differences between the *ab initio* treated frequencies versus classic phase diagram.

#### B.4. Desorption enthalpy and entropy interpolation on $\text{Pt}_{13}(\text{CO})_m$ structures

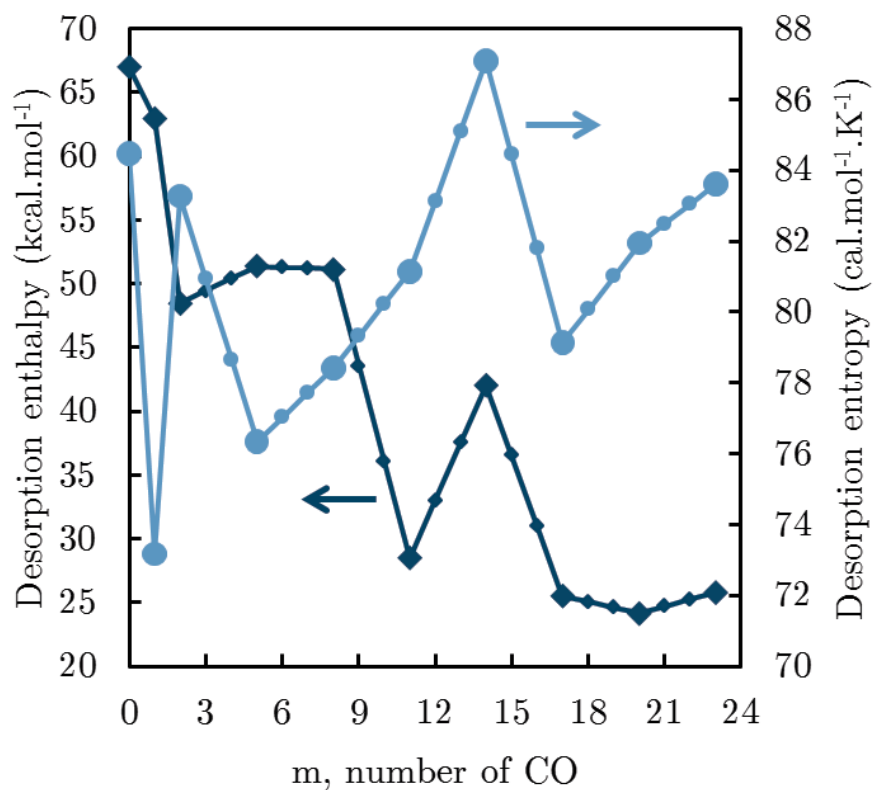


Figure 96: Average desorption enthalpy and entropy of the  $\text{Pt}_{13}(\text{CO})_m$  structures regarding CO coverage (large dots). Linear piecewise interpolation (small dots). Average has been made from 300K to 1000K.

B.5. Most stable structures found for the supported  $\text{Pt}_{13}(\text{CO})_m$  from *ab initio* calculations

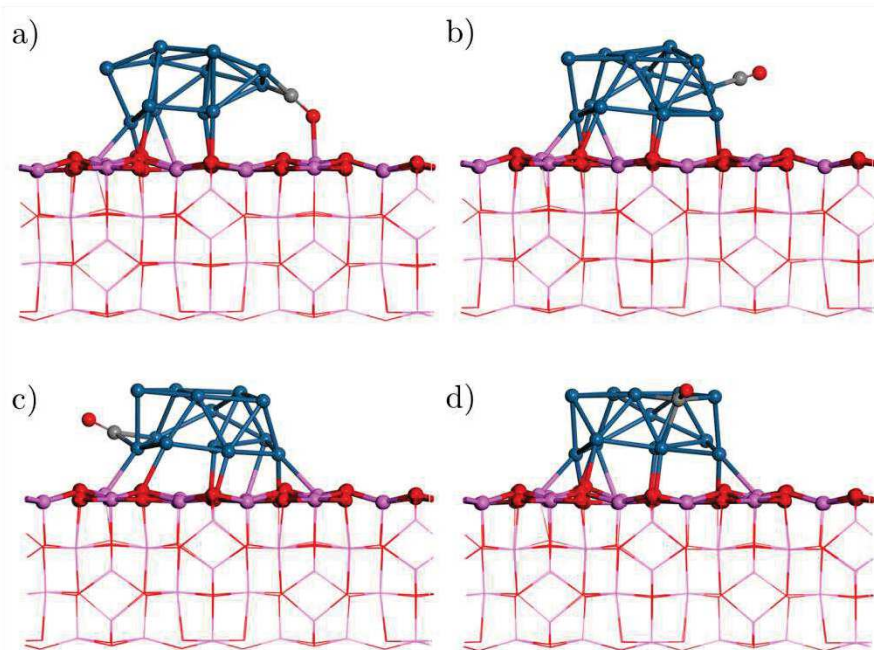


Figure 97: Illustration of  $\text{Pt}_{13}(\text{CO})$  typical structures found with a) the only alumina bonded CO, b) top c) bridge and d) hollow adsorption modes

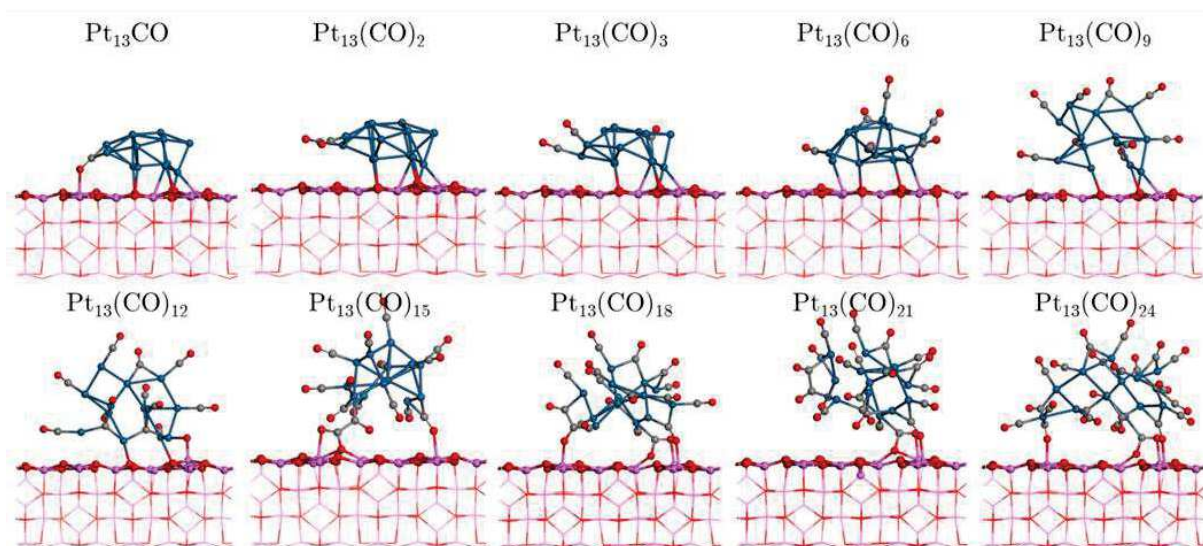


Figure 98: Illustrations of the supported  $\text{Pt}_{13}(\text{CO})_m$  structures

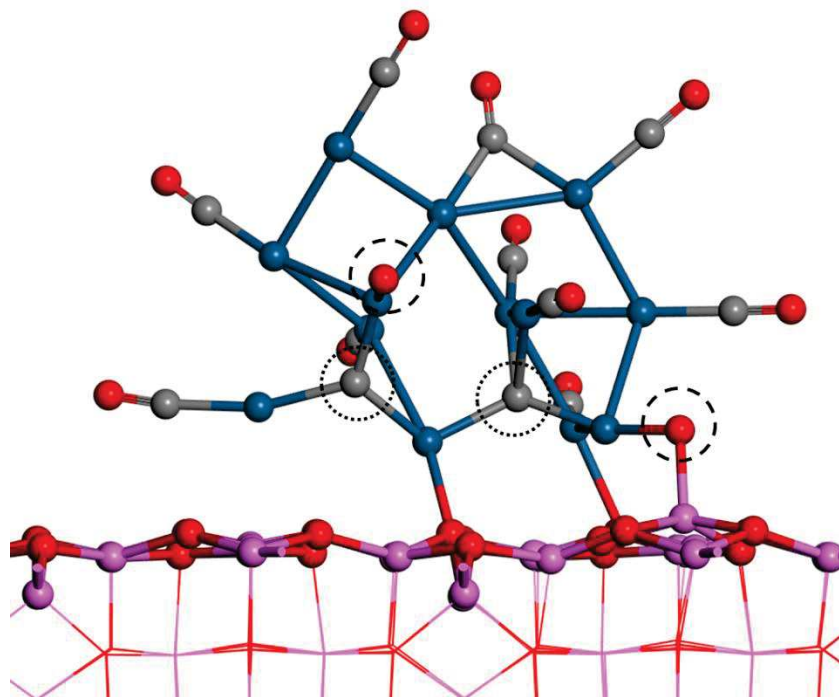


Figure 99: Backview the supported Pt<sub>13</sub>(CO)<sub>12</sub> structure with targeted carbon and oxygen atoms dissociated

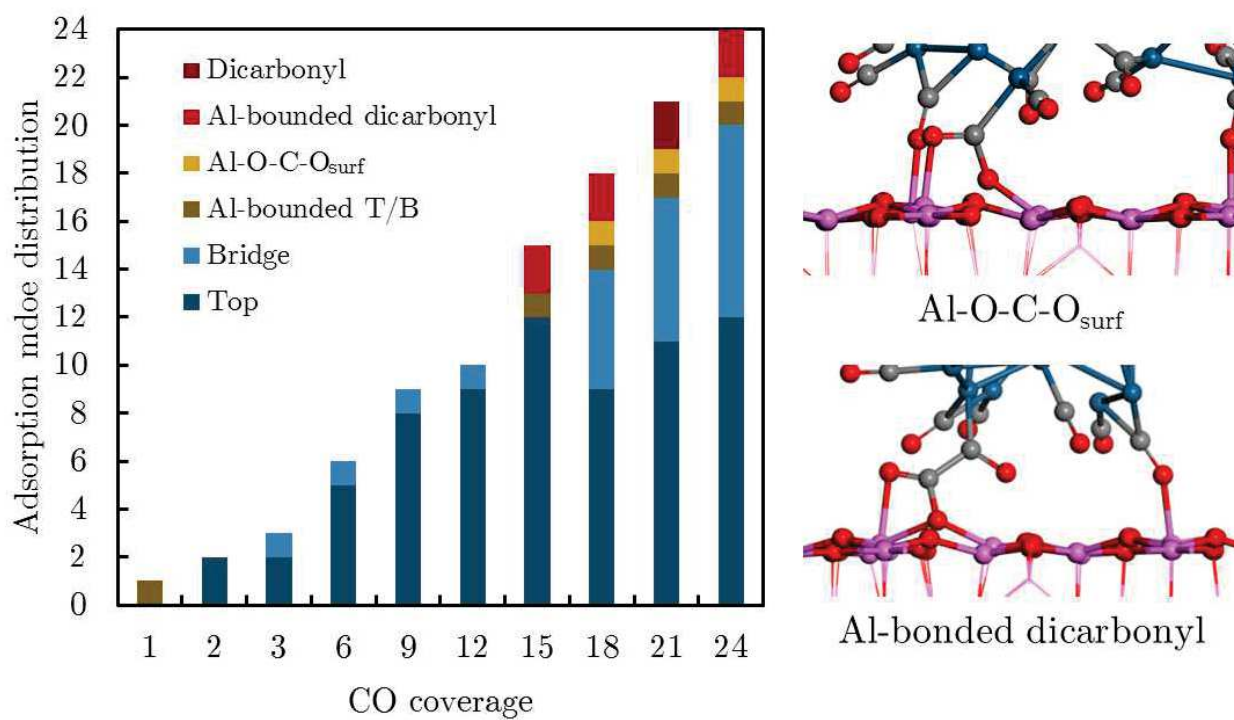


Figure 100: Population of adsorbed carbon monoxide according to their adsorption mode. The Al-bounded modes are characteristic of carbon monoxide linked to aluminum of the support.

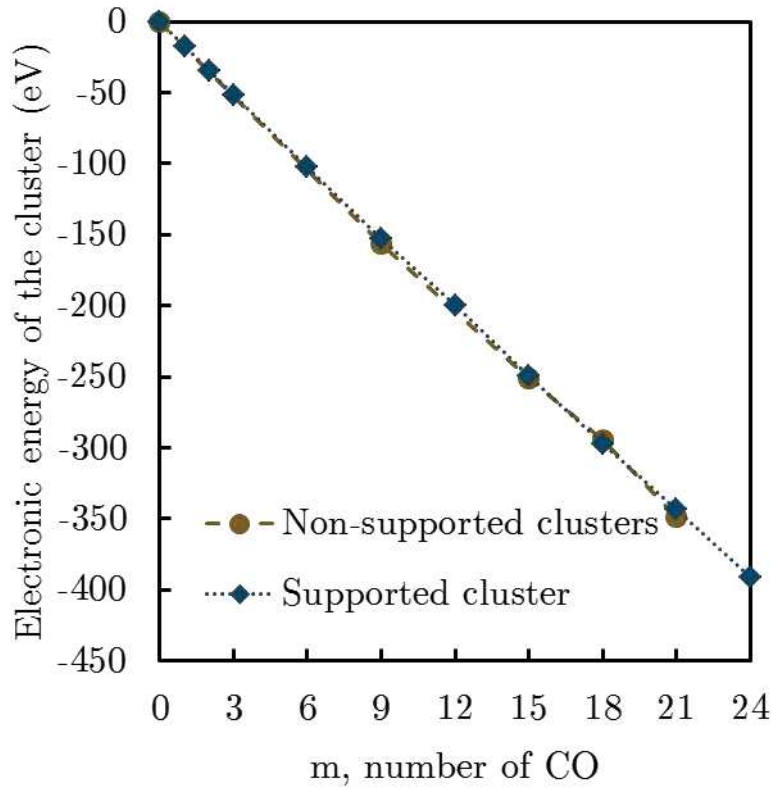


Figure 101: Electronic energy of the cluster only ( $\text{Pt}_{13}(\text{CO})_m$ , without alumina) for both supported and non-supported  $\text{Pt}_{13}(\text{CO})_m$  structures according to CO coverage. For supported structures, this energy is determined using single point calculation by equation (88).

$$E_{cluster} = E_{\text{Pt}_{13}(\text{CO})_m/\gamma\text{-Al}_2\text{O}_3} - E_{\gamma\text{-Al}_2\text{O}_3} \quad (88)$$

## B.6. Bader charges for the supported $\text{Pt}_{13}(\text{CO})_m$ structures

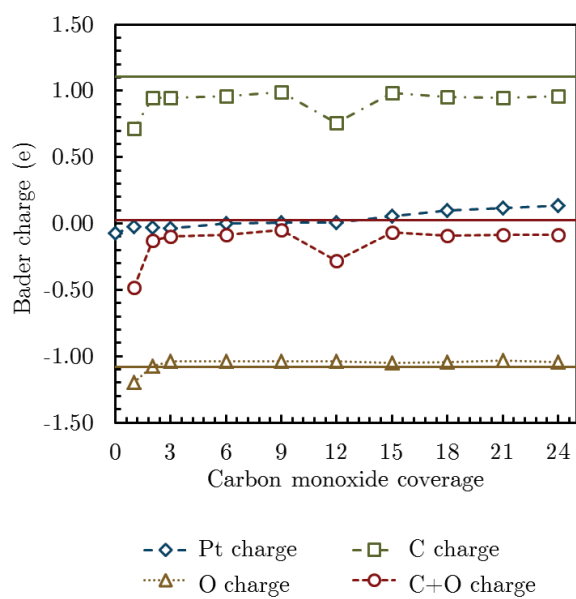


Figure 102: Bader charges of the elements present on the cluster. The straight lines deals with the CO gas charge.

## B.7. Experimental mass spectrometry recording during AEIR

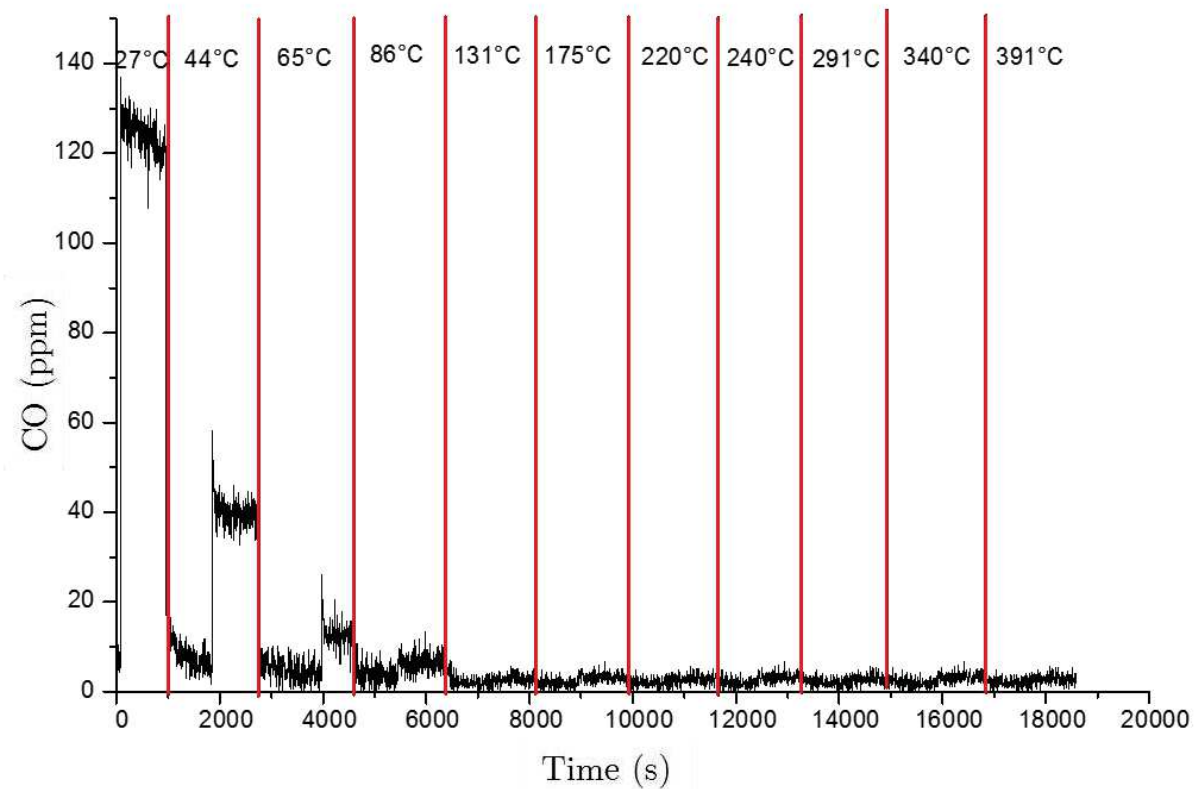


Figure 103: Carbon monoxide concentration recording from  $m/z=28$  signal of the mass spectrometer. Oxidation of CO into CO<sub>2</sub> lowers considerably CO signal above 86°C.

B.8. Extended study of CO sticking coefficient parameter  $s$  on the micro-kinetic scheme

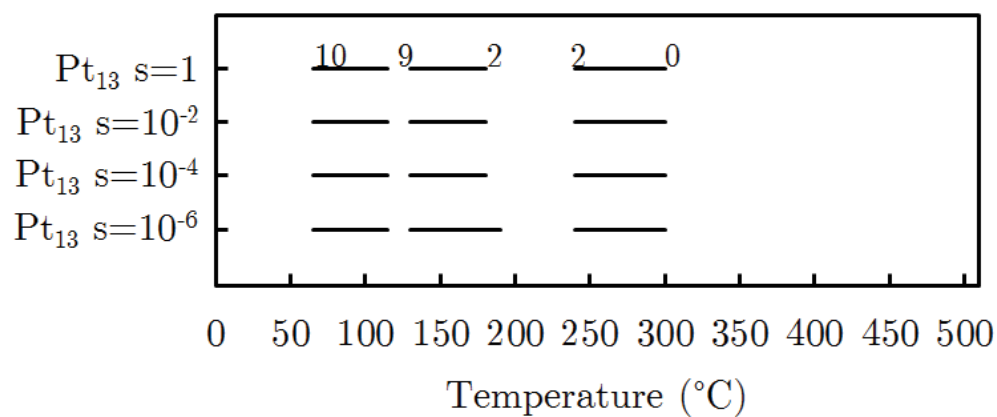


Figure 104: Carbon monoxide release temperature range according to CO sticking coefficient. The number of CO adspecies on  $Pt_{13}$  are displayed in the graph. Identical CO number were recorded for every CO sticking coefficients.

## B.9. Kinetic desorption parameters of $\text{Pt}_{13}(\text{CO})_m$ systems

Table 29: Reactions and kinetic parameters of the  $\text{Pt}_{13}(\text{CO})_m$  model with a sticking coefficient of 0.01

Adsorption reactions	Forward parameters			Backward parameters		
	Sticking coefficient	$\beta$	$E_{\text{adsorption}}$ (kcal.mol <sup>-1</sup> )	Pre-exponential factor (s <sup>-1</sup> )	$\beta$	$E_{\text{activation}}$ (kcal.mol <sup>-1</sup> )
$\text{CO} + \text{Pt}_{13} \leftrightarrow \text{Pt}_{13}(\text{CO})$	0.01	0.0	0.00	1.99E+28	0.5	67.0
$\text{CO} + \text{Pt}_{13}(\text{CO}) \leftrightarrow \text{Pt}_{13}(\text{CO})_2$	0.01	0.0	0.00	6.76E+25	0.5	62.9
$\text{CO} + \text{Pt}_{13}(\text{CO})_2 \leftrightarrow \text{Pt}_{13}(\text{CO})_3$	0.01	0.0	0.00	1.09E+28	0.5	48.6
$\text{CO} + \text{Pt}_{13}(\text{CO})_3 \leftrightarrow \text{Pt}_{13}(\text{CO})_4$	0.01	0.0	0.00	3.40E+27	0.5	49.5
$\text{CO} + \text{Pt}_{13}(\text{CO})_4 \leftrightarrow \text{Pt}_{13}(\text{CO})_5$	0.01	0.0	0.00	1.06E+27	0.5	50.5
$\text{CO} + \text{Pt}_{13}(\text{CO})_5 \leftrightarrow \text{Pt}_{13}(\text{CO})_6$	0.01	0.0	0.00	3.32E+26	0.5	51.4
$\text{CO} + \text{Pt}_{13}(\text{CO})_6 \leftrightarrow \text{Pt}_{13}(\text{CO})_7$	0.01	0.0	0.00	4.71E+26	0.5	51.4
$\text{CO} + \text{Pt}_{13}(\text{CO})_7 \leftrightarrow \text{Pt}_{13}(\text{CO})_8$	0.01	0.0	0.00	6.68E+26	0.5	51.2
$\text{CO} + \text{Pt}_{13}(\text{CO})_8 \leftrightarrow \text{Pt}_{13}(\text{CO})_9$	0.01	0.0	0.00	9.48E+26	0.5	51.2
$\text{CO} + \text{Pt}_{13}(\text{CO})_9 \leftrightarrow \text{Pt}_{13}(\text{CO})_{10}$	0.01	0.0	0.00	1.50E+27	0.5	43.5
$\text{CO} + \text{Pt}_{13}(\text{CO})_{10} \leftrightarrow \text{Pt}_{13}(\text{CO})_{11}$	0.01	0.0	0.00	2.36E+27	0.5	35.9
$\text{CO} + \text{Pt}_{13}(\text{CO})_{11} \leftrightarrow \text{Pt}_{13}(\text{CO})_{12}$	0.01	0.0	0.00	3.72E+27	0.5	28.2
$\text{CO} + \text{Pt}_{13}(\text{CO})_{12} \leftrightarrow \text{Pt}_{13}(\text{CO})_{13}$	0.01	0.0	0.00	1.01E+28	0.5	33.0
$\text{CO} + \text{Pt}_{13}(\text{CO})_{13} \leftrightarrow \text{Pt}_{13}(\text{CO})_{14}$	0.01	0.0	0.00	2.75E+28	0.5	37.6
$\text{CO} + \text{Pt}_{13}(\text{CO})_{14} \leftrightarrow \text{Pt}_{13}(\text{CO})_{15}$	0.01	0.0	0.00	7.48E+28	0.5	42.3
$\text{CO} + \text{Pt}_{13}(\text{CO})_{15} \leftrightarrow \text{Pt}_{13}(\text{CO})_{16}$	0.01	0.0	0.00	1.97E+28	0.5	36.6
$\text{CO} + \text{Pt}_{13}(\text{CO})_{16} \leftrightarrow \text{Pt}_{13}(\text{CO})_{17}$	0.01	0.0	0.00	5.17E+27	0.5	31.1
$\text{CO} + \text{Pt}_{13}(\text{CO})_{17} \leftrightarrow \text{Pt}_{13}(\text{CO})_{18}$	0.01	0.0	0.00	1.36E+27	0.5	25.6
$\text{CO} + \text{Pt}_{13}(\text{CO})_{18} \leftrightarrow \text{Pt}_{13}(\text{CO})_{19}$	0.01	0.0	0.00	2.18E+27	0.5	25.1
$\text{CO} + \text{Pt}_{13}(\text{CO})_{19} \leftrightarrow \text{Pt}_{13}(\text{CO})_{20}$	0.01	0.0	0.00	3.49E+27	0.5	24.6
$\text{CO} + \text{Pt}_{13}(\text{CO})_{20} \leftrightarrow \text{Pt}_{13}(\text{CO})_{21}$	0.01	0.0	0.00	5.59E+27	0.5	24.2
$\text{CO} + \text{Pt}_{13}(\text{CO})_{21} \leftrightarrow \text{Pt}_{13}(\text{CO})_{22}$	0.01	0.0	0.00	7.40E+27	0.5	24.6
$\text{CO} + \text{Pt}_{13}(\text{CO})_{22} \leftrightarrow \text{Pt}_{13}(\text{CO})_{23}$	0.01	0.0	0.00	9.79E+27	0.5	25.4
$\text{CO} + \text{Pt}_{13}(\text{CO})_{23} \leftrightarrow \text{Pt}_{13}(\text{CO})_{24}$	0.01	0.0	0.00	1.30E+28	0.5	25.8

## Appendices C: Carbon monoxide oxidation on Pt/ $\gamma$ -Al<sub>2</sub>O<sub>3</sub>

### C.1. Pt<sub>13</sub>O<sub>n</sub>(CO)<sub>m</sub> *ab initio* structures

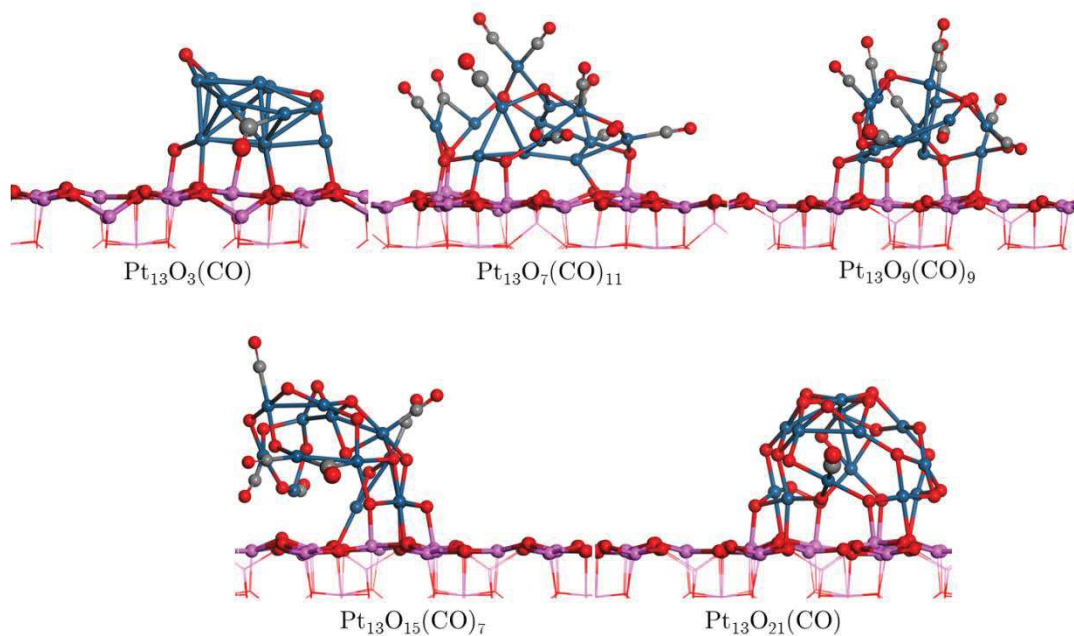


Figure 105: Illustrations of *ab initio* co-adsorbed Pt<sub>13</sub>O<sub>n</sub>(CO)<sub>m</sub> structures without the potential oxygen that take part to CO oxidation.

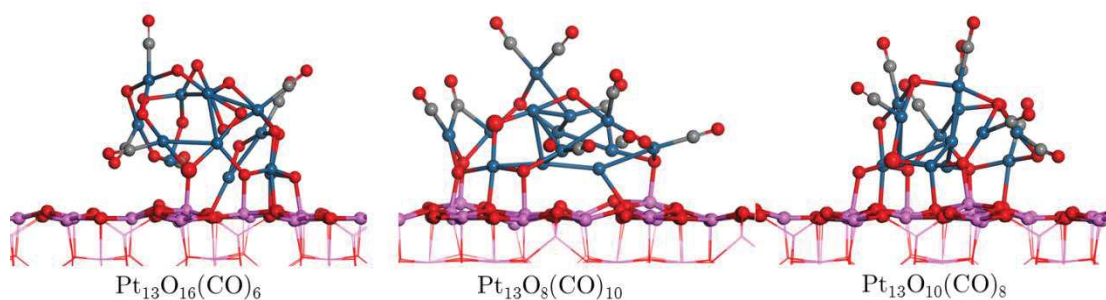


Figure 106: Illustrations of *ab initio* co-adsorbed Pt<sub>13</sub>O<sub>n</sub>(CO)<sub>m</sub> structures without the potential CO that take part to oxidation. Pt<sub>13</sub>O<sub>4</sub> and Pt<sub>13</sub>O<sub>22</sub> are displayed in chapter 3.

### C.2. Thermodynamic diagram snapshots

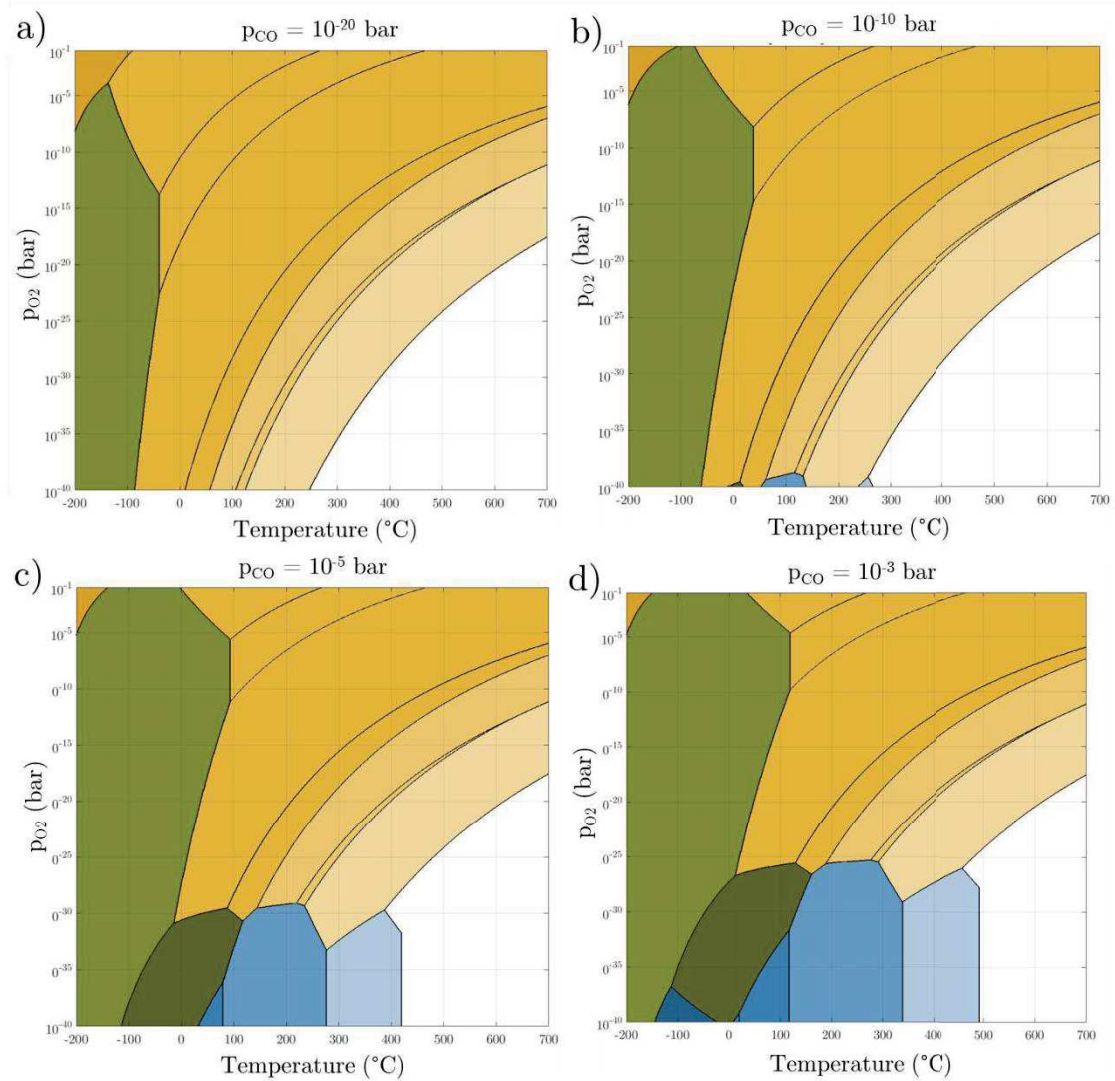


Figure 107: Thermodynamic diagram (pO<sub>2</sub>,T) for several pCO. White: Pt<sub>13</sub>. From dark to light green: Pt<sub>13</sub>O<sub>8</sub>(CO)<sub>11</sub> and Pt<sub>13</sub>O<sub>22</sub>(CO). From dark to light blue: Pt<sub>13</sub>(CO)<sub>24</sub>, Pt<sub>13</sub>(CO)<sub>18</sub>, Pt<sub>13</sub>(CO)<sub>15</sub>, Pt<sub>13</sub>(CO)<sub>9</sub> and Pt<sub>13</sub>(CO)<sub>2</sub>. From dark to light yellow: Pt<sub>13</sub>O<sub>32</sub>, Pt<sub>13</sub>O<sub>24</sub>, Pt<sub>13</sub>O<sub>22</sub>, Pt<sub>13</sub>O<sub>20</sub>, Pt<sub>13</sub>O<sub>16</sub>, Pt<sub>13</sub>O<sub>10</sub>, Pt<sub>13</sub>O<sub>8</sub> and Pt<sub>13</sub>O<sub>4</sub>.

### C.3. $\text{Pt}_{13}\text{O}_n(\text{CO})_m(\text{CO}_2)$ *ab initio* structures

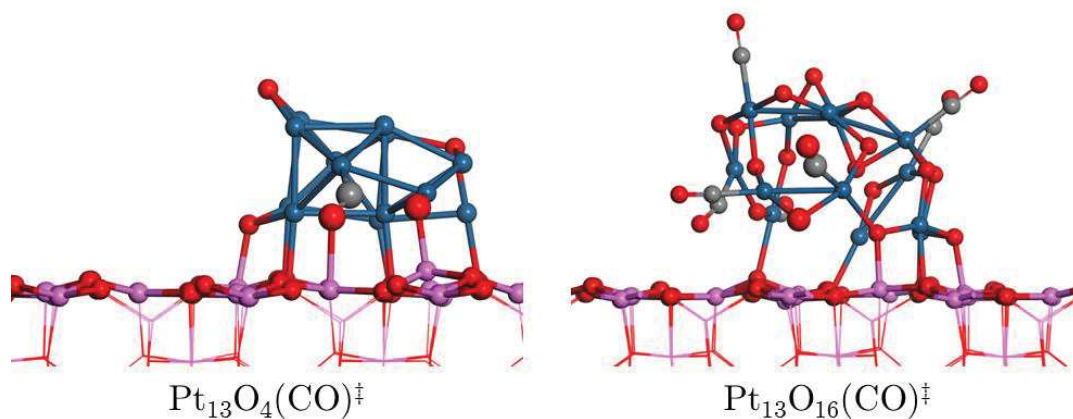


Figure 108: Illustrations of the transition states found for CO oxidation.

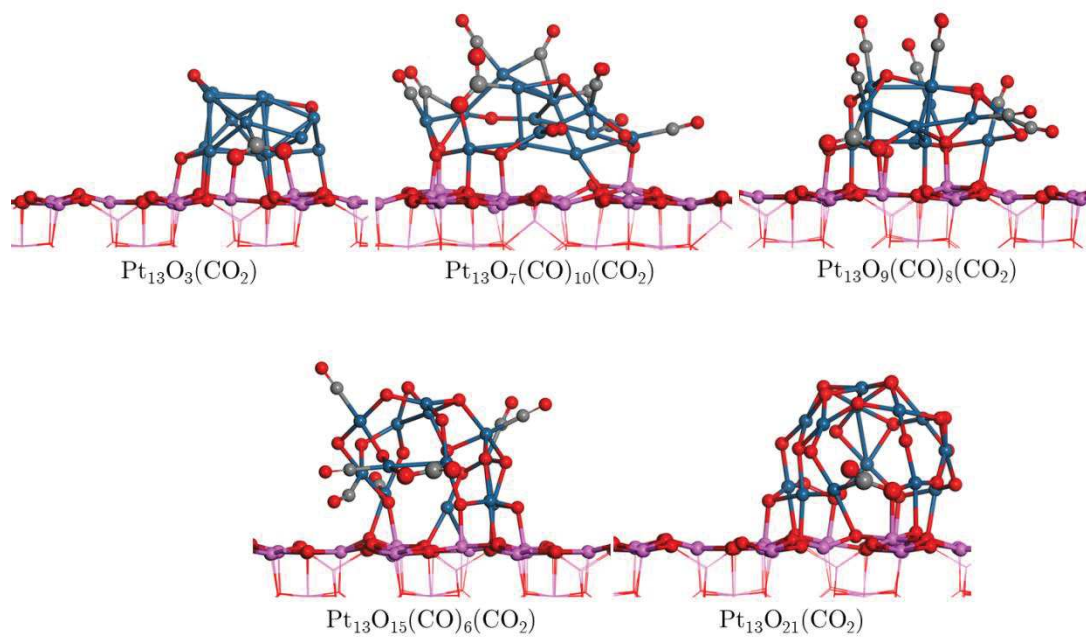


Figure 109: Illustrations of potential final states from co-adsorbed structures. The produced  $\text{CO}_2$  molecule is depicted with larger balls.

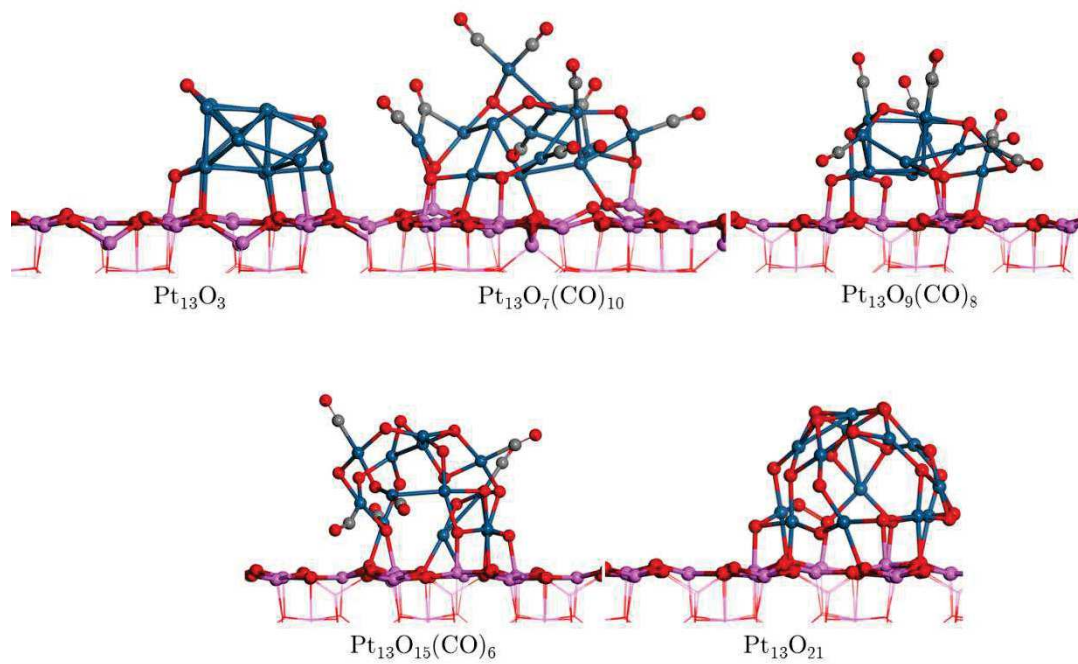


Figure 110: Illustrations of the final states structure after removing CO<sub>2</sub> molecule.

### C.4. Bader charge analyses of $\text{Pt}_{13}\text{O}_n(\text{CO})_m$ structures

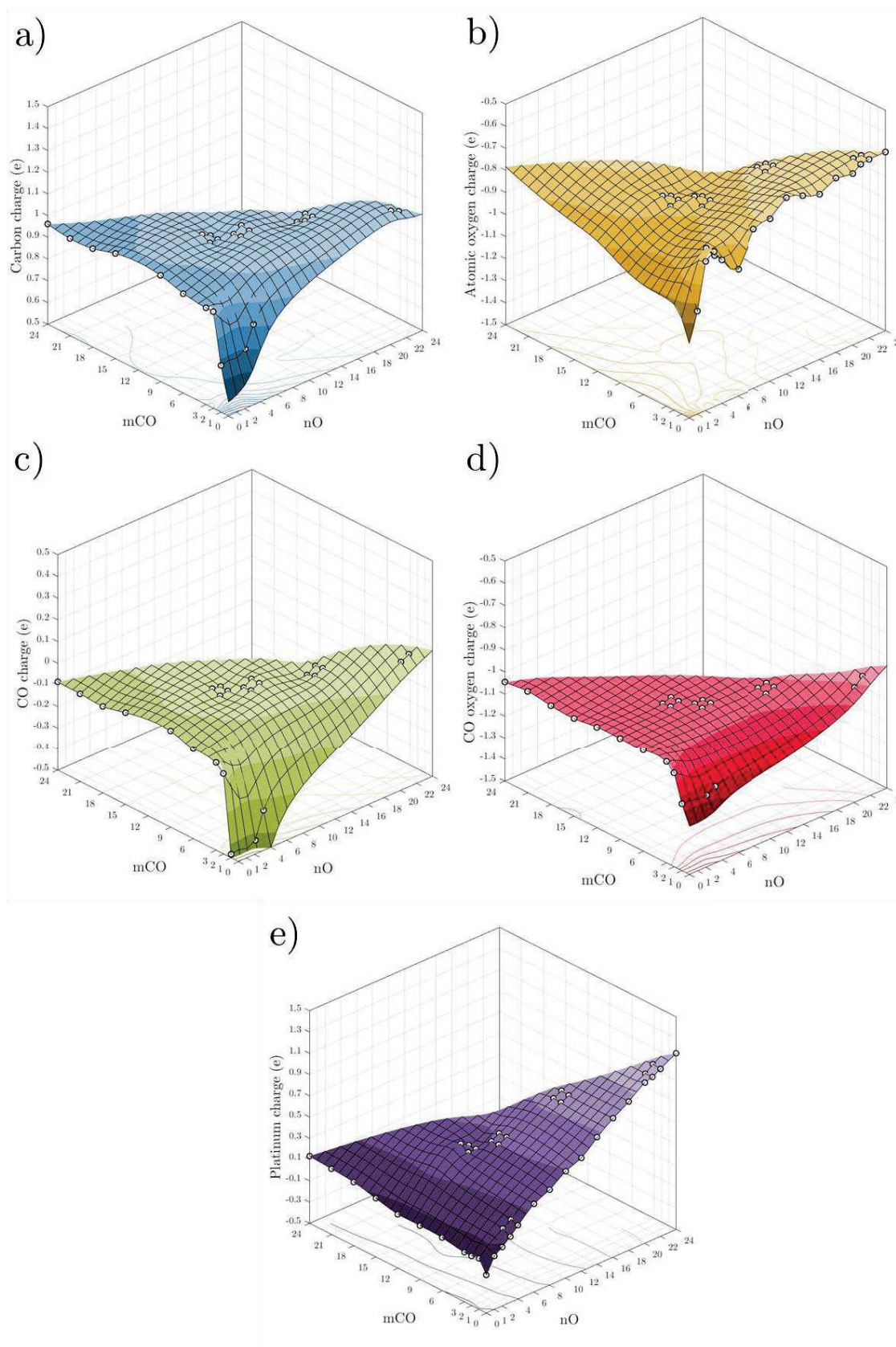


Figure 111: Bader charge analysis of a) carbon, b) atomic oxygen, c) CO molecule, d) CO oxygen and e) platinum. Thin spline interpolation gives a qualitative trend between data points.

### C.5. $\text{Pt}_{13}\text{O}_n(\text{CO})_m(\text{CO}_2)\text{H}_2\text{O}$ *ab initio* structures

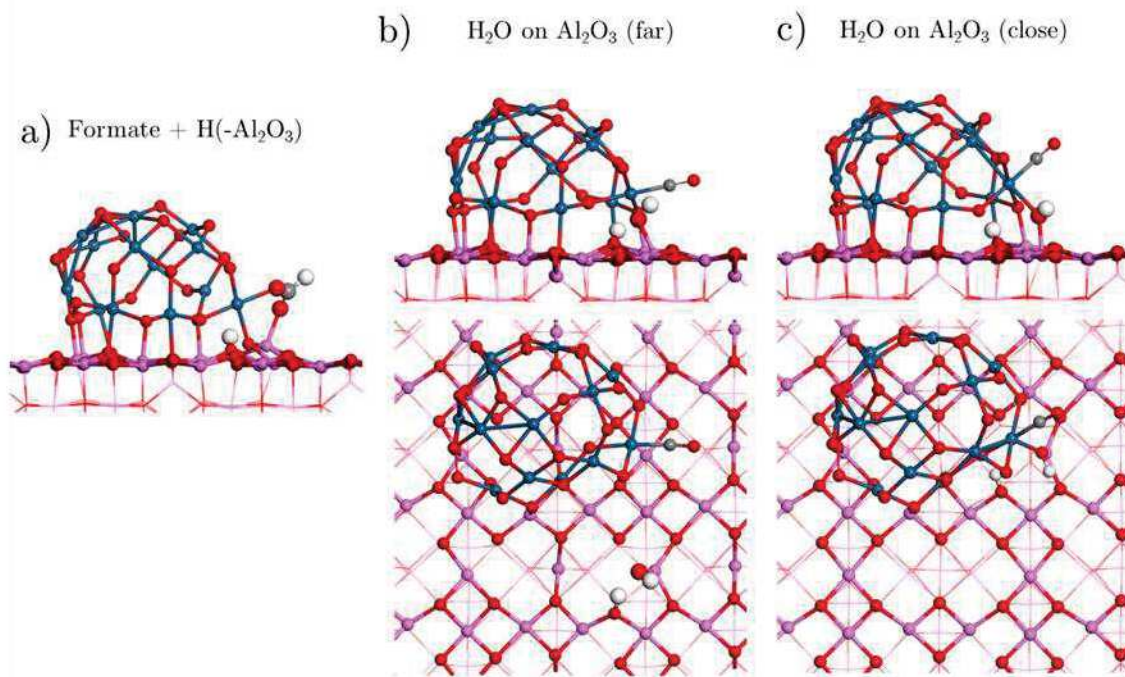


Figure 112: Illustration of inserted water in  $\text{Pt}_{13}\text{O}_{22}(\text{CO})$ .



Figure 113: Illustration of inserted water in  $\text{Pt}_{13}\text{O}_{21}(\text{CO}_2)$ .

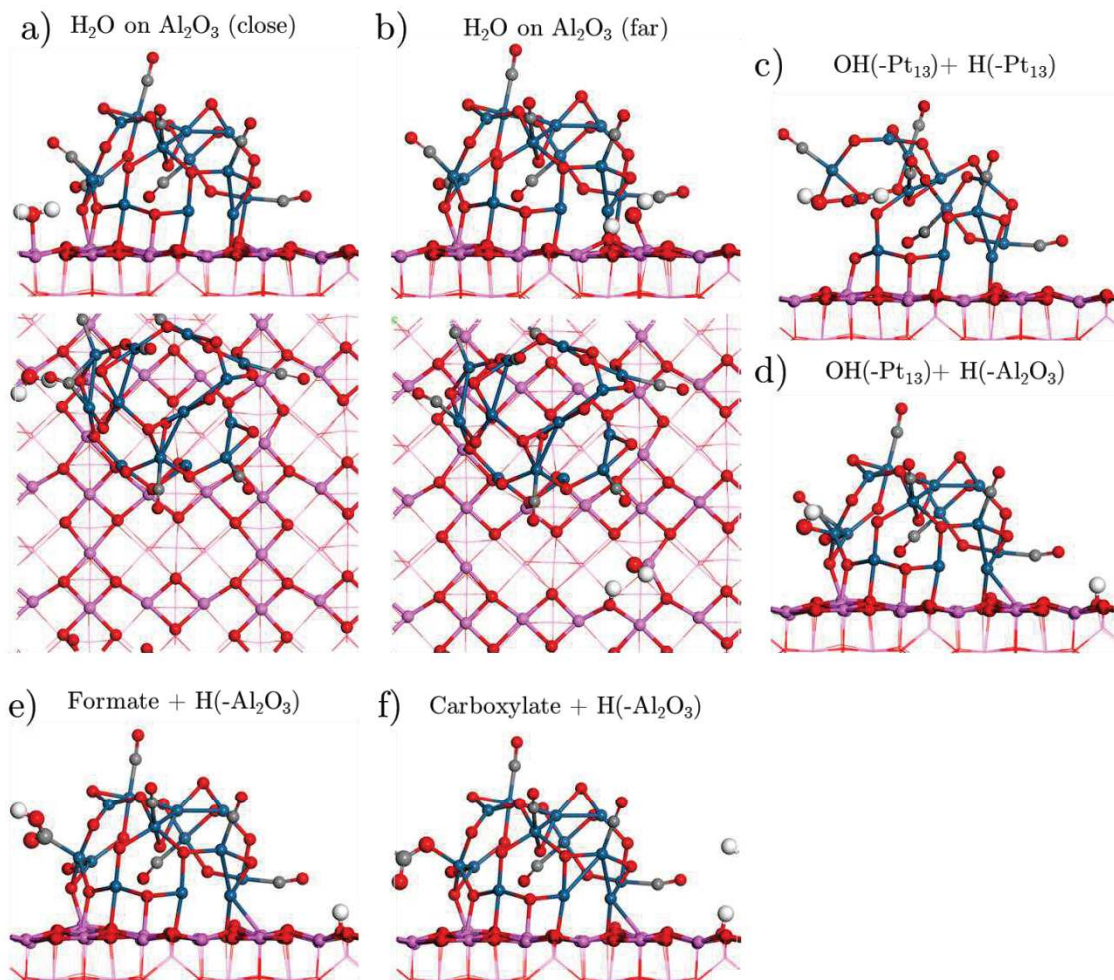


Figure 114: Illustration of inserted water in  $\text{Pt}_{13}\text{O}_{16}(\text{CO})_7$  structures.

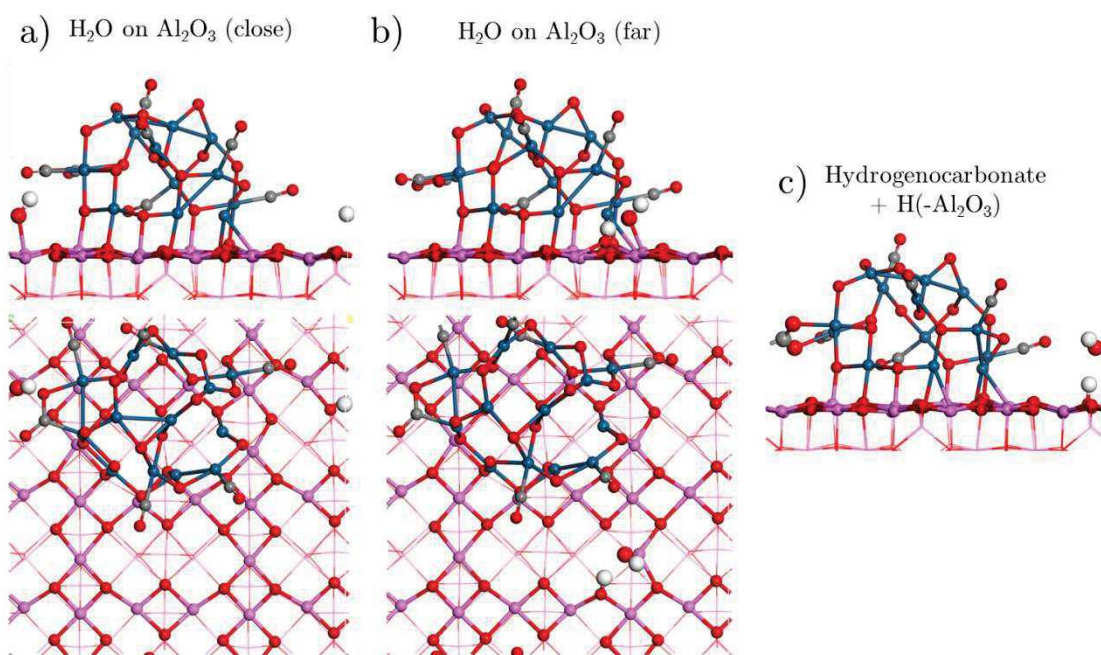


Figure 115: Illustration of inserted water in  $\text{Pt}_{13}\text{O}_{15}(\text{CO})_6(\text{CO}_2)$  structures.

## C.6. Simulation of $\text{O}_2$ and CO-TPD with CO oxidation scheme

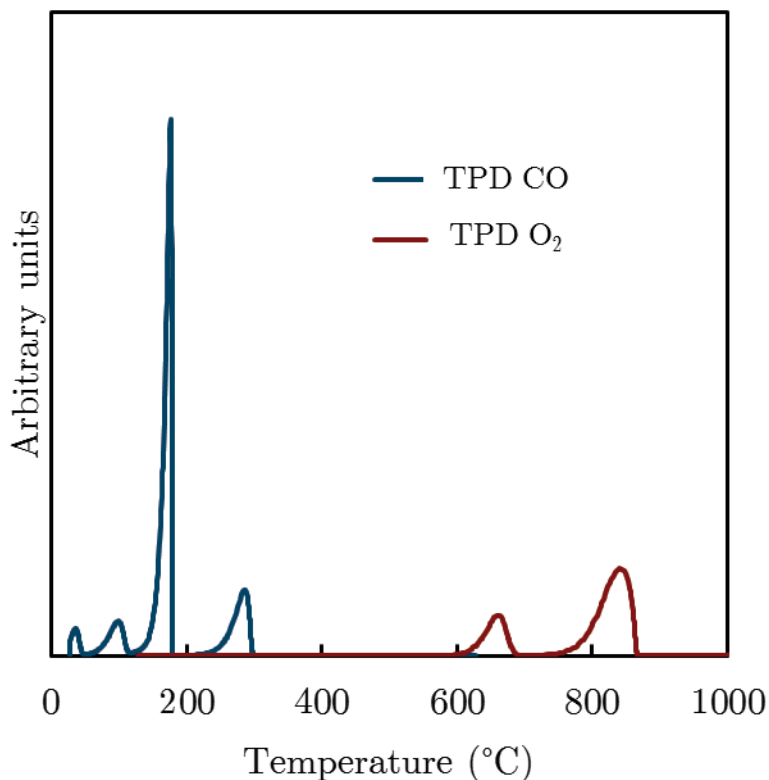


Figure 116: Simulation of  $\text{O}_2$  and CO-TPD with sticking coefficient set to unity and identical gas flow and surface species as in Chapters 3 and 4.

## C.7. Chemkin calculation conditions for CO oxidation

Script 1: Chemkin initial conditions typical script for CO oxidation. Surface fraction and temperature window are however varying considering the chosen model.

```
! problem type definition
! physical property
!Surface_Temperature ! Surface Temperature Same as Gas Temperature
! reactor dimension definition
! species property
! solver control
! output control and other misc. property
!
! problem type definition
!
```

```

TGIV ! Fix Gas Temperature
TRAN ! Transient Solver
!
! physical property
!
!Surface_Temperature ! Surface Temperature Same as Gas Temperature
IFAC 0.1 ! Ignition Noise Filtering Factor
PRES 1.0 ! Pressure (atm)
SCCM 50.0 ! Volumetric Flow Rate in SCCM (standard-cm3/min@298.15K)
TPRO 0.0 300.0 ! Temperature (K)
TPRO 6000.0 800.0 ! Temperature (K)
VOL 0.0244 ! Volume (cm3)
!
! reactor dimension definition
!
AREA 808.0 ! Internal Surface Area (cm2)
!
! species property
!
REAC CO 0.001 ! Reactant Fraction (mole fraction)
REAC HE 0.899 ! Reactant Fraction (mole fraction)
REAC O2 0.1 ! Reactant Fraction (mole fraction)
SURF Pt13O12(CO)10 0.05 ! Surface Fraction (site fraction)
SURF Pt13O12(CO)11 0.95 ! Surface Fraction (site fraction)
XEST CO 0.001 ! Initial Gas Fraction (mole fraction)
XEST HE 0.899 ! Initial Gas Fraction (mole fraction)
XEST O2 0.1 ! Initial Gas Fraction (mole fraction)
!
! solver control
!
ADAP ! Save Additional Adaptive Points
ASTEPS 20 ! Use Solver Integration Steps
ATLS 1.0E-6 ! Sensitivity Absolute Tolerance
ATOL 1.0E-18 ! Absolute Tolerance
HO 1.0E-25 ! Initial Step (sec)
MAXIT 4 ! Maximum Number of Iterations
NNEG ! Force Non-negative Solution
RELAXC ! Relaxed Iteration
RTLS 0.0001 ! Sensitivity Relative Tolerance
RTOL 1.0E-8 ! Relative Tolerance
SCOR ! Staggered Corrector Method
TIME 6000.0 ! End Time (sec)
!
! output control and other misc. property
!
EPSR 0.01 ! Threshold for Rate of Production
EPSS 0.001 ! Threshold for Species Sensitivity

```

EPST 0.001 ! Threshold for Temperature Sensitivity  
GFAC 1.0 ! Gas Reaction Rate Multiplier  
PRNT 3 ! Print Level Control  
SFAC 1.0 ! Surface Reaction Rate Multiplier  
SIZE 10000000 ! Solution Data Block Size (bytes)  
! Number of Continuation 0 ! Continuation Count  
END

## C.8. Kinetic parameters of MOL models

Table 30: Comparison between CO oxidation electronic and enthalpic energies

Reactions	$E_{\text{electronic}}$ (kcal.mol <sup>-1</sup> )	$E_{\text{activation}}$ (kcal.mol <sup>-1</sup> )
$\text{Pt}_{13}\text{O}_4(\text{CO}) \rightarrow \text{Pt}_{13}\text{O}_3(\text{CO}_2)$	11.8	61.7
$\text{Pt}_{13}\text{O}_{15}(\text{CO})_6(\text{CO}_2) \rightarrow \text{Pt}_{13}\text{O}_{16}(\text{CO})_7$	12.0	10.5

Table 31: Kinetics parameters of the MOL-Pt<sub>13</sub>O<sub>4</sub>(CO)-eq following Arrhenius-type rate constants.

Reactions	s or A (s <sup>-1</sup> )	n	$E_{\text{activation}}$ (kcal.mol <sup>-1</sup> )
$\text{Pt}_{13}\text{O}_3 + \text{CO}_2 \rightarrow \text{Pt}_{13}\text{O}_3(\text{CO}_2)$	1.0	0	0
$\text{Pt}_{13}\text{O}_3(\text{CO}_2) \rightarrow \text{Pt}_{13}\text{O}_3 + \text{CO}_2$	2.955E+42	0.5	81.7
$\text{Pt}_{13}\text{O}_4(\text{CO}) \rightarrow \text{Pt}_{13}\text{O}_3(\text{CO}_2)$	4.872E+29	1.0	61.7
$\text{Pt}_{13}\text{O}_3(\text{CO}_2) \rightarrow \text{Pt}_{13}\text{O}_4(\text{CO})$	1.274E+30	1.0	84.4

Table 32: Kinetics parameters of the MOL-Pt<sub>13</sub>O<sub>4</sub>(CO)-50 following Arrhenius-type rate constants.

Reactions	s or A (s <sup>-1</sup> )	n	$E_{\text{activation}}$ (kcal.mol <sup>-1</sup> )
$\text{Pt}_{13}\text{O}_3 + \text{CO}_2 \rightarrow \text{Pt}_{13}\text{O}_3(\text{CO}_2)$	1.0	0	0
$\text{Pt}_{13}\text{O}_3(\text{CO}_2) \rightarrow \text{Pt}_{13}\text{O}_3 + \text{CO}_2$	2.955E+42	0.5	81.7
$\text{Pt}_{13}\text{O}_4(\text{CO}) \rightarrow \text{Pt}_{13}\text{O}_3(\text{CO}_2)$	4.903E+28	1.0	61.7
$\text{Pt}_{13}\text{O}_3(\text{CO}_2) \rightarrow \text{Pt}_{13}\text{O}_4(\text{CO})$	1.283E+29	1.0	84.4

Table 33: Kinetics parameters of the MOL-Pt<sub>13</sub>O<sub>16</sub>(CO)<sub>7</sub> following Arrhenius-type rate constants.

Reactions	s or A (s <sup>-1</sup> )	n	$E_{\text{activation}}$ (kcal.mol <sup>-1</sup> )
-----------	---------------------------	---	---

$\text{Pt}_{13}\text{O}_{15}(\text{CO})_6 + \text{CO}_2 \rightarrow \text{Pt}_{13}\text{O}_{15}(\text{CO})_6(\text{CO}_2)$	1.0	0	0
$\text{Pt}_{13}\text{O}_{15}(\text{CO})_6(\text{CO}_2) \rightarrow \text{Pt}_{13}\text{O}_{15}(\text{CO})_6 + \text{CO}_2$	3.968E+28	0.5	0
$\text{Pt}_{13}\text{O}_{16}(\text{CO})_7 \rightarrow \text{Pt}_{13}\text{O}_{15}(\text{CO})_6(\text{CO}_2)$	1.910E+10	1.0	10.5
$\text{Pt}_{13}\text{O}_{15}(\text{CO})_6(\text{CO}_2) \rightarrow \text{Pt}_{13}\text{O}_{16}(\text{CO})_7$	2.009E+10	1.0	34.7

### C.9. DES-Pt<sub>13</sub>O<sub>4</sub>(CO): reaction fluxes and surface species

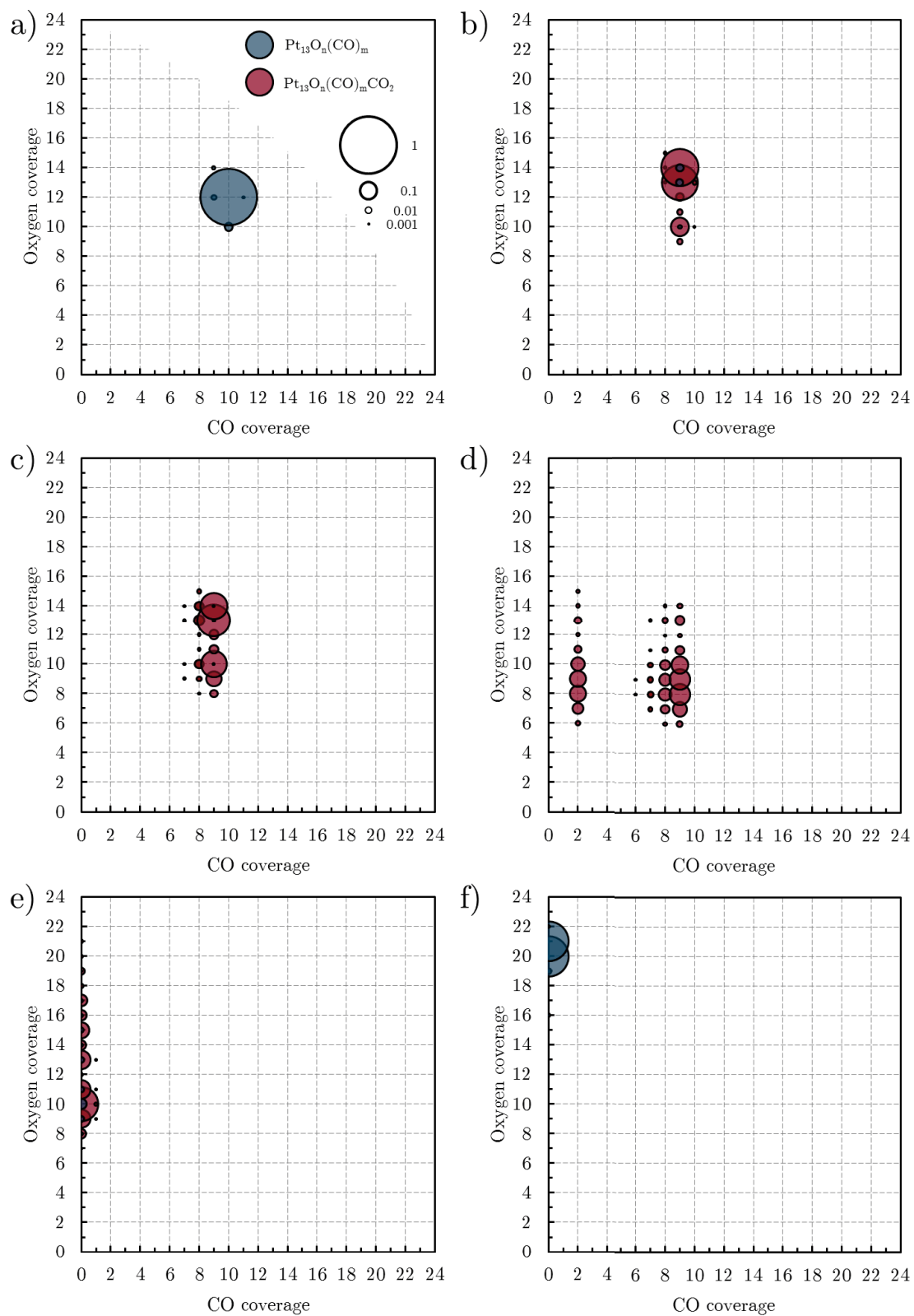


Figure 117: Surface species during CO oxidation with DES-Pt<sub>13</sub>O<sub>4</sub>(CO) model at a) 80°C, b) 140°C, c) 160°C, d) 170°C, e) 180°C and f) 200°C.

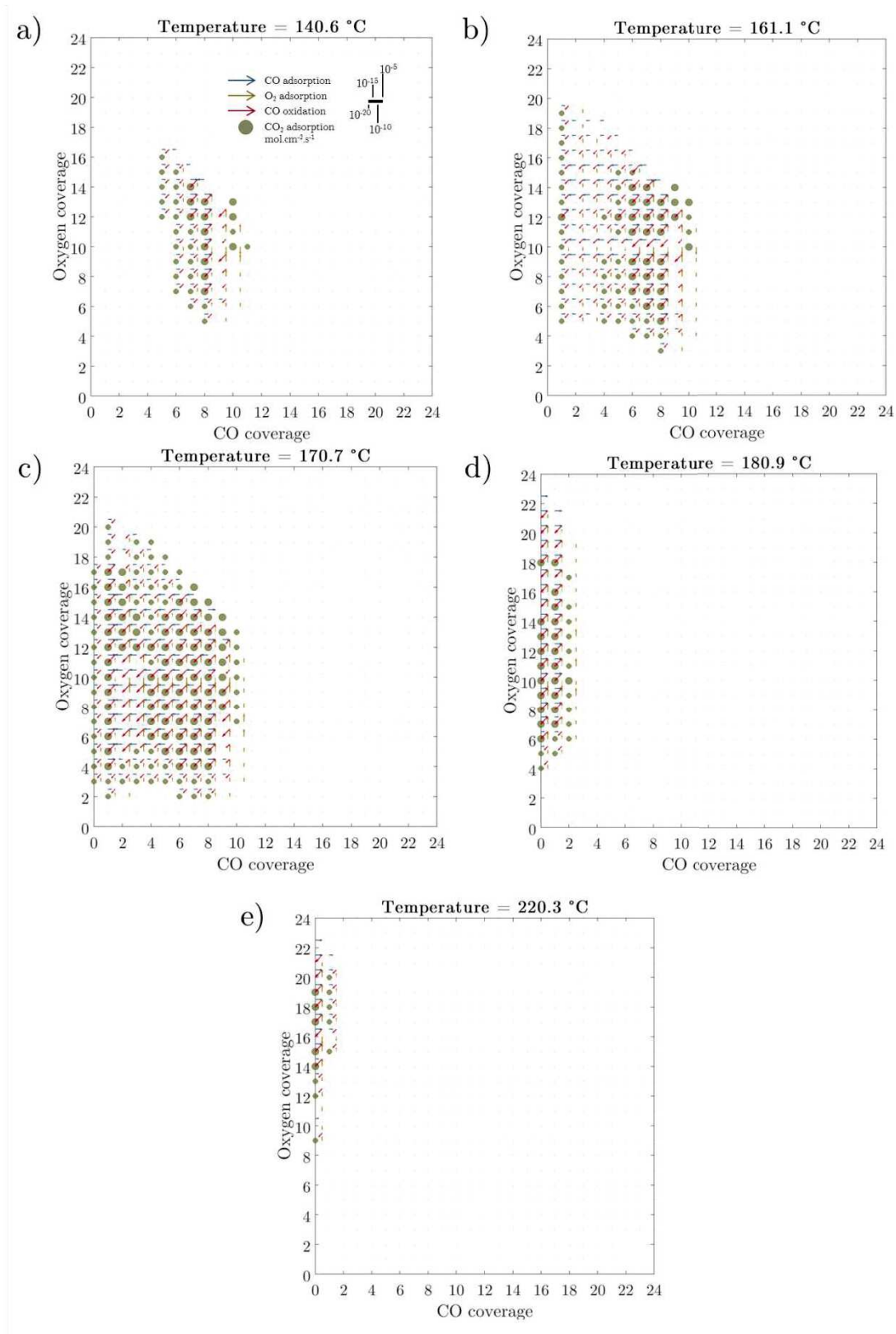


Figure 118: Reaction fluxes during CO oxidation with DES-Pt<sub>13</sub>O<sub>4</sub>(CO) model.

### C.10. DES-Pt<sub>13</sub>O<sub>16</sub>(CO)<sub>7</sub>: reaction fluxes and surface species

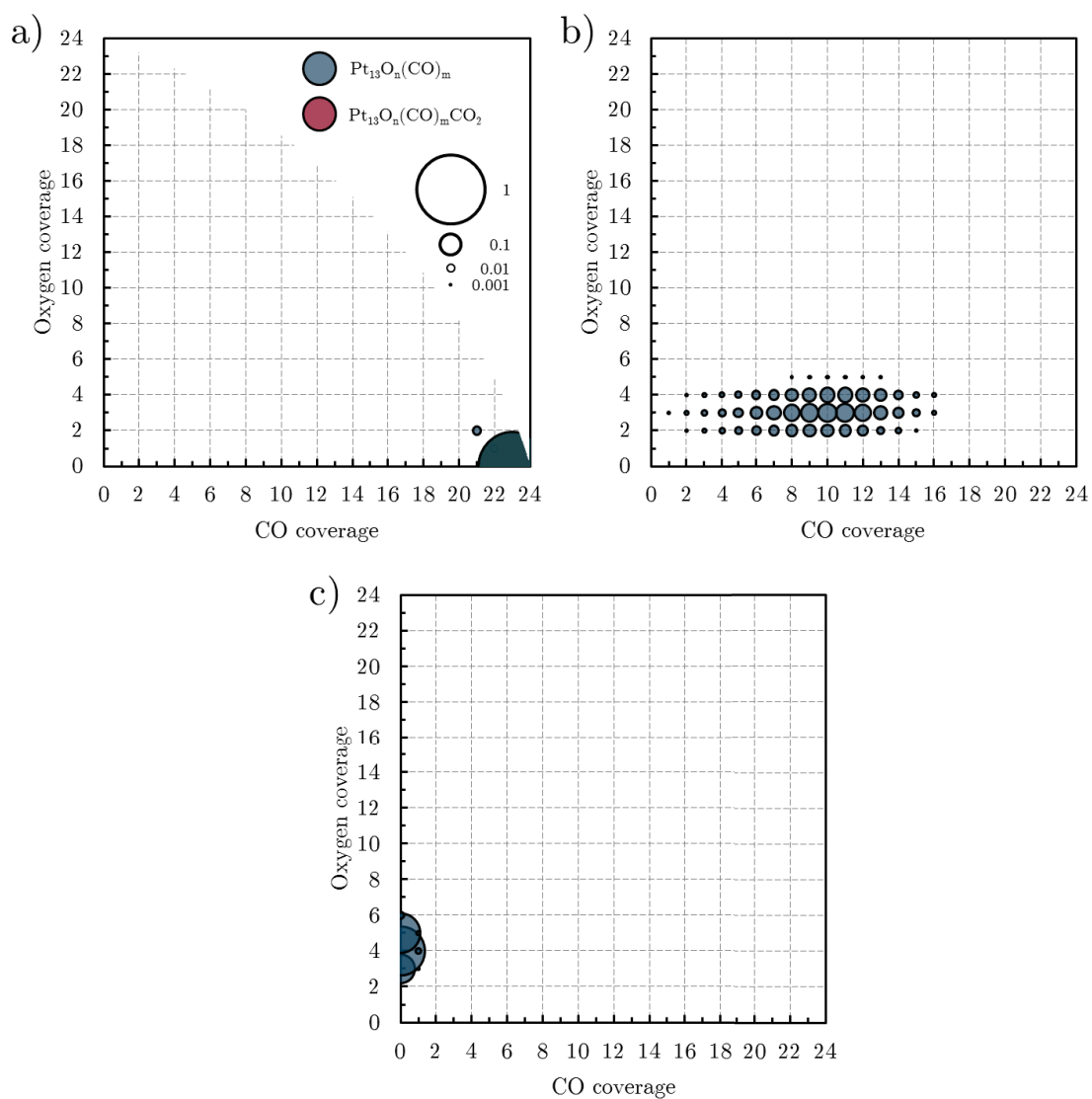


Figure 119: Surface species during DES-Pt<sub>13</sub>O<sub>16</sub>(CO)<sub>7</sub> simulation through oxidation of CO. Oxidation appears starts at a) -82.5°C, in progress at b) -82°C and almost finished around c) -81°C.

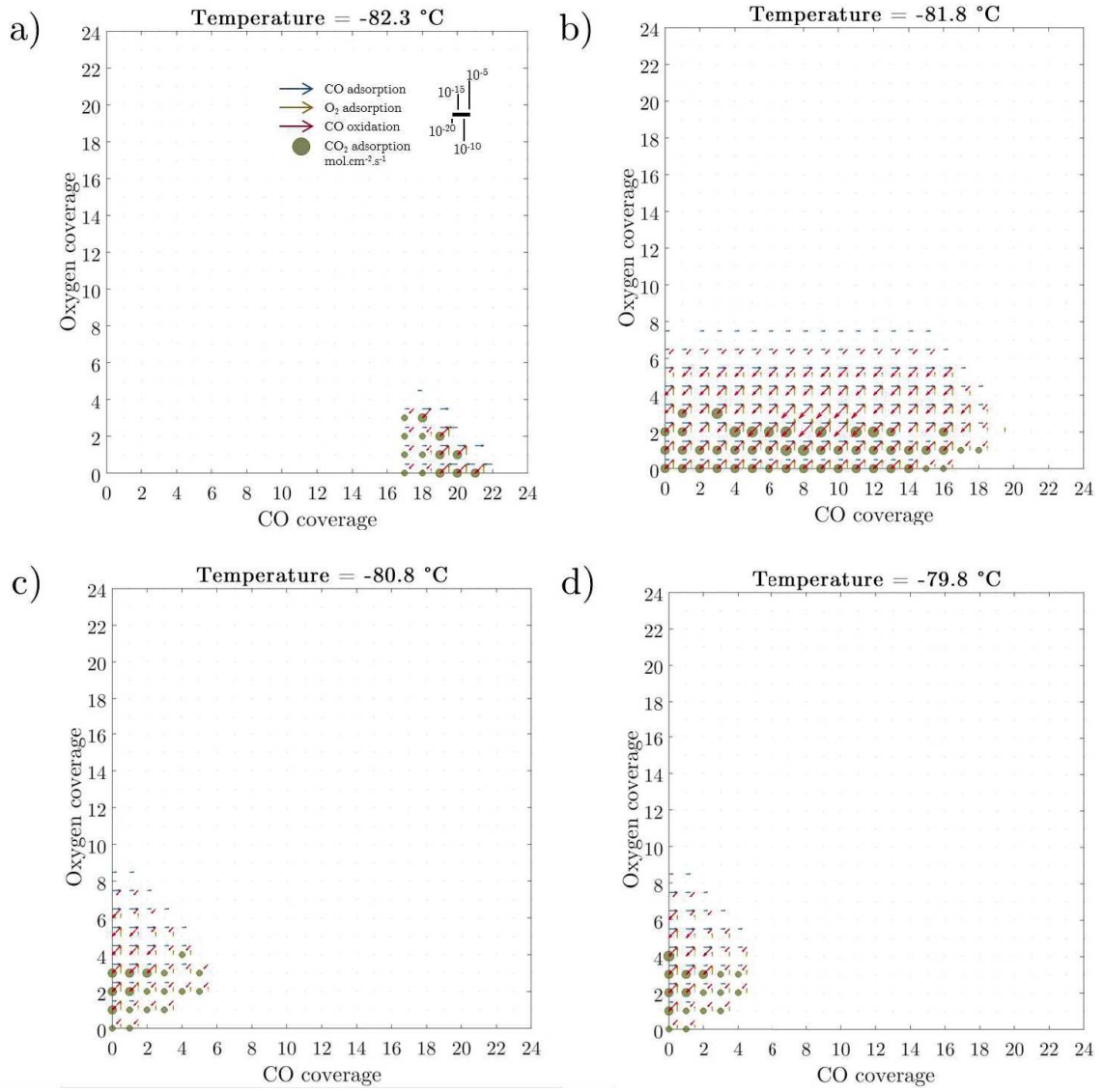


Figure 120: Reaction fluxes during CO oxidation with DES-Pt<sub>13</sub>O<sub>16</sub>(CO)<sub>7</sub> model.

### C.11. VAR models: CO<sub>2</sub> desorption parameters

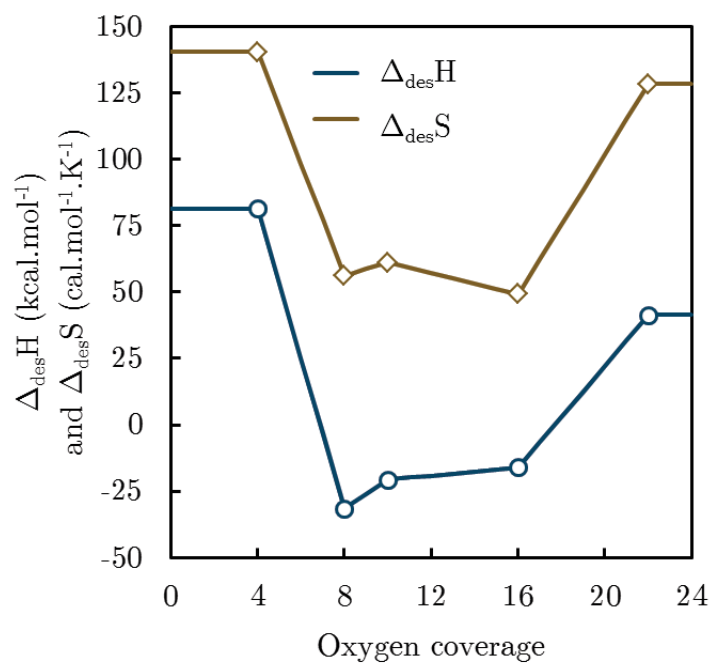


Figure 121: *Ab initio* determined CO<sub>2</sub> desorption enthalpy and entropy (dots) and their linear interpolation (lines) according to oxygen coverage. These interpolations are used for CO oxidation VAR and CPX models.

### C.12. VAR- $\text{Pt}_{13}\text{O}_4(\text{CO})$ : reaction fluxes and surface species

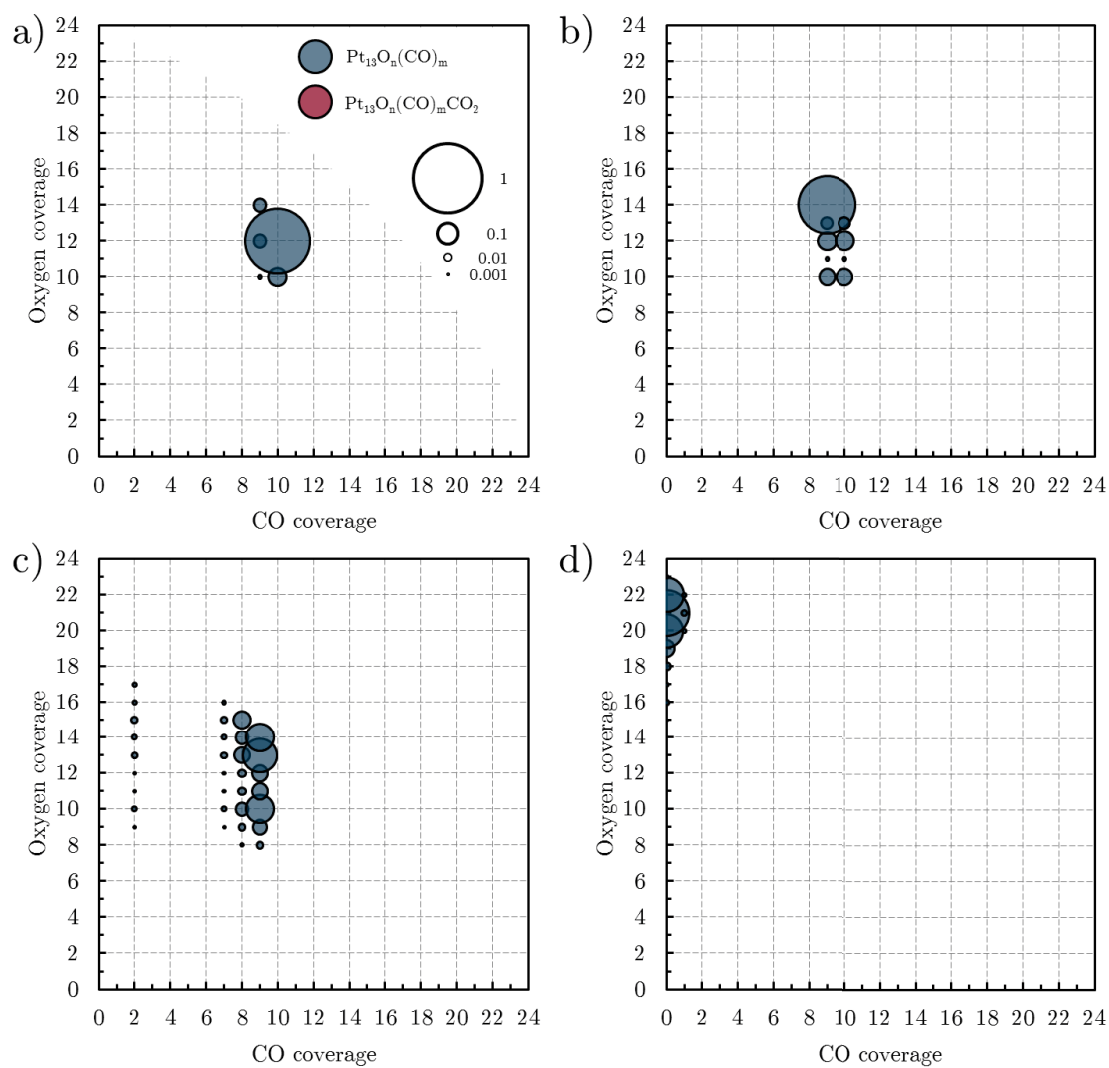


Figure 122: Surface species during CO oxidation with VAR- $\text{Pt}_{13}\text{O}_4(\text{CO})$  model at a) 90°C, b) 110°C, c) 130°C and d) 150°C.

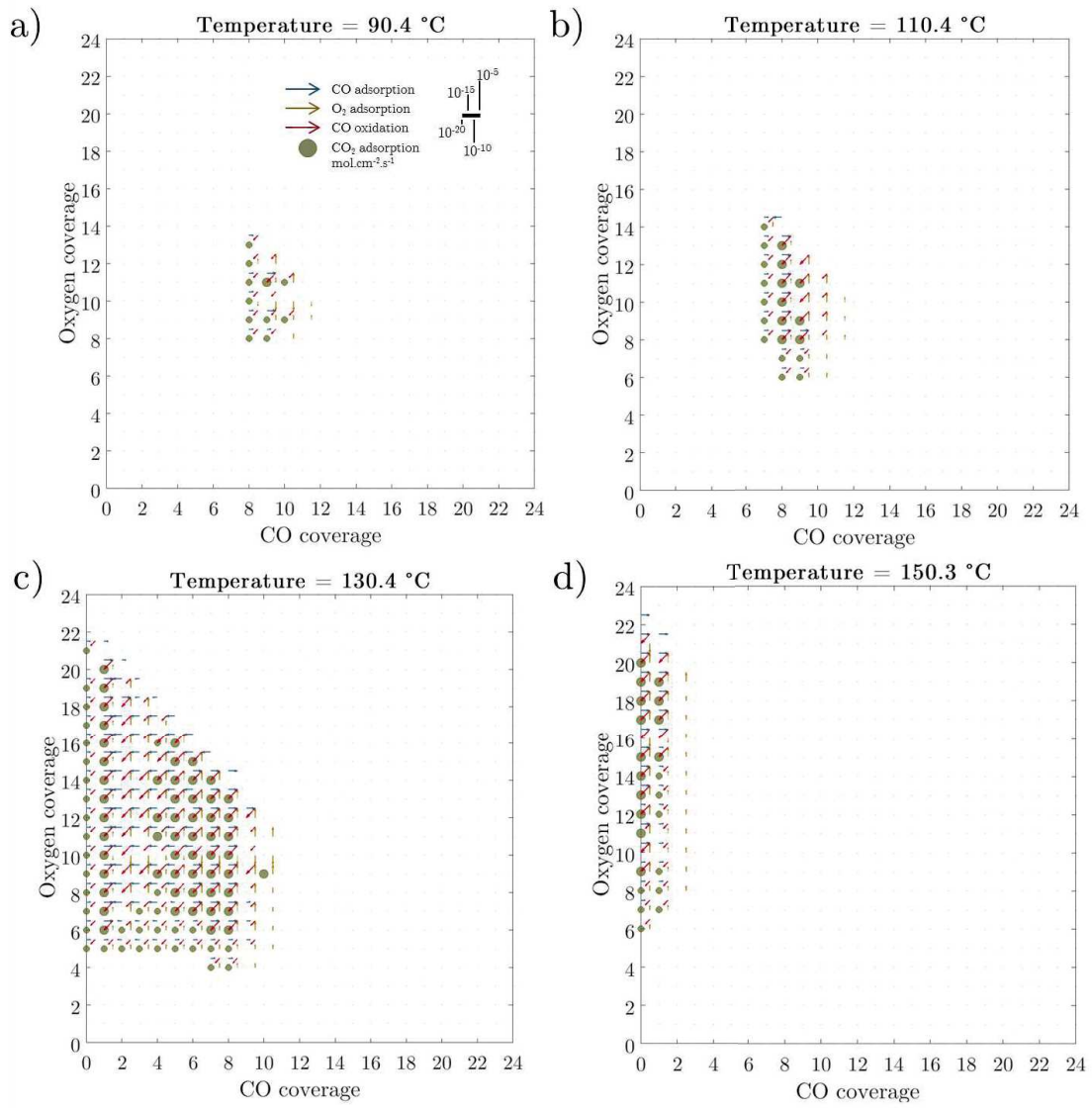


Figure 123: Reaction fluxes during CO oxidation with VAR-Pt<sub>13</sub>O<sub>4</sub>(CO) model.

### C.13. VAR-Pt<sub>13</sub>O<sub>16</sub>(CO)<sub>7</sub>: reaction fluxes and surface species

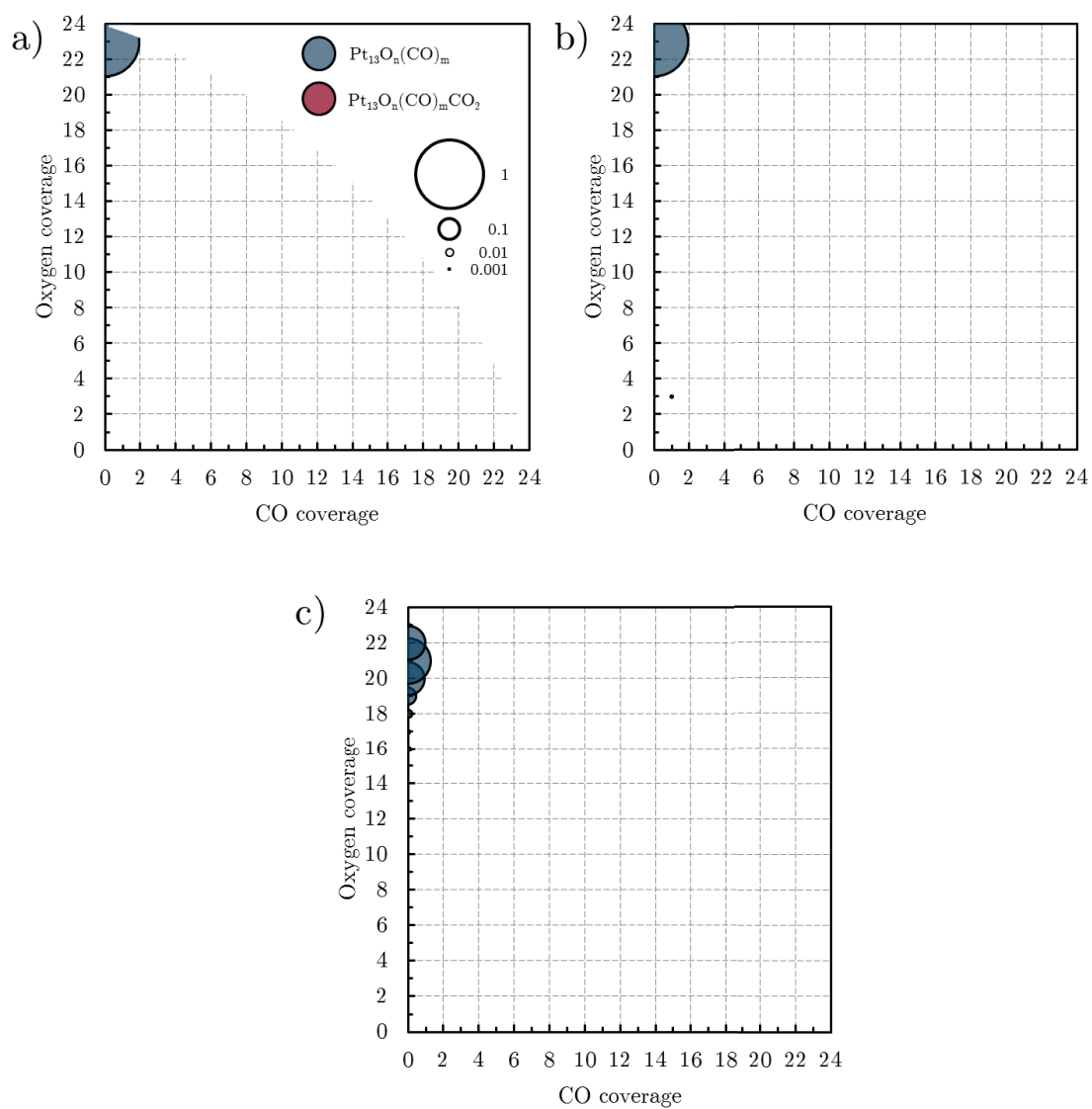


Figure 124: Surface species during CO oxidation with VAR-Pt<sub>13</sub>O<sub>16</sub>(CO)<sub>7</sub> model at a) 50°C, b) 80°C and c) 150°C.

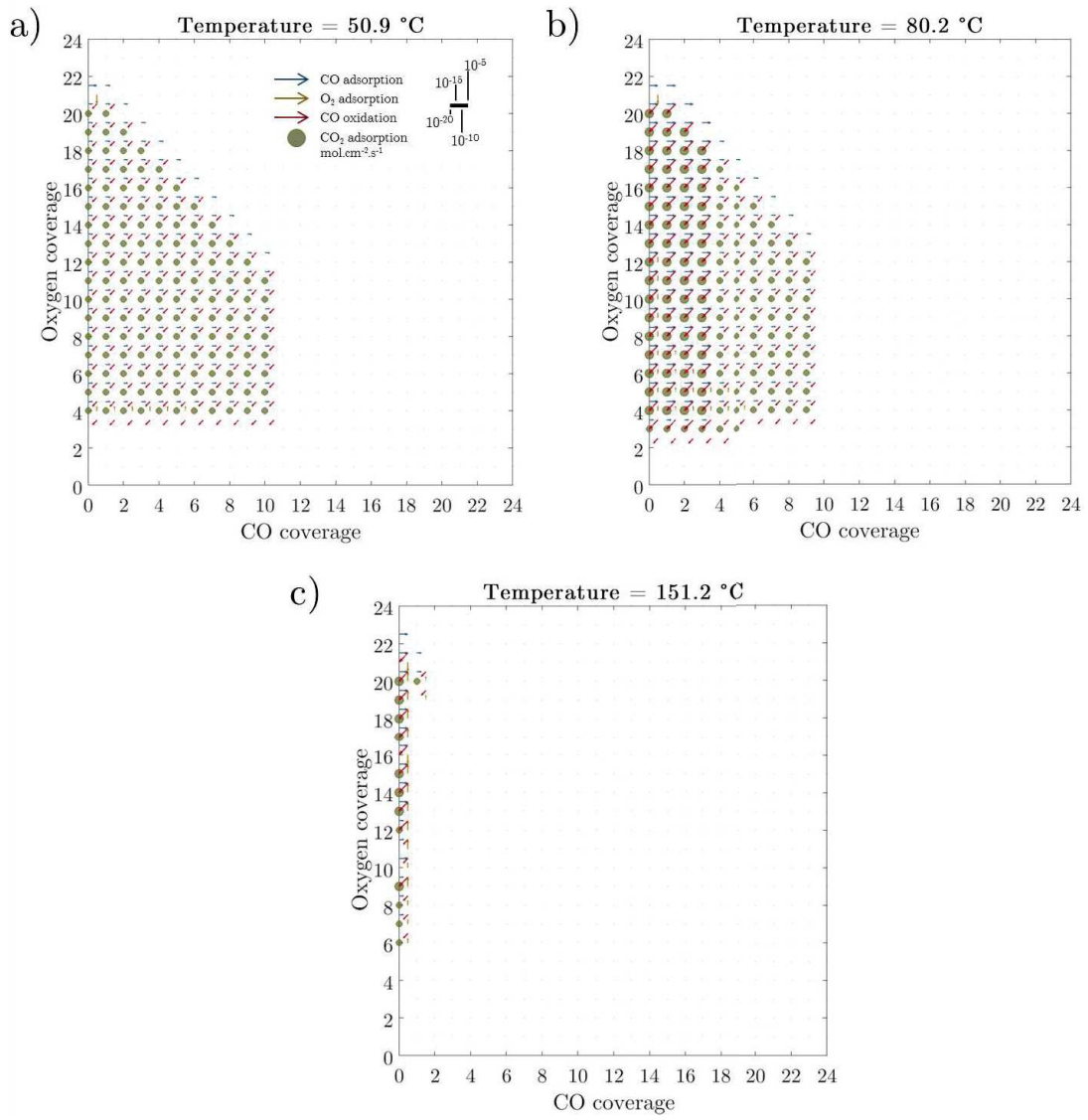


Figure 125: Reaction fluxes during CO oxidation with VAR-Pt<sub>13</sub>O<sub>16</sub>(CO)<sub>7</sub>.

C.14.  $\text{CPX}_{\text{sp1}}\text{-Pt}_{13}\text{O}_4(\text{CO})\text{-eq}$ : reaction fluxes and surface species

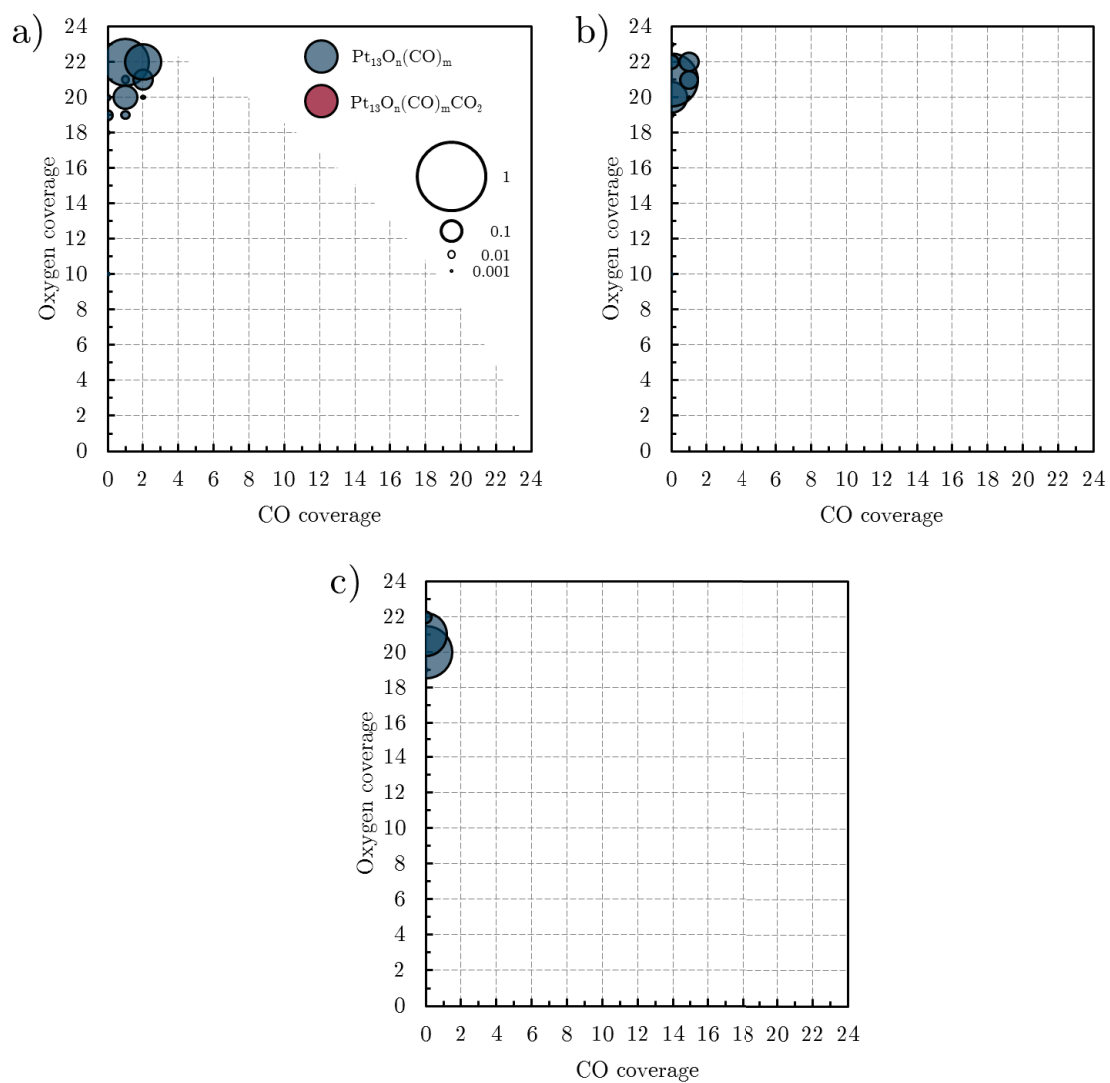


Figure 126: Surface species during CO oxidation with VAR- $\text{Pt}_{13}\text{O}_4(\text{CO})$  model at a) 130°C, b) 150°C and c) 190°C.

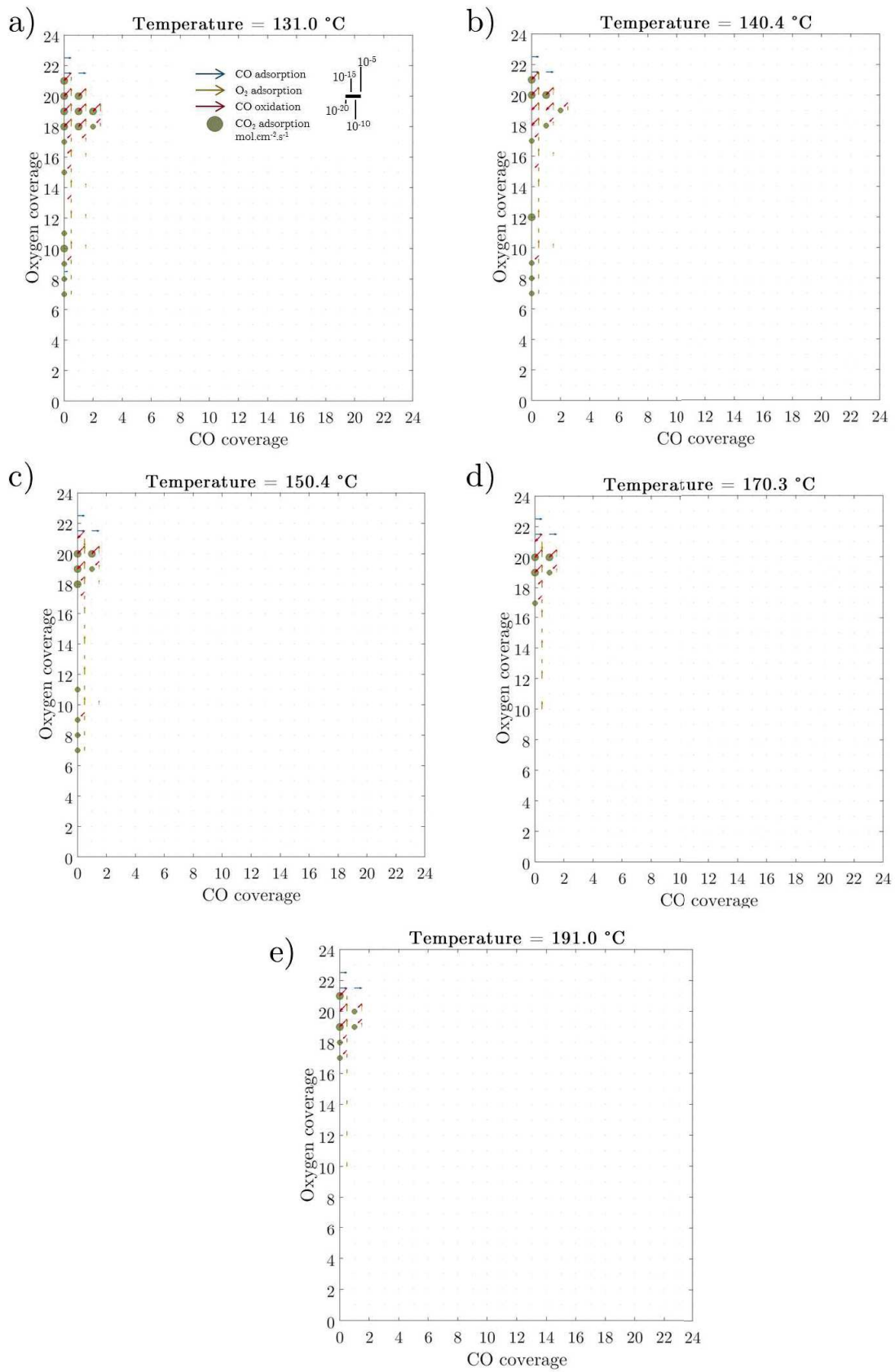


Figure 127: Reaction fluxes during CO oxidation with CPXspl-Pt<sub>13</sub>O<sub>4</sub>(CO).

## Appendices D: Light hydrocarbons oxidation

### D.1. Infrared differential spectra during methanol and propene oxidation

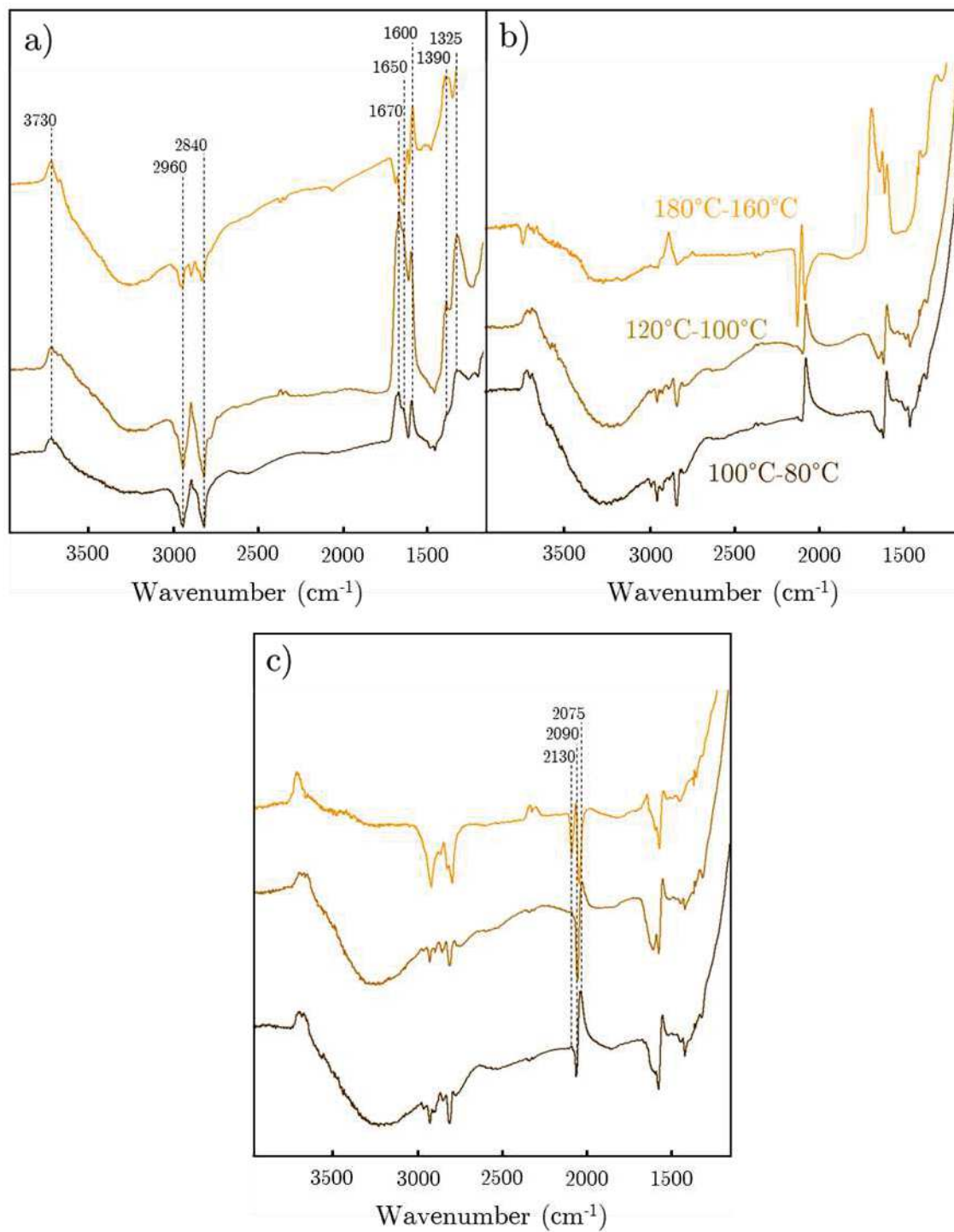


Figure 128: Consecutive differential spectra for a) methanol oxidation (3500ppm), b) with 800ppm CO and c) with 2000ppm CO. The three bands corresponds, from the draker to the lighter: 100°C-80°C, 120°C-100°C and 180°C-160°C.

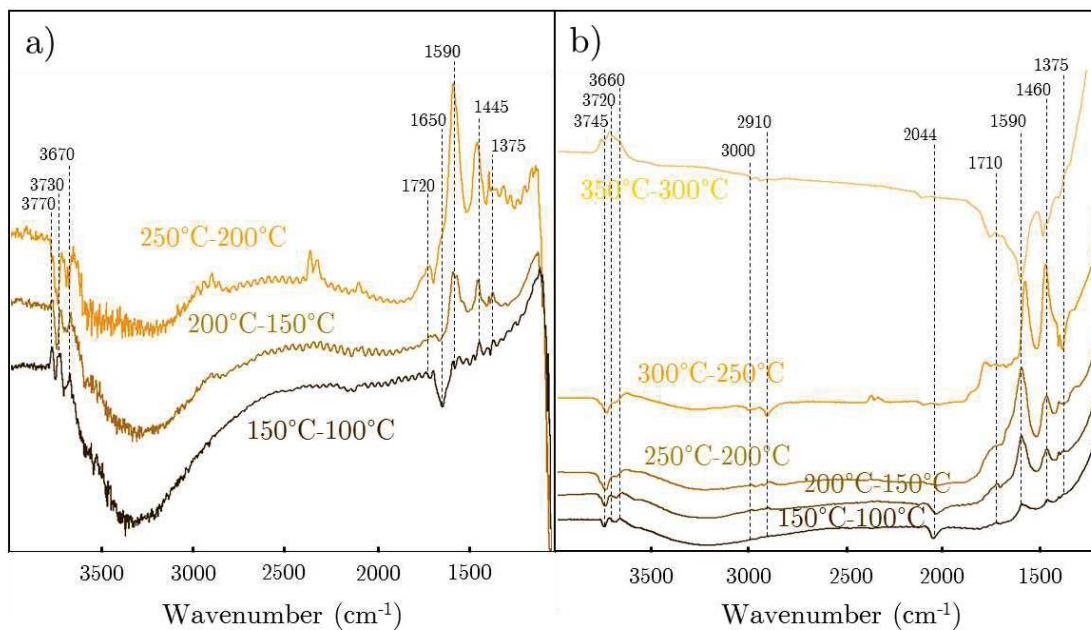
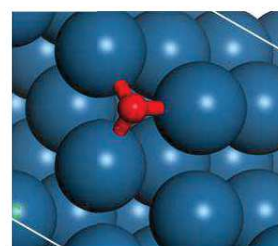
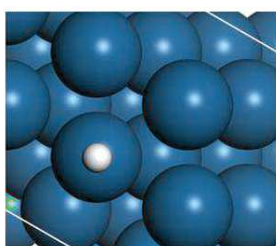
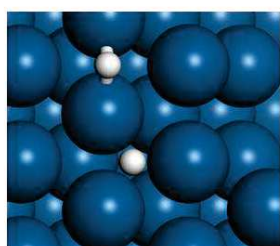
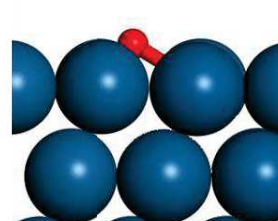
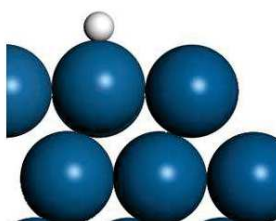
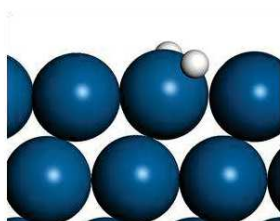


Figure 129: Consecutive differential spectra for a) propene oxidation alone (3500ppm) and b) with 1000ppm CO (1800 ppm C<sub>3</sub>H<sub>6</sub>). Interferences are observed for pure propene oxidation due to cristal windows in the experimental set-up.

## D.2. $C_0$ adsorbed species

a) Dihydrogen  $H_2$       b) Hydrogen  $H^*$       c) Oxygen  $O^*$



d) Dioxygen  $O_2^*$       e) Hydroxyl  $OH^*$       f) Water  $H_2O^*$

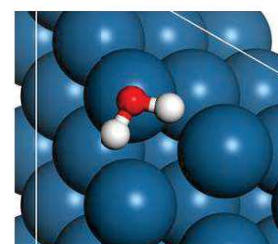
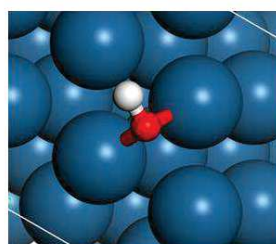
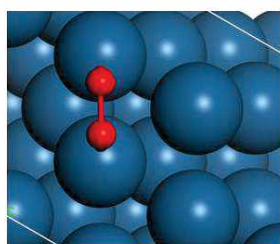
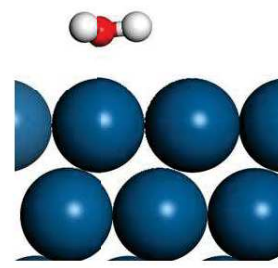
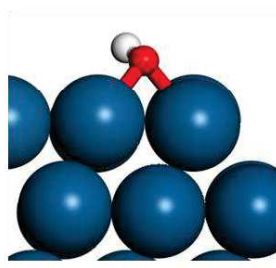
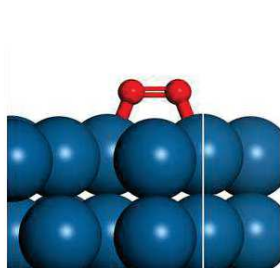


Figure 130: Illustrations of *ab initio* calculated  $C_0$  adsorbed species on Pt(111).

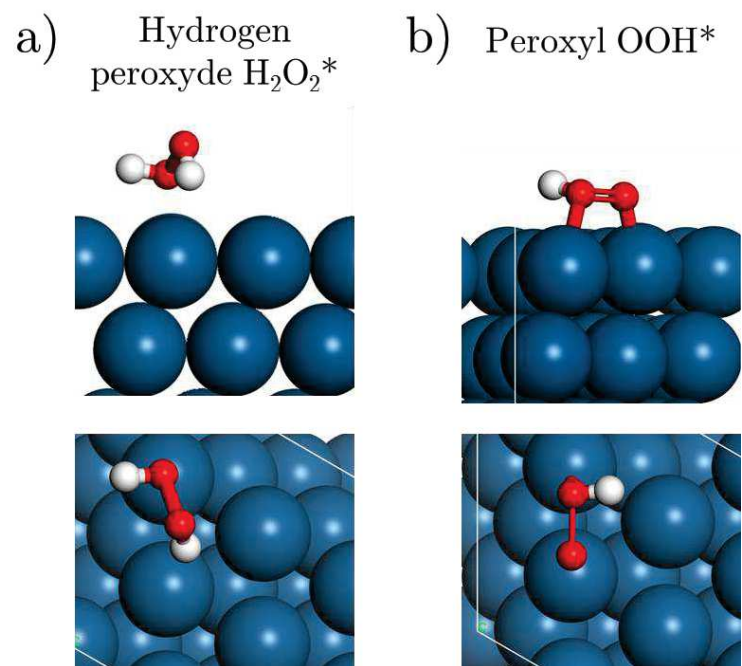


Figure 131: Illustrations of *ab initio* calculated  $\text{C}_0$  adsorbed species on Pt(111) (continuation).

### D.3. C<sub>1</sub> adsorbed species

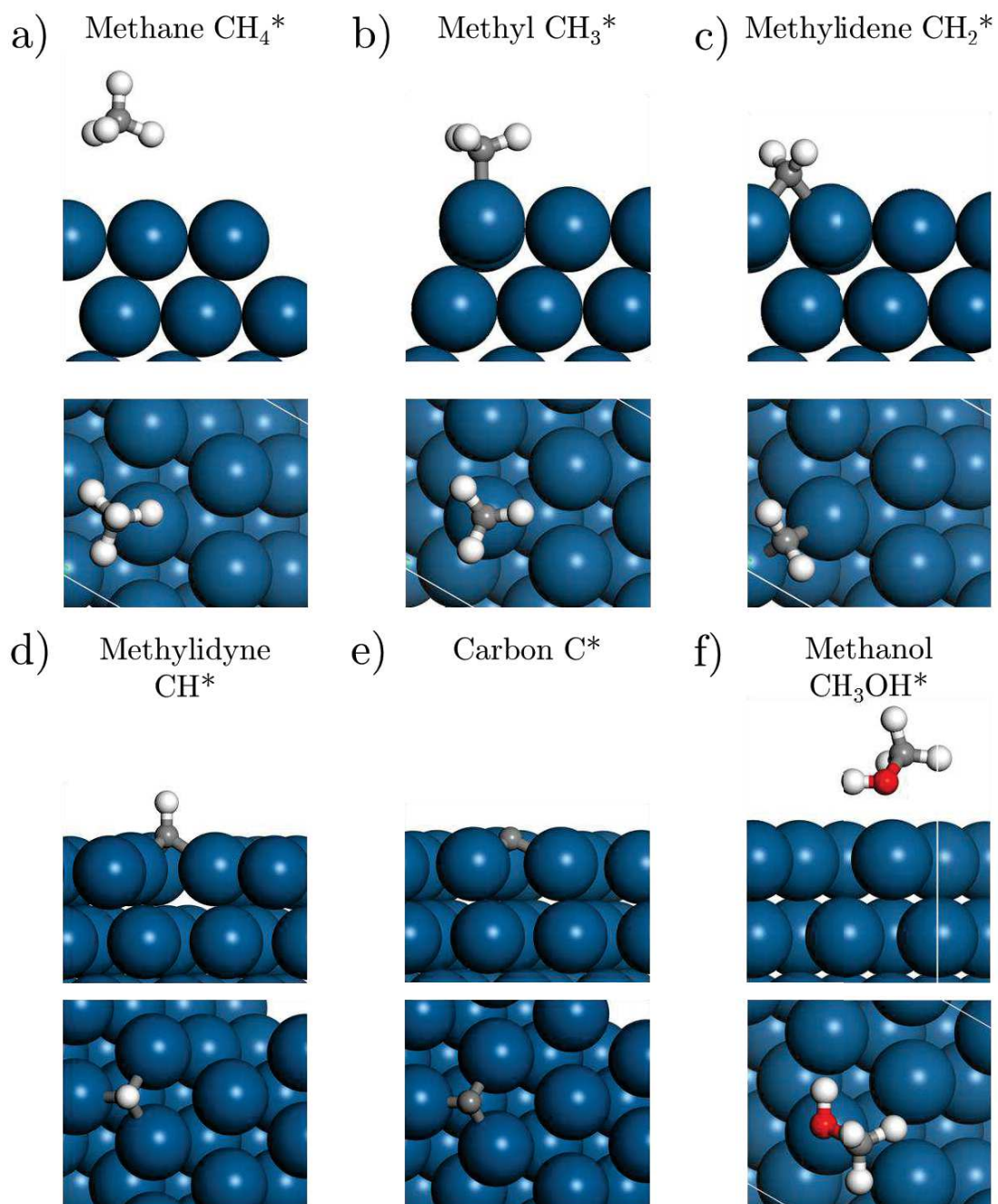


Figure 132: Illustrations of *ab initio* calculated C<sub>1</sub> adsorbed species on Pt(111).

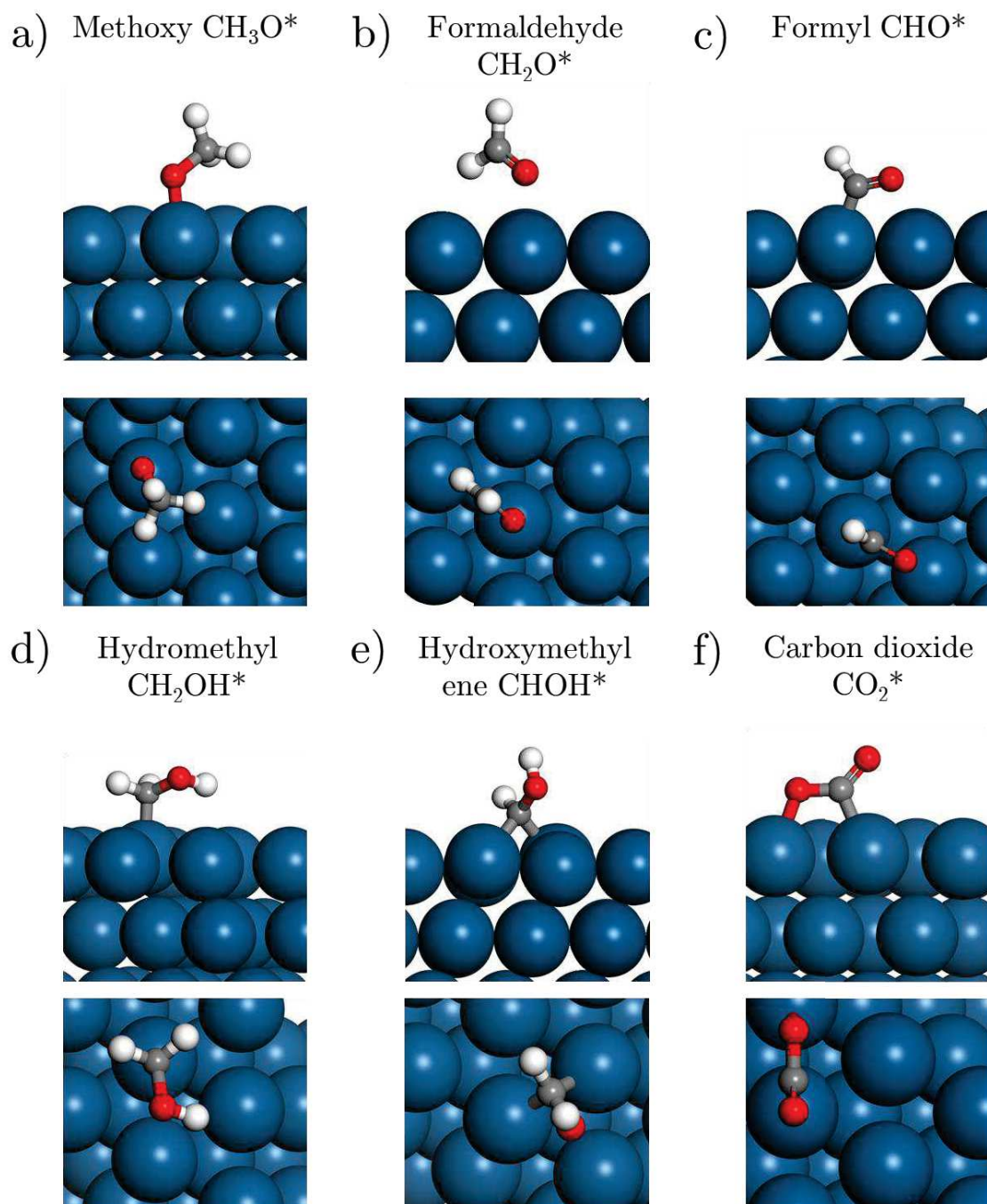


Figure 133: Illustrations of *ab initio* calculated  $\text{C}_1$  adsorbed species on Pt(111) (continuation).

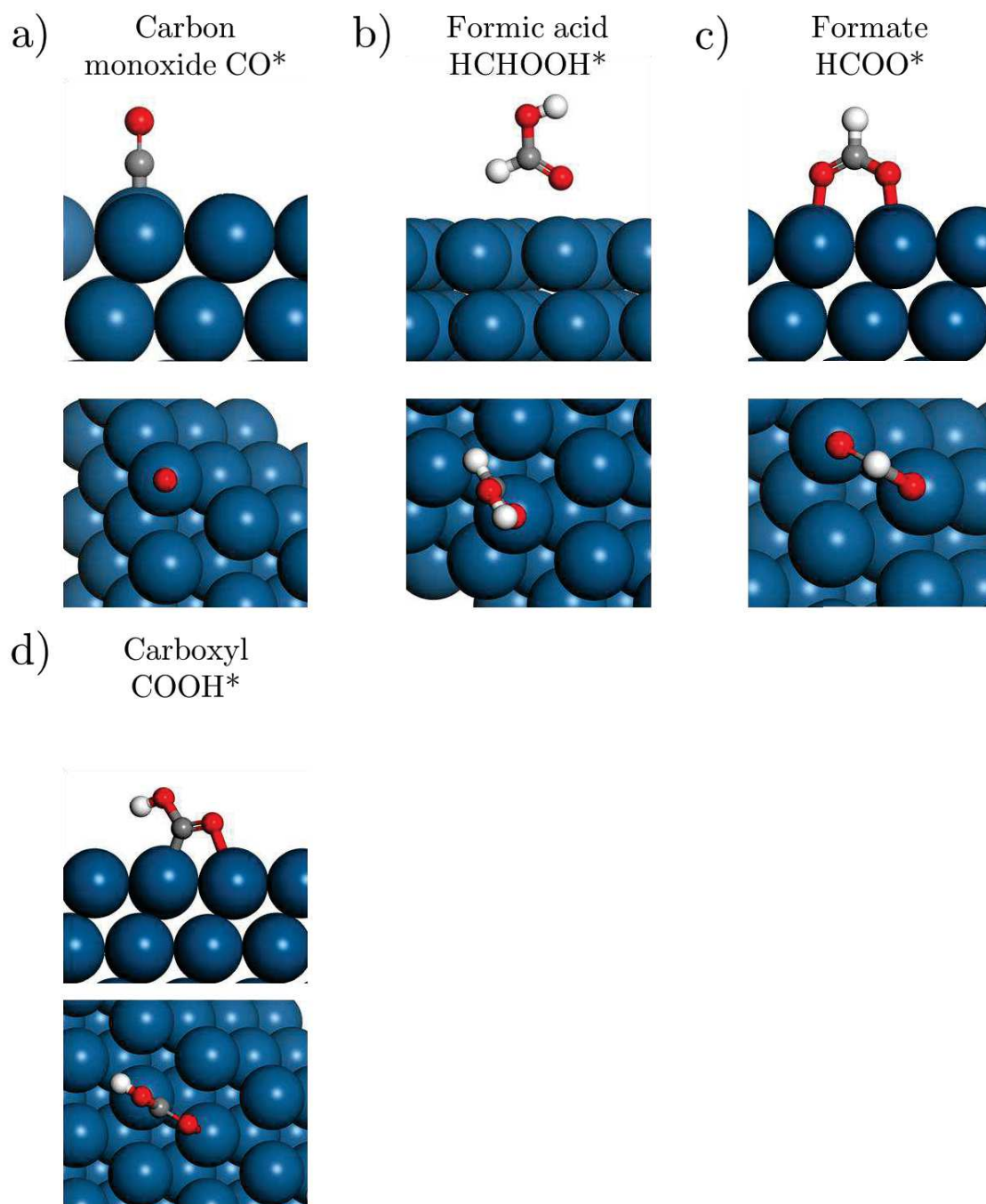
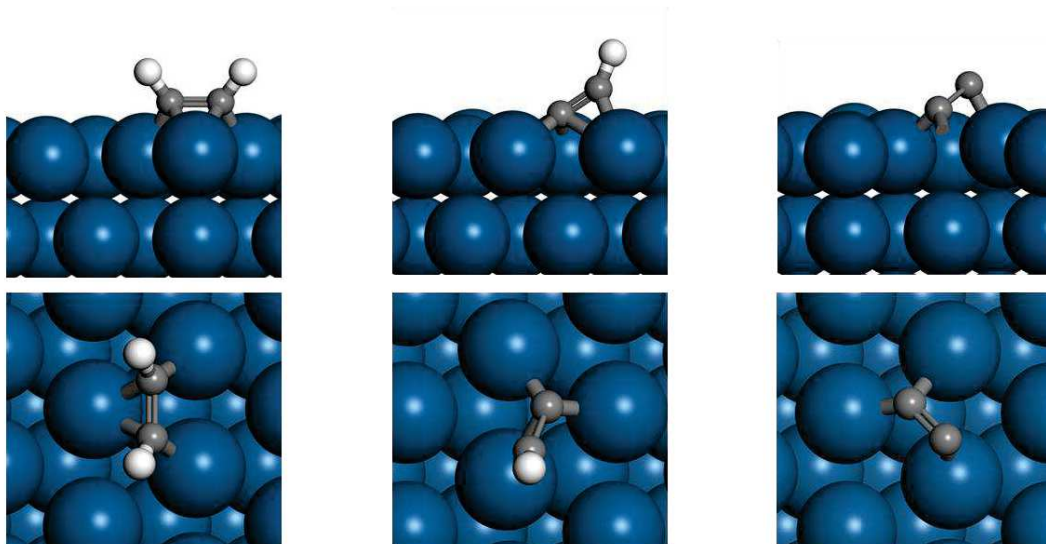


Figure 134: Illustrations of *ab initio* calculated adsorbed species on Pt(111) (continuation).

#### D.4. C<sub>2</sub> adsorbed species

- a) Acetylene CHCH\*      b) CCH\*      c) Dicarbon CC\*



- d) Ethylene CH<sub>2</sub>CH<sub>2</sub>\*      e) Vinyl CHCH<sub>2</sub>\*      f) Vinylidene CCH<sub>2</sub>\*

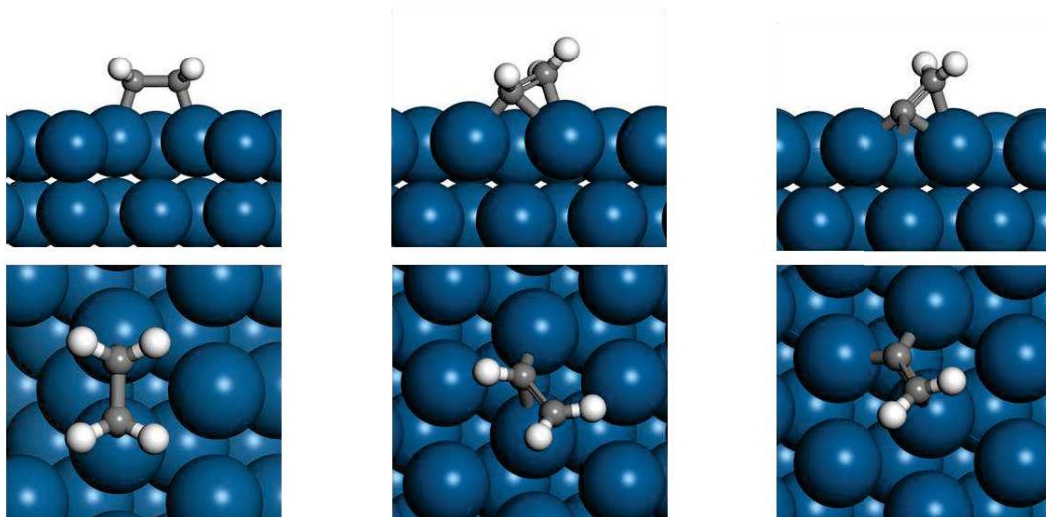


Figure 135: Illustrations of *ab initio* calculated C<sub>2</sub> adsorbed species on Pt(111).

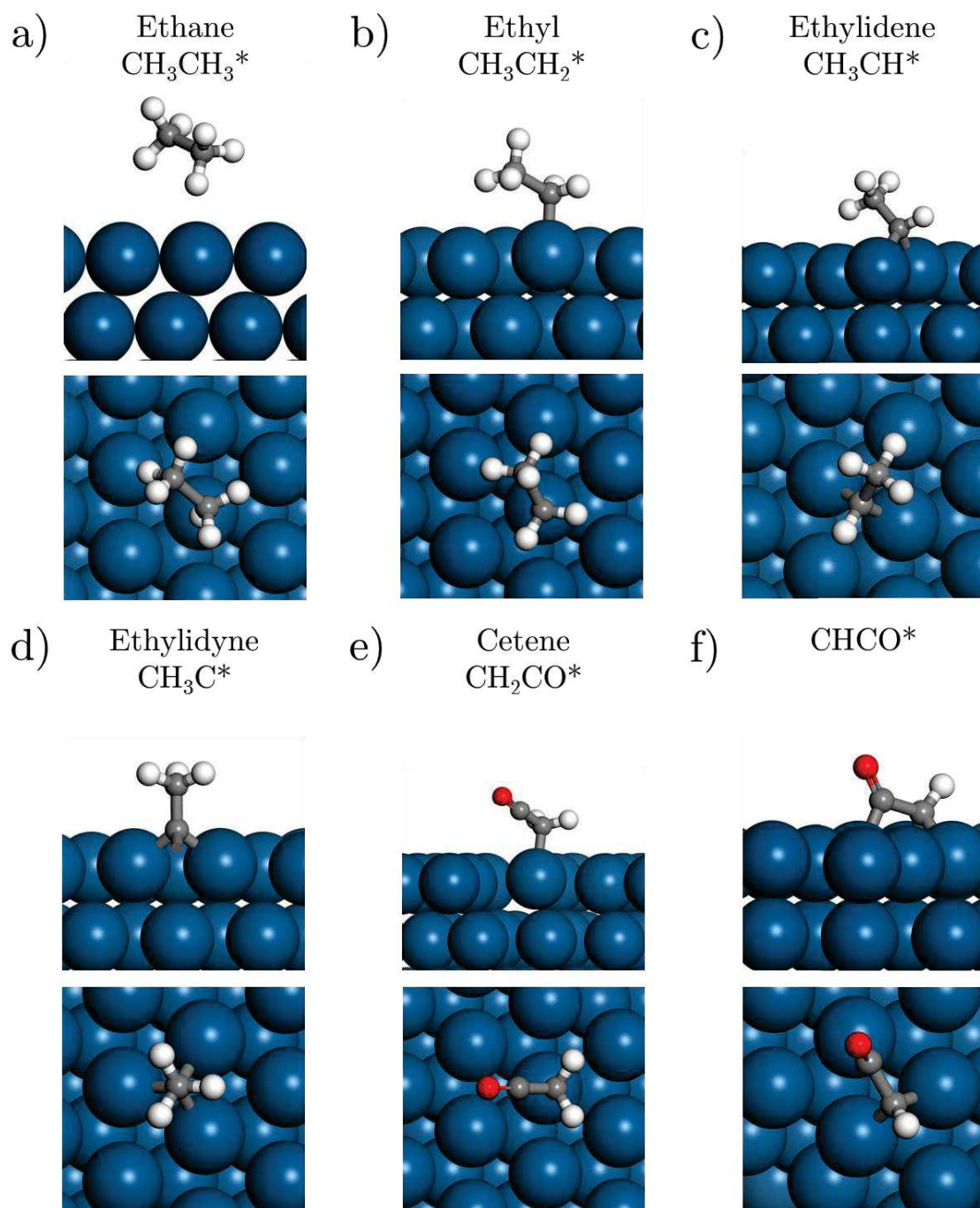


Figure 136: Illustrations of *ab initio* calculated  $\text{C}_2$  adsorbed species on Pt(111) (continuation).

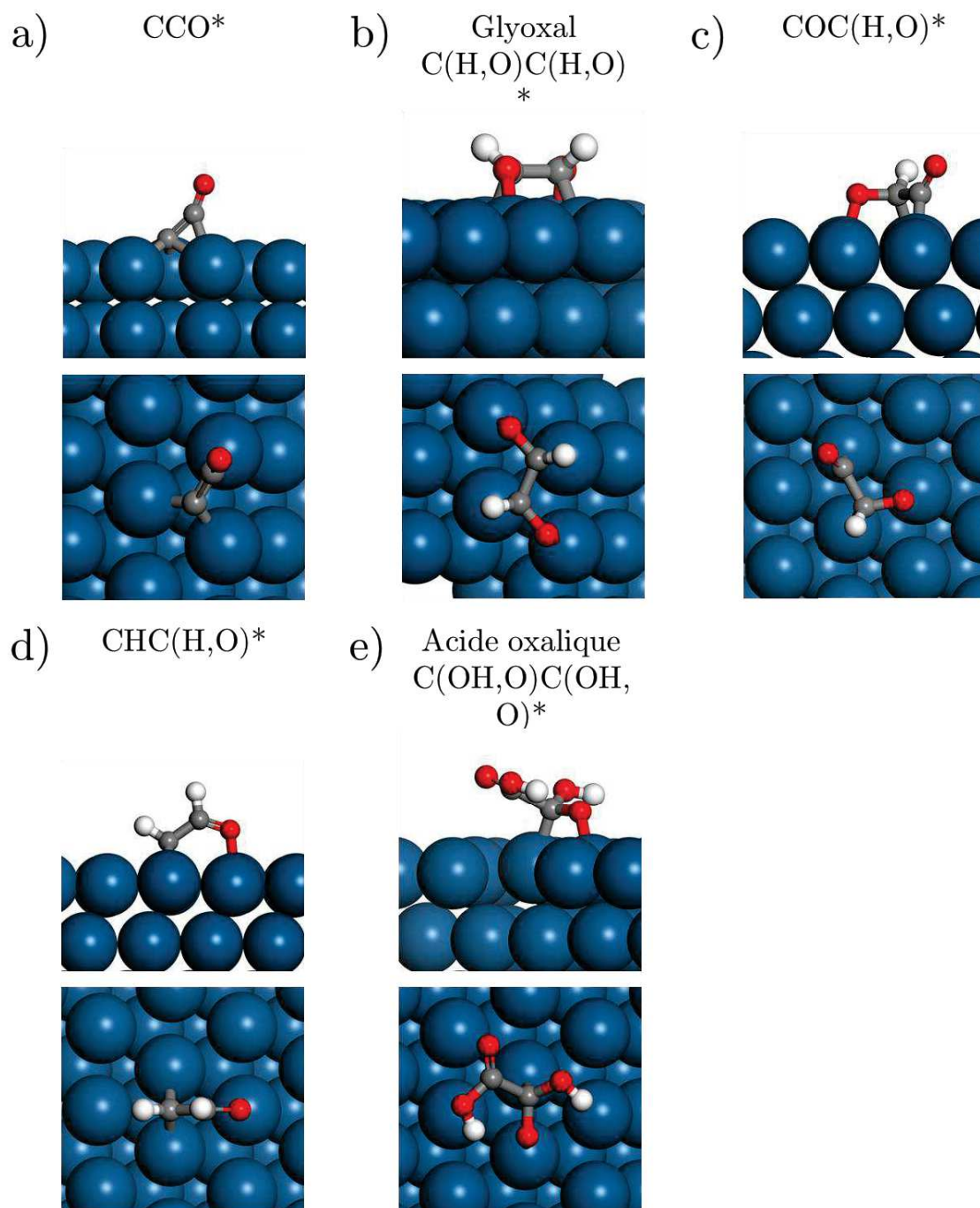


Figure 137: Illustrations of *ab initio* calculated  $\text{C}_2$  adsorbed species on Pt(111) (continuation).

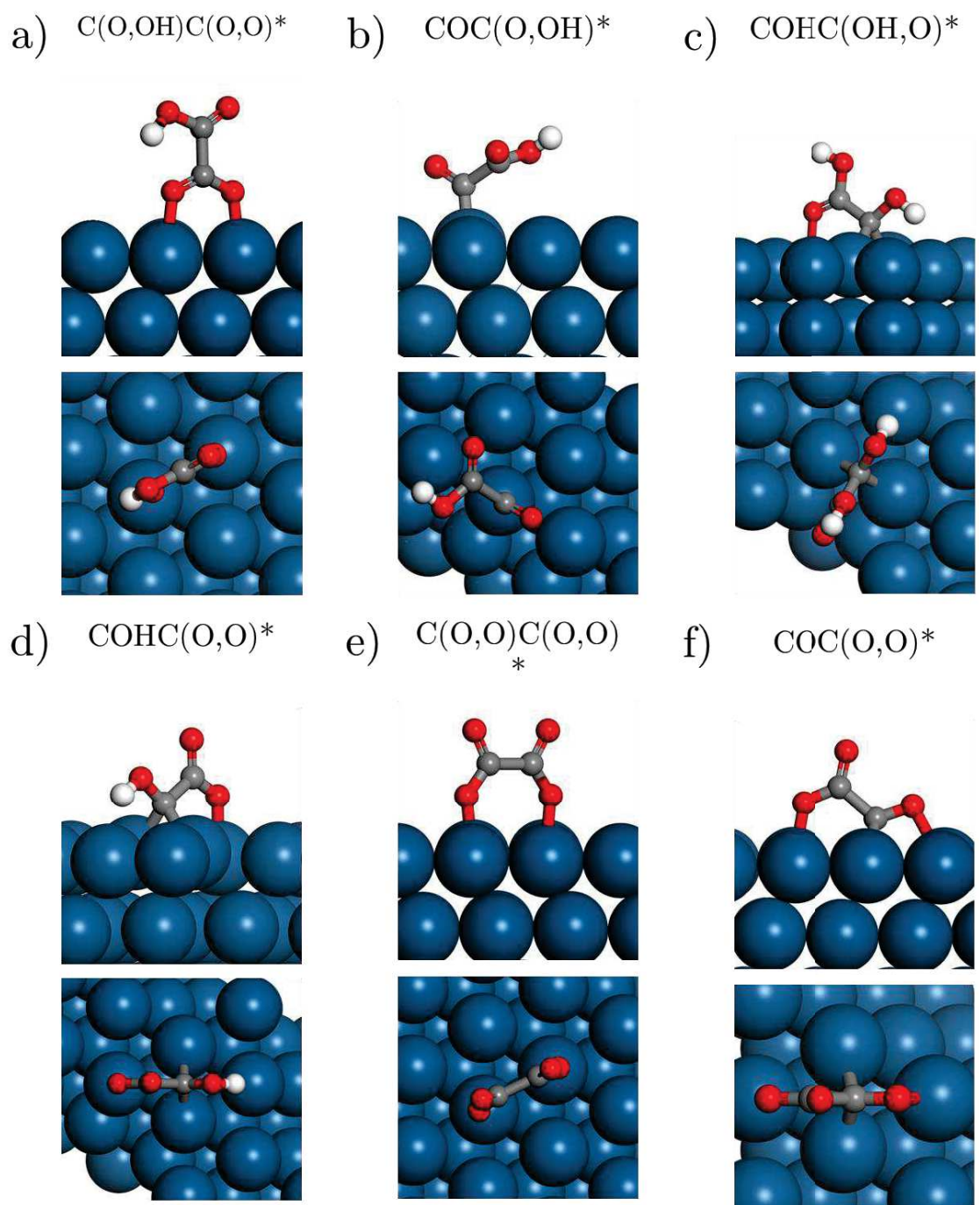


Figure 138: Illustrations of *ab initio* calculated  $C_2$  adsorbed species on Pt(111) (continuation).

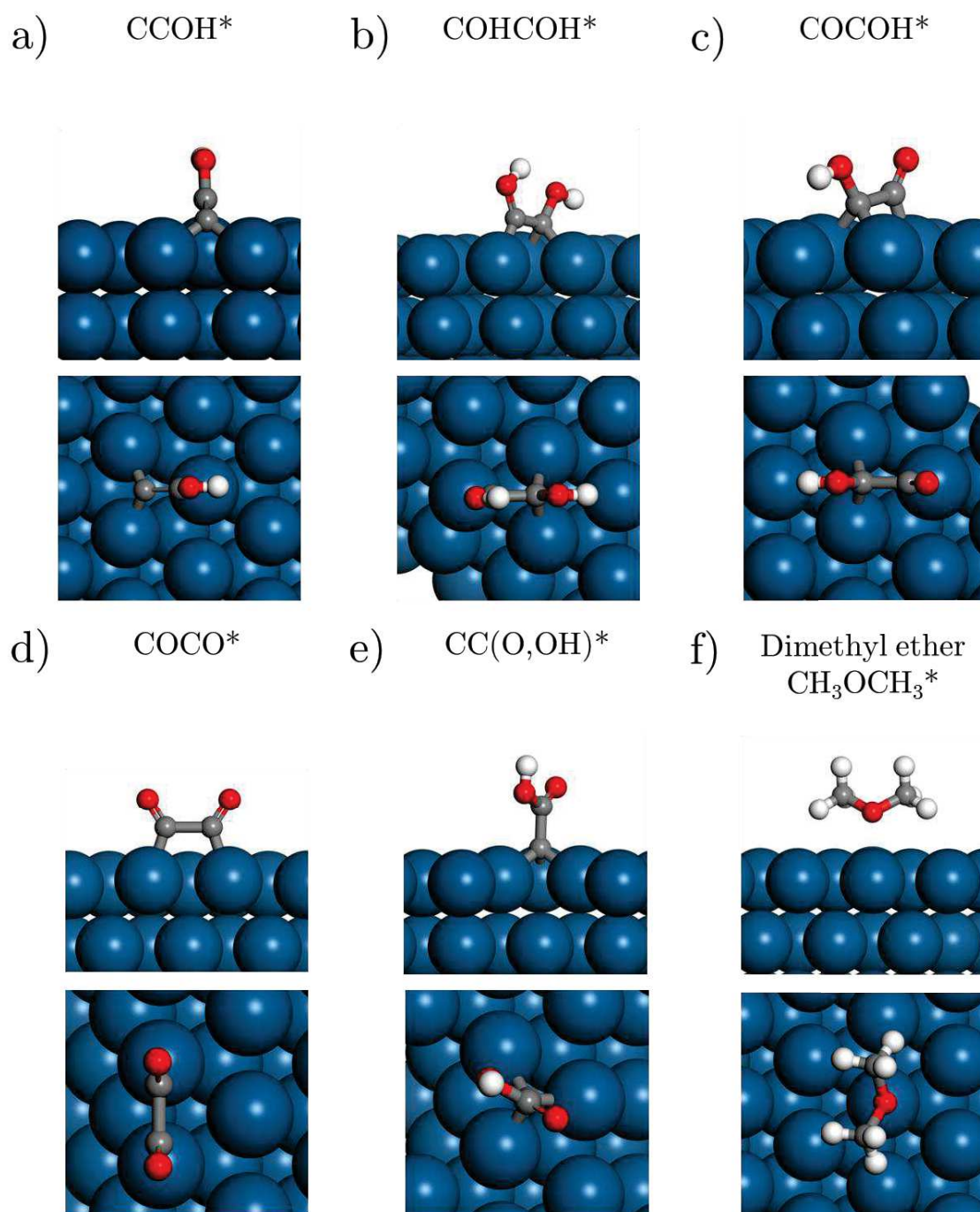


Figure 139: Illustrations of *ab initio* calculated C<sub>2</sub> adsorbed species on Pt(111) (continuation).

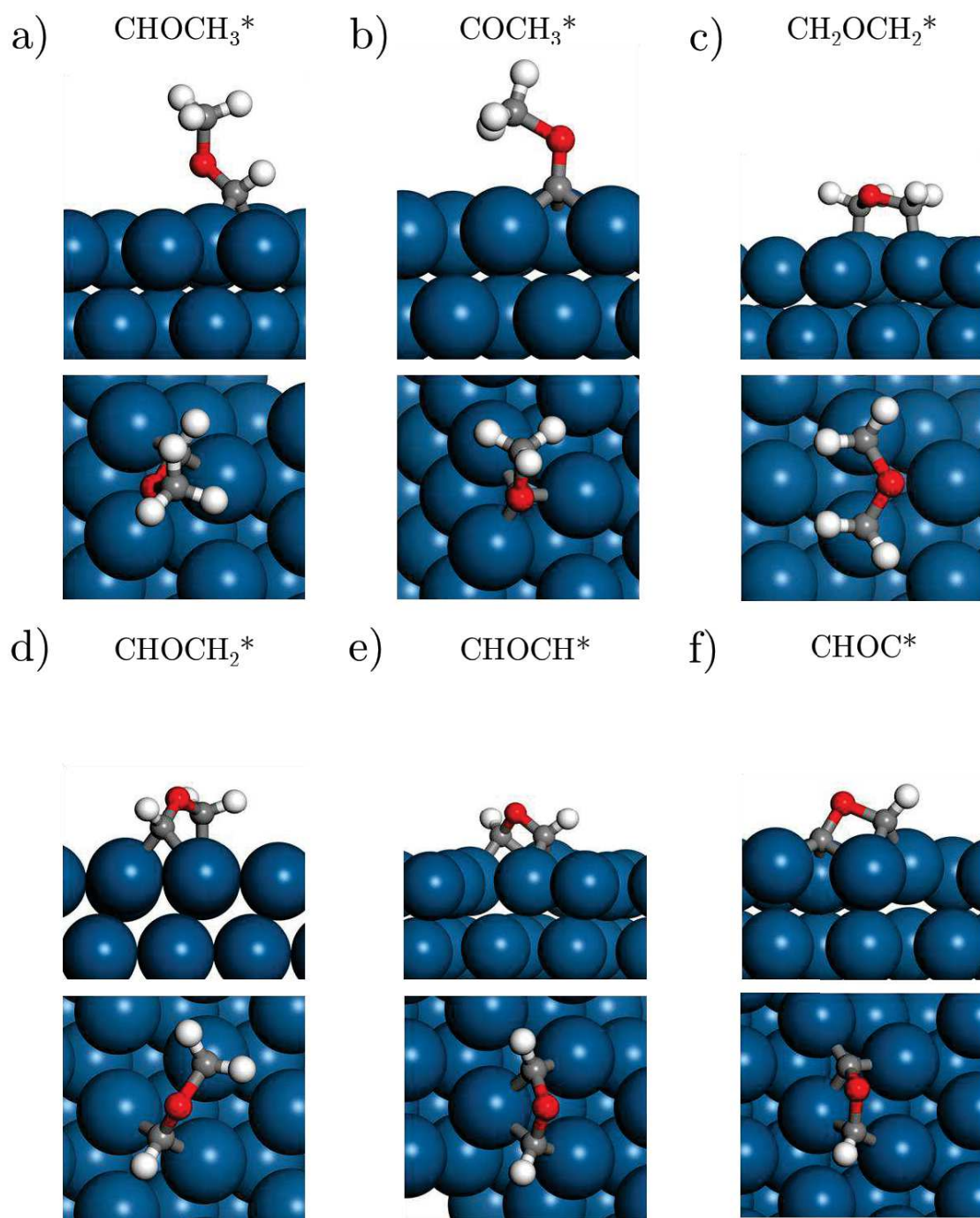


Figure 140: Illustrations of *ab initio* calculated  $\text{C}_2$  adsorbed species on Pt(111) (continuation).

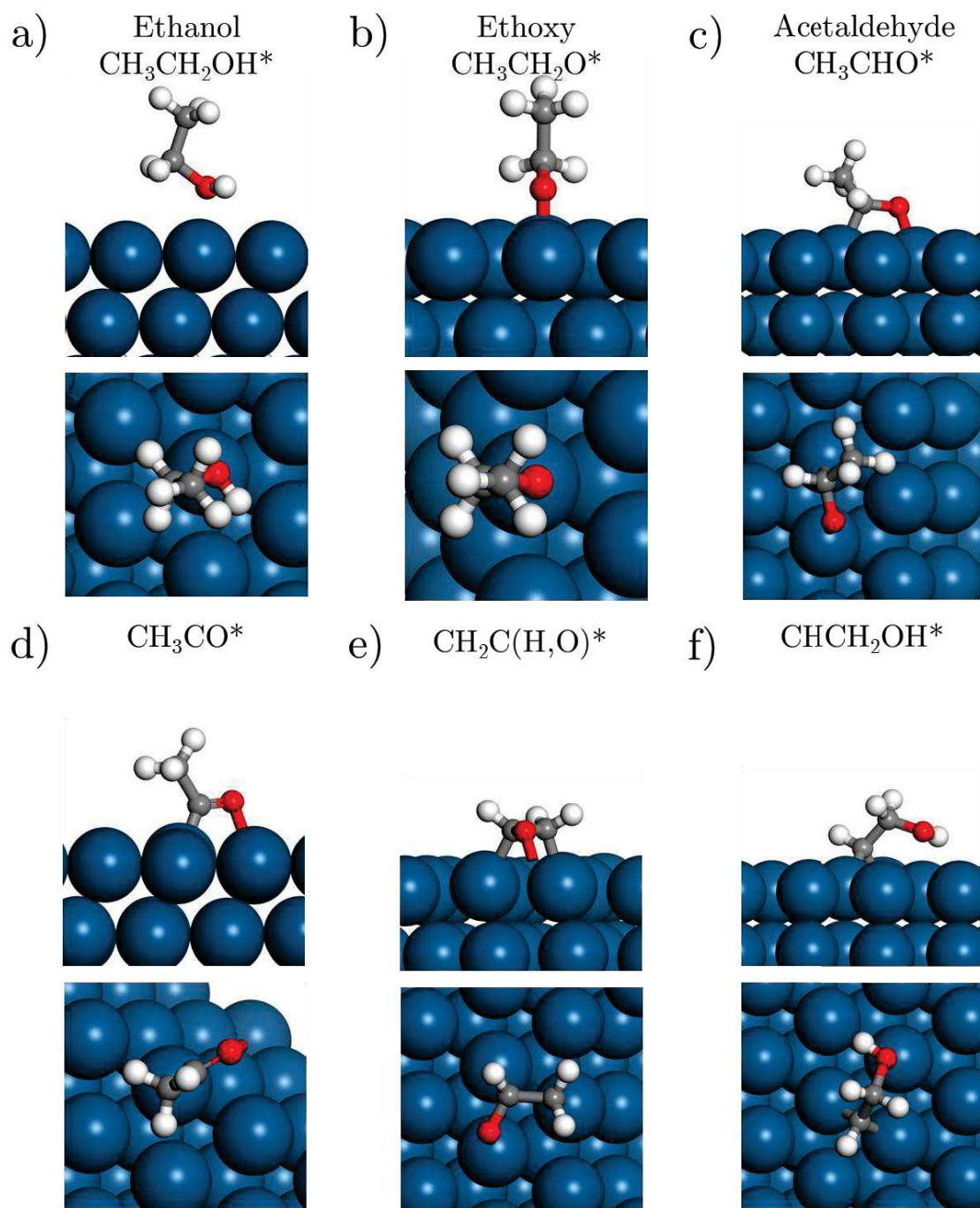


Figure 141: Illustrations of *ab initio* calculated  $\text{C}_2$  adsorbed species on Pt(111) (continuation).

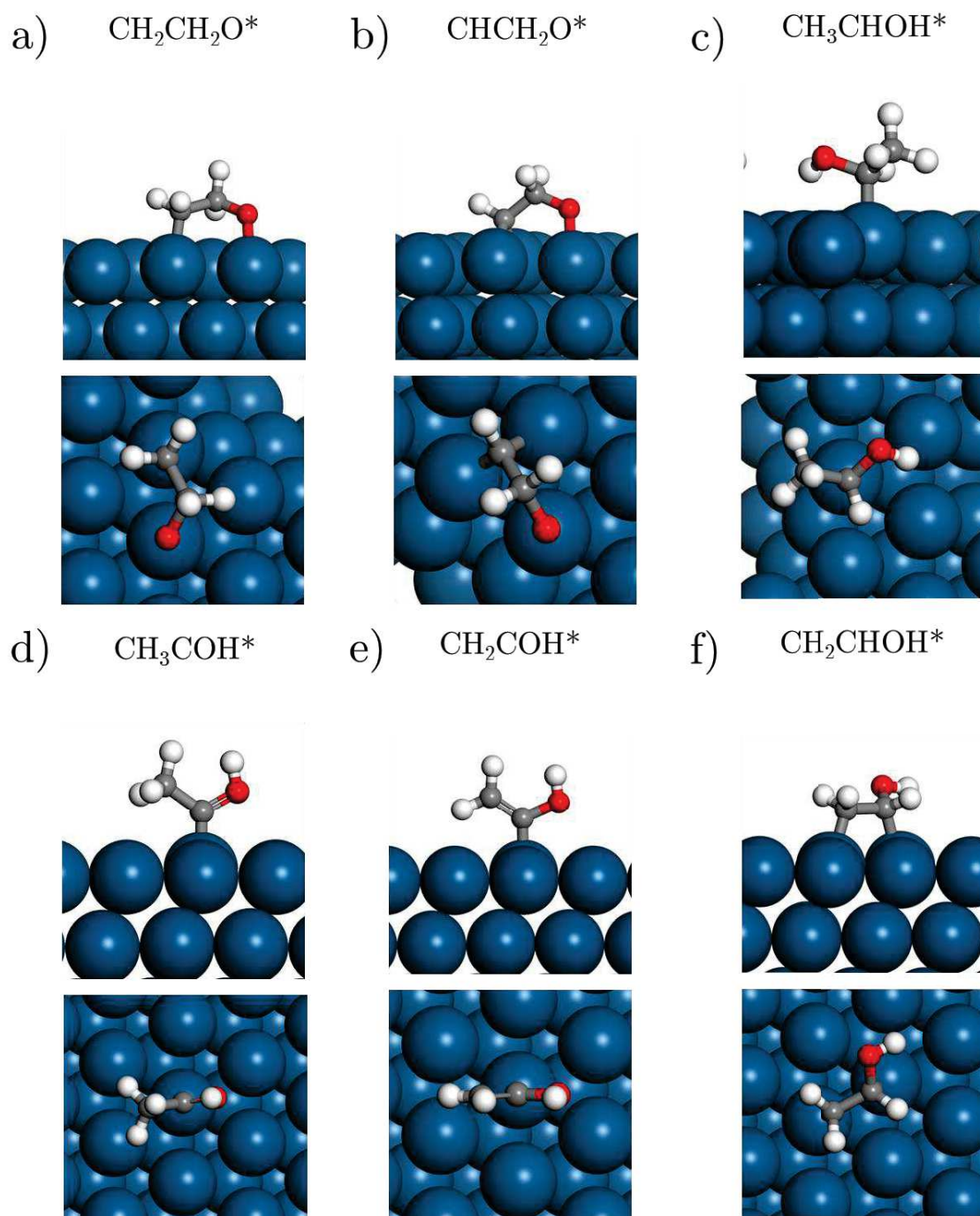


Figure 142: Illustrations of *ab initio* calculated  $\text{C}_2$  adsorbed species on Pt(111) (continuation).

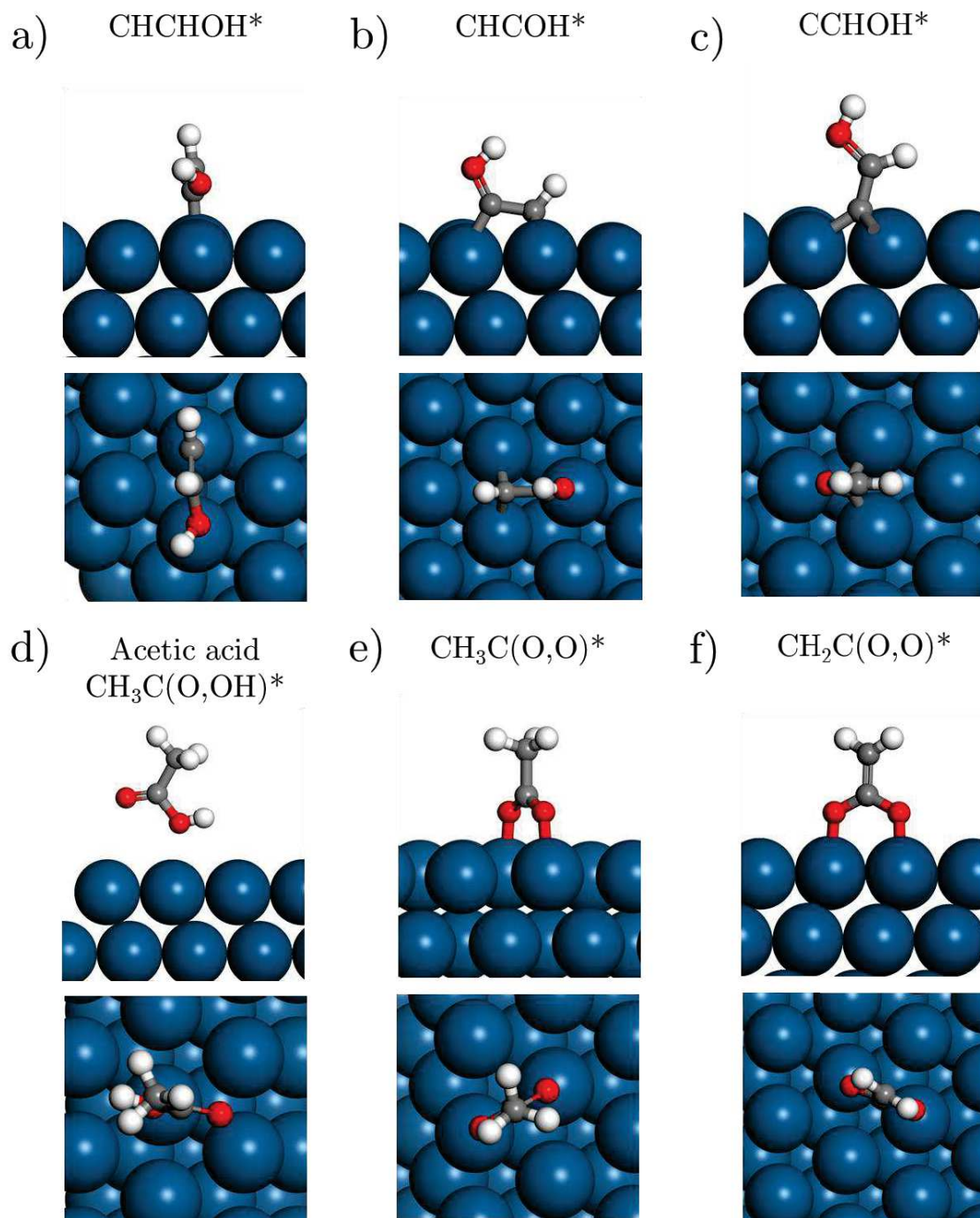
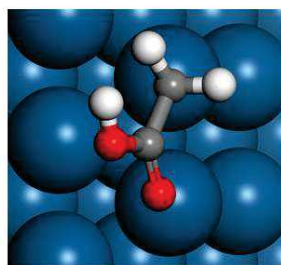
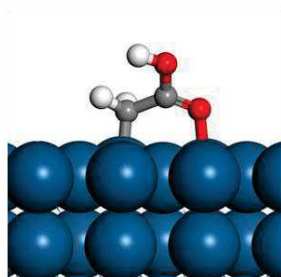
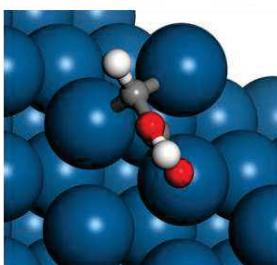
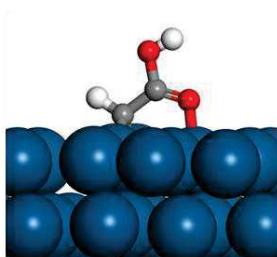


Figure 143: Illustrations of *ab initio* calculated  $\text{C}_2$  adsorbed species on Pt(111) (continuation).

a)  $\text{CH}_2\text{C}(\text{O},\text{OH})^*$



b)  $\text{CHC}(\text{O},\text{OH})^*$



c)  $\text{CC}(\text{O},\text{OH})^*$

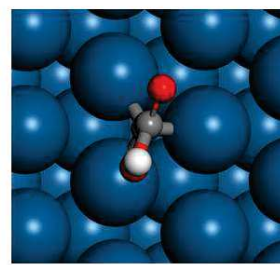
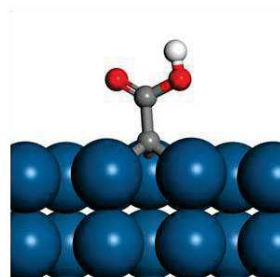


Figure 144: Illustrations of *ab initio* calculated  $\text{C}_2$  adsorbed species on Pt(111) (continuation).

## D.5. C<sub>3</sub> adsorbed species

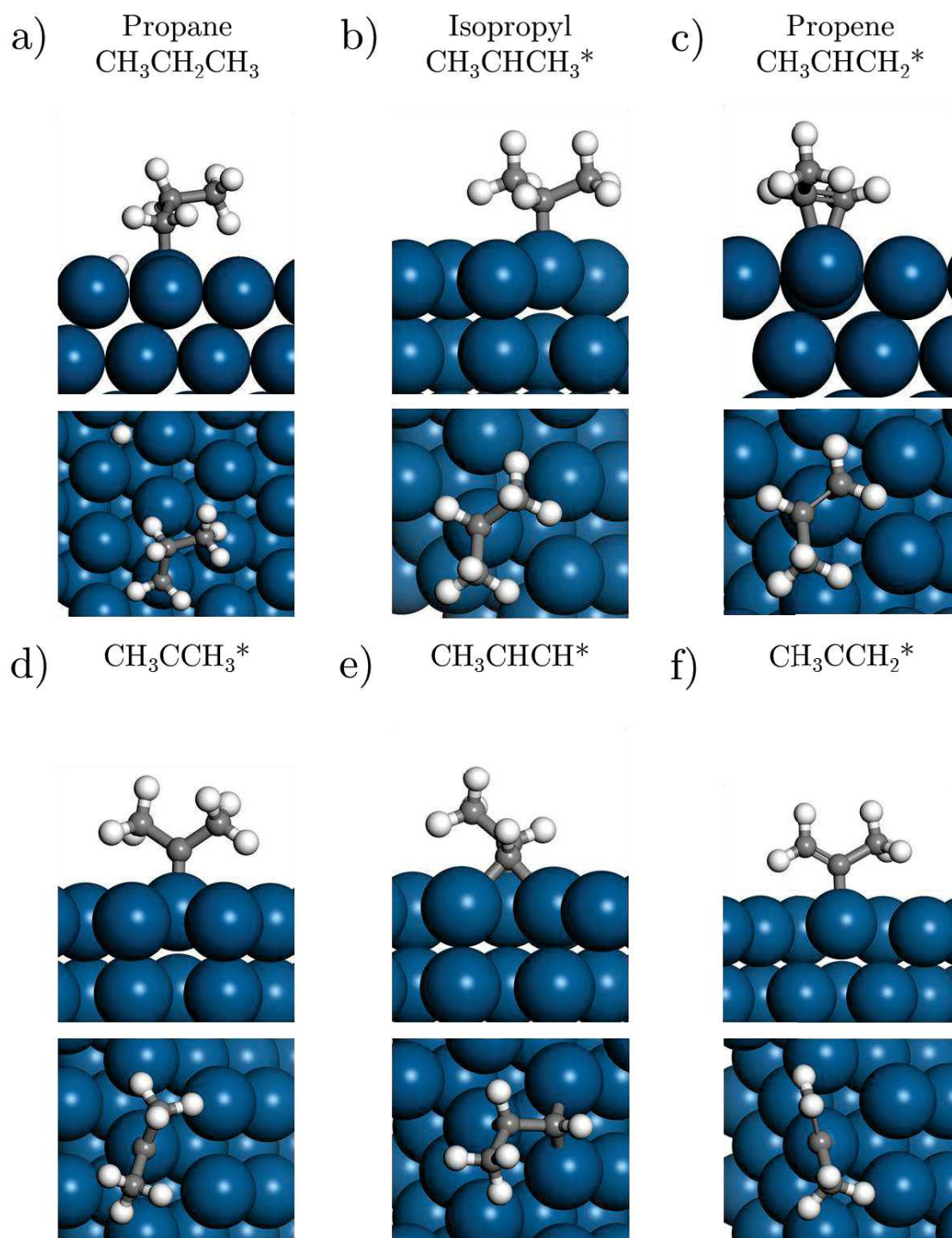
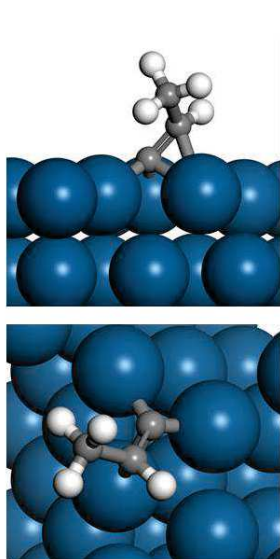
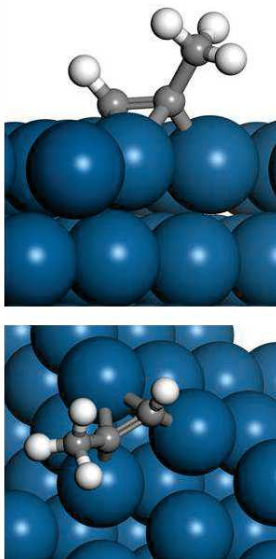


Figure 145: Illustrations of *ab initio* calculated C<sub>3</sub> adsorbed species on Pt(111).

a)  $\text{CH}_3\text{CHC}^*$



b) Propyne  
 $\text{CH}_3\text{CCH}^*$



c)  $\text{CH}_2\text{CCH}_2^*$

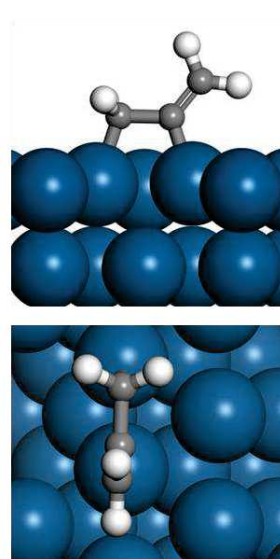


Figure 146: Illustrations of *ab initio* calculated  $\text{C}_3$  adsorbed species on Pt(111) (continuation).

# List of figures

Figure 1: Composition example of an untreated exhaust at the Diesel engine outlet, in volume <sup>21</sup> .....	19
Figure 2: Hydrocarbon concentrations after Diesel engine (iso-octane fuel) with richness ratios from 0.081 to 0.283, adapted from Dec and Davisson <sup>17</sup> .....	20
Figure 3: Mechanism of combustion of hydrocarbons in the engine <sup>36,37</sup> .....	21
Figure 4: Scheme of Diesel aftertreatment line, adapted from Sassi <i>et al.</i> technical notes <sup>40,41</sup> . The Diesel oxidation catalyst is generally placed after the engine. Particulate filter and deNO <sub>x</sub> systems. Exhaust Gas recirculation (abbreviated EGR) system is sometimes installed on the line to lower NO <sub>x</sub> emissions. The muffler is present to reduce noise emitted by the engine.....	23
Figure 5: Detailed view of a Diesel oxidation catalyst <sup>41</sup> .....	24
Figure 6: Electron microscopy of channels of a monolith a) without and b) with washcoat <sup>50</sup> .....	25
Figure 7: Phenomena of deactivation of the catalyst and its support, adapted from Sassi <i>et. al</i> <sup>41</sup> . 1) metallic diffusion, 2) oxide poisoning, 3) sintering, 4) encapsulation and 5) catalyst poisoning. Some are due to high temperature or catalyst/oxide instabilities (1,3,4) but also too hydrocarbon/CO rich gas (2,5).....	27
Figure 8: The three common adsorption modes are (a) top, (b) bridge and (c,d) hollow fcc and hcp. Moreover real Pt(111) surface can hold defects such as terraces (1), steps (2), holes (3), adatoms (4) and corners (5) whose reactivities are probably different. The surface of the material is obviously more complex, involving other crystallographic facets (such as Pt(100)) and crystalline defects in the volume (interstitial atoms, dislocations, grain boundaries). .....	28
Figure 9: STEM images of fresh catalyst 0.3% wt. platinum (a,b) before and (c,d) after dechlorination. STEM images of fresh catalyst 1% wt. platinum (e,f). .....	36
Figure 10: Particle size distribution of the 0.3% wt. platinum loaded catalyst before and after dechlorination (respectively 79 and 143 probed particles). Particle size distribution of the 1% wt. platinum loaded catalyst (289 probed particles).....	37
Figure 11: a) Micro-reactor scheme with the pelletized catalyst in yellow. Mass spectrometer can be placed either at the inlet or at the outlet of the reactor. b) represents the monocrystalline windows needed to reactor sealing and IR beam transmission through the cell, and c) fixed bed reactor scheme. The catalyst in yellow was placed in powder form on sintered-glass filter.....	38

Figure 12: a) Top view and b) side view of the Pt(111) surface model. Black lines correspond to the perodic box limits. ....	48
Figure 13: a) Side view of Pt <sub>13</sub> /γ-Al <sub>2</sub> O <sub>3</sub> and b) top view of Pt <sub>13</sub> /γ-Al <sub>2</sub> O <sub>3</sub> with aluminum nomenclature. Black lines correspond to the perodic box limits.....	49
Figure 14: Electronic energy of the O <sub>2</sub> (g) system with O-O bond length guesses made by VASP (crosses), during geometry optimisation. The dotted line is the interpolated electronic energy. ....	50
Figure 15: Schematic diagrams of the NEB method for a systems with two coordinate (q <sub>A</sub> ,q <sub>B</sub> ). The potential isosurfaces (black), the MEP (red) and the NEB path (blue) are represented. Representation of the forces exerted on a geometry.....	53
Figure 16: a) Eley-Rideal and b) Langmuir-Hinshelwood mecanisms. Surface diffusion of reactants and products also happens onto the catalyst.....	57
Figure 17: Illustration of Chemkin input and output files. ....	61
Figure 18: Representations and adjacency matrices associated with the search for reactions between CH <sub>3</sub> O* and CH* adspecies with possible CH <sub>2</sub> O* and CH <sub>2</sub> *. products. a) and b) represent the reagents and their adjacency matrix with the actual links (in blue). c) is the adjacency matrices of the reactive system. Figure d) shows, from c), the chosen destroyed link (in yellow) and the binding possibility to be created (in green), as well as the selected link created (in purple). e) and f) represent the products and their matrices separated since d).....	67
Figure 19: UBI-QEP and DFT adsorption energies of methanol, considering multiple adsorption modes. Molecular modelling only gives top Pt-O bond stable configuration, meaning that the other adsorption modes should be less stabilizing than the top one, whereas UBI-QEP predicts the oppositie trend. ....	69
Figure 20 : a) Lennard-Jones one dimensional potential according to one reaction coordinate, that corresponds to the average AB-surface distance, and b) the multi-dimensional unity bond index (UBI) potential diagram. Adapted from Shustorovich and coworkers <sup>147,148</sup> .....	69
Figure 21 : Relative intensity of oxygen (m/z=32) during the Temperature-Programmed Desorption with the 0.3 wt % and 1 wt % Pt/γ-Al <sub>2</sub> O <sub>3</sub> catalysts. ....	75
Figure 22 : Adsorption energies per O <sub>2</sub> for a single O atom on the supported Pt <sub>13</sub> cluster, as a function of the distance to the support compared to Pt(111)-0.25 ML. The distance to the support corresponds to the difference between oxygen and mean aluminum of the first alumina layer z coordinates.....	76
Figure 23 : Illustration of top (a), bridge (b) and hollow (c) typical sites with bimetallic (Al, Pt) bridge (d) and hollow (Al, Pt, Pt) sites (e). Platinum atoms are in blue, alumina in pink and oxygen in red. ....	78
Figure 24 : Mean adsorption energies of O <sub>2</sub> according to the oxygen coverage for supported Pt <sub>13</sub> O <sub>n</sub> structures and Pt(111). #Légaré <sup>166</sup> , *Pang <i>et al.</i> <sup>167</sup> , †Schneider and coworkers <sup>175</sup> .....	79

Figure 25 : Phase diagram for supported Pt <sub>13</sub> O <sub>n</sub> according to temperature and partial pressure of oxygen. The structures of the systems exhibiting a significant stability domain are also depicted (side views).....	80
Figure 26 : Comparison of platinum-oxygen phase diagrams at P <sub>O2</sub> =0.1 bar according to the nature of the surface. #Légaré <sup>166</sup> , *Phase diagram of the bulk platinum in presence of only O <sub>2</sub> by HSC Chemistry data, •Schneider and co-workers <sup>175</sup> , ‡Schneider and coworkers <sup>183,184</sup> .....	81
Figure 27 : (a) Interaction energy between the alumina support and the oxidized platinum clusters. (b) Average Pt-Pt, Pt-O <sub>support</sub> and Pt-O <sub>cluster</sub> bond lengths, and minimum Pt-Al length as a function of oxygen coverage. The maximal bond lengths were set to 3.8 Å for Pt-Pt and 2.5 Å for other bonds. Dotted lines corresponds to the two-layers structures whereas plain lines are hemispheric structures data. ....	82
Figure 28 : Mean Bader charge per Pt (blue) and cluster O (red) atoms. The cross-shaped dots represent the two-layers structures while the full dots stand for hemispheric structures.....	83
Figure 29 : Dissociation barriers from initial state Pt <sub>13</sub> O <sub>n</sub> to Pt <sub>13</sub> O <sub>n+2</sub> , and Pt(111)O <sub>n</sub> to Pt(111)O <sub>n+2</sub> . The energies are displayed relatively to each initial state energy.....	84
Figure 30 : (a) Predicted O <sub>2</sub> concentration profile during O <sub>2</sub> -TPD with Pt(111) and Pt <sub>13</sub> , with TPD experiments on highly-dispersed Pt/γ-Al <sub>2</sub> O <sub>3</sub> . (b) Impact of sticking coefficient and of a typical errors (± 3.6 kcal.mol <sup>-1</sup> for enthalpies and ± 3.6 cal.mol <sup>-1</sup> .K <sup>-1</sup> for entropies) on Pt <sub>13</sub> kinetic model with a 5°C.min <sup>-1</sup> temperature ramp and starting with the Pt <sub>13</sub> O <sub>20</sub> structure. The O <sub>2</sub> -TPD experiments of <sup>A</sup> Olsson <i>et al.</i> <sup>200</sup> and <sup>B</sup> Parker <i>et al.</i> <sup>197</sup> are also reported. The lines represent the range of occurrence of O <sub>2</sub> release and the crosses the associated rate-of-desorption maxima. ....	86
Figure 31 : (a) Logarithm of the rate constants (in s-1) at the peak temperature for Pt <sub>13</sub> O <sub>n</sub> kinetic mechanism. The sticking coefficient of O <sub>2</sub> is 10 <sup>-2</sup> . (b) Predominant surface species during TPD experiments with distinct scheme structure. The impact of the pre-exponential factor of the two surface reaction A is studied as well as the two paths involving Pt <sub>13</sub> O <sub>n-TL</sub> or Pt <sub>13</sub> O <sub>n-HM</sub> independently. The sticking coefficient of O <sub>2</sub> is 10 <sup>-2</sup> . The reference scheme is the darker one. ....	88
Figure 32: Illustrations of the single carbon monoxide adsorption modes found. The a) most strongly adsorbed and only alumina engaged site and b) top, c) bridge and d) hollow typical sites.....	93
Figure 33: Comparison of the average adsorption energies of one adsorption of CO and atomic oxygen on the Pt <sub>13</sub> cluster and Pt(111). The work on non-supported cluster Pt <sub>38</sub> and Pt <sub>55</sub> from •Johnston <sup>235</sup> <i>et al.</i> is stated. <i>Ab initio</i> data are reported for Pt(111) by † Dupont <i>et al.</i> <sup>231</sup> (GGA PBE) and ‡ Schimka <i>et al.</i> <sup>230</sup> (RPA).....	94
Figure 34: a) Determination of the distance of platinum atoms from the support and b) average distance to the support of the 13 platinum of the cluster according to CO coverage. The bars corresponds to minima and maxima values. ....	96

Figure 35: a) Electronic interactions between the alumina and the cluster in presence of oxygen and CO. b) Mean adsorption energy of CO according to the carbon monoxide coverage for  $\text{Pt}_{13}(\text{CO})_m$  and Pt(111) structures. One monolayer in the present work corresponds to  $\text{Pt}_{13}(\text{CO})_{12}$  structure, as 12 platinum are initially at the cluster surface. The work of <sup>†</sup>Allian *et al.*<sup>163</sup> (RPBE) and coworkers, <sup>‡</sup>Shan *et al.*<sup>234</sup> (RPBE) and <sup>•</sup>Orita and Inada<sup>233</sup> (PBE) for stepped surfaces are also reported. .... 96

Figure 36: Phase diagram of supported  $\text{Pt}_{13}(\text{CO})_m$  structures according to temperature and partial pressure of CO. The structures of the systems exhibiting a significant stability domain are also depicted (side views)..... 98

Figure 37: Illustrations of a)  $\text{Pt}_{13}\text{O}_4(\text{CO})$  and b)  $\text{Pt}_{13}\text{O}_{22}(\text{CO})$  structures. .... 99

Figure 38: Experimental and molecular modelling correspondance between adsorption mode notations.....100

Figure 39: AEIR spectra during CO adsorption at 25°C on reduced catalyst (black line) and oxidized catalyst (red line). ....101

Figure 40: AEIR spectra band deconvolution for the (a) oxidised and the (b) reduced sample Pt/ $\gamma$ - $\text{Al}_2\text{O}_3$ . ....101

Figure 41: (a) AEIR spectra during the adsorption of 0.3%CO/He on reduced sample and (b) oxidized sample. Some spectrum overlap. ....102

Figure 42: Evolution of the coverage of linear and bridged CO species for the reduced sample (a) and the oxidized catalyst (b). Comparison of experimental data (symbols) and theoretical curves (lines).....103

Figure 43: Experimental and calculated CO enthalpic heats of adsorption compared to DFT adsorption enthalpy. For  $\text{Pt}_{13}(\text{CO})_m$  with  $m > 1$  and  $\text{Pt}(111)_{1\text{ML}}$  structures, mean enthalpies are displayed. ....105

Figure 44: Experimental and calculated C-O bond vibration wavenumber normalized to gas CO (2126  $\text{cm}^{-1}$  found by *ab initio* calculation). ....106

Figure 45: (a) TPD-CO simulation with  $\text{Pt}_{13}(\text{CO})_m$  mechanism and relative intensity of CO ( $m/z=28$ ) during the Temperature-Programmed Desorption on highly-dispersed 1 wt. % Pt/ $\gamma$ - $\text{Al}_2\text{O}_3$ .  $\text{CO}_2$  release ( $m/z=44$ ) is also shown. (b) Impact *ab initio* typical error ( $\pm 3.6 \text{ kcal.mol}^{-1}$  for enthalpies and  $\pm 3.6 \text{ cal.mol}^{-1}.\text{K}^{-1}$  for entropies) on  $\text{Pt}_{13}(\text{CO})_m$  kinetic model with a  $5^\circ\text{C}.\text{min}^{-1}$  temperature ramp. Experimental TPD of <sup>•</sup>Di Maggio<sup>225</sup> ( $10^\circ\text{C}/\text{s}$  rate), <sup>†</sup>Gland and McClellan<sup>211</sup> ( $10^\circ\text{C}/\text{s}$ ) and <sup>‡</sup>Ertl *et al.*<sup>96</sup> ( $15^\circ\text{C}/\text{s}$ ) are reported. For alumina supported platinum, the TPD of <sup>#</sup>Herz and McCready<sup>210</sup> with a 0.90 Pt dispersion is displayed.....108

Figure 46: Relative sensitivities of the pre-exponential factors relative to CO at the peak temperatures for the most sensitive two-sides reactions for the  $\text{Pt}_{13}(\text{CO})_m$  kinetic mechanism with transition structures. The CO sticking coefficient is  $10^{-2}$ . ....110

Figure 47: Carbon monoxide Temperature Programmed Desorption on Pt/ $\gamma$ - $\text{Al}_2\text{O}_3$ -o and Pt/ $\gamma$ - $\text{Al}_2\text{O}_3$ -r (1000ppm CO, 10%  $\text{O}_2$ ).....115

Figure 48: a)  $\text{O}_2$  and CO partial order during CO oxidation on pre oxidised catalyst Pt/ $\gamma$ - $\text{Al}_2\text{O}_3$ -o and (1000ppm CO, 10%  $\text{O}_2$ ), and b) Apparent activation energy

determination of CO oxidation on Pt/ $\gamma$ -Al <sub>2</sub> O <sub>3</sub> -o in kcal.mol <sup>-1</sup> , calculated below 20% conversion. ....	117
Figure 49: Illustrations of co-adsorbed Pt <sub>13</sub> O <sub>n</sub> (CO) <sub>m</sub> structures, with potential atomic oxygen and adsorbed CO as bigger atoms. ....	120
Figure 50: Atomic oxygen adsorption electronic energy per O <sub>2</sub> according to CO and oxygen coverage. The Pt <sub>13</sub> O <sub>n</sub> data derive from Figure 24 in Chapter 3. Other energies are calculated according to Pt <sub>13</sub> O <sub>n</sub> (CO) <sub>m</sub> and the related Pt <sub>13</sub> (CO) <sub>m</sub> structure, following equation (42). Interpolation is a thin-plate spline made by Matlab. ....	121
Figure 51: Carbon monoxide adsorption electronic energy according to CO and oxygen coverage. The Pt <sub>13</sub> (CO) <sub>m</sub> data derive from Figure 35b in Chapter 4. Other energies are calculated according to Pt <sub>13</sub> O <sub>n</sub> (CO) <sub>m</sub> and the related Pt <sub>13</sub> O <sub>n</sub> structure, following equation (42). The interpolation between data points is thin-plate spline. ....	122
Figure 52: Metal support interaction according to CO and oxygen coverage. The Pt <sub>13</sub> (CO) <sub>m</sub> data derive from Figure 27a in Chapter 3 and Figure 35a in Chapter 4 for Pt <sub>13</sub> O <sub>n</sub> ones. Co-adsorbed structure interactions are calculated according to equation (44). The interpolation between data points is thin-plate spline. ....	123
Figure 53: Thermodynamic diagram (p <sub>O2</sub> ,p <sub>CO</sub> ,T) with a fixed CO partial pressure of 0.1 bars. ....	124
Figure 54: Carbon dioxide adsorption electronic energy according to CO and oxygen coverage. The adsorption energies were calculated according to equation (41). The interpolation between data points is thin-plate spline. ....	127
Figure 55: Scheme of the two possible hydroxyl assisted pathways according to <i>ab initio</i> calculated structures. The first pathway (a) pass through carboxylate adspecies thanks to OH migration from the alumina to the cluster. The second one leads to formate by the mean of hydroxyl O-H bond break. The adsorption modes displayed here are not representative. ....	130
Figure 56: Electronic energies of initial, final and intermediate systems corresponding to a) the formate path (Figure 55) and b) the carboxylate path. Energy of the initial state is set to zero. ....	131
Figure 57: Illustration of the kinetic-type reactions engaged in DES, VAR and CPX models, with a given Pt <sub>13</sub> O <sub>n</sub> (CO) <sub>m</sub> surface specie. ....	133
Figure 58: Carbon dioxide gas fraction outlet of the MOL and DES models of CO TPR simulations. For the molecular models, the initial surface specie was the reduced one. Desorption models Temperature windows were adapted to observe the CO <sub>2</sub> release, keeping a 5°C.min <sup>-1</sup> ramp. Other initial conditions calculation are displayed in Script 1 (appendices). ....	134
Figure 59: Carbon dioxide outlet gas fraction with VAR and CPX models during CO TPR simulations. Temperature windows were adapted to observe the CO <sub>2</sub> release, keeping a 5°C.min <sup>-1</sup> ramp. The main initial surface specie is Pt <sub>13</sub> O <sub>12</sub> (CO) <sub>10</sub> . Other initial conditions calculation are displayed in Script 1 (appendices). ....	136

Figure 60: Illustration inter- and extrapolation of the extrapolation used to determine Pt13On(CO) <sub>m</sub> thermodynamic parameters used to calculate kinetic parameters. The case of CO desorption enthalpy is illustrated here with a) nearest neighbor and b) thin spline plates extrapolation.....	137
Figure 61: CO <sub>2</sub> desorption of simulated CO-TPR using VAR kinetic parameter sets with sticking coefficient variations. The main initial surface specie is Pt <sub>13</sub> O <sub>12</sub> (CO) <sub>10</sub> . Other initial conditions calculation are displayed in Script 1 (appendices). Sticking coefficient were changed from 1 to 10 <sup>-4</sup> one at a time. ....	138
Figure 62: Experimental temperature programmed reaction of methanol/CO mixtures, using a 2°C.min <sup>-1</sup> temperature ramp and 3500ppm CH <sub>3</sub> OH (8% O <sub>2</sub> ). a) Methanol conversion with distinct CO concentrations and b) related methanol oxidation activation energies determination, in kcal.mol <sup>-1</sup> .....	146
Figure 63: Experimental data about temperature programmed reaction of methanol/CO mixtures, using a 2°C.min <sup>-1</sup> temperature ramp and 3500ppm CH <sub>3</sub> OH. a) CO conversion with distinct methanol concentrations and b) related CO oxidation activation energies determination.....	147
Figure 64: Activation energies of methanol/CO mixture oxidation according to CO/CH <sub>3</sub> OH ratio. Methanol activation energies are set in brown, while CO ones are in red. Linear characteristics of the methanol activation energies trend are displayed. The inlet gas mixtures are also reminded. ....	148
Figure 65: Solid infrared absorbance spectra during methanol oxidation (3500ppm, 8% vol. O <sub>2</sub> ) according to temperature. ....	150
Figure 66: Solid infrared absorbance spectra during methanol/CO mixture oxidation (3500ppm, 800ppm CO, 8% vol. O <sub>2</sub> ) according to temperature. ....	150
Figure 67: Temperature programmed reaction of the propene/CO mixtures (10% O <sub>2</sub> ). a) Propene conversion with and without carbon monoxide and b) related propene oxidation activation energies determination (in kcal.mol <sup>-1</sup> ).....	152
Figure 68: Temperature programmed desorption of the propene/CO mixtures (10% O <sub>2</sub> ). Carbon monoxide conversion during TPR of the propene/CO mixture, and CO oxidation alone.....	153
Figure 69: Solid infrared absorbance spectra during propene oxidation (3300ppm C <sub>3</sub> H <sub>6</sub> , 8% vol. O <sub>2</sub> ) according to temperature. ....	153
Figure 70: Solid infrared absorbance spectra during propene/CO mixture oxidation (1800ppm C <sub>3</sub> H <sub>6</sub> , 1000ppm CO, 8% vol. O <sub>2</sub> ) according to temperature.....	154
Figure 71: Adsorption energies for atoms on Pt(111) with one radical per cell. For GGA PBE, the work of <sup>α</sup> Qiang <i>et al.</i> <sup>277</sup> and <sup>β</sup> Stamatakis <i>et al.</i> <sup>278</sup> are reported. PW91 fonctionnal has been used by <sup>γ</sup> Ferrin <i>et al.</i> <sup>279</sup> , <sup>δ</sup> Mavrikakis <i>et al.</i> <sup>280</sup> , <sup>ε</sup> Psofogiannakis <i>et al.</i> <sup>281</sup> and <sup>ζ</sup> Chak-Tong <i>et al.</i> <sup>282</sup> . Pt(111) surface was modelled <i>via</i> clusters using B3LYP functional in <sup>η</sup> Goddard <i>et al.</i> <sup>283</sup> , <sup>θ</sup> Jacob <i>et al.</i> <sup>284</sup> and <sup>ε</sup> Psofogiannakis <i>et al.</i> <sup>281</sup> .....	156
Figure 72: Adsorption energies of C <sub>0</sub> -C <sub>3</sub> selected molecules at low coverage on Pt(111) with one radical per cell. The work of <sup>κ</sup> Saliccioli <i>et al.</i> <sup>287</sup> , <sup>β</sup> Stamatakis <i>et al.</i> <sup>278</sup> ,	

<sup>u</sup> Vlachos <i>et al.</i> <sup>288</sup> , <sup>v</sup> Honkala <i>et al.</i> <sup>289</sup> , <sup>λ</sup> Gautier <i>et al.</i> <sup>118</sup> , <sup>δ</sup> Mavrikakis <i>et al.</i> <sup>280</sup> , <sup>π</sup> Alcalà <i>et al.</i> <sup>290</sup> , <sup>ξ</sup> Aleksandrov <i>et al.</i> <sup>291</sup> , <sup>η</sup> Goddard <i>et al.</i> <sup>283</sup> and <sup>θ</sup> Jacob <i>et al.</i> <sup>284</sup> are reported.....	157
Figure 73: <i>Ab initio</i> determined adsorption energies and bond lengths of Pt-OR adsorbed species on Pt(111) with one radical per cell.....	160
Figure 74: <i>Ab initio</i> determined adsorption energies and bond lengths of Pt-CR adsorbed species with one radical per cell.....	161
Figure 75: Surface species proportions of the simulated adsorption step of methanol with the OXY micro-kinetic model. Gas inlet consist in 8% O <sub>2</sub> and 1000ppm CH <sub>3</sub> OH at 30°C. ....	164
Figure 76: TPR simulation of methanol with the OXY model. Gas inlet consists into 8% O <sub>2</sub> and 1000 ppm of CH <sub>3</sub> OH at 30°C. A 5°C/min ramp is applied. a) Outlet produced gas concentrations and b) surface species proportions. ....	165
Figure 77: TPR simulation of methanol with the MET model. Gas inlet consist in 8% O <sub>2</sub> and 1000ppm CH <sub>3</sub> OH at 30°C. A 5°C/min ramp is applied. a) Outlet produced gas concentrations and b) surface species proportions. This leads to the RED kinetic model. ....	166
Figure 78: Energies and illustrations of Pt <sub>13</sub> O <sub>20</sub> structure through the optimisation process: optimisation – velocity-scaled molecular dynamics at 600K and 5fs. The initial (0K) and final structures were obtained by geometry optimisation (quench for the final structure). Aluminum: purple, oxygen: red, platinum: blue. ....	174
Figure 79: a) Relative signals of oxygen (m/z=32) and water (m/z=18) during the O <sub>2</sub> -TPD 1 wt % Pt/Al <sub>2</sub> O <sub>3</sub> with a dehydration temperatures of 300°C and 600°C for 1 hour prior to the TPD experiment. b) Relative signals of water (m/z=32) during TPD experiments on 1 wt % Pt/Al <sub>2</sub> O <sub>3</sub> according to different dehydration conditions.....	175
Figure 80: Definitive temperature process during TPD experiments.....	176
Figure 81: Deconvolution fit of the MS signal m/z=32 recorded during TPD for the 0.3wt % Pt/γ-Al <sub>2</sub> O <sub>3</sub> catalyst using three Gaussian-type fitting curves. The global fit curve is the sum of the three Gaussian curves.....	176
Figure 82: Deconvolution fit of the MS signal m/z=32 for the 1wt % Pt/γ-Al <sub>2</sub> O <sub>3</sub> catalyst using three Gaussian-type fitting curves. The global fit curve is the sum of the three Gaussian curves. ....	177
Figure 83: Illustrations of simulated Pt(111)-nO surfaces (top views) with no oxygen (a), 0.25ML (b), 0.5ML (c), 0.75ML (d) and 1ML (e). Platinum atoms are in blue, oxygen in red. ....	178
Figure 84: Thermodynamic diagram (p <sub>O2</sub> ,T) for the adsorption of atomic O on Pt(111). ....	179
Figure 85: Illustrations of the two-layers Pt <sub>13</sub> O <sub>n</sub> structures (side views).....	180
Figure 86: Illustrations of the hemispheric Pt <sub>13</sub> O <sub>n</sub> structures (side views). ....	180
Figure 87: Number of bonds between the cluster and the support (Pt-Al, Al-O <sub>cluster</sub> and Pt-O <sub>support</sub> ). The maximum bond length for the count was 2.5 Å. Dotted lines	

corresponds to the two-layers structures whereas plain lines are hemispheric structures data. ....	181
Figure 88: Configurations of initial, transition and final states for the three coverages investigated for dissociation of O <sub>2</sub> on Pt <sub>13</sub> O <sub>n</sub> /γ-Al <sub>2</sub> O <sub>3</sub> . The oxygen atoms engaged in dissociation are set in brown. ....	182
Figure 89: Configurations of initial, transitions and final states for the two coverages investigated for dissociation of O <sub>2</sub> on Pt(111). ....	183
Figure 90: Dissociation activation energy for the supported Pt <sub>13</sub> system. Diamonds are the DFT-determined values, lines are the piecewise linear trends chosen in the kinetic model. ....	184
Figure 91: Illustrations of the non-supported Pt <sub>13</sub> (CO) <sub>m</sub> structures. <i>Ab initio</i> calculations characteristics were identical to the supported clusters except that Kpoint was set to 5x5x5. The initial guesses were build with a cuboctaedric 13-platinum aggregate (close to Pt <sub>13</sub> final structure in this figure) with top adsorbed CO. ....	186
Figure 92: Illustrations of a) Pt(111)(CO) <sub>0.25ML</sub> , b) Pt(111)O <sub>0.25ML</sub> (CO) <sub>0.25ML</sub> and Pt(111)(CO) <sub>1ML</sub> . ....	186
Figure 93: Illustration of the velocity-scaled molecular dynamics of Pt <sub>13</sub> (CO) <sub>9</sub> . ....	187
Figure 94: Phase diagram with system entropies calculated with <i>ab initio</i> imaginary and real treated frequencies. Colors corresponds to the same species as untreated diagram. ....	188
Figure 95: Phase diagram differences between the <i>ab initio</i> treated frequencies versus classic phase diagram. ....	189
Figure 96: Average desorption enthalpy and entropy of the Pt <sub>13</sub> (CO) <sub>m</sub> structures regarding CO coverage (large dots). Linear piecewise interpolation (small dots). Average has been made from 300K to 1000K. ....	190
Figure 97: Illustration of Pt <sub>13</sub> (CO) typical structures found with a) the only alumina bonded CO, b) top c) bridge and d) hollow adsorption modes ....	191
Figure 98: Illustrations of the supported Pt <sub>13</sub> (CO) <sub>m</sub> structures. ....	191
Figure 99: Backview the supported Pt <sub>13</sub> (CO) <sub>12</sub> structure with targeted carbon and oxygen atoms dissociated ....	192
Figure 100: Population of adsorbed carbon monoxide according to their adsorption mode. The Al-bounded modes are characteristic of carbon monoxide linked to aluminum of the support. ....	192
Figure 101: Electronic energy of the cluster only (Pt <sub>13</sub> (CO) <sub>m</sub> , without alumina) for both supported and non-supported Pt <sub>13</sub> (CO) <sub>m</sub> structures according to CO coverage. For supported structures, this energy is determined using single point calculation by equation (88). ....	193
Figure 102: Bader charges of the elements present on the cluster. The straight lines deals with the CO gas charge. ....	194
Figure 103: Carbon monoxide concentration recording from m/z=28 signal of the mass spectrometer. Oxidation of CO into CO <sub>2</sub> lowers considerably CO signal above 86°C. ....	195

Figure 104: Carbon monoxide release temperature range according to CO sticking coefficient. The number of CO adspecies on Pt <sub>13</sub> are displayed in the graph. Identical CO number were recorded for every CO sticking coefficients. ....	196
Figure 105: Illustrations of <i>ab initio</i> co-adsorbed Pt <sub>13</sub> O <sub>n</sub> (CO) <sub>m</sub> structures without the potential oxygen that take part to CO oxidation. ....	198
Figure 106: Illustrations of <i>ab initio</i> co-adsorbed Pt <sub>13</sub> O <sub>n</sub> (CO) <sub>m</sub> structures without the potential CO that take part to oxidation. Pt <sub>13</sub> O <sub>4</sub> and Pt <sub>13</sub> O <sub>22</sub> are displayed in chapter 3.....	198
Figure 107: Thermodynamic diagram (p <sub>O2</sub> ,T) for several p <sub>CO</sub> . White: Pt <sub>13</sub> . From dark to light green: Pt <sub>13</sub> O <sub>8</sub> (CO) <sub>11</sub> and Pt <sub>13</sub> O <sub>22</sub> (CO). From dark to light blue: Pt <sub>13</sub> (CO) <sub>24</sub> , Pt <sub>13</sub> (CO) <sub>18</sub> , Pt <sub>13</sub> (CO) <sub>15</sub> , Pt <sub>13</sub> (CO) <sub>9</sub> and Pt <sub>13</sub> (CO) <sub>2</sub> . From dark to light yellow: Pt <sub>13</sub> O <sub>32</sub> , Pt <sub>13</sub> O <sub>24</sub> , Pt <sub>13</sub> O <sub>22</sub> , Pt <sub>13</sub> O <sub>20</sub> , Pt <sub>13</sub> O <sub>16</sub> , Pt <sub>13</sub> O <sub>10</sub> , Pt <sub>13</sub> O <sub>8</sub> and Pt <sub>13</sub> O <sub>4</sub> . ....	199
Figure 108: Illustrations of the transition states found for CO oxidation. ....	200
Figure 109: Illustrations of potential final states from co-adsorbed structures. The produced CO <sub>2</sub> molecule is depicted with larger balls. ....	200
Figure 110: Illustrations of the final states structure after removing CO <sub>2</sub> molecule. ...	201
Figure 111: Bader charge analysis of a) carbon, b) atomic oxygen, c) CO molecule, d) CO oxygen and e) platinum. Thin spline interpolation gives a qualitative trend between data points.....	203
Figure 112: Illustration of inserted water in Pt <sub>13</sub> O <sub>22</sub> (CO). ....	203
Figure 113: Illustration of inserted water in Pt <sub>13</sub> O <sub>21</sub> (CO <sub>2</sub> ). ....	203
Figure 114: Illustration of inserted water in Pt <sub>13</sub> O <sub>16</sub> (CO) <sub>7</sub> structures. ....	204
Figure 115: Illustration of inserted water in Pt <sub>13</sub> O <sub>15</sub> (CO) <sub>6</sub> (CO <sub>2</sub> ) structures. ....	205
Figure 116: Simulation of O <sub>2</sub> and CO-TPD with sticking coefficient set to unity and identical gas flow and surface species as in Chapters 3 ad 4. ....	205
Figure 117: Surface species during CO oxidation with DES-Pt <sub>13</sub> O <sub>4</sub> (CO) model at a) 80°C, b) 140°C, c) 160°C, d) 170°C, e) 180°C and f) 200°C.....	211
Figure 118: Reaction fluxes during CO oxidation with DES-Pt <sub>13</sub> O <sub>4</sub> (CO) model. ....	211
Figure 119: Surface species during DES-Pt <sub>13</sub> O <sub>16</sub> (CO) <sub>7</sub> simulation through oxidation of CO. Oxidation appears starts at a) -82.5°C, in progress at b) -82°C and almost finished around c) -81°C.....	212
Figure 120: Reaction fluxes during CO oxidation with DES-Pt <sub>13</sub> O <sub>16</sub> (CO) <sub>7</sub> model.....	213
Figure 121: <i>Ab initio</i> determined CO <sub>2</sub> desorption enthalpy and entropy (dots) and their linear interpolation (lines) according to oxygen coverage. These interpolations are used for CO oxidation VAR and CPX models.....	214
Figure 122: Surface species during CO oxidation with VAR-Pt <sub>13</sub> O <sub>4</sub> (CO) model at a) 90°C, b) 110°C, c) 130°C and d) 150°C.....	215
Figure 123: Reaction fluxes during CO oxidation with VAR-Pt <sub>13</sub> O <sub>4</sub> (CO) model.....	216
Figure 124: Surface species during CO oxidation with VAR-Pt <sub>13</sub> O <sub>16</sub> (CO) <sub>7</sub> model at a) 50°C, b) 80°C and c) 150°C. ....	217
Figure 125: Reaction fluxes during CO oxidation with VAR-Pt <sub>13</sub> O <sub>16</sub> (CO) <sub>7</sub> . ....	218

Figure 126: Surface species during CO oxidation with VAR-Pt <sub>13</sub> O <sub>4</sub> (CO) model at a) 130°C, b) 150°C and c) 190°C.....	219
Figure 127: Reaction fluxes during CO oxidation with CPXspl-Pt <sub>13</sub> O <sub>4</sub> (CO).....	220
Figure 128: Consecutive differential spectra for a) methanol oxidation (3500ppm), b) with 800ppm CO and c) with 2000ppm CO. The three bands corresponds, from the draker to the lighter: 100°C-80°C, 120°C-100°C and 180°C-160°C.....	222
Figure 129: Consecutive differential spectra for a) propene oxidation alone (3500ppm) and b) with 1000ppm CO (1800 ppm C <sub>3</sub> H <sub>6</sub> ). Interferences are observed for pure propene oxidation due to cristal windows in the experimental set-up.....	222
Figure 130: Illustrations of <i>ab initio</i> calculated C <sub>0</sub> adsorbed species on Pt(111). .....	223
Figure 131: Illustrations of <i>ab initio</i> calculated C <sub>0</sub> adsorbed species on Pt(111) (continuation). .....	224
Figure 132: Illustrations of <i>ab initio</i> calculated C <sub>1</sub> adsorbed species on Pt(111). .....	225
Figure 133: Illustrations of <i>ab initio</i> calculated C <sub>1</sub> adsorbed species on Pt(111) (continuation). .....	226
Figure 134: Illustrations of <i>ab initio</i> calculated adsorbed species on Pt(111) (continuation). .....	227
Figure 135: Illustrations of <i>ab initio</i> calculated C <sub>2</sub> adsorbed species on Pt(111). .....	228
Figure 136: Illustrations of <i>ab initio</i> calculated C <sub>2</sub> adsorbed species on Pt(111) (continuation). .....	229
Figure 137: Illustrations of <i>ab initio</i> calculated C <sub>2</sub> adsorbed species on Pt(111) (continuation). .....	230
Figure 138: Illustrations of <i>ab initio</i> calculated C <sub>2</sub> adsorbed species on Pt(111) (continuation). .....	231
Figure 139: Illustrations of <i>ab initio</i> calculated C <sub>2</sub> adsorbed species on Pt(111) (continuation). .....	232
Figure 140: Illustrations of <i>ab initio</i> calculated C <sub>2</sub> adsorbed species on Pt(111) (continuation). .....	233
Figure 141: Illustrations of <i>ab initio</i> calculated C <sub>2</sub> adsorbed species on Pt(111) (continuation). .....	234
Figure 142: Illustrations of <i>ab initio</i> calculated C <sub>2</sub> adsorbed species on Pt(111) (continuation). .....	235
Figure 143: Illustrations of <i>ab initio</i> calculated C <sub>2</sub> adsorbed species on Pt(111) (continuation). .....	236
Figure 144: Illustrations of <i>ab initio</i> calculated C <sub>2</sub> adsorbed species on Pt(111) (continuation). .....	237
Figure 145: Illustrations of <i>ab initio</i> calculated C <sub>3</sub> adsorbed species on Pt(111). .....	238
Figure 146: Illustrations of <i>ab initio</i> calculated C <sub>3</sub> adsorbed species on Pt(111) (continuation). .....	239



# List of tables

Table 1: Some PAHs detected in the Diesel exhaust by several studies <sup>11,19,23,27-29,32,34,38,39</sup> . The structural formula corresponds to the name in bold. ....	22
Table 2: Elemental composition of the used Pt/ $\gamma$ -Al <sub>2</sub> O <sub>3</sub> catalysts determined <i>via</i> X-ray fluorescence. ....	35
Table 3: Temperature Programmed characteristics concerning O <sub>2</sub> and CO desorption on Pt- $\gamma$ -Al <sub>2</sub> O <sub>3</sub> . ....	40
Table 4: Commonly used GGA functionals in <i>ab initio</i> molecular modelling with their main advantages and drawbacks. ....	46
Table 5: Molecular dynamics characteristics for Pt <sub>13</sub> / $\gamma$ -Al <sub>2</sub> O <sub>3</sub> models.....	51
Table 6: Selected species for estimated mechanisms used for light hydrocarbons oxidation in Chapter 6. ....	64
Table 7: Average adsorption energy per O <sub>2</sub> , at low oxygen coverage. ....	77
Table 8: Dissociation and association barriers for O <sub>2</sub> dissociation on Pt(111) and Pt <sub>13</sub> O <sub>n</sub> cluster .....	84
Table 9: Heats of adsorption of each species for the two catalytic materials.....	103
Table 10: Carbon monoxide oxidation characteristics on Pt/Al <sub>2</sub> O <sub>3</sub> in excess of oxygen compared to carbon monoxide. The CO oxidation temperature range as well as T <sub>50%</sub> is presented. Dispersion were determined using *hydrogen chemisorption titration.....	116
Table 11: Partial order and activation energies previously obtained for CO oxidation. ....	117
Table 12: Partial order and activation energies previously obtained for CO oxidation. ....	118
Table 13: Carbon dioxide adsorption characteristics on Pt <sub>13</sub> O <sub>n</sub> (CO) <sub>m</sub> structures. Electronic adsorption energy and adsorption modes are gathered.....	126
Table 14: Data on the transition states found for CO oxidation. Electronic oxidation energy and structural information are displayed.....	128
Table 15: Adsorption energies of water on alumina on initial and final structures. The symbol * indicates dissociated water into H* and HO*. Illustrations of the structures are visible in Figure 112(b,c), Figure 114(a,b) and Figure 115(a,b) in appendices. ....	129
Table 16: Kinetic model characteristics according to reaction type and coverage dependences. ....	132
Table 17: Experimental and simulated apparent activation energies for CO-TPR according to VAR-Pt <sub>13</sub> O <sub>4</sub> (CO) and CPXspl kinetic models.....	138

Table 18: Operating conditions for pure methanol and methanol/CO mixtures oxidation experiments. ....	145
Table 19: Determination of solid IR vibrationnal modes during methanol oxidation according to literature <sup>274,275</sup> .....	148
Table 20: Operating conditions for propene and propene/CO gas mixture oxidation TPR.....	151
Table 21: Characteristics of radical adsorption on Pt(111) determined <i>via ab initio</i> molecular modelling on a Pt(111) surface with one radical per cell. ....	158
Table 22: Micro-kinetic characteristics of the C <sub>0</sub> -C <sub>1</sub> models through the three versions (RAW, RED and DES).....	162
Table 23: Surface species proportions after a one hour adsorption step (1000 ppm CH <sub>3</sub> OH, 8% O <sub>2</sub> ). ....	163
Table 24: Atomic heat of adsorption per O <sub>2</sub> found for Pt(111) systems .....	178
Table 25: Transition state characteristics for Pt <sub>13</sub> O <sub>n</sub> and Pt(111) structures.....	183
Table 26: Reactions and kinetic parameters of the Pt(111) model with a sticking coefficient of 0.01 .....	184
Table 27: Reactions and kinetic parameters of the Pt <sub>13</sub> O <sub>n</sub> model with a sticking coefficient of 0.01 .....	184
Table 28: Imaginary wavenumbers of the Pt <sub>13</sub> (CO) <sub>m</sub> structures .....	187
Table 29: Reactions and kinetic parameters of the Pt <sub>13</sub> (CO) <sub>m</sub> model with a sticking coefficient of 0.01 .....	197
Table 30: Comparison between CO oxidation electronic and enthalpic energies .....	208
Table 31: Kinetics parameters of the MOL-Pt <sub>13</sub> O <sub>4</sub> (CO)-eq following Arrhenius-type rate constants.....	208
Table 32: Kinetics parameters of the MOL-Pt <sub>13</sub> O <sub>4</sub> (CO)-50 following Arrhenius-type rate constants.....	208
Table 33: Kinetics parameters of the MOL-Pt <sub>13</sub> O <sub>16</sub> (CO) <sub>7</sub> following Arrhenius-type rate constants.....	208

# References

- (1) Sinflet, J. H. Catalytic reforming, in Handbook of Heterogeneous Catalysis; Ertl, G., Knözinger, E., Weitkamp, J.; Eds.; Wiley: Weinheim 1997, 1939–1955.
- (2) Védrine, J. C.; Korotchenkov, G. S. *Metal oxides in heterogeneous catalysis*; Metal oxides series; Elsevier: Amsterdam, 2018.
- (3) Chheda, J. N.; Huber, G. W.; Dumesic, J. A. Liquid-phase catalytic processing of biomass-derived oxygenated hydrocarbons to fuels and chemicals. *Angewandte Chemie* 2007, *46*, 7164–7183.
- (4) Lykhach, Y.; Bruix, A.; Fabris, S.; Potin, V.; Matolínová, I.; Matolín, V.; Libuda, J.; Neyman, K. M. Oxide-based nanomaterials for fuel cell catalysis. *Catalysis Science & Technology* 2017, *7*, 4315–4345.
- (5) Heck, R. M.; Farrauto, R. J. Automobile exhaust catalysts. *Applied Catalysis A: General* 2001, *221*, 443–457.
- (6) Russell, A.; Epling, W. S. Diesel Oxidation Catalysts. *Catalysis Reviews* 2011, *53*, 337–423.
- (7) Boudart, M. Catalysis by supported materials. *Adv. Catal.* 1969, *20*, 153–166.
- (8) Nørskov, J. K.; Bligaard, T.; Rossmeisl, J.; Christensen, C. H. Towards the computational design of solid catalysts. *Nature chemistry* 2009, *1*, 37–46.
- (9) Chizallet, C.; Raybaud, P. Density functional theory simulations of complex catalytic materials in reactive environments. *Catalysis Science & Technology* 2014, *4*, 2797–2813.
- (10) Sharma, N.; Gupta, T.; Singh, A.; Agarwal, A.; Eastwood, P. *Air pollution and control, 2017.*, Springer 978-981-10-7184-3.
- (11) Degobert, P. *Automobile et pollution*; Technip, 2000.
- (12) Girard, J. W.; Cavataio, G.; Lambert, C. K. The Influence of Ammonia Slip Catalysts on Ammonia, N<sub>2</sub>O and NO<sub>x</sub> Emissions for Diesel Engines. *Society of Automotive Engineers* 2007, 2007-01-1572.
- (13) Prockop, L. D.; Chichkova, R. I. Carbon monoxide intoxication: an updated review. *Journal of the neurological sciences* 2007, *262*, 122–130.
- (14) Arin, L. M.; Warneck, P. Reaction of Ozone with Carbon Monoxide. *The journal of physical chemistry letters* 1972, *76*, 1514–1516.
- (15) Miller, J. A.; Bowman, C. T. Mechanism and modeling of nitrogen chemistry in combustion. *Progress in Energy and Combustion Science* 1989, *15*, 287–338.

- (16) Rankovic, N. Modélisation multi-échelles en catalyse environnementale: application au piège à NO<sub>x</sub>. Thèse de doctorat. Génie des procédés et technologies avancées; Université Pierre et Marie Curie, IFP Energies nouvelles, 2012.
- (17) Dec, J.; Davisson, M.; Sjöberg, M.; Leif, R.; Hwang, W. Detailed HCCI Exhaust Speciation and the Sources of Hydrocarbon and Oxygenated Hydrocarbon Emissions. *Society of Automotive Engineers* 2008, 2008-01-0053.
- (18) Alves, C. A.; Vicente, A.; Gomes, J.; Nunes, T.; Duarte, M.; Bandowe, B. Polycyclic aromatic hydrocarbons (PAHs) and their derivatives (oxygenated-PAHs, nitrated-PAHs and azaarenes) in size-fractionated particles emitted in an urban road tunnel. *Atmospheric Research* 2016, 180, 128–137.
- (19) Caplain, I.; Cazier, F.; Nouali, H.; Mercier, A.; Déchaux, J.; Nollet, V.; Joumard, R.; André, J.; Vidon, R. Emissions of unregulated pollutants from European gasoline and diesel passenger cars. *Atmospheric Environment* 2006, 40, 5954–5966.
- (20) Mellouki, A.; Wallington, T. J.; Chen, J. Atmospheric chemistry of oxygenated volatile organic compounds: impacts on air quality and climate. *Chemical reviews* 2015, 115, 3984–4014.
- (21) NGK Spark Plugs Company. Exhaust and harmful emissions. <https://www.ngk.de/en/technology-in-detail/lambda-sensors/basic-exhaust-principles/exhaust-and-harmful-emissions/> (accessed January 24, 2017).
- (22) Lox, E. *Handbook of Heterogeneous Catalysis*. 11.2 Automotive Exhaust Treatment; Wiley-VCH, 1999.
- (23) Schauer, J. J.; Kleeman, M. J.; Cass, G.; Simoneit, B. R. T. Measurement of Emissions from Air Pollution Sources. *Environmental Science & Technology* 1999, 33, 1578–1587.
- (24) Farrugia J.; Olson K. Evaluation of a High Speed, High Resolution Gas Chromatography Instrument for Exhaust Hydrocarbon Speciation. *Society of Automotive Engineers* 2005, 2005-01-0683.
- (25) Lev-on, M.; LeTavec, C.; Uihlein, J.; Alleman, T. L.; Lawson, D. R.; Vertin, K.; Thompson, G. J.; Gautman, M.; Wayne, S.; Zielinska, B.; Sagebiel, J. Chemical Speciation of Exhaust Emissions from Trucks and Buses Fueled on Ultra-Low Sulfur Diesel and CNG. *Society of Automotive Engineers* 2002, 2002-01-0432.
- (26) Schmitz, T.; Hassel, D.; Weber, F. Determination of VOC-components in the exhaust of gasoline and diesel passenger cars. *Atmospheric Environment* 2000, 34, 4639–4647.
- (27) Lee, S. C.; Chiu, M. Y.; Ho, K. F.; Zou, S. C.; Wang, X. Volatile organic compounds (VOCs) in urban atmosphere of Hong Kong. *Chemosphere* 2002, 48, 375–382.
- (28) Lanning, L. A.; Smith, K. W.; Tennant, C. J. A New Method for Diesel HC Collection and Speciation. *Society of Automotive Engineers* 2000, 2000-01-2951.
- (29) Kado, N. Y.; Okamoto, R. A.; Kuzmicky, P. A.; Kobayashi, R.; Ayala, A.; Gebel, M. E.; Rieger, P. L.; Maddox, C.; Zafonte, L. Emissions of Toxic Pollutants from

- Compressed Natural Gas and Low Sulfur Diesel-Fueled Heavy-Duty Transit Buses Tested over Multiple Driving Cycles. *Environmental Science & Technology* 2005, *39*, 7638–7649.
- (30) Riddle, S. G.; Jakober, C. A.; Robert, M. A.; Cahill, T. M.; Charles, M. J.; Kleeman, M. J. Large PAHs detected in fine particulate matter emitted from light-duty gasoline vehicles. *Atmospheric Environment* 2007, *41*, 8658–8668.
- (31) Neumann, K. H.; Schürmann, D.; Kohoutek, P.; Beyersdorf, J.; Hartung; Nagel C.; Schulze, J. Unregulated Exhaust Gas Components of Modern Diesel Passenger Cars. *Society of Automotive Engineers* 1999, 1999-01-0514.
- (32) Schulz, H.; Bandeira De Melo, G.; Ousmanov, F. Volatile organic compounds and particulates as components of diesel engine exhaust gas. *Combustion and flame* 1999, *118*, 179–190.
- (33) Homann, K. H.; Wellmann, C. Arrhenius Parameters for the Reactions of O Atoms with Some Alkynes in the Range 300-1300 K. *Berichte der Bunsengesellschaft für physikalische Chemie* 1983, *87*, 527–532.
- (34) Corrêa, S. M.; Arbilla, G. Aromatic hydrocarbons emissions in diesel and biodiesel exhaust. *Atmospheric Environment* 2006, *40*, 6821–6826.
- (35) Nguyen, T. Q.; Escaño, Mary Clare Sison; Nakanishi, H.; Kasai, H.; Maekawa, H.; Osumi, K.; Sato, K. DFT+U study on the oxygen adsorption and dissociation on CeO<sub>2</sub>-supported platinum cluster. *Applied Surface Science* 2014, *288*, 244–250.
- (36) Sarathy, S.; Farooq, A.; Kalghatgi, G. T. Recent progress in gasoline surrogate fuels. *Progress in Energy and Combustion Science* 2018, *65*, 67–108.
- (37) Gardiner, W. C. *Gas-Phase Combustion Chemistry*; Springer New York: New York, NY, 2000.
- (38) Borrás, E.; Tortajada-Genaro, L. A.; Vázquez, M.; Zielinska, B. Polycyclic aromatic hydrocarbon exhaust emissions from different reformulated diesel fuels and engine operating conditions. *Atmospheric Environment* 2009, *43*, 5944–5952.
- (39) Elvers, B. *Handbook of fuels. Energy Sources for Transportation*; Wiley-VCH, 2008.
- (40) Sassi, A.; Rohart, E.; Belot, G. Post-traitement des émissions polluantes des moteurs thermiques à combustion interne - Moteurs à allumage par compression. *Technique de l'ingénieur* 2011, *BM2509 V1*.
- (41) Sassi, A.; Rohart, E.; Belot, G. Post-traitement des émissions polluantes des moteurs thermiques à combustion interne - Moteurs à allumage commandé. *Technique de l'ingénieur* 2011, *BM2508 V1*.
- (42) Chadderton, J.; Child, D.; Deighton, J. Particulate filter, and system and method for cleaning same, 1996, Patent number US005551971A.
- (43) Dettling, J. C.; Skomoroski, R. Catalyzed Diesel exhaust particulate filter, 1992, Patent number US005100632A.
- (44) Ludecke, O. A.; Rosebrock, T. L. Diesel engine exhaust particulate filter with intake throttling incineration control, 1980, Patent number US-4211075.

- (45) Coq, B.; Delahay, G.; Fajulas, F.; Kieger S.; Neveu, B.; Peudpiece, J. B. Process for removing the nitrogen oxides from the exhaust gases using the selective catalytic reduction with ammonia, without formation of dinitrogen oxide, 2004, Patent number EP0914866A1.
- (46) Hong-Xin, L.; Bjorn, M., W.; Cormie, E. Novel microporous crystalline material comprising a molecular sieve or zeolite having an 8-ring pore opening structure and methods of making and using same, 2007, Patent number WO2008118434A1.
- (47) Koltsakis, G. C.; Haralampous, O. A.; Koutoufaris, I. Z. Applications of Multi-layer Catalyst Modeling in deNO<sub>x</sub> and DPF Systems. *Society of Automotive Engineers* 2010, 2010-01-0893.
- (48) Beck, D. D.; Sommers, J. W.; DiMaggio, C. L. Axial characterization of oxygen storage capacity in close-coupled lightoff and underfloor catalytic converters and impact of sulfur. *Applied Catalysis B: Environmental* 1997, 11, 273–290.
- (49) Maunula, T.; Suopanki, A.; Torkkell, K.; Härkönen, M. The Optimization of Light-duty Diesel Oxidation Catalysts for Preturbo, Closed-coupled and Underfloor Positions. *Society of Automotive Engineers* 2004, 2004-01-3021.
- (50) Haas, F.; Fuess, H. Structural Characterization of Automotive Catalysts. *Advanced Engineering Materials* 2005, 7, 899–913.
- (51) Volter, J.; Lietz, G.; Spindler, H.; Lieske, H. Role of metallic and oxidic platinum in the catalytic combustion of n-heptane. *Journal of Catalysis* 1987, 104, 375–380.
- (52) Chen, M.; Schmidt L. D. Morphology and Composition in Reactive of Pt-Pd Alloy Atmospheres. *Journal of Catalysis* 1978, 198–218.
- (53) Beutel, T. W.; Dettling, J. C.; Hollobaugh, D. O.; Mueller, T. W. Pt-Pd diesel oxidation catalyst with CO/HC light-off and HC storage function, 2006, Patent number US7576031B2.
- (54) Watanabe, T.; Kawashima, K.; Tagawa, Y.; Tashiro, K.; Anoda, H.; Ichioka, K.; Sumiya, S.; Zhang, G. New DOC for Light Duty Diesel DPF System. *Society of Automotive Engineers* 2007, 2007-01-1920.
- (55) Skoglundh, M.; Löwendahl, L. O.; Otterated, J.-E. Combinations of platinum and palladium on alumina supports as oxidation catalysts. *Applied Catalysis* 1991, 77, 9–20.
- (56) Oh, S. H.; Cavendish, J. C. Mathematical modeling of catalytic converter lightoff. *AIChE* 1985, 31, 935–942.
- (57) Tronci, S.; Baratti, R.; Gavriilidis, A. Catalytic converter design for minimisation of cold-start emissions. *Chemical Engineering Communications* 1999, 173, 53–77.
- (58) Jaree, A.; Budman, H.; Hudgins, R. R.; Silveston, P. L.; Yakhnin, V.; Menzinger, M. Temperature excursions in packed bed reactors with an axial variation of catalyst activity. *Catalysis Today* 2001, 69, 137–146.
- (59) Koplín, T. J.; Domke, I.; Castellano, C. R.; Koermer, G.; Schrof, W.; Feuerhake, R.; Schornick, G.; Cristadoro, A.; Schönfelder, D.; Hibst, H.; Gregor, C. M.; Ten, T. Metal oxide support material containing nanoscaled iron-platinum group metal particles, 2009, Patent number WO2011073120 A1.

- (60) Kim, C. H.; Qi, G.; Dahlberg, K.; Li, W. X. Strontium-doped perovskites rival platinum catalysts for treating NO<sub>x</sub> in simulated diesel exhaust. *Science* 2010, *327*, 1624–1627.
- (61) Schön, A.; Dacquin, J.-P.; Dujardin, C.; Granger, P. Catalytic Activity and Thermal Stability of LaFe<sub>1-x</sub>Cu<sub>x</sub>O<sub>3</sub> and La<sub>2</sub>CuO<sub>4</sub> Perovskite Solids in Three-Way-Catalysis. *Topics in Catalysis* 2016, 300–330.
- (62) Schön, A.; Dujardin, C.; Dacquin, J.-P.; Granger, P. Enhancing catalytic activity of perovskite-based catalysts in three-way catalysis by surface composition optimisation. *Catalysis Today* 2015, *258*, 543–548.
- (63) Arai, H.; Machida, M. Thermal stabilization of catalyst supports and their application to high-temperature catalytic combustion. *Applied Catalysis A: General* 1996, *138*, 161–176.
- (64) Chu, Y., F.; Ruckenstein, E. On the sintering of platinum on alumina model catalyst. *Journal of Catalysis* 1978, *55*, 281–298.
- (65) Fiedrow, R. M.; Wanke, S. E. The sintering of supported metal catalysts. *Journal of Catalysis* 1976, *43*, 34–42.
- (66) Harris, P. J. F. The sintering of platinum particles in an alumina-supported catalyst: further transmission electron microscopy studies. *Journal of Catalysis* 1986, *97*, 527–542.
- (67) Adibi, P. T. Z. In situ studies of platinum catalyst sintering. Thesis for the degree of doctor of philosophy; Chalmers university of technology, Göteborg, Sweden, 2016.
- (68) Dautzenberg, F.; Wolters, H., B., M. State of dispersion of platinum in alumina-supported catalysts. *Journal of Catalysis* 1978, *51*, 26–39.
- (69) Sabatier, P. La Catalyse en Chimie Organique, Librairie Polytechnique. *Béranger, Paris* 1913.
- (70) Deutschmann, O.; Knözinger, H.; Kochloefl, K.; Turek, T. Heterogeneous Catalysis and Solid Catalysts, 1. Fundamentals. *Ullmann's Encyclopedia of Industrial Chemistry*; Wiley-VCH Verlag GmbH & Co. KGaA: Weinheim, Germany, 2000.
- (71) Putna, E. S.; Vohs, J. M.; Gorte, R. J. Oxygen desorption from alpha-Al<sub>2</sub>O<sub>3</sub> (0001) supported Rh, Pt and Pd particles. *Surface Science* 1997, *391*, L1178-L1182.
- (72) Diehl, F. Deep catalytic oxidation of heavy hydrocarbons representative of diesel engine over Pt/Al<sub>2</sub>O<sub>3</sub>; Université Pierre et Marie Curie, IFPEN, 1998.
- (73) Haneda, M.; Sasaki, M.; Hamada, H.; Ozawa, M. Effect of Pt Dispersion on the Catalytic Activity of Supported Pt Catalysts for Diesel Hydrocarbon Oxidation. *Topics in Catalysis* 2013, *56*, 249–254.
- (74) Van Santen, R. A.; Neurock, M. *Molecular heterogeneous catalysis. A conceptual and computational approach*; Wiley-VCH: Weinheim, Cambridge, 2006.
- (75) Philippot K.; Serp P. *Nanomaterials in Catalysis. Chapter 1 : Concepts in Nanocatalysis*; Wiley-VCH, 2013.
- (76) Roduner, E. Size matters: why nanomaterials are different. *Chemical Society reviews* 2006, *35*, 583–592.

- (77) Xu, L.; McCabe, R.; Tennison, P.; Jen, H.-W. Laboratory and Vehicle Demonstration of “2nd-Generation” LNT + in-situ SCR Diesel Emission Control Systems. *Society of Automotive Engineers International* 2011, *4*, 158–174.
- (78) Johnson, T. V. Vehicular Emissions in Review. *Society of Automotive Engineers International* 2012, *5*, 216–234.
- (79) Bray, J. M.; Skavdahl, I. J.; McEwen, J.-S.; Schneider, W. F. First-principles reaction site model for coverage-sensitive surface reactions. *Surface Science* 2014, *622*, L1-L6.
- (80) Mhadeshwar, A. B.; Vlachos, D. G. A Catalytic Reaction Mechanism for Methane Partial Oxidation at Short Contact Times, Reforming, and Combustion, and for Oxygenate Decomposition and Oxidation on Platinum. *Ind. Eng. Chem. Res.* 2007, *46*, 5310–5324.
- (81) Mhadeshwar, A. B.; Vlachos, D. G. Microkinetic Modeling for Water-Promoted CO Oxidation, Water–Gas Shift, and Preferential Oxidation of CO on Pt. *The Journal of Physical Chemistry B* 2004, *108*, 15246–15258.
- (82) Reuter, K. Ab Initio Thermodynamics and First-Principles Microkinetics for Surface Catalysis. *Catalysis Letters* 2016, *146*, 541–563.
- (83) Saliciccoli, M.; Stamatakis, M.; Caratzoulas, S.; Vlachos, D. G. A review of multiscale modeling of metal-catalyzed reactions. *Chemical Engineering Science* 2011, *66*, 4319–4355.
- (84) Blackman, G. S.; Xu, M.-L.; Ogletree, D., F.; Van Hove, M. A.; Somorjai, G. Mix of Molecular Adsorption Sites Detected for Disordered CO on Pt(111) by Diffuse Low-Energy Electron Diffraction. *Physical review letters* 1988, *61*, 2352–2355.
- (85) Campbell C. T.; Ertl, G.; Kuipers, H.; Segner, J. A molecular beam study of the adsorption and desorption of oxygen from a Pt(111) surface. *Surface Science* 1981, *107*, 220–236.
- (86) Campbell C. T.; Ertl, G.; Kuipers, H.; Segner, J. A molecular beam investigation of the interactions of CO with a Pt(111) surface. *Surface Science* 1981, *107*, 207–219.
- (87) Maestri, M.; Reuter, K. Semiempirical rate constants for complex chemical kinetics: first-principles assessment and rational refinement. *Angewandte Chemie* 2011, *50*, 1194–1197.
- (88) Larmier, K.; Nicolle, A.; Chizallet, C.; Cadran, N.; Maury, S.; Lamic-Humblot, A.; Marceau, E.; Lauron-Pernot, H. Influence of Coadsorbed Water and Alcohol Molecules on Isopropyl Alcohol Dehydration on gamma-alumina. *ACS Catalysis* 2016, *6*, 1905–1920.
- (89) Saeys, M.; Reyniers, M.; Thybaut, J.; Neurock, M.; Marin, G. First-principles based kinetic model for the hydrogenation of toluene. *Journal of Catalysis* 2005, *236*, 129–138.
- (90) Sabbe, M. K.; van Geem, K. M.; Reyniers, M.-F.; Marin, G. B. First principle-based simulation of ethane steam cracking. *AIChE* 2011, *57*, 482–496.

- (91) Matera, S.; Blomberg, S.; Hoffmann, M. J.; Zetterberg, J.; Gustafson, J.; Lundgren, E.; Reuter, K. Evidence for the Active Phase of Heterogeneous Catalysts through In Situ Reaction Product Imaging and Multiscale Modeling. *ACS Catalysis* 2015, 5, 4514–4518.
- (92) Christiansen, M. A.; Mpourmpakis, G.; Vlachos, D. G. DFT-driven multi-site microkinetic modeling of ethanol conversion to ethylene and diethyl ether on  $\gamma$ -Al<sub>2</sub>O<sub>3</sub> (111). *Journal of Catalysis* 2015, 323, 121–131.
- (93) Foppa, L.; Margossian, T.; Kim, S. M.; Müller, C.; Copéret, C.; Larmier, K.; Comas-Vives, A. Contrasting the Role of Ni/Al<sub>2</sub>O<sub>3</sub> Interfaces in Water-Gas Shift and Dry Reforming of Methane. *Journal of the American Chemical Society* 2017, 139, 17128–17139.
- (94) Rankovic, N.; Chizallet, C.; Nicolle, A.; Da Costa, P. Multiscale Modeling of Barium Sulfate Formation from BaO. *Ind. Eng. Chem. Res.* 2013, 52, 9086–9098.
- (95) Jasper, A. W.; Pelzer, K. M.; Miller, J. A.; Kamarchik, E.; Harding, L. B.; Klippenstein, S. J. Predictive a Priori Pressure-Dependent Kinetics. *Science* 2014, 346, 1212–1215.
- (96) Ertl, G.; Neumann M.; Streit K. M. Chemisorption of CO on the Pt(111) surface. *Surface Science* 1977, 64, 393–410.
- (97) Bleakley, K.; Hu, P. A Density Functional Theory Study of the Interaction between CO and O on a Pt Surface. *Journal of the American Chemical Society* 1999, 121, 7644–7652.
- (98) Zhdanov, V. P.; Kasemo, B. Simulation of oxygen desorption from Pt(111). *Surface Science* 1998, 415, 403–410.
- (99) Deutschmann, O.; Behrendt, F.; Warnatz, J. Modelling and simulation of heterogeneous oxidation of methane on a platinum foil. *Catalysis Today* 1994, 21, 461–470.
- (100) Quiceno, R.; Pérez-Ramírez, J.; Warnatz, J.; Deutschmann, O. Modeling the high-temperature catalytic partial oxidation of methane over platinum gauze. *Applied Catalysis A: General* 2006, 303, 166–176.
- (101) Chabane, A. Modelling of the heat and mass transfers near reactive walls : application to the oxidation of carbonaceous compounds in after-treatment devices; Université Paris-Saclay, Rueil-Malmaison, 2015.
- (102) Lagauche, M.; Larmier, K.; Jolimaitre, E.; Barthelet, K.; Chizallet, C.; Favergeon, L.; Pijolat, M. Thermodynamic Characterization of the Hydroxyl Group on the  $\gamma$ -Alumina Surface by the Energy Distribution Function. *The Journal of Physical Chemistry C* 2017, 121, 16770–16782.
- (103) Genty, E.; Sangnier, A.; Dhainaut, F.; Matrat, M.; Chizallet, C.; Dujardin, C. True intermediate and spectator species in the CO oxidation on Pt/Al<sub>2</sub>O<sub>3</sub>: Combination of modelling and operando SSITKA-IR methodology. *Submitted to ACS Catalysis*.
- (104) Bourane, A.; Bianchi, D. Oxidation of CO on a Pt/Al<sub>2</sub>O<sub>3</sub> catalyst. *Journal of Catalysis* 2003, 220, 3–12.

- (105) Bourane, A.; Dulaurent, O.; Chandès, K.; Bianchi, D. Heats of adsorption of the linear CO species on a Pt/Al<sub>2</sub>O<sub>3</sub> catalyst using FTIR spectroscopy. *Applied Catalysis A: General* 2001, *214*, 193–202.
- (106) Jbir, I.; Paredes-Nunez, A.; Khaddar-Zine, S.; Ksibir, Z.; Meunier, F.; Bianchi, D. Heat of adsorption of CO on EUROPT-1 using the AEIR method. *Applied Catalysis A: General* 2015, *505*, 309–318.
- (107) Derrouiche, S.; Gravejat, P.; Bassou, B.; Bianchi, D. Impact of potassium on the heats of adsorption of adsorbed CO species on supported Pt particles by using the AEIR method. *Applied Surface Science* 2007, *253*, 5894–5898.
- (108) Bourane, A.; Bianchi, D. Oxidation of CO on a Pt/Al<sub>2</sub>O<sub>3</sub> catalyst. *Journal of Catalysis* 2004, *222*, 499–510.
- (109) Pillonel, P.; Derrouiche, S.; Bourane, A.; Gaillard, F.; Vernoux, P.; Bianchi, D. Impact of the support on the heat of adsorption of the linear CO species on Pt-containing catalysts. *Applied Catalysis A: General* 2005, *278*, 223–231.
- (110) Kresse, G.; Hafner, J. Ab initio molecular-dynamics simulation of the liquid-metal–amorphous-semiconductor transition in germanium. *Physical Review B* 1994, *49*, 14251–14269.
- (111) Kresse, G.; Furthmüller, J. Efficiency of ab-initio total energy calculations for metals and semiconductors using a plane-wave basis set. *Computational Materials Science* 1996, *6*, 15–50.
- (112) Hohenberg, P.; Kohn, W. Inhomogeneous Electron Gas. *Physical Review B* 1964, *136*, 864–870.
- (113) Kohn, W.; Sham, L. J. Self-Consistent Equations Including Exchange and Correlation Effects. *Physical Review A* 1965, *140*, 1133–1138.
- (114) Vosko, S. H.; Wilk, L.; Nusair, M. Accurate spin-dependent electron liquid correlation energies for local spin density calculations: a critical analysis. *Canadian Journal of Physics* 1980, *58*, 1200–1211.
- (115) Perdew, J.; Wang, Y. Accurate and simple analytic representation of the electron-gas correlation energy. *Physical Review B* 1992, *45*, 13244–13249.
- (116) Wellendorff, J.; Silbaugh, T. L.; Garcia-Pintos, D.; Nørskov, J. K.; Bligaard, T.; Studt, F.; Campbell, C. T. A benchmark database for adsorption bond energies to transition metal surfaces and comparison to selected DFT functionals. *Surface Science* 2015, *640*, 36–44.
- (117) Perdew, J.; Burke, K.; Ernzerhof, M. Generalized Gradient Approximation Made Simple. *Physical review letters* 1996, *77*, 3865–3868.
- (118) Gautier, S.; Steinmann, S. N.; Michel, C.; Fleurat-Lessard, P.; Sautet, P. Molecular adsorption at Pt(111). How accurate are DFT functionals? *Physical chemistry chemical physics* 2015, *17*, 28921–28930.
- (119) Hammer, B.; Hansen, L. B.; Nørskov, J. K. Improved adsorption energetics within density-functional theory using revised Perdew-Burke-Ernzerhof functionals. *Physical Review B* 1999, *59*, 7413–7421.

- (120) Wellendorff, J.; Lundgaard, K. T.; Møgelhøj, A.; Petzold, V.; Landis, D. D.; Nørskov, J. K.; Bligaard, T.; Jacobsen, K. W. Density functionals for surface science. *Physical Review B* 2012, *85*, 316.
- (121) Digne, M.; Sautet, P.; Raybaud, P.; Euzen, P.; Toulhoat, H. Hydroxyl Groups on  $\gamma$ -Alumina Surfaces. *Journal of Catalysis* 2002, *211*, 1–5.
- (122) Digne, M.; Sautet, P.; Raybaud, P.; Euzen, P.; Toulhoat, H. Use of DFT to achieve a rational understanding of acid? *Journal of Catalysis* 2004, *226*, 54–68.
- (123) Gorczyca, A.; Moizan, V.; Chizallet, C.; Proux, O.; Del Net, W.; Lahera, E.; Hazemann, J.-L.; Raybaud, P.; Joly, Y. Monitoring morphology and hydrogen coverage of nanometric Pt/ $\gamma$ -Al<sub>2</sub>O<sub>3</sub> particles by in situ HERFD-XANES and quantum simulations. *Angewandte Chemie* 2014, *53*, 12426–12429.
- (124) Raybaud, P.; Chizallet, C.; Mager-Maury, C.; Digne, M.; Toulhoat, H.; Sautet, P. From  $\gamma$ -alumina to supported platinum nanoclusters in reforming conditions. *Journal of Catalysis* 2013, *308*, 328–340.
- (125) Hu, C. H.; Chizallet, C.; Mager-Maury, C.; Corral-Valero, M.; Sautet, P.; Toulhoat, H.; Raybaud, P. Modulation of catalyst particle structure upon support hydroxylation. *Journal of Catalysis* 2010, *274*, 99–110.
- (126) Mager-Maury, C.; Bonnard, G.; Chizallet, C.; Sautet, P.; Raybaud, P. H<sub>2</sub>-Induced Reconstruction of Supported Pt Clusters. *ChemCatChem* 2011, *3*, 200–207.
- (127) Jahel, A. N.; Moizan-Baslé, V.; Chizallet, C.; Raybaud, P.; Olivier-Fourcade, J.; Jumas, J.-C.; Avenier, P.; Lacombe, S. Effect of Indium Doping of  $\gamma$ -Alumina on the Stabilization of PtSn Alloyed Clusters Prepared by Surface Organostannic Chemistry. *The Journal of Physical Chemistry C* 2012, *116*, 10073–10083.
- (128) Sanville, E.; Kenny, S. D.; Smith, R.; Henkelman, G. Improved grid-based algorithm for Bader charge allocation. *Journal of computational chemistry* 2007, *28*, 899–908.
- (129) Henkelman, G.; Arnaldsson, A.; Jónsson, H. A fast and robust algorithm for Bader decomposition of charge density. *Computational Materials Science* 2006, *36*, 354–360.
- (130) Verlet, L. Computer Experiments on Classical Fluids. I. Thermodynamical Properties of Lennard-Jones Molecules. *Physical Review* 1967, *159*, 98–103.
- (131) Fleurat-Lessard, P.; Dayal, P. <http://pflurat.free.fr/ReactionPath.php>. Accessed April 2nd 2016.
- (132) Pulay, P. Convergence acceleration of iterative sequences. the case of scf iteration. *Chemical Physics Letters* 1980, *73*, 393–398.
- (133) Berzelius, J. J. Quelques Idées sur une nouvelle Force agissant dans les Combinaisons des Corps Organiques. *Annal. Chim. Phys.* 1836, *61*, 146–151.
- (134) Langmuir, I. Forces Near the Surfaces of Molecules. *Chem. Rev.* 1930, *6*.
- (135) Vannice, M. A. *Kinetics of catalytic reactions*; Springer: New York, 2005.
- (136) Arrhenius, S. On the Reaction Velocity of the Inversion of Cane Sugar by Acids. *Z. Phys. Chem.* 1889, *4*, 226.

- (137) Dumesic, J. A. *The microkinetics of heterogeneous Catalysis*; American Chemical Society, 1993.
- (138) Eyring H. The activated complex and the absolute rate of chemical reactions. *Chemical reviews* 1935, *17*, 65–77.
- (139) Evans, G.; Polanyi, M. Some applications of the transition state method to the calculation of reaction velocities, especially in solutions 1935.
- (140) Evans, G.; Polanyi, M. On the introduction of thermodynamic variables into reaction kinetics 1936.
- (141) Susnow, R. G.; Dean, A. M.; Green, W. H.; Peczak, P.; Broadbelt, L. J. Rate-Based Construction of Kinetic Models for Complex Systems. *The Journal of Physical Chemistry A* 1997, *101*, 3731–3740.
- (142) Touchard, S.; Fournet, R.; Glaude, P. A.; Warth, V.; Battin-Leclerc, F.; Vanhove, G.; Ribaucour, M.; Minetti, R. Modeling of the oxidation of large alkenes at low temperature. *Proceedings of the Combustion Institute* 2005, *30*, 1073–1081.
- (143) Vandewiele, N. M.; van Geem, K. M.; Reyniers, M.-F.; Marin, G. B. Genesys: Kinetic model construction using chemo-informatics. *Chemical Engineering Journal* 2012, *207-208*, 526–538.
- (144) Gao, C. W.; Allen, J. W.; Green, W. H.; West, R. H. Reaction Mechanism Generator. *Computer Physics Communications* 2016, *203*, 212–225.
- (145) Goldsmith, C. F.; West, R. H. Automatic Generation of Microkinetic Mechanisms for Heterogeneous Catalysis. *The Journal of Physical Chemistry C* 2017, *121*, 9970–9981.
- (146) Shustorovich, E. M. The UBI-QEP method: A practical theoretical approach to understanding chemistry on transition metal surfaces. *Surface Science Reports* 1998, *31*, 1–119.
- (147) Shustorovich, E. M.; Zeigarnik, A. V. The UBI-QEP method: Basic formalism and applications to chemisorption phenomena on transition metal surfaces. Chemisorption energetics. *Russian Journal of Physical Chemistry* 2006, *80*, 4–30.
- (148) Gates B., C. Supported metal clusters: synthesis, structure and catalysis. *Chemical reviews* 1995, *95*, 511–522.
- (149) Chen, A.; Holt-Hindle, P. Platinum-based nanostructured materials: synthesis, properties, and applications. *Chemical reviews* 2010, *110*, 3767–3804.
- (150) Bell, A. T. The Impact of Nanoscience on Heterogeneous Catalysis. *Science* 2003, *299*, 1688–1691.
- (151) Sun, G.; Sautet, P. Metastable Structures in Cluster Catalysis from First-Principles: Structural Ensemble in Reaction Conditions and Metastability Triggered Reactivity. *Journal of the American Chemical Society* 2018, *140*, 2812–2820.
- (152) Sattler, J. J.; Ruiz-Martinez, J.; Santillan-Jimenez, E.; Weckhuysen, B. M. Catalytic dehydrogenation of light alkanes on metals and metal oxides. *Chemical reviews* 2014, *114*, 10613–10653.

- (153) Avenier, P.; Bazer-Bachi, D.; Bazer-Bachi, F.; Chizallet, C.; Deleau, F.; Diehl, F.; Gornay, J.; Lemaire, E.; Moizan-Basle, V.; Plais, C.; Raybaud, P.; Richard, F.; Lacombe, S. Catalytic Reforming. *Oil & Gas Science and Technology* 2016, *71*, 41–59.
- (154) Burch, R. Knowledge and Know-How in Emission Control for Mobile Applications. *Catalysis Reviews* 2011, *46*, 271–334.
- (155) Le Goff, P.-Y.; Kostka, W.; Ross, J. Catalytic Reforming, In Springer Handbook of Petroleum Technology; Springer, Ed. 2017.
- (156) Morozan, A.; Joussetme, B.; Palacin, S. Low-platinum and platinum-free catalysts for the oxygen reduction reaction at fuel cell cathodes. *Energy & Environmental Science* 2011, *4*, 1238–1254.
- (157) Gasteiger, H. A.; Kocha, S. S.; Sompalli, B.; Wagner, F. T. Activity benchmarks and requirements for Pt, Pt-alloy, and non-Pt oxygen reduction catalysts for PEMFCs. *Applied Catalysis B: Environmental* 2005, *56*, 9–35.
- (158) Marković, N. M.; Schmidt, T. J.; Stamenković, V.; Ross, P. N. Oxygen Reduction Reaction on Pt and Pt Bimetallic Surfaces: A Selective Review. *Fuel Cells* 2001, *1*, 105–106.
- (159) European commission. *Critical raw materials for the EU*, 2010.
- (160) Roduner, E. Size matters: why nanomaterials are different. *Chemical Society reviews* 2006, *35*, 583–592.
- (161) Roldan Cuenya, B.; Behafarid, F. Nanocatalysis : Size- and shape-dependent chemisorption and catalytic reactivity. *Surface Science Reports* 2015, *70*, 135–187.
- (162) Allian, A. D.; Takanabe, K.; Fujidala, K. L.; Hao, X.; Truex, T. J.; Cai, J.; Buda, C.; Neurock, M.; Iglesia, E. Chemisorption of CO and mechanism of CO oxidation on supported platinum nanoclusters. *Journal of the American Chemical Society* 2011, *133*, 4498–4517.
- (163) García-Diéguez, M.; Chin, Y.-H.; Iglesia, E. Catalytic reactions of dioxygen with ethane and methane on platinum clusters. *Journal of Catalysis* 2012, *285*, 260–272.
- (164) Weaver, J. F.; Chen, J.-J.; Gerrard, A. L. Oxidation of Pt(111) by gas-phase oxygen atoms. *Surface Science* 2005, *592*, 83–103.
- (165) Légaré, P. Interaction of oxygen with the Pt(111) surface in wide conditions range. A DFT-based thermodynamical simulation. *Surface Science* 2005, *580*, 137–144.
- (166) Pang, Q.; Zhang, Y.; Zhang, J.-M.; Xu, K.-W. Structural and electronic properties of atomic oxygen adsorption on Pt(111). *Applied Surface Science* 2011, *257*, 3047–3054.
- (167) Elg, A.-P.; Eisert, F.; Rosén, A. The temperature dependence of the initial sticking probability of oxygen on Pt(111) probed with second harmonic generation. *Surface Science* 1997, *382*, 57–66.
- (168) Hwang, C.-P.; Yeh, C.-T. Platinum-oxide species formed by oxidation of platinum crystallites supported on alumina. *Journal of Molecular Catalysis A: Chemical* 1996, *112*, 295–302.

- (169) Fantauzzi, D.; Mueller, J. E.; Sabo, L.; van Duin, Adri C T; Jacob, T. Surface Buckling and Subsurface Oxygen: Atomistic Insights into the Surface Oxidation of Pt(111). *ChemPhysChem* 2015, *16*, 2797–2802.
- (170) Salmerón, M.; Brewer, L.; Somorjai, G. A. The Structure and Stability of Surface Platinum Oxide and of Oxides of Other Noble Metals. *Surface Science* 1981, *112*, 207–228.
- (171) Krasnikov, S. A.; Murphy, S.; Berdunov, N.; McCoy, A. P.; Radican, K.; Shvets, I. V. Self-Limited Growth of Triangular PtO<sub>2</sub> Nanoclusters on the Pt(111) Surface. *Nanotechnology* 2010, *21*, 335301.
- (172) Devarajan, S. P.; Hinojosa, J. A.; Weaver, J. F. STM study of high-coverage structures of atomic oxygen on Pt(111). *Surface Science* 2008, *602*, 3116–3124.
- (173) Van Spronsen, M. A.; Frenken, J. W. M.; Groot, I. M. Observing the oxidation of platinum. *Nature communications* 2017, *8*, 429.
- (174) Bray, J. M.; Smith, J. L.; Schneider, W. F. Coverage-Dependent Adsorption at a Low Symmetry Surface. *Topics in Catalysis* 2014, *57*, 89–105.
- (175) Jenkins, S.; Petersen, M.; King, D. Comparative theory of missing-row reconstructions: Pt{110}, Pt{211} and Pt{311}. *Surface Science* 2001, *494*, 159–165.
- (176) Euzen, P.; Raybaud, P.; Krokidis, X.; Toulhoat, H.; Loarer, J. L.; Jolivet, J.-P.; Froidefond, C. Alumina, In Handbook of Porous Solids; Schüth, F., Sing, K. S. W., Weitkamp, J., Eds.; Wiley-VCH: Weinheim, 2002.
- (177) Sinkler, W.; Sanchez, S. I.; Bradley, S. A.; Wen, J.; Mishra, B.; Kelly, S. D.; Bare, S. R. Aberration-Corrected Transmission Electron Microscopy and In Situ XAFS Structural Characterization of Pt/ $\gamma$ -Al<sub>2</sub>O<sub>3</sub> Nanoparticles. *ChemCatChem* 2015, *7*, 3779–3787.
- (178) Nellist, P. D.; Pennycook, S. J. Direct Imaging of the Atomic Configuration of Ultradispersed Catalysts. *Science* 1996, *274*, 413–415.
- (179) Vayssilov, G. N.; Petrova, G. P.; Shor, E. A. I.; Nasluzov, V. A.; Shor, A. M.; St Petkov, P.; Rösch, N. Reverse hydrogen spillover on and hydrogenation of supported metal clusters: insights from computational model studies. *Physical chemistry chemical physics* 2012, *14*, 5879–5890.
- (180) Trinchero, A.; Klacar, S.; Paz-Borbón, L. O.; Hellman, A.; Grönbeck, H. Oxidation at the Subnanometer Scale. *The Journal of Physical Chemistry C* 2015, *119*, 10797–10803.
- (181) Zhang, W.; Sumer, A.; Jellinek, J.; Cheng, D. Morphology Tailoring of Pt Nanocatalysts for the Oxygen Reduction Reaction. *ChemNanoMat* 2015, *1*, 482–488.
- (182) Xu, Y.; Shelton, W. A.; Schneider, W. F. Effect of particle size on the oxidizability of platinum clusters. *The journal of physical chemistry. A* 2006, *110*, 5839–5846.
- (183) Xu, Y.; Shelton, W. A.; Schneider, W. F. Thermodynamic equilibrium compositions, structures, and reaction energies of Pt(x)O(y) (x = 1-3) clusters

- predicted from first principles. *The journal of physical chemistry. B* 2006, *110*, 16591–16599.
- (184) Jennings, P. C.; Aleksandrov, H. A.; Neyman, K. M.; Johnston, R. L. DFT studies of oxygen dissociation on the 116-atom platinum truncated octahedron particle. *Physical chemistry chemical physics* 2014, *16*, 26539–26545.
- (185) Jennings, P. C.; Aleksandrov, H. A.; Neyman, K. M.; Johnston, R. L. A DFT study of oxygen dissociation on platinum based nanoparticles. *Nanoscale* 2014, *6*, 1153–1165.
- (186) Hu, C. H.; Chizallet, C.; Toulhoat, H.; Raybaud, P. Structural, Energetic, and Electronic Trends in Low-Dimensional Late-Transition-Metal Systems. *Physical Review B* 2009, *79*, 195416.
- (187) Li, L.; Larsen, A. H.; Romero, N. A.; Morozov, V. A.; Glinsvad, C.; Abild-Pedersen, F.; Greeley, J.; Jacobsen, K. W.; Nørskov, J. K. Investigation of Catalytic Finite-Size-Effects of Platinum Metal Clusters. *The journal of physical chemistry letters* 2013, *4*, 222–226.
- (188) Holby, E. F.; Greeley, J.; Morgan, D. Thermodynamics and Hysteresis of Oxide Formation and Removal on Platinum (111) Surfaces. *The Journal of Physical Chemistry C* 2012, *116*, 9942–9946.
- (189) Fu, Q.; Yang, J.; Luo, Y. A First Principles Study on the Dissociation and Rotation Processes of a Single O<sub>2</sub> Molecule on the Pt(111) Surface. *The Journal of Physical Chemistry C* 2011, *115*, 6864–6869.
- (190) Zhu, T.; Sun, S.-G.; van Santen, Rutger A.; Hensen, E. J. M. Reconstruction of Clean and Oxygen-Covered Pt(110) Surfaces. *The Journal of Physical Chemistry C* 2013, *117*, 11251–11257.
- (191) Liu, D.-J.; Evans, J. W. Interactions between oxygen atoms on Pt(100): implications for ordering during chemisorption and catalysis. *ChemPhysChem* 2010, *11*, 2174–2181.
- (192) Watwe, R. M.; Cortright, R. D.; Mavrikakis, M.; Norskov, J. K.; Dumesic, J. A. Density Functional Theory Studies of the Adsorption of Ethylene and Oxygen on Pt(111) and Pt<sub>3</sub>Sn(111). *The Journal of chemical physics* 2001, *114*, 4663–4668.
- (193) Nguyen, T. Q.; Escaño, M. C. S.; Nakanishi, H.; Kasai, H.; Maekawa, H.; Osumi, K.; Sato, K. DFT+U study on the oxygen adsorption and dissociation on CeO<sub>2</sub>-supported platinum cluster. *Applied Surface Science* 2014, *288*, 244–250.
- (194) Mei, D.; Kwak, J. H.; Hu, J.; Cho, S. J.; Szanyi, J.; Allard, L. F.; Peden, C. H. F. Unique Role of Anchoring Penta-Coordinated Al<sup>3+</sup> Sites in the Sintering of  $\gamma$ -Al<sub>2</sub>O<sub>3</sub> - Supported Pt Catalysts. *The journal of physical chemistry letters* 2010, *1*, 2688–2691.
- (195) Wang, X.; Van Bokhoven, J. A.; Palagin, D. Ostwald ripening versus single atom trapping: towards understanding platinum particle sintering. *Physical chemistry chemical physics* 2017, *19*, 30513–30519.
- (196) Parker, D. H.; Bartram, M. E.; Koel, B. E. Study of high coverages of atomic oxygen on the Pt(111) surface. *Surface Science* 1989, *217*, 489–510.

- (197) Badan, C.; Farber, R. G.; Heyrich, Y.; Koper, Marc T. M.; Killelea, D. R.; Juurlink, L. B. F. Step-Type Selective Oxidation of Platinum Surfaces. *The Journal of Physical Chemistry C* 2016, *120*, 22927–22935.
- (198) Wang, C.-B.; Yeh, C.-T. Effects of Particle Size on the Progressive Oxidation of Nanometer Platinum by Dioxygen. *Journal of Catalysis* 1998, *178*, 450–456.
- (199) Olsson, L.; Westerberg, B.; Persson, H.; Fridell, E.; Skoglundh, M.; Andersson, B. A Kinetic Study of Oxygen Adsorption/Desorption and NO Oxidation over Pt/Al<sub>2</sub>O<sub>3</sub> Catalysts. *The Journal of Physical Chemistry B* 1999, *103*, 10433–10439.
- (200) Mihai, O.; Creaser, D.; Olsson, L. Adsorption and Oxidation Investigations over Pt/Al<sub>2</sub>O<sub>3</sub> Catalyst. *Catalysts* 2016, *6*, 73.
- (201) Wartnaby, C. E.; Stuck, A.; Yeo, Y. Y.; King, D. A. Microcalorimetric Heats of Adsorption for CO, NO, and Oxygen on Pt{110}. *The Journal of Physical Chemistry* 1996, *100*, 12483–12488.
- (202) Dessal, C.; Sangnier, A.; Chizallet, C.; Dujardin, C.; Morfin, F.; Rousset, J. L.; Aouine, M.; Afanasiev. Atmosphere-Dependent Stability and Mobility of Catalytic Pt single Atoms and Clusters on  $\gamma$ -Al<sub>2</sub>O<sub>3</sub> submitted.
- (203) Bonzel, H. P.; Ku, R. On the kinetics of oxygen adsorption on a Pt(111) surface. *Surface Science* 1973, *40*, 85–101.
- (204) Hopster, H.; Ibach, H.; Comsa, G. Catalytic Oxidation of Carbon Monoxide on Stepped Platinum(111) Surfaces. *Journal of Catalysis* 1977, *46*, 37–48.
- (205) Deutschmann, O.; Behrendt, F.; Warnatz, J. Modelling and simulation of heterogeneous oxidation of methane on a platinum foil. *Catalysis Today* 1994, *21*, 461–470.
- (206) Gland, J. L.; Korchak, V. N. The adsorption of oxygen on a stepped platinum single crystal surface. *Surface Science* 1978, *75*, 733–750.
- (207) Schwaha, K.; Bechtold, E. The adsorption of oxygen on the stepped Pt(S)-[9(111)x(111)] face. *Surface Science* 1977, *65*, 277–286.
- (208) Yin, C.; Negreiros, F. R.; Barcaro, G.; Beniya, A.; Sementa, L.; Tyo, E. C.; Bartling, S.; Meiwes-Broer, K.-H.; Seifert, S.; Hirata, H.; Isomura, N.; Nigam, S.; Majumder, C.; Watanabe, Y.; Fortunelli, A.; Vajda, S. Alumina-supported sub-nanometer Pt<sub>10</sub> clusters. *Journal of Materials Chemistry A* 2017, *5*, 4923–4931.
- (209) Herz, R. K.; McCready, D. F. Identification of a weak adsorption state of carbon monoxide on highly dispersed, alumina-supported platinum. *Journal of Catalysis* 1982, *81*, 358–368.
- (210) Gland, J. L.; McClellan, M. R. Carbon monoxide adsorption on the kinked Pt(321) surface. *Surface Science* 1981, *112*, 63–77.
- (211) Ogletree, D., F.; Van Hove, M. A.; Somorjai, G. Leed intensity analysis of the structures of clean Pt(111) and of CO adsorbed on Pt(111) in the c(4x2) arrangement. *Surface Science* 1986, *173*, 351–365.
- (212) Steininger, H.; Lehwald, S.; Ibach, H. On the adsorption of CO on Pt(111). *Surface Science* 1982, *123*, 264–282.

- (213) Heyden, B. E.; Bradshaw, A. M. The adsorption of CO on Pt(111) studied by infrared reflection—Absorption spectroscopy. *Surface Science* 1983, *125*, 787–802.
- (214) Hammer, B.; Nielsen, O. H.; Nørskov, J. K. Structure sensitivity in adsorption: CO interaction with stepped and reconstructed Pt surfaces. *Catalysis Letters* 1997, *46*, 31–35.
- (215) Shigeishi, R. A.; King, D. A. Chemisorption of carbon monoxide on platinum {111}: Reflection-absorption infrared spectroscopy. *Surface Science* 1976, *58*, 379–396.
- (216) Hayden, B. E.; Kretzschmar, K.; Bradshaw, A. M.; Greenler, R. G. An infrared study of the adsorption of CO on a stepped platinum surface. *Surface Science* 1985, *149*, 394–406.
- (217) Greenler, R. G.; Burch, K. D.; Kretzschmar, K.; Klauser, R.; Bradshaw, A. M.; Hayden, B. E. Stepped single-crystal as models for small catalysts particles. *Surface Science* 1985, *152/153*, 338–345.
- (218) Cybulskis, V. J.; Wang, J.; Pazmiño, J. H.; Ribeiro, F. H.; Delgass, W. N. Isotopic transient studies of sodium promotion of Pt/Al<sub>2</sub>O<sub>3</sub> for the water–gas shift reaction. *Journal of Catalysis* 2016, *339*, 163–172.
- (219) Couble, J.; Bianchi, D. Experimental microkinetic approach of the CO/H<sub>2</sub> reaction on Pt/Al<sub>2</sub>O<sub>3</sub> using the Temkin formalism. 1. Competitive chemisorption between adsorbed CO and hydrogen species in the absence of reaction. *Journal of Catalysis* 2017, *352*, 672–685.
- (220) Vannice, M. A.; Twu, C. C. Extinction coefficients and integrated intensities for linear- and bridged-bonded CO on platinum. *The Journal of chemical physics* 1981, *75*, 5944–5948.
- (221) Bourane, A.; Bianchi, D. Heats of adsorption of the linear CO species on Pt/Al<sub>2</sub>O<sub>3</sub> using infrared spectroscopy. *Journal of Catalysis* 2003, *218*, 447–452.
- (222) Bourane, A.; Dulaurent, O.; Bianchi, D. Heats of Adsorption of the Linear CO Species Adsorbed on a Pt/Al<sub>2</sub>O<sub>3</sub> Catalyst in the Presence of Coadsorbed Species Using FTIR Spectroscopy. *Langmuir* 2001, *17*, 5496–5502.
- (223) Bourane, A.; Derrouiche, S.; Bianchi, D. Impact of Pt dispersion on the elementary steps of CO oxidation by O<sub>2</sub> over Pt/Al<sub>2</sub>O<sub>3</sub> catalysts. *Journal of Catalysis* 2004, *228*, 288–297.
- (224) Luo, J. S.; Tobin, R. G.; Lambert, D. K.; Fisher, G. B.; DiMaggio, C. L. CO adsorption site occupation on Pt(335): a quantitative investigation using TPD and EELS. *Surface Science* 1992, No. 274, 53–62.
- (225) Grinberg, I.; Yourdshahyan, Y.; Rappe, A. M. CO on Pt(111) puzzle: A possible solution. *Journal of chemical physics* 2002, *117*, 2264–2270.
- (226) Feibelman, P. J.; Hammer, B.; Nørskov, J. K.; Wagner, F.; Scheffler, M.; Stumpf, R.; Watwe, R.; Dumesic, J. The CO/Pt(111) Puzzle. *The Journal of Physical Chemistry B* 2001, *105*, 4018–4025.

- (227) Gajdos, M.; Eichler, A.; Hafner J. CO adsorption on close-packed transition and noble metal surfaces: Trends from ab initio calculations. *Journal of Physics: Condensed Matter* 2004, *16*, 1141–1164.
- (228) B. Hammer, Y. Morikawa, J. K. Norskov. CO Chemisorption at Metal Surfaces and Overlayers. *Physical review letters* 1996, *76*, 2141–2144.
- (229) Schimka, L.; Harl, J.; Stroppa, A.; Gruneis, A.; Marsman, M.; Mittendorfer, F.; Kresse, G. Accurate surface and adsorption energies from many-body perturbation theory. *Nature materials* 2010, *9*, 741–744.
- (230) Dupont, C.; Jugnet, Y.; Loffreda, D. Theoretical evidence of PtSn alloy efficiency for CO oxidation. *Journal of the American Chemical Society* 2006, *128*, 9129–9136.
- (231) Wang, J. G.; Li, W. X.; Borg, M.; Gustafson, J.; Mikkelsen, A.; Pedersen, T. M.; Lundgren, E.; Weissenrieder, J.; Klikovits, J.; Schmid, M.; Hammer, B.; Andersen, J. N. One-dimensional PtO<sub>2</sub> at Pt steps: formation and reaction with CO. *Physical review letters* 2005, *95*, 256102.
- (232) Orita, H.; Inada, Y. DFT investigation of CO adsorption on Pt(211) and Pt(311) surfaces from low to high coverage. *The journal of physical chemistry. B* 2005, *109*, 22469–22475.
- (233) Shan, B.; Zhao, Y.; Hyun, J.; Kapur, N.; Nicholas, J. B.; Cho, K. Coverage-Dependent CO Adsorption Energy from First-Principles Calculations. *The Journal of Physical Chemistry C* 2009, *113*, 6088–6092.
- (234) Davis, J. B.; Baletto, F.; Johnston, R. L. The Effect of Dispersion Correction on the Adsorption of CO on Metallic Nanoparticles. *The journal of physical chemistry. A* 2015, *119*, 9703–9709.
- (235) Pedersen, M. O.; Bocquet, M. L.; Sautet, P.; Laegsgaard, E.; Stensgaard, I.; Besenbacher, F. CO Pt(111) : binding site assignment from the interplay between measured and calculated STM images. *Chemical Physics Letters* 1999, *299*, 403–409.
- (236) Sangnier, A.; Chizallet, C.; Matrat, M.; Nicolle, N.; Dujardin, C. A multi-scale approach to the dissociative adsorption of oxygen on highly-dispersed Pt/ $\gamma$ -Al<sub>2</sub>O<sub>3</sub>. *Submitted to ACS Catalysis*.
- (237) Longwitz, S. R.; Schnadt, J.; Vestergaard, E. K.; Vang, R. T.; Stensgaard, I.; Brune, H.; Besenbacher, F. High-Coverage Structures of Carbon Monoxide Adsorbed on Pt(111) Studied by High-Pressure Scanning Tunneling Microscopy. *The Journal of Physical Chemistry B* 2004, *108*, 14497–14502.
- (238) Barth, R.; Pitchai, R.; Anderson, R., L.; Verykios, X. E. Thermal Desorption-Infrared Study of Carbon Monoxide by Alumina-Supported Platinum. *Journal of Catalysis* 1989, *116*, 61–70.
- (239) Bourane, A.; Dulaurent, O.; Bianchi, D. Heats of Adsorption of Linear and Multibound Adsorbed CO Species on a Pt/Al<sub>2</sub>O<sub>3</sub> Catalyst Using in Situ Infrared Spectroscopy under Adsorption Equilibrium. *Journal of Catalysis* 2000, *196*, 115–125.

- (240) Keren, I.; Sheintuch, M. Modeling and analysis of spatiotemporal oscillatory patterns during CO oxidation in the catalytic converter. *Chemical Engineering Science* 2000, *55*, 1461–1475.
- (241) Carlsson, P.; Osterlund, L.; Thormahlen, P.; Palmqvist, A.; Fridell, E.; Jansson, J.; Skoglundh, M. A transient in situ FTIR and XANES study of CO oxidation over Pt/Al<sub>2</sub>O<sub>3</sub> catalysts. *Journal of Catalysis* 2004, *226*, 422–434.
- (242) Sales, B. C.; Turner J. E.; Maple, M. B. Oscillatory oxidation of CO over Pt, Pd and Ir catalysts: theory. *Surface Science* 1981, *114*, 381–394.
- (243) Salomons, S.; Votsmeier, M.; Hayes, R. E.; Drochner, A.; Vogel, H.; Gieshof, J. CO and H<sub>2</sub> oxidation on a platinum monolith diesel oxidation catalyst. *Catalysis Today* 2006, *117*, 491–497.
- (244) Salomons, S.; Hayes, R. E.; Votsmeier, M.; Drochner, A.; Vogel, H.; Malmberg, S.; Gieshoff, J. On the use of mechanistic CO oxidation models with a platinum monolith catalyst. *Applied Catalysis B: Environmental* 2007, *70*, 305–313.
- (245) Voltz, S. E.; Morgan, C. R.; Liederman, D.; Jacob, S. M. Kinetic Study of Carbon Monoxide and Propylene Oxidation on Platinum Catalysts. *Industrial & Engineering Chemistry Product Research and Development* 1973, *12*, 294–301.
- (246) Langmuir I. The mechanism of the catalytic action of platinum in the reactions  $2\text{CO} + \text{O}_2 = 2\text{CO}$ , and  $2\text{H}_2 + \text{O}_2 = 2\text{H}_2\text{O}$ . *Zeit. Physik. Chem.* 1922, *53*, 84–111.
- (247) Alayon, E.; Singh, J.; Nachtegaal, M.; Harfouche, M.; van Bokhoven, J. A. On highly active partially oxidized platinum in carbon monoxide oxidation over supported platinum catalysts. *Journal of Catalysis* 2009, *263*, 228–238.
- (248) Gracia, F.; Bollmann, L.; Wolf, E.; Miller, J.; Kropf, A. In situ FTIR, EXAFS, and activity studies of the effect of crystallite size on silica-supported Pt oxidation catalysts. *Journal of Catalysis* 2003, *220*, 382–391.
- (249) Singh, J.; Van Bokhoven, J. A. Structure of alumina supported platinum catalysts of different particle size during CO oxidation using in situ IR and HERFD XAS. *Catalysis Today* 2010, *155*, 199–205.
- (250) Yang, J.; Tschamber, V.; Habermacher, D.; Garin, F.; Gilot, P. Effect of sintering on the catalytic activity of a Pt based catalyst for CO oxidation. *Applied Catalysis B: Environmental* 2008, *83*, 229–239.
- (251) Szabó, A.; Henderson, M. A.; Yates, J. T. Oxidation of CO by oxygen on a stepped platinum surface. *The Journal of chemical physics* 1992, *96*, 6191–6202.
- (252) Siera, J.; Van Silfhout, R.; Rutten, F.; Nieuwenhuys, B. E. A Comparative Kinetic Study of the CO-O<sub>2</sub> Reaction Over Pt-Rh (111), (100), (410) and (210) Single Crystal Surfaces. *Surface Science and Catalysis Elsevier* 1991, *71*, 395–407.
- (253) Wang, C.-B.; Lin, H.-K.; Hsu, S.-N.; Huang, T.-H.; Chiu, H.-C. Enthalpies of reduction–oxidation of alumina-supported platinum. *Journal of Molecular Catalysis A: Chemical* 2002, *188*, 201–208.
- (254) Atalik, B.; Uner, D. Structure sensitivity of selective CO oxidation over Pt/γ-Al<sub>2</sub>O<sub>3</sub>. *Journal of Catalysis* 2006, *241*, 268–275.

- (255) Hendriksen, B. L. M.; Bobaru, S.; Frenken, J. W. M. Bistability and oscillations in CO oxidation studied with scanning tunnelling microscopy inside a reactor. *Catalysis Today* 2005, *105*, 234–243.
- (256) Slavinskaya, E. M.; Stonkus, O. A.; Gulyaev, R. V.; Ivanova, A. S.; Zaikovskii, V. I.; Kuznetsov, P. A.; Boronin, A. I. Structural and chemical states of palladium in Pd/Al<sub>2</sub>O<sub>3</sub> catalysts under self-sustained oscillations in reaction of CO oxidation. *Applied Catalysis A: General* 2011, *401*, 83–97.
- (257) Ertl, G. Reactions at surfaces: from atoms to complexity (Nobel Lecture). *Angewandte Chemie* 2008, *47*, 3524–3535.
- (258) Krischer, K.; Eiswirth, M.; Ertl, G. Oscillatory CO oxidation on Pt(110). *The Journal of chemical physics* 1992, *96*, 9161–9172.
- (259) Eiswirth, M.; Ertl, G. Kinetic oscillations in the catalytic CO oxidation on a Pt(110) surface. *Surface Science* 1986, *177*, 90–100.
- (260) Jakubith, S.; Rotermund, H. H.; Engel, W.; Oertzen, A. von; Ertl, G. Spatiotemporal concentration patterns in a surface reaction: Propagating and standing waves, rotating spirals, and turbulence. *Physical review letters* 1990, *65*, 3013–3016.
- (261) Ivanova, A. S.; Slavinskaya, E. M.; Gulyaev, R. V.; Zaikovskii, V. I.; Stonkus, O.; Danilova, I. G.; Plyasova, L. M.; Polukhina, I. A.; Boronin, A. I. Metal–support interactions in Pt/Al<sub>2</sub>O<sub>3</sub> and Pd/Al<sub>2</sub>O<sub>3</sub> catalysts for CO oxidation. *Applied Catalysis B: Environmental* 2010, *97*, 57–71.
- (262) Kalamaras, C. M.; Olympiou, G. G.; Efstathiou, A. M. The water-gas shift reaction on Pt/ $\gamma$ -Al<sub>2</sub>O<sub>3</sub> catalyst. *Catalysis Today* 2008, *138*, 228–234.
- (263) Boubnov, A.; Gänzler, A.; Conrad, S.; Casapu, M.; Grunwaldt, J.-D. Oscillatory CO Oxidation Over Pt/Al<sub>2</sub>O<sub>3</sub> Catalysts Studied by In situ XAS and DRIFTS. *Topics in Catalysis* 2013, *56*, 333–338.
- (264) Liu, H.; Jia, A.; Yuwang; Luo, M.; Lu, J. Enhanced CO oxidation over potassium-promoted Pt/Al<sub>2</sub>O<sub>3</sub> catalysts. *Chinese Journal of Catalysis* 2015, *36*, 1976–1986.
- (265) Cant N. W.; Hicks P. C.; Lennon B. S. Steady-State Oxidation of Carbon Monoxide over Supported Noble Metals with Particular Reference to Platinum. *Journal of Catalysis* 1978, *54*, 372–383.
- (266) Dobrin, S. CO oxidation on Pt nanoclusters, size and coverage effects: a density functional theory study. *Physical chemistry chemical physics* 2012, *14*, 12122–12129.
- (267) Qiao, B.; Wang, A.; Yang, X.; Allard, L. F.; Jiang, Z.; Cui, Y.; Liu, J.; Li, J.; Zhang, T. Single-atom catalysis of CO oxidation using Pt<sub>1</sub>/FeO<sub>x</sub>. *Nature chemistry* 2011, *3*, 634–641.
- (268) Digne, M.; Sautet, P.; Raybaud, P.; Euzen, P.; Toulhoat, H. Hydroxyl Groups on  $\gamma$ -Alumina Surfaces. *Journal of Catalysis* 2002, *211*, 1–5.
- (269) Healy, D.; Donato, N. S.; Aul, C. J.; Petersen, E. L.; Zinner, C. M.; Bourque, G.; Curran, H. J. Isobutane ignition delay time measurements at high pressure and detailed chemical kinetic simulations. *Combustion and flame* 2010, *157*, 1540–1551.

- (270) Healy, D.; Donato, N. S.; Aul, C. J.; Petersen, E. L.; Zinner, C. M.; Bourque, G.; Curran, H. J. n-Butane. *Combustion and flame* 2010, *157*, 1526–1539.
- (271) Vincent, R. S.; Lindstedt, R. P.; Malik, N. A.; Reid, I.; Messenger, B. E. The chemistry of ethane dehydrogenation over a supported platinum catalyst. *Journal of Catalysis* 2008, *260*, 37–64.
- (272) Wu, J. C. S.; Fan, Y.-C.; Lin, C.-A. Deep Oxidation of Methanol Using a Novel Pt/Boron Nitride Catalyst. *Ind. Eng. Chem. Res.* 2003, *42*, 3225–3229.
- (273) Busca, G. Infrared studies of the reactive adsorption of organic molecules over metal oxides and of the mechanisms of their heterogeneously-catalyzed oxidation. *Catalysis Today* 1996, *27*, 457–496.
- (274) Busca, G.; Lamotte, J.; Lavalley, J.-C.; Lorenzelli, V. FT-IR study of the adsorption and transformation of formaldehyde on oxide surfaces. *Journal of American Chemical Society* 1987, *109*, 5197–5202.
- (275) Haneda, M.; Watanabe, T.; Kamiuchi, N.; Ozawa, M. Effect of platinum dispersion on the catalytic activity of Pt/Al<sub>2</sub>O<sub>3</sub> for the oxidation of carbon monoxide and propene. *Applied Catalysis B: Environmental* 2013, *142-143*, 8–14.
- (276) Fu, Q.; Yang, J.; Luo, Y. A First Principles Study on the Dissociation and Rotation Processes of a Single O<sub>2</sub> Molecule on the Pt(111) Surface. *The Journal of Physical Chemistry C* 2011, *115*, 6864–6869.
- (277) Stamatakis, M.; Chen, Y.; Vlachos, D. G. First-Principles-Based Kinetic Monte Carlo Simulation of the Structure Sensitivity of the Water–Gas Shift Reaction on Platinum Surfaces. *The Journal of Physical Chemistry C* 2011, *115*, 24750–24762.
- (278) Ferrin, P.; Kandoi, S.; Nilekar, A. U.; Mavrikakis, M. Hydrogen adsorption, absorption and diffusion on and in transition metal surfaces: a DFT study. *Surface Science* 2012, *606*, 679–689.
- (279) Greeley, J.; Mavrikakis, M. Competitive Paths for Methanol Decomposition on Pt(111). *Journal of the American Chemical Society* 2004, *126*, 3910–3919.
- (280) Psfogiannakis, G.; St-Aman, A.; Ternan, M. Methane oxidation mechanism on Pt(111): A cluster model study. *The Journal of Physical Chemistry B* 2006, *110*, 24593–24605.
- (281) Meng-Sheng Liao; Chak-Tong Au; Ching-Fai Ng. Methane dissociation on Ni, Pd, Pt and Cu metal (111) surfaces — a theoretical comparative study. *Chemical Physics Letters* 1997, *272*, 445–452.
- (282) Jacob, T.; Goddard, W. A. Chemisorption of (CH<sub>x</sub> and C<sub>2</sub>H<sub>y</sub>) hydrocarbons on Pt(111) clusters and surfaces from DFT studies. *The journal of physical chemistry. B* 2005, *109*, 297–311.
- (283) Jacob, T. The Mechanism of Forming H<sub>2</sub>O from H<sub>2</sub> and O<sub>2</sub> over a Pt Catalyst via Direct Oxygen Reduction. *Fuel Cells* 2006, *6*, 159–181.
- (284) Christmann, K.; Ertl, G.; Pignet, T. Adsorption of hydrogen on a Pt(111) surface. *Surface Science* 1976, *54*, 365–392.

- (285) Burch, R.; Crittle, D. J.; Hayes, M. J. C–H bond activation in hydrocarbon oxidation on heterogeneous catalysts. *Catalysis Today* 1999, *47*, 229–234.
- (286) Saliccioli, M.; Edie, S. M.; Vlachos, D. G. Adsorption of Acid, Ester, and Ether Functional Groups on Pt: Fast Prediction of Thermochemical Properties of Adsorbed Oxygenates via DFT-Based Group Additivity Methods. *The Journal of Physical Chemistry C* 2012, *116*, 1873–1886.
- (287) Saliccioli, M.; Chen, Y.; Vlachos, D. G. Density Functional Theory-Derived Group Additivity and Linear Scaling Methods for Prediction of Oxygenate Stability on Metal Catalysts: Adsorption of Open-Ring Alcohol and Polyol Dehydrogenation Intermediates on Pt-Based Metals. *The Journal of Physical Chemistry C* 2010, *114*, 20155–20166.
- (288) Nykänen, L.; Honkala, K. Density Functional Theory Study on Propane and Propene Adsorption on Pt(111) and PtSn Alloy Surfaces. *The Journal of Physical Chemistry C* 2011, *115*, 9578–9586.
- (289) Alcala, R. DFT studies for cleavage of C-C and C-O bonds in surface species derived from ethanol on Pt(111). *Journal of Catalysis* 2003, *218*, 178–190.
- (290) Basaran, D.; Aleksandrov, H. A.; Chen, Z.-X.; Zhao, Z.-J.; Rösch, N. Decomposition of ethylene on transition metal surfaces M(111). A comparative DFT study of model reactions for M=Pd, Pt, Rh, Ni. *Journal of Molecular Catalysis A: Chemical* 2011, *344*, 37–46.
- (291) Kua, J.; Faglioni, F.; Goddard, W. A. Thermochemistry for Hydrocarbon Intermediates Chemisorbed on Metal Surfaces: CH<sub>n</sub>-m(CH<sub>3</sub>)<sub>m</sub> with n=1, 2, 3 and m≤n on Pt, Ir, Os, Pd, Rh, and Ru. *Journal of the American Chemical Society* 2000, *122*, 2309–2321.
- (292) Aleksandrov, H. A.; Moskaleva, L. V.; Zhao, Z.-J.; Basaran, D.; Chen, Z.-X.; Mei, D.; Rösch, N. Ethylene conversion to ethynidyne on Pd(111) and Pt(111). *Journal of Catalysis* 2012, *285*, 187–195.
- (293) Marceau, E.; Che, M.; Saint-Just, J.; Tatibouët, J. M. Influence of chlorine ions in Pt/Al<sub>2</sub>O<sub>3</sub> catalysts for methane total oxidation. *Catalysis Today* 1996, *29*, 415–419.
- (294) Gracia, F. J.; Miller, J. T.; Kropf, A. J.; Wolf, E. E. Kinetics, FTIR, and Controlled Atmosphere EXAFS Study of the Effect of Chlorine on Pt-Supported Catalysts during Oxidation Reactions. *Journal of Catalysis* 2002, *209*, 341–354.
- (295) Todd H. Ballinger and John T. Yates. IR spectroscopic detection of Lewis acid sites on alumina using adsorbed carbon monoxide. Correlation with aluminum-hydroxyl group removal.
- (296) Liu, X. DRIFTS Study of Surface of  $\gamma$ -Alumina and Its Dehydroxylation. *The Journal of Physical Chemistry C* 2008, *112*, 5066–5073.